DEVELOPMENT OF AN EFFECTIVE MULTI-OBJECTIVE OPTIMIZATION STRATEGY FOR THE MANUFACTURING OF RESIN TRANSFER MOULDED COMPOSITE PARTS

Submitted in partial fulfilment of the requirements for the award of the degree of

DOCTOR OF PHILOSOPHY

in

CHEMICAL ENGINEERING

by

Mrs. ZADE ANITA DNYANBA

(Roll No. 718151)

Under the Supervision of

Prof. RAGHU RAJA PANDIYAN KUPPUSAMY

Assistant Professor

Department of Chemical Engineering

National Institute of Technology

Warangal – 506004, India.

February 2024

**Dedicated
To
My Parents**

CERTIFICATE

This is to certify that the thesis entitled **"Development of an Effective Multi-Objective Optimization Strategy for the Manufacturing of Resin Transfer Moulded Composite Parts",** that is being submitted by **Mrs. Zade Anita Dnyanba,** in partial fulfilment for the award of Doctor of Philosophy (**PhD)** in the Department of Chemical Engineering, National Institute of Technology, Warangal, is a record of bonafide work carried out by her under my guidance and supervision. The results embodied in this thesis have not been submitted to any other Universities or Institutes for the award of any degree or diploma.

Prof. Raghu Raja Pandiyan Kuppusamy

Assistant Professor

Department of Chemical Engineering

National Institute of Technology, Warangal, India.

DECLARATION

This is to certify that the work presented in the thesis entitled **"Development of an Effective Multi-Objective Optimization Strategy for the Manufacturing of Resin Transfer Moulded Composite Parts"**, is a bonafide work done by me under the supervision of **Prof. Raghu Raja Pandiyan Kuppusamy**, and it was not submitted elsewhere for the award of any degree.

I declare that this written submission represents my idea in my own words and where other's ideas or words have not been included. I have adequately cited and referenced the sources. I also declare that I have adhered to all principles of academic honesty and integrity and have not misinterpreted, fabricated or falsified any idea/data/fact/source in my submission.

I understand that any violation of the above will be a cause for disciplinary action by the Institute and can also evoke penal action from the sources which have thus not been properly cited or from whom proper permission has not been taken when needed.

Date: (Mrs. Zade Anita Dnyanba)

Place: Warangal   Research Scholar,

                                                                         Roll No.718151

ACKNOWLEDGEMENT

Abstract

The resin transfer moulding (RTM) technique is a widely used liquid composite moulding (LCM) process due to its advantages of uniform thickness and good surface finish for manufacturing complex composite parts. However, the RTM process is not practised widely due to the cost involved in developing mould design and process parameters. A proper mould design requires designing an effective injection strategy which contains the least number and appropriate positions of injection ports and vents that result in minimum mould filling time without dry spot content. As well, the judicious choice of mould heating time-temperature cycle is required for the effective curing process. In addition, the cognition on resin gelation-cure kinetics-rheokinetics and reinforcement mat permeabilities are the essentially required material parameters for the successful development of the RTM process. On the contrary, RTM being the closed moulding process, it is difficult to visualize resin flow and sense resin curing. Therefore, it becomes a hard task to analyse influential mould fill and cure process parameters through experimental trials and thus, the development of composite parts via the RTM process is confined.

To address these challenges, this research proposes a simulation-based optimization framework utilizing supervised learning algorithms to automate and optimize the RTM process. In this framework, simulation packages are coupled with optimization algorithms to autonomously determine optimal design and process parameters. The study introduces a robust and cost-effective methodology to simulate and optimize RTM mould-filling and curing processes using an in-house coded multi-objective optimization (MOO) algorithm integrated with process simulation via multi-phase porous flow, transient heat transfer and resin cure kinetics models. This framework was implemented using COMSOL Livelink for MATLAB focusing on manufacturing a vinyl ester-glass fiber-reinforced automotive bonnet and an RTM6-carbon fiber-reinforced aircraft wing flap.

Initially, vinyl ester and RTM6 resins were thermally characterized to develop the cure process windows through which the appropriate time-temperature cure cycles were identified for the curing of composite parts. From the thermal characterization of neat resins, the modified Kamal and Sourour model was effectively fitted to the experimental data of the degree of cure versus the rate of cure for both vinyl ester and RTM6 resins. Subsequently, the permeabilities of reinforcement fibre mats were measured using mould-filling experiments for their applicability in the mould-filling simulations. The effective permeability of 2.0×10^{-9} m^2 and

1.0×10^{-9} m^2 were obtained using the mould-filling experiments for woven roving glass and carbon fibre mats, respectively.

In the mould-filling phase, novel in-house coded Multi-Objective Stochastic-Optimization (MOSO) and Non-dominated Sorting Differential Evolution (NSDE) algorithms were developed and implemented to optimize the mould-fill phase. The NSDE algorithm was implemented for simultaneous optimization of two objectives namely, dry spot content and mould-fill time by changing the locations of gates and vents at the fixed input numbers of gates and vents. Consecutively, the MOSO algorithm was implemented for simultaneous optimization of three objectives namely, dry spot content, mould-fill time and total number of ports by simultaneously changing both the numbers as well as locations of gates and vents. The effect of race-tracking was also investigated using higher permeability values at the composite part-cut edges. Then, the efficacy of the proposed algorithms was examined with the trial and error process model simulations. From the comparative assessment, the trial and error process required more iterations with trials in numbering and positioning ports and manual efforts for obtaining a single optimal solution. Conversely, the MOO algorithms were automated and needed less manual effort and problem-specific experience to obtain the number of Pareto optimal solutions. In comparison to the NSDE algorithm, the MOSO algorithm predicted less dry-spot content, number of ports, mould-fill time and uniform resin flow-front progressions with lesser functional evaluations and computational time.

In the curing phase, a novel in-house coded NSDE algorithm was developed and implemented for the simultaneous minimization of composite part thermal gradients and cure process time for both the studied composite parts. The efficacy of the proposed algorithm was examined with the in-house coded non-dominated sorting genetic algorithm (NSGA-II) and trial-error process simulations in terms of a thermal gradient, cure-time, and cure progression at the applied temperature cycles. From the results, the NSDE algorithm was found to be effective in achieving faster convergence with less cure process and computational time when compared to the NSGA-II algorithm. The NSDE algorithm performed effectively in terms of thermal gradient and cure-time with the automated predictions of the mould heating parameters when compared with the trial-error process for both the composite parts.

This research significantly contributes to the field by introducing efficient and automated optimization algorithms for RTM composite parts by enhancing both manufacturing precision and time efficiency.

Keywords: Mould Filling, Curing, Multi-objective Optimization, Trial-and-Error Process Model Simulation, Reinforcement Mat Permeability, Curing Kinetics.

Table of Contents

List of Figures

List of Tables

Abbreviations

PMC	Polymer Matrix Composite
LCM	Liquid Composite Moulding
RTM	Resin Transfer Moulding
VARTM	Vacuum Assisted Resin Transfer Moulding
VARI	Vacuum Assisted Resin Infusion
FVM	Finite Volume Method
FEM	Finite Element Method
CVFEM	hybrid Control Volume Finite Element Method
LIMS	Liquid Injection Moulding Simulation
MOO	Multi-Objective Optimization
GA	Genetic Algorithm
PSO	Particle Swarm Optimization
ACO	Ant Colony Optimization
CSA	Cuckoo Search Algorithm
DE	Differential Evolution
NSDE	Non-dominated Sorting Differential Evolution
NSGA-II	Non-dominated Sorting Genetic Algorithm-II
MOSO	Multi-Objective Stochastic Optimization
ANN	Artificial Neural Network
ANFIS	Adaptive Neuro-Fuzzy Inference System
SQP	Sequential Quadratic Programming
DSC	Differential Scanning Calorimetry
1D	One Dimensional
2D	Two Dimensional
MFs	membership functions
RMSE	Root Mean Square Error
NFEs	Number of Function Evaluations

Symbols

ρ	Density, Kg m^{-3}
C_P	Heat Capacity, Jkg^{-1}K^{-1}
k	Thermal Conductivity, W m^{-1}K^{-1}
T	Temperature, K
α	Degree of Cure
$K(T)$	Kinetic Rate Constant, Minutes^{-1}
E	Activation Energy, kJ mol^{-1}
R	Ideal Gas Constant, J K^{-1}mol^{-1}
A	Frequency Factor, Minutes^{-1}
$\boldsymbol{K}$	Reinforcement Mat Permeability, m^2
μ	Viscosity, Pa-s
$\vec{u}$	Velocity Vector, m s^{-1}
$\emptyset$	Porosity of Fibre Mat
P	Pressure, Pa
θ	Fluid Volume Function
γ	Initialization Factor, m s^{-1}
ε	Interface Thickness, m
ΔH	Heat of Reaction, J m^{-3}

Chapter 1

Introduction

1.1 Composites

Composites are formed by combining two or more constituents having different properties. The major materials used are reinforcement fibre mats which carry the structural load and the resin matrix system which holds the fibre together. The different reinforcement materials that can be used are fibres, whiskers and particulates and the resin matrix materials that can be used are polymers, metals and ceramics. Based on the type of matrix, the composites are classified as polymer matrix composites, metal matrix composites and ceramic matrix composites[1].

1.1.1 Polymer Matrix Composites

Polymer Matrix Composite (PMC) [2] uses a polymer as the matrix and a fibre as the reinforcement. The resin matrix spreads the load applied to the composite between each of the individual fibres and also protects the fibres from damage caused by weathering, abrasion and impact. Depending upon the type of polymer matrix used, PMCs are classified into thermoplastic PMC and thermoset PMC. Thermoplastic matrix is highly viscous and their viscosity ranges million times more than that of water. The production of PMCs is difficult as the matrix is supplied in solid form and it is difficult to make them flow through reinforcement fibre. Thermoplastic matrix does not crosslink and hence, the composite parts are flexible and reformable. The thermoplastic matrix can be either amorphous or semi-crystalline. In the amorphous phase, plastic molecules are randomly arranged whereas in crystalline plastics they are arranged in an orderly fashion. The thermoset PMC uses a thermoset resin as the polymer

matrix which is 50 to 500 times more viscous than that of water. Thermoset resins can be cross-linked and converted to hard solids using a curing agent and/or with elevated temperature. After curing, thermoset PMCs cannot be re-melted or reformed. Some of the commonly used thermoset polymer matrices are polyesters, epoxies, phenolics, polyurethanes, polyimides etc.[3].

1.1.2 Applications of Polymer Matrix Composites

Polymer matrix composites are used in different sectors of the industry such as marine, energy, infrastructure, aerospace, automotive and sports. The major characteristics of polymer matrix composites are lightweight-high strength and environmentally friendly which results in increased fuel efficiency and reduced CO_2 emission [4].

The worldwide polymer composites market distribution in the early years between 2002 and 2005 is given in **Figure 1.1**. North America was the highest contributor to the composite market i.e. 39%, followed by Europe (34%), Asia (24%) and the remaining 3% was contributed by the rest of the world. The percentage segregation of PMCs in different sectors of industry is given in **Figure 1.2**. The transport sector is the highest one i.e. 35% contains aerospace, automotive, marine and railway divisions. Subsequently, the construction sector (31%) includes applications from civil engineering, followed by the sports sector (10%), electrical engineering sector (14%) and then other sectors of the industry (10%). Although this data was collected between 2004 and 2006, still it represents closely to the present scenario[5].
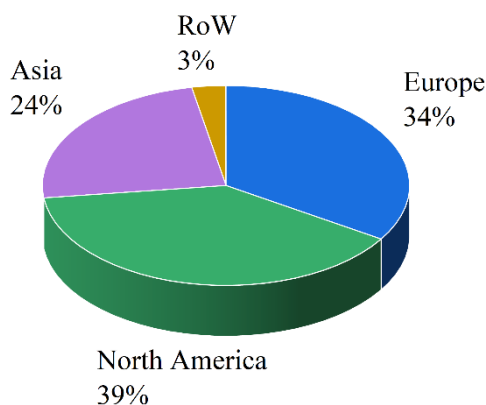
| **Figure 1. 1 The Worldwide Market of Composite Materials** | **Figure 1. 2 The Percentage Segregation of PMCs in Different Sectors of Industry** |
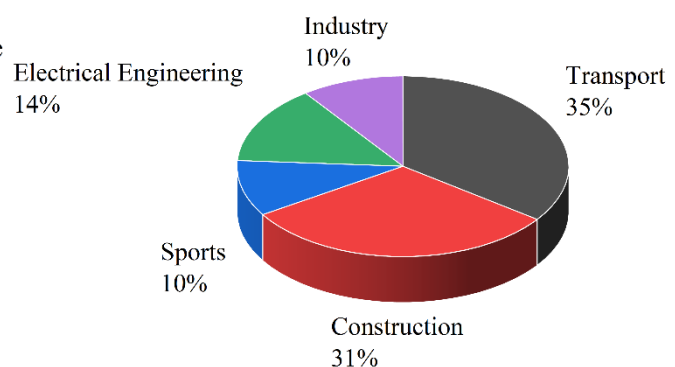
Nowadays, the world is seeking techniques for reducing CO_2 emissions and increasing fuel efficiency in different transportation sectors. Weight reduction is one of the effective ways to reduce CO_2 emissions and enhance the fuel efficiency of a vehicle. From the reported studies,

every 10% reduction in vehicle weight results in a 7% improvement in fuel economy[6]. In addition to the different characteristics of composite materials such as corrosion resistance, thermal conduction and high strength, composite materials contribute to the weight reduction of 15% to 40% in the automobile sector[7]. From the reported studies, the United States automotive composite market revenue has continuously increased in the last decade as shown in **Figure 1.3**. From **Figure 1.3**, it can be seen that the automotive market revenue in 2014 was 200 million USD and it was expected to reach around 700 million USD by 2025 [7]. Around 65% of polymer matrix composites were used for automobile exterior and interior parts from the global application and the remaining 35% were used for structural and powertrain components as shown in **Figure 1.4** [8].
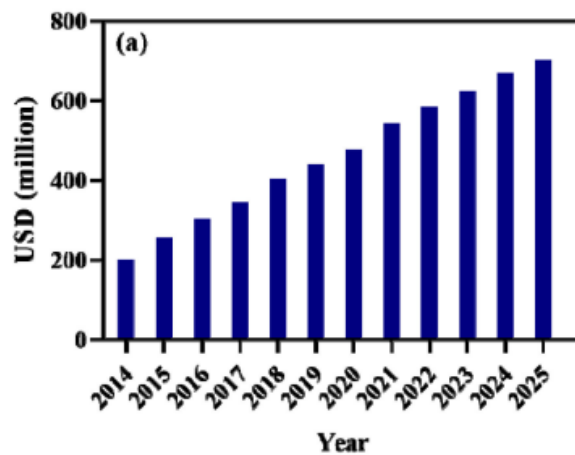
Figure 1. 3 The Automotive Polymer Composite Market Revenue of the United States (From 2014 to 2025) [7]
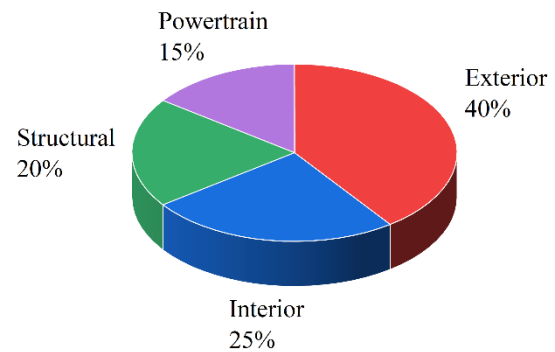
Figure 1. 4 Global Application of Polymer Composites in Various Automotive Components [8]

The structural materials of Airbus 350 and Boeing 787 contain 50% composites as shown in **Figure 1.5a**. The Boeing 787 was found 21% more fuel efficient [9] than the previous models as per the reported studies by All Nippon Airlines Co., Ltd. The recent unmanned aerial vehicles contain 60-90% composites as shown in **Figure 1.5b** [10].
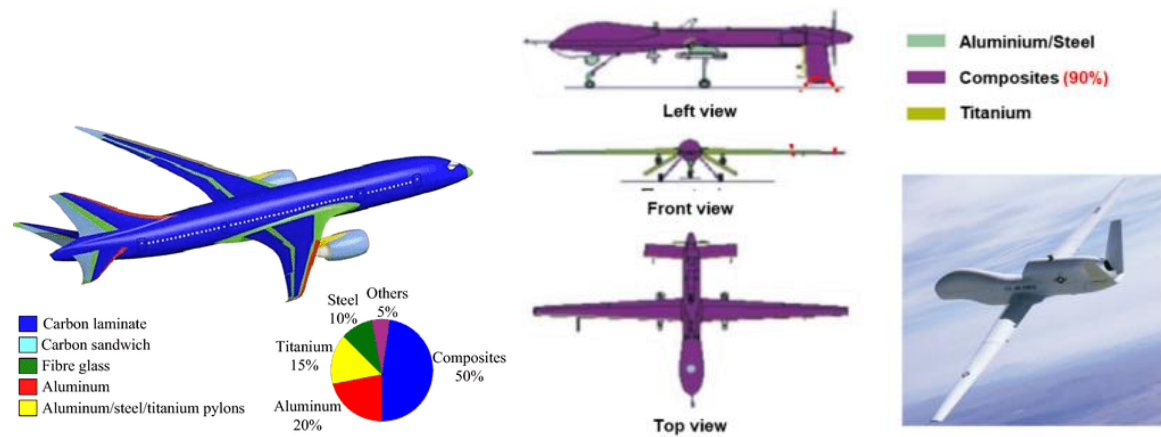
Figure 1. 5 Applications of Composites Structures in the Aerospace Industry: (a) Commercial Aircraft (Boeing 787) [9], (b) Unmanned Aerial Vehicles (MQ-1 Predator) [10]

1.1.3 Processing Methods

The main purpose of polymer composite processing methods is to bring the resin and reinforcement fibre together in the required shape of the product targeting minimum voids with maximum resin-fibre wet-out. Various composite production techniques such as hand lay-up, filament winding, pultrusion, compression moulding, Liquid Composite Moulding (LCM) and autoclave moulding are currently practised. However, the choice of the composite production process for a particular application is governed by the trade-off between lower manufacturing cost, high-performance parts, higher production rate and ease in making complex geometries. LCM techniques such as Resin Transfer Moulding (RTM), Vacuum Assisted Resin Transfer Moulding (VARTM) and Vacuum Assisted Resin Infusion (VARI) have taken a promising interest over the traditional methods in structural applications due to their ability to manufacture good finished complex structures with increased fibre volume fractions [11].

1.1.4 Resin Transfer Moulding Process

The resin transfer moulding technique is a widely used LCM process in the automotive and aerospace field due to its ability to manufacture high-performance composite parts [12]. RTM is a closed mould process that minimizes styrene emissions and material wastage. RTM becomes a competitive composite manufacturing process to the other traditional methods due to its selective reinforcement and accurate fibre management, incorporation of inserts and ability to produce net shape complex structures and hollow shapes [13]. The stages followed in the RTM process for making the composite part are given in **Figure 1.6**. At first, the fibre is cut to the required shape of mould called a preform. Then, the preform is loaded between the two solid airtight halves of the mould. After closing the mould, the resin is injected through

4

the appropriately located gates at constant injection pressure or flow rate. As the pressurized resin is injected through the gates, the air inside the cavity dispels out from the vents. Complete resin impregnation of fibre preform with minimum mould filling time and minimum voids is the objective of the mould filling stage [14]. This requires optimal mould design that delivers optimal numbers and locations of gates and vents and optimal pressure and temperature distributions.

When the mould is filled, the resin injection is stopped and the resin is allowed to cure and post-processed to obtain the finished composite part. The resin is allowed to cure either at room temperature or at elevated temperature which depends on the choice of the resin selected based on the application. During the curing process, heat is applied to the mould as per the recommended time-temperature-cure cycle of the specific resin. During curing, with an increase in temperature, resin undergoes chemical change predominantly through free radical polymerization and forms a networked three-dimensional structure with exothermal heat. Also, the resin undergoes physical change due to cross-linking from liquid to gel state and then to rigid solid state [15]. Minimum cure time and thermal gradient with the maximum degree of cure is the objective of the curing stage. The exothermal heat generated during resin curing can lead to temperature overshoots and thus, affects the quality of the manufactured composite part. Hence, the optimal design of the curing phase requires a well-defined mould heating temperature profile to reduce thermal overshoots and gradients [16]. After the successful completion of the curing stage, the cured composite part is extracted from the mould.
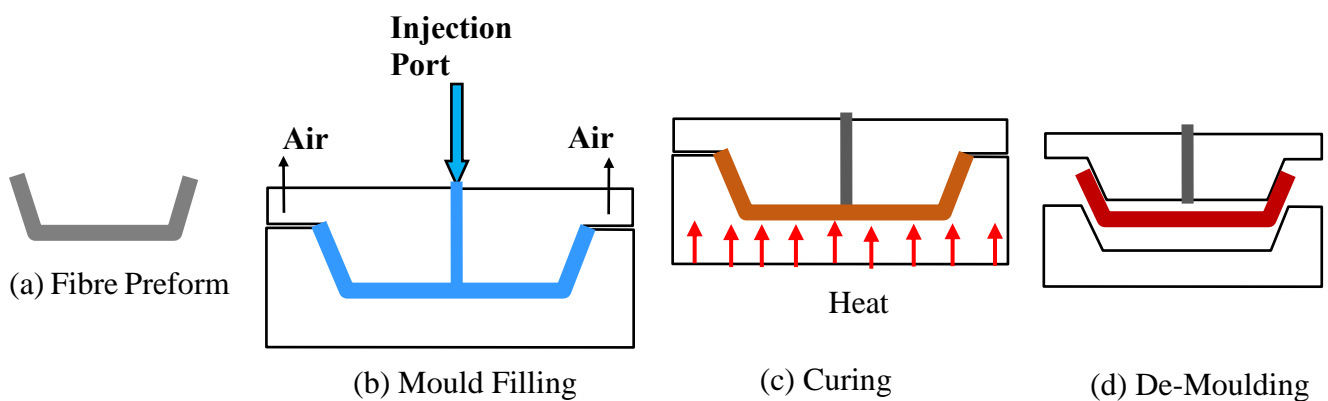
Figure 1. 6 Major Stages of the RTM Process

1.2 Motivations

In spite of several advantages, the RTM process is still not practised by small-scale industries due to the development cost involved in the development of effective mould design

and process parameters for a specific application [17], [18]. A proper mould design requires designing of effective injection strategy which contains the least number and appropriate positions of injection ports and vents that result in minimum mould filling time without dry spot content [19]. The judicious choice of injection pressure or injection flow rate, line or point injection ports and port diameter are required for the accomplished mould-filling process [20]. As well, the judicious choice of mould heating time-temperature cycle is required for the effective curing process [21]. In addition, the cognition on resin gelation-cure kinetics-rheokinetics and reinforcement mat permeabilities are the essentially required material parameters for the successful development of the RTM process [22], [23]. On the contrary, RTM being the closed moulding process, it is difficult to visualize resin flow and sense resin curing [24]. Therefore, it becomes a hard task to analyse influential mould fill and cure process parameters through experimental trials and thus, the development of industrial composite components via the RTM process is confined [25].

Alternatively, researchers are practising various LCM process simulation packages to predict the suitable configurations of gates and vents during mould design. These simulation tools are relatively easy and cost-effective to predict the various configurations of mould design and process parameters when compared to trial and error experimental methods [26]. Because new mould design and its alteration for each configuration of gates and vents are expensive and intricate through trial experiments. Also, there is added material cost for developing mould design and process parameters through iterative trial experimentations [27]. The most commonly used numerical tools through various simulation packages are Finite Volume Method (FVM), Finite Element Method (FEM) and hybrid Control Volume Finite Element Method (CVFEM). Moreover, the numerical tools used by researchers are specially developed simulation tools for the isothermal LCM processes such as PAM-RTM, RTMSIM, LIMS3D, LIMS, RTM-Worx [28]–[33]etc. However, these simulation packages lack the ability to improve mould design or the process parameters on their own via supervised learning iterations [34]. In recent trends, researchers have introduced the simulation-based optimization framework where simulation packages are coupled with the optimization algorithms as shown in **Figure 1.7** [20]. At first, the mould filling and curing processes are evaluated for given input parameters using numerical simulations. Then, the processes are analysed for a predefined objective function and constraints. Subsequently, the optimization algorithm search for new candidate solutions and send them to the simulator for process evaluations. Hence, the coupling of new candidate solution generation (search) and the process assessment (evaluation) forms the simulation-based optimization framework. These simulation-based optimization

frameworks will enable them to attain the optimal design and process parameters on their own using supervised learning algorithms [35], [36].
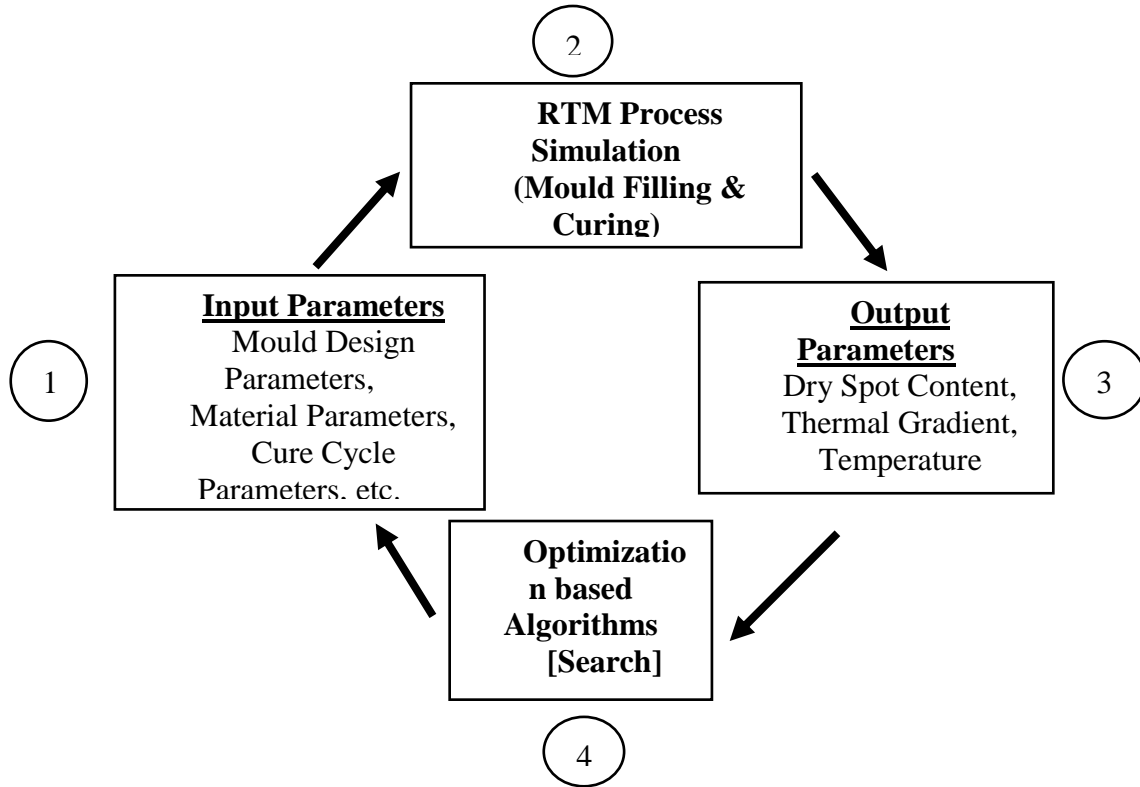
Figure 1. 7 Simulation-Based Optimization Framework

1.3. Numerical Optimization

Although there are several optimization algorithms developed by the researchers, the selection of an effective optimization algorithm is problem-specific based on the No Free Lunch Theorem [37]. Implementation of an unsuitable algorithm results in unsatisfactory performance and unnecessary wastage of computational costs. Thus, the effective design of the RTM process depends on the type of optimization problem and the selection of a proper optimization algorithm. Commonly, an optimization problem contains one or more objective functions, design variables or constraints [38]. The general formulation of any type of optimization problem is given below,

$$\max_{X}/\min f_k(X) \qquad k = 1, 2, \dots, N$$

Subject to,

$$h_l(X) = 0 \qquad l = 1, 2, \dots, L$$

$$g_m(X) \leq 0 \qquad m = 1, 2, \dots M$$

$$lb \leq X \leq ub \qquad X = (x_1, x_2, \ldots x_d)^T$$

here, $f_k(X)$ is the scalar objective function which has to maximize or minimize, $h_l(X)$ represents the J number of equality constraints also called active constraints, $g_m(X)$ represents the M number of inequality constraints and X is the vector of d-dimensional design variables. The optimization problems can be classified in different ways as follows [39]:

1. Single-variable and multi-variable optimization problems contain a single or more than one design variable, respectively.

2. Discrete and continuous optimization problems contain the discrete and continuous set of design variables, respectively.

3. In the constrained optimization approaches design variables change by satisfying certain constraints whereas, in unconstrained optimization problems, design variables are free to change without any constraints.

4. When there is a single objective to optimize, such problems are called single-objective optimization problems and problems which contain multiple conflicting objectives to optimize, such problems are called multi-objective optimization problems. Multi-objective optimization (MOO) problem contains more than one objective that conflicts with each other. Hence, there will be more optimal solutions which are represented in terms of Pareto fronts. The best optimal solutions are called non-dominated solutions as shown in **Figure 1.8**.

5. The optimality procedure of a problem depends on time for the dynamic optimization problems whereas the optimal design does not depend on time for the static types
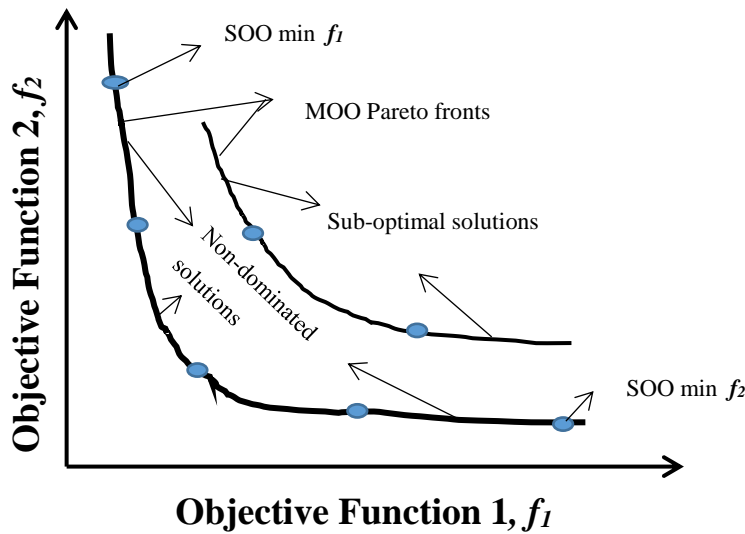
Figure 1. 8 Pareto Front for Minimization of Two Conflicting Objective Functions

After the formulation of the optimization problem in the above-mentioned standard form, the task is to solve it using an appropriate optimization technique. There are different types of optimization techniques based on the nature of the optimization problem which are classified as [40]:

1. Deterministic algorithms: These methods are heavily based on exploitation search mechanisms in which the solutions improve with iterations within the local domain as shown in **Figure 1.9**. These algorithms have higher convergence rates due to their deep understanding of search space and efficient navigation in the neighbourhood search points. However, these algorithms are more dependent on initial guesses and more prone to get stuck in local optima. Optimization techniques namely Newton's method, secant method, simplex method, and box-complex method fall into the deterministic algorithms category.

2. Stochastic algorithms: These algorithms are heavily based on exploration search mechanisms in which a randomly generated population covers the whole search space as shown in **Figure 1.8**. Therefore, these algorithms are less prone to local stagnation and increase the probability of obtaining a global optimal solution. However, extreme exploration results in a slower convergence rate and unnecessary wastage of computational resources. Optimization techniques based on the Genetic Algorithm (GA), Particle Swarm Optimization (PSO) algorithm, Ant Colony Optimization (ACO) algorithm and Cuckoo Search Algorithm (CSA) fall into the stochastic algorithms [41]–[43].

3. Hybrid algorithms: In this method, two or more algorithms are combined so that the potential aspects are counted and the weaker aspects are eliminated. Hybrid algorithms are mostly the integration of local search strategies with global search based algorithms. A hybrid Box-Complex method with Cuckoo Search (BC-CS) algorithm, hybrid PSO with Genetic algorithm and hybrid Nelder-Mead PSO (NM-PSO) algorithm can be the best examples of hybrid algorithms [44]–[46]. The development of robust hybrid algorithms is still an active area of research to address the complexity of real-world applications.
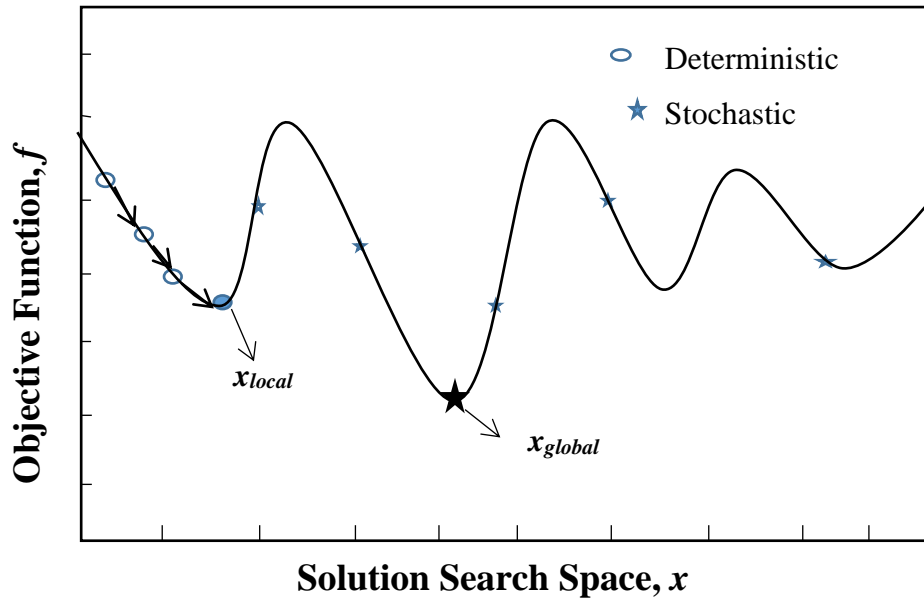
Figure 1. 9 Convergence Flow of Optimal Solution for Stochastic and Deterministic Techniques

Recently, composite practitioners have started highlighting the investigation of how well the optimization algorithm performs for the given problem of interest. This will guide the selection of appropriate optimization algorithms for future optimization studies. The appropriate choice of optimization algorithm for the given composite manufacturing problem will open the door to obtaining the best optimal solutions and reducing the wastage of computational resources, time and money [47], [48].

1.4. Bibliometric Analysis

A bibliometric analysis was conducted on August 21, 2023, utilizing the Web of Science core database. A collection of 2391 articles was obtained through the primary search term 'Resin Transfer Moulding' within the topics section. Bibliometric network visualization was carried out using the VOSviewer software [49], as depicted in **Figure 1.10**. The analysis focused on bibliometric coupling occurrences of author keywords that appeared more than 8 times. Out of a pool of 4276 keywords, 157 keywords met this threshold and were consequently selected for further examination. From these 157 keywords, the cumulative strength of co-occurrence links with other keywords was computed. This computation guided the selection of keywords with the highest total link strength. Among these keywords, resin transfer moulding, mechanical properties, polymer matrix composites, permeability and others emerged as prominent author keywords.
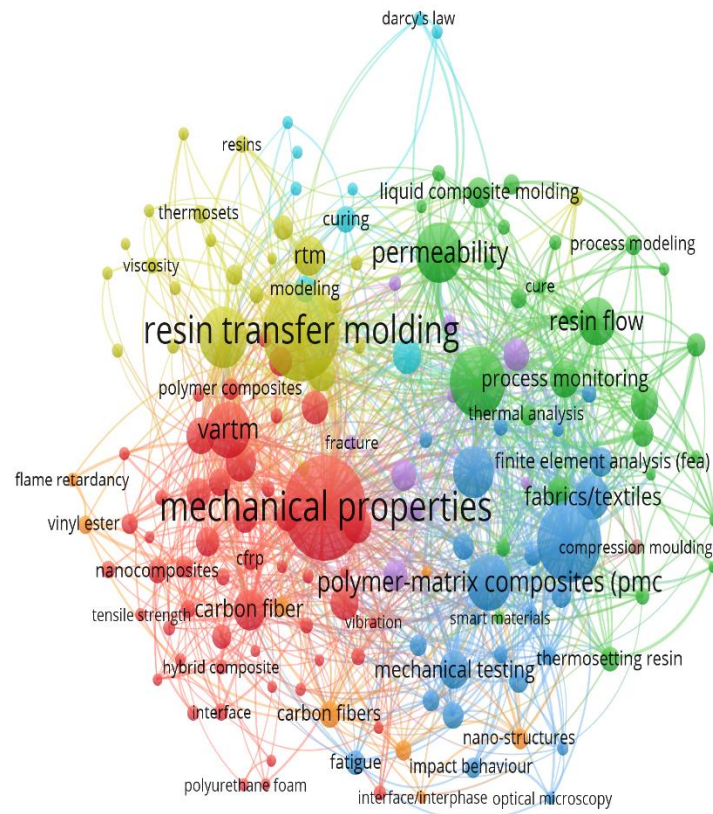
Figure 1. 10 Schematic Representation of the Bibliographic Networking Diagram Obtained from the Web of Science Core Database through the Search Conducted on August 21, 2023.

Figure 1.11 shows the network visualization of bibliographic coupling between countries for the searched phrases related to resin flow and curing process. The bibliographic coupling for more than 5 documents of a country were analyzed. Out of 75 countries, 48 countries met this coupling criterion and thus, were chosen. From the 48 countries, the total strength of bibliographic coupling links with other countries was computed and the countries with greatest total link strength were selected. From Figure 9, it can be seen that the USA has the greatest link strength followed by China, South Korea, Japan, Canada and India.

Figure 1. 11 Schematic Representation of the Bibliographic Coupling between Countries Obtained from the Web of Science Core Database through the Search Conducted on August 21, 2023.

1.5. Research Gaps

From the detailed literature review included in Chapters 2 - 5, it was found that the researchers addressed RTM mould filling and curing simulations independently and no straight reports were found on the development of multi-objective optimization algorithms with the coupling of multi-phase porous flow, transient heat transfer and resin cure kinetics models to address the complete RTM process optimization.

Researchers have handled the optimizations of mould fill and cure phases separately using variants of GA. However, from the comparative studies, the Differential Evolution (DE) algorithm performed significantly better than GA for multi-objective optimization problems [50]. Notably, there were no reports on the development of the non-dominated sorting differential evolution (NSDE) algorithm for the simultaneous optimization of the RTM mould fill and cure phases. Also, there were no straight reports found on the development of robust optimization techniques for multiple-complex industrial composite structures with varied resin-fibre properties.

The development of an effective injection strategy that contains the least numbers and appropriate positions of mould gates-vents is vital to attain the optimized RTM mould fill phase. From the literature review, it was found that the optimization of mould gate and vent locations was addressed independently using various heuristic and deterministic optimization techniques. However, there were no reports found on the development of a multi-objective stochastic optimization (MOSO) algorithm that predicts the simultaneous optimization of gate-vent numbers and positions with the prediction of minimum dry spot content and mould fill time.

Prior to this work, there were no published works on the development of a resin cure process window for the selection of appropriate time-temperature cycles for the composite cure. Consequently, there were no reports found to obtain the time-temperature-cure difference window that evaluates the cure differences and the rate of cure differences between neat resin and composite panel. A detailed review of the present status, research gaps and research work proposed related to this thesis is tabulated in **Table 1.1**.

Table 1. 1 Research Gaps and Proposed Novelties

Present Status	Research Gaps	Research Proposed
Few MOO techniques were reported for the RTM process optimization based on variants of GA.	No global optimization techniques other than GA were used for RTM process optimization. From the literature review, the optimization techniques namely PSO, DE and CSA were proved to be efficient for other applications than the GA.	Developed a non-dominated sorting differential evolution algorithm (NSDE) for RTM process optimization.
Optimization techniques for gates and vents location optimization were developed for the constant numbers of gates and vents.	No optimization algorithm was developed which can simultaneously predict the optimal numbers and locations of gates and vents.	Developed a multi-objective stochastic optimization algorithm (MOSO) which simultaneously optimizes both the numbers and locations of gates and vents with the prediction of

		minimum dry spot content and mould fill time.
Optimization techniques for multi-dwell thermal profile optimization were developed for thick and ultra-thick composite components based on variants of GA.	No algorithm based on the differential evolution technique was developed for the optimization of the composite panel cure process.	Developed a robust NSDE algorithm for multi-dwell thermal profile optimization. The efficacy of the developed algorithm was tested for various applications with variations in the composite part thickness and raw materials.

Novelties

1. Developed a time-temperature-cure process window for neat vinyl ester and RTM6 resins using thermal characterizations for its applicability in RTM cure process simulations.

2. Developed a reinforcement mat permeability model as a function of material and process parameters using mould-filling experiments for its applicability in RTM mould-filling simulation.

3. Developed a methodology to simulate and optimize the RTM mould-filling and curing processes through a framework based on simulation-driven optimization. This was accomplished by integrating a multi-objective optimization algorithm with process simulation through coupled multi-phase porous flow, transient heat transfer and resin cure kinetics models. The developed framework was implemented using COMSOL Livelink for MATLAB.

4. Developed novel in-house NSDE and MOSO algorithms to optimize the RTM mould-filling and curing processes.

1.6. Research Objectives

The main objective of this work is to develop a robust one-shot multi-objective optimization algorithm for the sustainable manufacturing of resin transfer moulded composite parts. An optimized mould-filling and curing process is the prerequisite for the development of composite parts through the RTM process for a specific application. The optimized mould-filling phase requires an effective injection strategy to deliver the optimal number and locations

of gates and vents with minimum dry spot content and mould-filling time. The optimized curing phase requires an appropriate time-temperature cure cycle to deliver minimum thermal gradient and cure time.

The following sub-objectives were framed to accomplish the main objective of developing a robust multi-objective optimization algorithm for the sustainable manufacturing of resin transfer moulded composite parts.

Sub-Objective 1. Development of time-temperature-cure process window for neat vinyl ester and RTM6 resins using thermal characterizations for its applicability in RTM cure process simulations.

Sub-Objective 2. Measurement of reinforcement mat permeabilities using mould filling experiments for its applicability in RTM mould filling simulations.

Sub-Objective 3. Development of an optimized RTM mould-filling phase through trial and error process model simulations, novel in-house coded non-dominated sorting differential evaluation (NSDE) and multi-objective stochastic optimization (MOSO) algorithms.

Sub-Objective 4. Development of optimized isothermal and non-isothermal curing processes through trial and error process model simulations and in-house coded NSDE and Non-dominated Sorting Genetic Algorithm-II (NSGA-II) optimization algorithms.

1.7. Research Roadmap

In this research, a glass fibre-vinyl ester-based automotive bonnet and carbon fibre-RTM6 mono-component epoxy resin-based aircraft wing flap were selected as the composite parts for the development of robust multi-objective optimization algorithms for the sustainable RTM manufacturing process. Initially, the vinyl ester and RTM6 resins were thermally characterized to develop the cure process windows through which the appropriate time-temperature cure cycles were identified for the curing of composite parts. Then, the permeabilities of glass and carbon fibre woven roving mats were measured using mould-filling experiments. The reinforcement mat permeabilities and the resin cure kinetics were the prerequisites required for the RTM mould-filling and curing simulations.

In this work, the RTM process optimization for studied composite parts was developed using two approaches namely: (i) Trial-and-error process model simulation, and (ii) Simulation-based optimization framework. The trial and error mould-filling process model simulation was performed by manually changing the number and locations of gates and vents to deliver the effective injection strategy with minimum dry spot content and mould-filling

time. The trial and error curing process model simulation was performed by manually changing the mould-heating parameters to deliver the optimal thermal-cure cycle with minimum thermal gradient and cure time. Subsequently, a simulation-based optimization framework was developed by integrating the in-house coded optimization algorithm with process model simulation via COMSOL live link for MATLAB.

To optimize the mould-filling phase, a novel in-house coded non-dominated sorting differential evaluation (NSDE) and multi-objective stochastic optimization (MOSO) algorithms were developed. The NSDE algorithm was developed for the simultaneous minimization of dry spot content and mould-fill time by changing the locations of mould gates and vents with a constraint of pre-fixed port numbers. The MOSO algorithm was developed for the simultaneous minimization of dry spot content, mould-fill time and the total number of ports by changing the numbers and locations of gates and vents.

A two-dwell and one-dwell thermal profiles / time-temperature cure cycles were designed for the cure phase optimization of the automotive bonnet and aircraft wing flap composite parts, respectively. The NSDE and NSGA-II algorithms were developed for the simultaneous minimization of thermal gradients and cure time by changing the mould heating parameters for the studied composite parts.

Finally, a comparative assessment was made between the optimized mould-filling and cure phase results obtained from the trial and error process simulations and the developed optimization algorithms for the studied composite parts. **Figure 1.12** shows the complete workflow involved in this research.

Automotive Bonnet ← Composite Parts → Aircraft Wing Flap

Vinyl Ester Resin
Glass Fibre Mat

RTM6 Resin
Carbon Fibre Mat

Resin Characterization
- Cure Kinetics Model

Raw Material Characterization

Fibre Characterization
- Permeability

Trial and Error RTM Process Model Simulations
- Manually Changing the Design and Process Parameters

Development of RTM Technology
- Mould Filling Phase
- Curing Phase

Simulation based Optimization Framework
- Coupling of Multi-objective Optimization Algorithm with COMSOL Multi-Physics Simulator via COMSOL Live Link for MATLAB

1. Mould Filling Phase Optimization
- Effective Injection Strategy
- Dry Spot Content
- Fill Time
2. Cure Phase Optimization
- Design of Thermal-Cure Cycle
- Thermal Gradient
- Cure Time

Mould Filling Phase Optimization

Curing Phase Optimization

Development of In-House Coded NSDE Algorithm (Gate & Vent: Location Optimization)
- Dry Spot Content
- Mould-Filling Time

Development of In-House Coded MOSO Algorithm (Gate & Vent: Number and Location Optimization)
- Dry Spot Content
- Mould-Filling Time
- Total Number of Ports

Development of In-House Coded NSDE Algorithm and NSGA-II (Multi-Dwell Mould Heating Parameter Optimization)
- Thermal Gradient
- Cure Time

Comparative Investigation between Trial & Error Process Model Simulations and Developed Optimization Algorithms

Figure 1. 12 Roadmap of Proposed Research Work

1.8. Organization of Thesis

The thesis is structured to provide a comprehensive exploration of the development of robust multi-objective optimization algorithms for the RTM manufacturing process. The following chapters collectively address key aspects of the research, each contributing to the overarching objectives of optimizing the RTM mould-filling and curing processes. The organization of the thesis is summarized as follows:

Chapter 1: Introduction

This chapter provides an overview of polymer matrix composites, their applications, and processing methods. It emphasizes the significance of the mould-filling and curing phases in resin transfer moulding (RTM) and explores the motivation behind optimizing the RTM process using simulation-based optimization. Research gaps identified through a thorough literature review are presented along with the formulation of research objectives and the scope of the study.

Chapter 2: Development of Time-Temperature-Cure Process Window for Neat Resins

Chapter 2 presents an in-depth literature review on cure kinetics and the thermal characterizations of neat vinyl ester and RTM6 resins using Differential Scanning Calorimetry (DSC) experiments. It defines cure kinetics models and establishes time-temperature-cure process windows for both resins. The outcome of this chapter namely cure kinetic parameters and time-temperature cure cycles are applied in chapter 5 for RTM cure process simulation as part of objective 1.

Chapter 3: Reinforcement Mat Permeability Characterization using Mould-Filling Experiments.

This chapter extensively reviews the literature on reinforcement mat permeability and introduces a coupled mould-filling simulation and experimental-based approach to determine mat permeability. It introduces the use of Adaptive Neuro-Fuzzy Inference System (ANFIS) and Artificial Neural Network (ANN) models to predict reinforcement mat permeability based on material and process parameters using experimental data. The permeability data for glass and carbon fibre mats obtained in this chapter are employed in chapter 4 during mould-filling simulations, contributing to objective 2.

Chapter 4. Development of an Optimized RTM Mould-Filling Process using Multi-Objective Optimization Algorithms

Focusing on the mould-filling phase of the RTM process, this chapter conducts a thorough literature review and implementation of process model simulations using the COMSOL multi-physics simulator. It also incorporates in-house coded NSDE and MOSO MOO algorithms for enhancing mould-filling efficiency. Additionally, the chapter carries out comparative analyses between trial and error mould-filling process model simulations and the developed optimization algorithms as part of objective 3.

Chapter 5. Development of an Optimized RTM Curing Process using Multi-Objective Optimization Algorithms

This chapter delves into the curing phase of the RTM process, detailing the methodology and implementation of a simulation-based optimization framework using COMSOL Livelink for MATLAB. It presents a comparative analysis between trial and error curing process model simulations and the developed optimization algorithm as part of objective 4.

Chapter 6. Conclusions and Future Directions

The concluding chapter summarizes the major findings obtained from this research work. It also outlines potential areas for further research.

The section on thesis contributions provides the practical implications of the research outcomes applicable to industry and academia in the field of polymer composites. This section also includes a list of publications and conference participation that resulted from the research work.

Chapter 2

Development of Time-Temperature-Cure Process Window for Neat Resins

2.1 Introduction

Curing constitutes a pivotal stage in the production of high-quality composite parts within the RTM process. During curing, the resin undergoes a transformation, forming a three-dimensional networked structure through exothermic reactions [51]. This transformation involves transitioning from a liquid state to a gel-like intermediate state and eventually solidifying into a rigid structure [15]. Notably, inappropriate selection of cure cycle parameters, such as time and temperature, can lead to non-uniform curing and the development of residual stresses within the composite [16]. Consequently, the overall quality of the manufactured composite part can be compromised.

Therefore, achieving an optimal design for the curing phase necessitates the establishment of a precisely defined time-temperature cure cycle [52]. This approach aims to mitigate the occurrence of thermal overshoots and gradients, thereby enhancing the uniformity of the curing process [53]. In this context, the thermal characterization of the neat resin holds significant importance. This characterization offers valuable insights into the cure kinetics and cure cycle parameters [54]. By determining a well-defined time-temperature cure cycle for the resin, the number of experimental trials required during the RTM process can be reduced. This

streamlined approach contributes to obtaining the optimal thermal cure profile for composite parts, resulting in both time and cost savings [55].

Furthermore, the comprehensive understanding of the thermal characteristics of the neat resin holds broader implications. It serves as a foundational element for the design of composite parts that demonstrate durability and longevity, particularly when exposed to demanding service environments [56]. By comprehending the behaviour of the resin throughout the curing process, it becomes possible to tailor the manufacturing parameters to ensure consistent quality and reliable performance of the composite parts across various applications [57]. This knowledge empowers engineers and manufacturers to create composite structures that meet stringent requirements while minimizing the risks associated with thermal stresses and material degradation over time [58].

In this chapter, an in-depth thermal characterization of Vinyl Ester Resin (VER) and RTM6 resin was carried out to acquire essential insights into their cure kinetics. The primary objective was to establish a comprehensive understanding of the time-temperature cure cycle, which proves invaluable in facilitating the simulation of the Resin Transfer Molding (RTM) curing process. The subsequent subsections provide an extensive literature review of the cure kinetics of both these resins and the composites derived from them.

2.1.1 Bibliometric Analysis

A bibliometric analysis was conducted on August 9, 2023, utilizing the Web of Science core database. A total of 3825 articles were identified using the primary search term 'thermal characterization of resin' within the topics section. Bibliometric network visualization was carried out using the VOSviewer software [49], as depicted in Figure 2.1. Bibliometric coupling was analyzed for author keywords that occurred more than 5 times. Subsequently, keywords such as 'thermal properties,' 'epoxy resin,' 'composites,' 'characterization,' and 'thermal analysis' were explored.
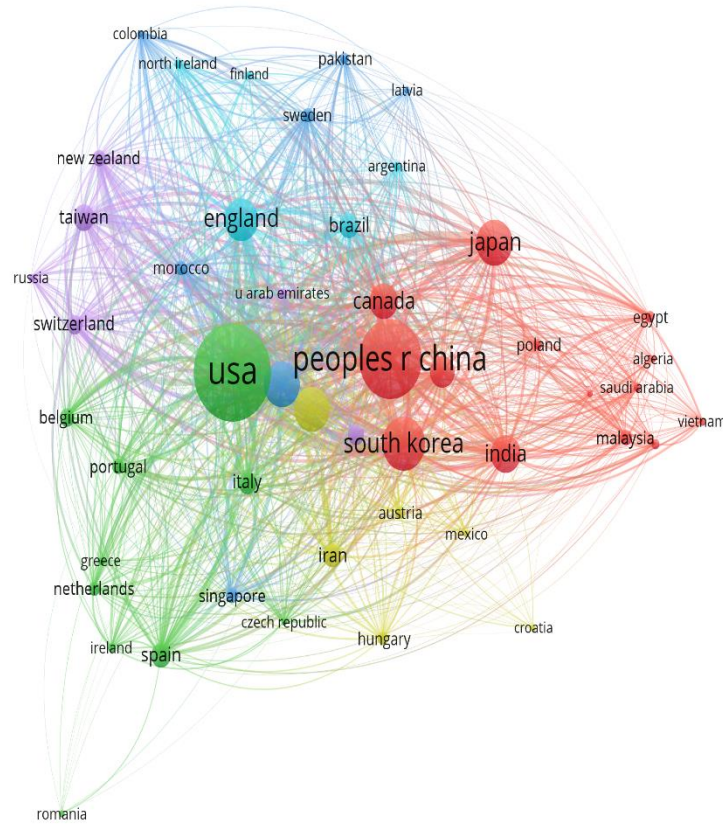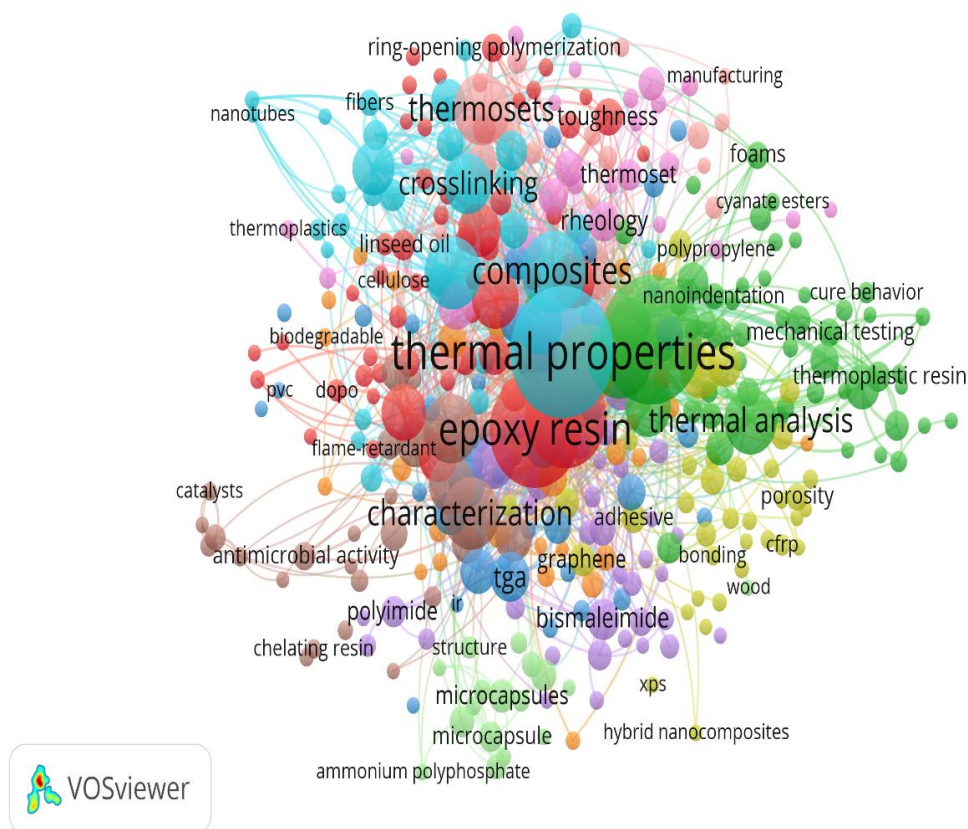
Figure 2. 1 Schematic Representation of the Bibliographic Networking Diagram Obtained from Web of Science Core Database through the Search Conducted on August 9th, 2023.

2.1.2 Literature Review

Researchers have dedicated significant effort to investigating the cure kinetics of neat resins, aiming to comprehend the curing process of composite components. This is crucial as the final quality of composite parts heavily relies on the state of the resin achieved at the culmination of the curing process. During the kinetics of resin cure, chemical transformations primarily occur through free radical polymerization, resulting in the creation of a three-dimensional network structure accompanied by the release of exothermal heat. Simultaneously, the resin undergoes physical alterations as it transitions from a liquid state to a gel state, ultimately solidifying into a rigid solid[59].

Researchers have extensively explored the cure kinetics of resins using a variety of experimental approaches, including Differential Scanning Calorimetry (DSC)[60], spectroscopy[61], rheometry[62], Thermal Gravimetric Analysis (TGA)[63], and Fourier Transform Infrared Spectroscopy (FTIR)[64]. These characterization techniques have unveiled the intricacies of resin cure kinetics, attributable to the occurrence of multiple crosslinking

chain reactions within the thermosetting polymer. To comprehend this complexity, various empirical models for cure rates have been devised to mimic the kinetic behaviour of thermosetting resins[65], [66].

Mathematically, empirical models for cure rate ($d\alpha/dt$) have been formulated as a function of temperature (T) and the degree of cure (α), represented as:

$$\frac{d\alpha}{dt} = K(T)f(\alpha) \tag{2.1}$$

Here, K(T) is the rate constant determined by the Arrhenius expression:

$$K(T) = Ae^{-E/RT} \tag{2.2}$$

Where A represents the frequency factor, E is the activation energy, R is the ideal gas constant, and T signifies temperature. The function f(α) is defined with respect to the degree of cure α. Among the various empirical models, the nth-order cure rate model [67], represented by **Equation (2.3)**, emerges as the simplest and most commonly employed two-parameter model:

$$\frac{d\alpha}{dt} = K(T)(1-\alpha)^n \tag{2.3}$$

In this equation, f(α) is defined in terms of $(1-\alpha)^n$, where 'n' denotes the reaction order. However, the nth-order model, while predicting higher initial cure rates, is not applicable for resin systems following autocatalytic kinetics. For such systems, a four-parameter autocatalytic kinetics cure rate model, as presented in **Equation (2.4)**, was proposed by Kamal and Sourour [68]:

$$\frac{d\alpha}{dt} = (K_1 + K_1\alpha^n)(1-\alpha)^m \tag{2.4}$$

In this model, 'k_1' and 'k_2' represent the cure rate constants, 'α' is the degree of cure, and 'm' and 'n' are the reaction orders. Nonetheless, this model does not account for incomplete curing and becomes ineffective in the later stages of the reaction. Researchers have addressed this limitation by modifying Kamal and Sourour's model to consider incomplete reactions, as summarized in **Table 2.1**.

Table 2. 1 Modified Forms of Kamal & Sourour Model

Kamal & Sourour Model	Equation	Parameters
Modified Form No. 1 [68]	$\frac{d\alpha}{dt} = k_1(1-\alpha)^{n_1} + k_2\alpha^m(1-\alpha)^{n_2}$	k_1, k_2, n_1, n_2, m
Modified Form No. 2 [69]	$\frac{d\alpha}{dt} = k_1(1-\alpha)^n + k_2(1-\alpha)^n\alpha^m$	k_1, k_2, n, m

Modified Form No. 3 [70]	$\dfrac{d\alpha}{dt} = (k_1 + k_2\alpha)(1 - \alpha)^2$	k_1, k_2, m
Modified Form No. 4 [71]	$\dfrac{d\alpha}{dt} = k\alpha^m(1 - \alpha)^n$	k, m, n
Modified Form No. 5 [72]	$\dfrac{d\alpha}{dt} = k(1 - \alpha)^n \, exp(m\alpha)$	k, n, m
Modified Form No. 6 [73]	$\dfrac{d\alpha}{dt} = k\alpha^m(1 - \alpha)^n(1 - \alpha)^p$	k, m, n, p

Despite the proliferation of empirical cure rate models, their applicability remains contingent on the resin system type. As different resin systems entail variations in kinetics and time-temperature cure cycles, researchers have scrutinized the stability of these models across diverse resin systems. Siddiqui et al.[74] delved into the complete cure kinetics of cyanate-ester resin using isothermal DSC scans, identifying multiple cure zones characterized by varying reaction orders. To accommodate this complexity, separate n^{th}-order kinetic models were employed for each zone. Javdanitehran et al.[75] adopted an iterative approach for isothermal cure kinetics modelling of an epoxy resin system using DSC scans. This iterative method estimates released enthalpy during each heat-up phase and determines the degree of cure, iteratively converging until stabilization. Cure kinetics modelling was then conducted using the Kamal and Sourour model in conjunction with the Rabinowitch approach.

Zhao and Hu devised a novel cure kinetics model for thermosetting resins employing an autocatalytic reaction mechanism. This innovative model incorporates temperature-dependent reaction orders instead of constant values. Vargas et al.[76] investigated polyester resin curing using NIR spectroscopy and ^{1}H-NMR relaxometry, employing an autocatalytic kinetic model to determine kinetic parameters based on catalyst and temperature concentrations. Jiangbo Lv et al.[77] explored the cure kinetics of phthalonitrile resin by varying proportions of the Melamine curing agent, and successfully validated the autocatalytic kinetic model using DSC scans. García-Martínez et al. [78] analyzed the curing and rheology kinetics of benzoxazine resin for potential use in liquid composite moulding processes. By combining DSC and rheological experiments, they obtained crucial parameters including reaction order, viscoelastic properties, and resin gelation and vitrification temperatures. Hwang et al. [79]

ingeniously coupled Dynamic Mechanical Analyzer (DMA) and DSC experiments with process model simulation to derive cure kinetics and rheology data for epoxy-amine resins. This comprehensive dataset facilitated the optimization of multi-dwell cure profiles for Out of Autoclave (OAA) processes.

In conclusion, researchers' meticulous investigations into resin cure kinetics have led to the development of diverse empirical models, each tailored to specific resin systems. In the subsequent subsections, a thorough literature review was undertaken to delve into the cure kinetics of Vinyl Ester Resin (VER) and RTM6 resin, aiming to capture essential insights into their respective curing processes. This undertaking is expected to considerably enhance our comprehension of the intricate curing dynamics associated with VER and RTM6 resin, thereby paving the way for the refinement of composite manufacturing techniques.

2.1.2.1 Vinyl Ester Resin

Vinyl Ester Resin (VER) is a widely utilized thermoset polymer in the composite industry, owing to its notable characteristics of high moisture and chemical resistance, coupled with commendable mechanical properties. VER possesses a unique amalgamation of attributes from both polyester and epoxy resins, rendering it a competitive alternative and a potential substitute for numerous other thermoset polymers[80]. The curing process of VER involves free radical polymerization and is significantly influenced by factors such as curing temperature, catalysts, and accelerators[81].

In a broader context, VER can undergo curing at either room temperature or elevated temperatures. Curing at room temperature may span from several minutes to hours, while elevated temperature curing might necessitate a relatively shorter timeframe, often on the order of minutes. Nevertheless, it's important to note that non-uniform curing can occur, particularly during elevated-temperature curing. This phenomenon can lead to the development of thermal stresses within the composite part. Consequently, achieving a well-defined time-temperature cure cycle for the neat resin becomes instrumental. This established cycle not only aids in addressing the challenges of non-uniform curing but also facilitates the proactive design of the composite cure cycle[82].

Researchers have extensively examined the cure kinetics of Vinyl Ester Resin (VER) through a range of experimental methodologies. Additionally, they have formulated various models to elucidate the kinetics of the curing process. Hong and Chung [83] for instance, employed DSC to analyze cure kinetics and devised a model that yielded a comprehensive time-temperature-transformation (TTT) cure plot. Sultania et al. [84] on the other hand,

investigated VER resin's cure kinetics using non-isothermal DSC experiments. They successfully matched the experimental data with a two-parameter autocatalytic model. In another study, Martin et al.[85] delved into VER cure kinetics using dynamic-mechanical thermal analysis (DMTA) and thermal scanning rheometry (TSR) under isothermal conditions. The apparent activation energy was derived from both the gel time and the complex viscosity versus time plot. COOK et al. [86] explored VER's cure kinetics by analyzing DSC and DMTA data while varying catalyst concentration and cure temperature under isothermal and non-isothermal settings. Notably, they observed an accelerated reaction rate and decreased gel time with higher concentrations of methyl-ethyl ketone peroxide (MEKP) catalyst.

Furthermore, researchers have investigated the efficacy of VER as a matrix in fibre-reinforced plastic composites. Ganesh Gupta K et al. [87] evaluated the performance of glass fibre-reinforced composites based on both epoxy and VER matrices. They quantified improvements of 22.54%, 21.83%, and 13.43% in tensile strength, interlaminar shear strength (ILSS), and flexural strength, respectively, for the VER-based composite over the epoxy-based counterpart. Similarly, Bonsu et al.[88] analyzed the performance of Glass Fiber Reinforced Vinyl Ester Epoxy (GFRP) and Basalt Reinforced Vinyl Ester Epoxy (BFRP) composites in terms of tensile, flexural, and impact strengths in seawater applications. They established a decrease in these strengths with prolonged seawater exposure. Notably, GFRP and BFRP composites exhibited comparable seawater ageing behaviour. Additionally, Thomason and Xypolias [89] conducted an extensive literature review focusing on the hydrothermal ageing applications of Glass Fiber Reinforced Vinyl Ester Epoxy (GFRP) composites. Their work underscores the increasing relevance of studying the long-term environmental effects on VE-based composites due to the expanding use of such materials.

2.1.2.2 RTM6 resin

The mono-component RTM6 resin, provided by Hexcel, has been specifically formulated for applications in the RTM process. Renowned for its usage in crafting high-performance carbon fibre-reinforced composites, this RTM6 resin stands as an endorsed choice for aerospace applications. Distinctive in its high viscosity, it undergoes pre-heating to 80°C before being infused into the RTM process. Extensive research has been directed toward comprehending the curing kinetics of RTM6 resins, employing a variety of experimental methodologies[90]–[92].

Navabpour et al. [93] conducted an exhaustive study on the cure kinetics of RTM6 resin utilizing both Differential Scanning Calorimetry (DSC) and a microwave-heated calorimeter.

Their investigation encompassed isothermal and dynamic scan conditions, leading to an in-depth analysis of cure reaction rates. Interestingly, despite a comparable cure reaction mechanism between the two calorimeters, the microwave heating calorimeter demonstrated a swifter cure reaction rate compared to the conventional DSC technique. Skordos and Partridge [94] devised a numerical approach for investigating cure kinetics modelling of RTM6 resin, utilizing data obtained from DSC experiments. This algorithm mirrors the chemical and physical behaviour of the resin, eliminating the need for parameter calculation that is characteristic of other empirical cure rate models. Instead, it hinges on a heuristic approach that aligns experimental data, offering a more accurate depiction of cure kinetics. Struzziero et al. [95] embarked on the development of a finite element model designed to measure the thermal conductivity of RTM6 resin in relation to curing temperature. By delving into an in-depth analysis of cure kinetics, they derived a thermal conductivity model contingent upon both the degree of cure and the curing temperature. Aduriz et al. [96] opted to study the cure cycle of RTM6 resin through refractive index measurements. Their findings indicated a linear increment in the degree of cure corresponding to an increase in refractive index, underscoring the potential for this measurement technique.

Numerous works have honed in on the analysis of cure cycles for RTM6 resins in the context of composite part manufacturing via the RTM process. Gross et al.[97] delved into the influence of alterations in the time-temperature profile of RTM6 resin on hydrostatic residual stresses generated within 3D woven composite parts. Through a modified cure cycle, involving heating, temperature stabilization, cooling, subsequent stabilization, and re-heating, they observed a reduction in residual stresses. Nawab et al. [98] employed the COMSOL multi-physics simulator to determine the residual stress induced in RTM6 matrix-based carbon woven composites. They integrated a heat transfer model along with cure kinetics to examine how variations in thermal properties impact both the degree of cure and thermal gradients.

In summary, the exploration of VER and RTM6 resin's cure kinetics has spurred a plethora of research activities, spanning multiple experimental techniques and modelling approaches. This collective effort has substantially expanded our understanding of VER and RTM6 resin behaviour, ultimately contributing to the refinement of the RTM process.

Through a comprehensive review of the existing literature, it becomes evident that researchers have been primarily engaged in investigating the kinetics of resin curing as a prerequisite for its application within the realm of composite manufacturing. Furthermore, it's apparent that these researchers have either developed cure kinetics models tailored to specific resin systems or scrutinized the robustness of these kinetics by employing a range of cure rate

models. To the best of the investigator's knowledge, prior to this work, no literature has been identified that directly addresses the formulation of time-temperature-cure process windows for resins. Moreover, a notable absence is noted in published works pertaining to the establishment of time-temperature-cure process windows for neat vinyl ester and RTM6 resins. This type of process window furnishes crucial insights into the progress of cure reactions and the required duration for a given temperature setting. The aim of this chapter is to develop a time-temperature-cure process window for neat vinyl ester and RTM6 resins, utilizing thermal characterizations to simulate the resin transfer moulding process. The steps involved in obtaining the cure process windows for both resins were provided in detail in **subsection 2.2.3**.

This comprehensive and systematic approach ensures the establishment of accurate and informative time-temperature-cure process windows, thereby contributing to an enhanced understanding of the curing dynamics for both the vinyl ester and RTM6 resins in the context of resin transfer moulding simulations.

2.2 Materials and Methods

2.2.1 Materials

The thermal cure analysis was conducted using two distinct resins: Derakane 8084 vinyl ester resin provided by Ashland and mono-component RTM6 resin supplied by Hexcel. These resins have been tailor-made for deployment within advanced liquid composite moulding processes. The curing of the vinyl ester resin was facilitated through the application of methyl ethyl ketone peroxide as the catalyst, complemented by cobalt octate serving as the accelerator—both of which were supplied by Hexcel.

2.2.2 Differential Scanning Calorimetric Experiments

Thermal characterization of neat vinyl ester and RTM6 resins was carried out using the TA Instrument DSC Q200 model. The process commenced with a dynamic DSC run conducted at a heating rate of 10°C/min, intended to determine the suitable temperatures for subsequent isothermal experiments. Isothermal DSC experiments were then conducted within the temperature range spanning from the onset to the peak resin cure temperatures, as identified from the dynamic DSC scan. These isothermal DSC experiments involved the measurement of heat flow over time, extending until the resin cure process was completed.

2.2.3 Cure Process Window using Cure Kinetics Modelling

The objective of cure kinetics modelling is to accurately establish the reaction rate of the curing process. To initiate this process, heat flow was measured over time at various isothermal temperatures using DSC until the reaction reached completion. The degree of cure at the time 't', denoted as $\alpha(t)$, can be deduced from the DSC heat flow curves through **Equation (2.5)**:

$$\alpha(t) = Q_{(t)} / Q_\infty \tag{2.5}$$

Here, for a given isothermal temperature, $Q_{(t)}$ represents the cumulative heat of reaction up to the curing time 't', which is depicted by the area beneath the heat flow curve at that time. On the other hand, Q_∞ signifies the total enthalpy of the reaction, encompassing the complete area under the heat flow curve.

The steps involved in constructing the time-temperature-cure process window are outlined as follows:

i. Initially, dynamic Differential Scanning Calorimetry (DSC) scans were conducted to determine the suitable temperatures for subsequent isothermal experiments.

ii. Subsequently, isothermal DSC experiments were executed, covering temperatures ranging from the initiation of curing to the peak resin cure temperatures as determined from the dynamic DSC scans. This process yielded a heat flow vs. time curve.

iii. Then, the heat flow vs. time curve was numerically integrated to obtain the total heat of reaction Q_∞ and the accumulative heat of reaction $Q_{(t)}$ at any instant time t.

iv. Next, the degree of cure $\alpha(t)$ was computed at each interval of time using **Equation (2.5)**, and the degree of cure vs. time curve was generated.

v. Subsequently, the degree of cure vs. time curve was numerically differentiated to obtain the rate of degree of cure vs. time curve.

vi. Following that, the rate of cure was fitted as a function of the degree of cure using non-linear regression analysis with the classic resin cure kinetics models and the cure kinetic parameters were obtained.

vii. The obtained experimental cure kinetics parameters were extrapolated for wide ranges of temperatures and thus, a time-temperature-cure process window was obtained for all possible processing conditions.

Non-isothermal DSC experiment

Isothermal DSC experiments
Heat flow $= f$ (time) at temperatures

Degree of cure $(\alpha) = f$ (time) at temperatures

Heat Flow

Time

$$\alpha(t) = \frac{Area\ at\ time\ t}{Total\ area}$$

Degree of cure

Time

Slope
$=$ rate of cure, $\frac{d\alpha}{dt}$

Rate of degree of cure $= f$ (time) at temperatures

Rate of cure

Time

Rate of cure $= f$ (degree of cure, temperature) using classic resin cure model

Time-Temperature-Cure Process Window

Figure 2. 2 Development of Time-Temperature-Cure Process Window using Resin Cure Kinetics

2.3 Results and Discussion

2.3.1 Vinyl Ester Resin Cure Kinetics

From the dynamic DSC scans the temperatures between 50°C and 100°C were selected for isothermal DSC experiments. It may be mentioned that the resin reactivity will be very low at temperatures below 50°C and the samples are needed to keep longer times at DSC for complete curing. Also, it may be mentioned that the resin reactivity will be very high at temperatures above 100°C and DSC may fail to sense the higher heat flow rates at the onset. Hence, temperatures between 50°C and 100°C were selected to conduct an isothermal DSC resin cure.

Figure 2.3 shows the heat flow vs. cure time at 50°C, 60°C and 70°C. From **Figure 2.3** it can be seen that the peak of the heat flow rate increases with increasing temperature and the time taken to reach the peak heat flow rate decreases. The isothermal heat flow vs. time data as given in **Figure 2.3** was numerically integrated to obtain the degree of cure using Equation 6, which is shown in **Figure 2.4**. From **Figure 2.4**, it is evident that at all the temperatures, the

degree of cure has a steep rise in the earlier stages of the curing, and at any given time, the higher the isothermal temperature, the higher the degree of cure. From **Figures 2.3 and 2.4**, the rate of cure vs degree of cure can be obtained from the steps explained in **subsection 2.2.3**.

Figure 2.5 shows the rate of cure versus cure conversion at different isothermal temperatures. As can be seen from **Figure 2.5**, the peak of the cure rate increases with increasing temperature and the peak cure rate is reached at the earlier conversions with increasing temperature. At a given temperature, the rate of cure increases with the degree of cure and attains a maximum at α<0.1, then gradually decreases and finally tends to zero. At a given conversion, the higher the isothermal temperature, the higher the rate of cure and the lesser the time to complete the cure reaction. Several rate models were tried to fit experimentally obtained cure rate versus the degree of cure for vinyl ester resin. From the results, it was found that the modified Kamal and Sourour autocatalytic form of the kinetic model fitted well with the experimental data. **Figure 2.5** shows comparisons between the experimental and modelled results and the respective kinetics model parameters were obtained using non-linear regression analysis. The modelled kinetic parameters and the correlation factors for different models are tabulated in **Table 2.2**.

The temperature dependency of the kinetic rate constants within the Modified Kamal & Sourour kinetics model has been assessed by fitting it to the Arrhenius formulation, illustrated in **Figure 2.6**. The optimal fitting of the Arrhenius equation, which establishes the correlation between rate constants and temperature, is represented by **Equation (2.2)**. The frequency factor (A) and activation energy (E) were determined as 1.04×10^9 min^{-1} and 61.19 kJ mol^{-1}, respectively. To project the behaviour of the resin cure across a range of temperatures, the parameters of the Modified Kamal & Sourour kinetics model were extrapolated. Consequently, the complete process window for the epoxy-vinyl ester resin was derived, visually depicted in **Figure 2.7**.
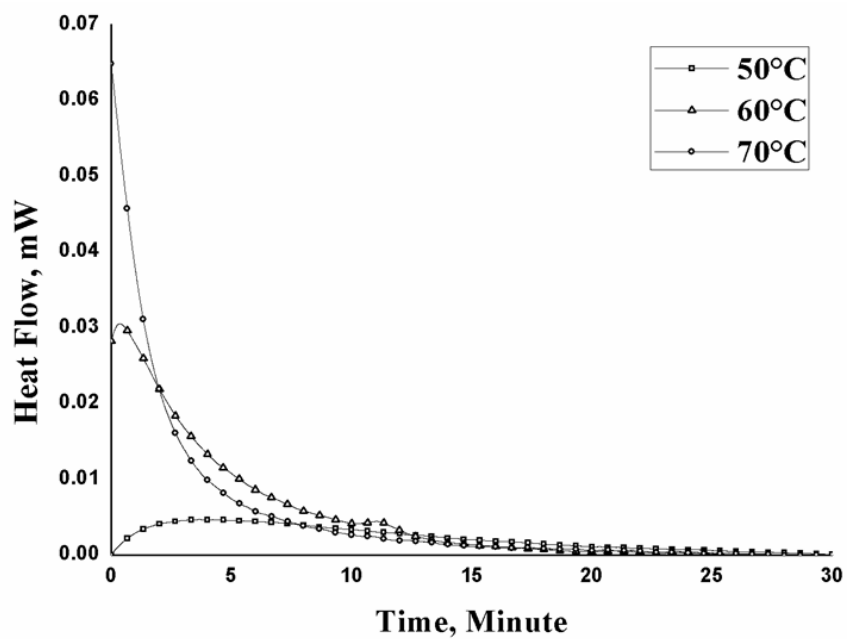
Figure 2. 3 Isothermal Heat Flow of Neat Vinyl Ester Resin
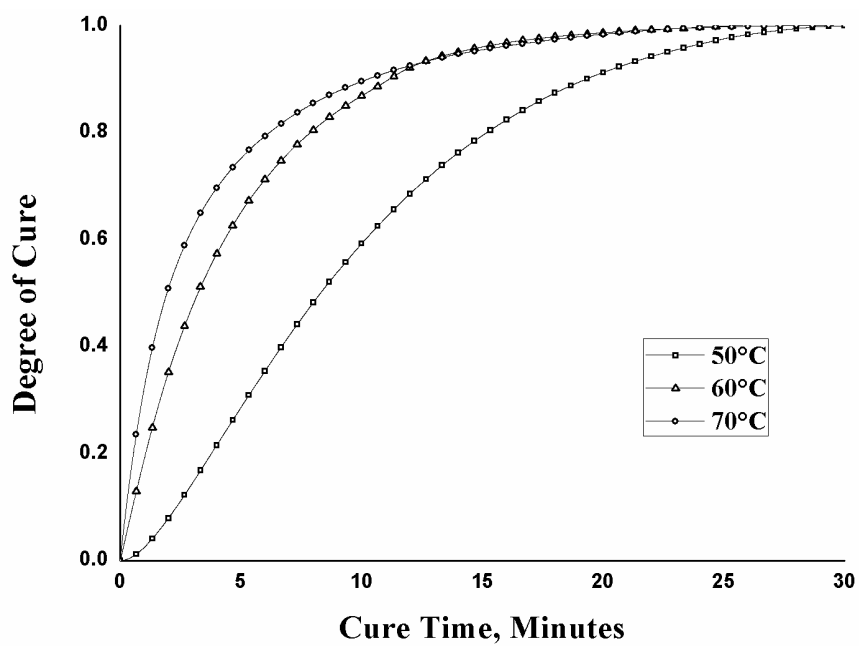
Figure 2. 4 Degree of Cure of Neat Vinyl Ester Resin

50°C		
60°C		
70°C		

Modified Kamal & Sourour 4 Kinetics

Modified Kamal & Sourour 4	y = k*(x^m)*((1-x)^n)		
Adj. R-Square	0.99919		70 deg C
		Value	Standard Error
k		0.4987	0.01405
m		0.0521	0.0108
n		1.7121	0.03514
Adj. R-Square	0.99791		60 deg C
		Value	Standard Error
k		0.2558	0.0086
m		0.0625	0.01384
n		1.2050	0.03549
Adj. R-Square	0.99537		50 deg C
		Value	Standard Error
k		0.1320	0.00456
m		0.2844	0.01697
n		0.8575	0.02829
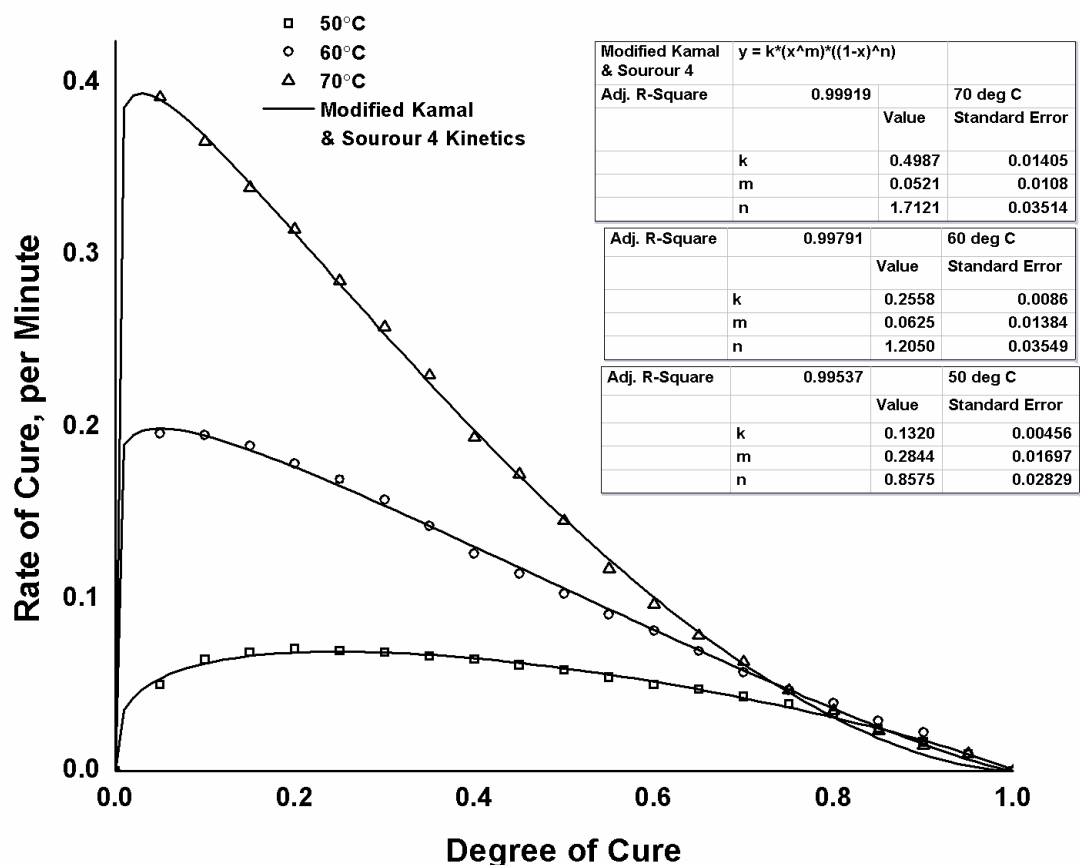
Figure 2. 5 Modified Kamal & Sourour Cure Kinetics of Vinyl Ester Resin

Table 2. 2 Cure Kinetics Rate Model Analysis for Vinyl Ester Resin

Rate Models	Parameters	Modelled Parameter Values with Goodness of Fit, R^2			Remarks
		50°C	60°C	70°C	
n^{th} Order Kinetics	k, n	$k = 0.0633$ $n = 0.3362$ $R^2 = 0.458$	$k = 0.170$ $n = 0.726$ $R^2 = 0.573$	$k = 0.314$ $n = 1.023$ $R^2 = 0.592$	No goodness of fit at all studied temperatures. The model is incapable of predicting autocatalytic kinetics
Kamal & Sourour (KS)	k_1, k_2, n, m	$k_1 = -1.5 \times 10^{-7}$ $k_2 = 0.0748$ $m = 2.8 \times 10^{-16}$ $n = 0.4773$ $R^2 = 0.898$	$k_1 = 0.1103$ $k_2 = 0.1103$ $m = -7.69 \times 10^{-16}$ $n = 1.069$ $R^2 = -0.995$	$k_1 = 0.217$ $k_2 = 0.217$ $m = -6.1 \times 10^{-16}$ $n = 1.55$ $R^2 = 0.998$	Negative rate constants, the Model fails at a lower temperature

KS Modified Form No. 1	k_1, k_2, n_1, n_2, m	$k_1 = 1.4\times10^{-4}$ $k_2 = 0.075$ $n_1 = 0.478$ $n_2 = 0.475$ $m = 3.9\times10^{-16}$ $R^2 = 0.892$	$k_1 = -0.086$ $k_2 = 0.306$ $n_1 = 0.778$ $n_2 = 0.975$ $m = -5.7\times10^{-16}$ $R^2 = 0.995$	$k_1 = 0.0017$ $k_2 = 0.515$ $n_1 = -0.537$ $n_2 = 1.784$ $m = 0.0645$ $R^2 = 0.999$	Too many model parameters, predicted negative reaction order, Model fails at a lower temperature
KS Modified Form No. 2	k_1, k_2, n, m	$k_1 = 0.025$ $k_2 = 0.0748$ $m = -0.014$ $n = -0.012$ $R^2 = 0.325$	$k_1 = -0.014$ $k_2 = 0.256$ $m = 0.063$ $n = 1.205$ $R^2 = -0.998$	$k_1 = 0.298$ $k_2 = 0.146$ $m = -0.024$ $n = 1.636$ $R^2 = 0.997$	Too many model parameters, predicted negative reaction order, Model fails at a lower temperature
KS Modified Form No. 3	k_1, k_2, m	$k_1 = 0.055$ $k_2 = 0.055$ $m = 0$ $R^2 = -0.352$	$k_1 = 0.1387$ $k_2 = 0.1387$ $m = 0$ $R^2 = -0.810$	$k_1 = 0.2415$ $k_2 = 0.2415$ $m = 0$ $R^2 = 0.975$	Predicted convergence issue
KS Modified Form No. 4	k, m, n	$k = 0.132$ $m = 0.284$ $n = 0.858$ $R^2 = 0.995$	$k = 0.2558$ $m = 0.0625$ $n = 1.205$ $R^2 = 0.998$	$k = 0.499$ $m = 0.0521$ $n = 1.712$ $R^2 = 0.999$	This model was capable of capturing both the degree of cure and the curing rate qualitatively and quantitatively at all the studied temperatures
KS Modified Form No. 5	k, n, m	$k = 0.045$ $m = 3.487$ $n = 2.022$ $R^2 = 0.692$	$k = 0.132$ $m = 5.326$ $n = 3.985$ $R^2 = 0.661$	$k = 0.231$ $m = 10.36$ $n = 8.12$ $R^2 = 0.698$	No goodness of fit at all the studied temperatures.

KS Modified Form No. 6	k, m, n, p	k = 0.132 m = 0.284 n = 0.429 p = 0.429 $R^2 = 0.995$	k = 0.256 m = 0.062 n = 0.556 p = 0.649 $R^2 = 0.998$	k = 0.499 m = 0.052 n = -11.63 p = 13.34 $R^2 = 0.999$	Too many model parameters predicted negative reaction order

Figure 2. 6 Arrhenius Plot for Vinyl Ester Resin Kinetics Model
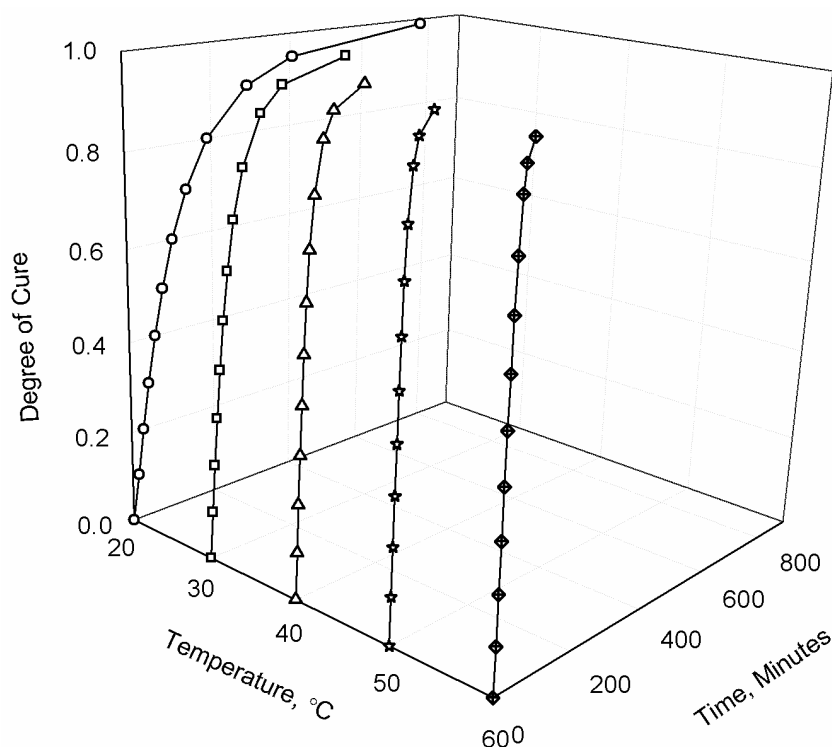
Figure 2. 7 Time-Temperature-Cure Process Window for Epoxy-Vinyl Ester Resin

2.3.2 RTM6 Resin Cure Kinetics

Figure 2.8 shows the heat flow curves obtained from a standard 10°C/min dynamic DSC scan. The total heat of reaction for the complete resin cure is obtained from the area under each heat flow curve. From **Table 2.3**, it can be seen that the heat of reaction for complete resin cure varies from 450 – 467 J/g and hence, an average of 458 J/g was used as heat of reaction for the simulation studies. From **Figure 2.8**, it is evident that the onset of the curing reaction is above 130°C and the maximum heat flow of the curing reaction occurs around 240°C. Also, the final temperature at the cure curve was found to be 300°C. It may be mentioned that the resin reactivity will be very low at temperatures below 130°C and the samples are needed to keep longer times at DSC for complete curing. Also, it may be mentioned that the resin reactivity is very high at temperatures above 240°C and DSC may fail to sense the higher heat flow rates at the onset. Hence, temperatures between 130°C and 240°C were selected to conduct an isothermal DSC resin cure.
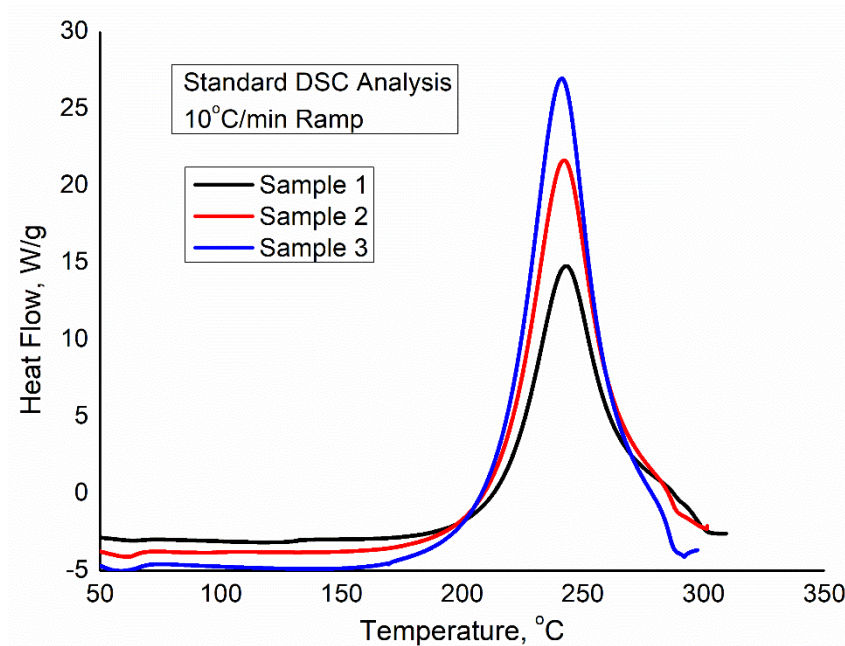
Figure 2. 8 The heat of Reaction of Neat RTM6 Resin

Table 2. 3 RTM6 – Heat of Reaction, Cure Onset, Peak and Final Cure Temperatures

Sample No.	DSC Mode	Weight of Sample, mg	Cure Onset Temperature, °C	Cure Peak Temperature, °C	Final Cure Temperature, °C	Heat of Reaction, J/g.
1	Dynamic Scan at 10°C/min	8	130	243	300	450.5
2	Dynamic Scan at 10°C/min	11.8	130	242	300	466.5
3	Dynamic Scan at 10°C/min	14.7	130	241	300	457.6

Figure 2.9 illustrates the heat flow versus process time at different isothermal temperatures 180°C, 200°C, 220°C and 240°C. With an increase in temperature, the peak heat flow increases and the curing time decreases. This may be attributed due to the increase in resin reactivity with an increase in process temperature. At first, the heat flow curve as shown in **Figure 2.9** was numerically integrated to obtain the degree of cure as a function of cure time at different isothermal temperatures. Then, the rate of cure is obtained by numerically differentiating the degree of cure versus time curves and the detailed procedure is illustrated in **Figure 2.2**. **Figure 2.10** shows the degree of cure versus cure time at different isothermal temperatures. From **Figure 2.10**, it is evident that at all the temperatures, the degree of cure has a steep rise in the

earlier stages of the curing, and at any given time, the higher the isothermal temperature, the higher the degree of cure. **Figure 2.11** shows the rate of cure versus cure conversion at different isothermal temperatures. As can be seen from **Figure 2.11**, the peak of the cure rate increases with increasing temperature and the peak cure rate is reached at the earlier conversions with increasing temperature. At a given temperature, the rate of cure increases with the degree of cure and attains a maximum at $0.3 < \alpha < 0.6$, then gradually decreases and finally tends to zero. At a given conversion, the higher the isothermal temperature, the higher the rate of cure and the lesser the time to complete the cure reaction.

Several rate models were tried to fit experimentally obtained cure rate versus the degree of cure for RTM6 resin. From the results, it was found that the classical Kamal and Sourour and the modified Kamal and Sourour autocatalytic form of kinetics models fit well with the experimental data. **Figure 2.11** shows comparisons between the experimental and modelled results and the respective kinetics model parameters were obtained using non-linear regression analysis. The modelled kinetic parameters are tabulated in **Table 2.4**.

Kamal and Sourour and modified Kamal and Sourour's models for RTM6 resin curing kinetics are given in **Equations (2.6 & 2.7)**, respectively. The best fit between the rate constants and temperature in terms of Arrhenius form is given in **Equations (2.8 – 2.10)**. The temperature dependence of the kinetic rate constants of the kinetics models has been determined by fitting to the Arrhenius form as shown in **Figure 2.12**. The associated activation energies and frequency factors obtained from Arrhenius plots are tabulated in Table 4.

$$\frac{d\alpha}{dt} = (1.31 \times 10^7 \times e^{-9953/T} + 8.98 \times 10^6 \times e^{-8116/T} \times \alpha^{0.983}) \times (1 - \alpha)^{1.203} \quad (2.6)$$

$$\frac{d\alpha}{dt} = (3.2 \times 10^6 \times e^{-7706/T} \times \alpha^{0.774}) \times (1 - \alpha)^{1.097} \quad (2.7)$$

$$\ln(k_1) = \frac{-9953}{T} + 16.39, \quad R^2 = 0.993 \quad (2.8)$$

$$\ln(k_2) = \frac{-8116}{T} + 16, \quad R^2 = 0.936 \quad (2.9)$$

$$\ln(k) = \frac{-7706}{T} + 14.98, \quad R^2 = 0.91 \quad (2.10)$$
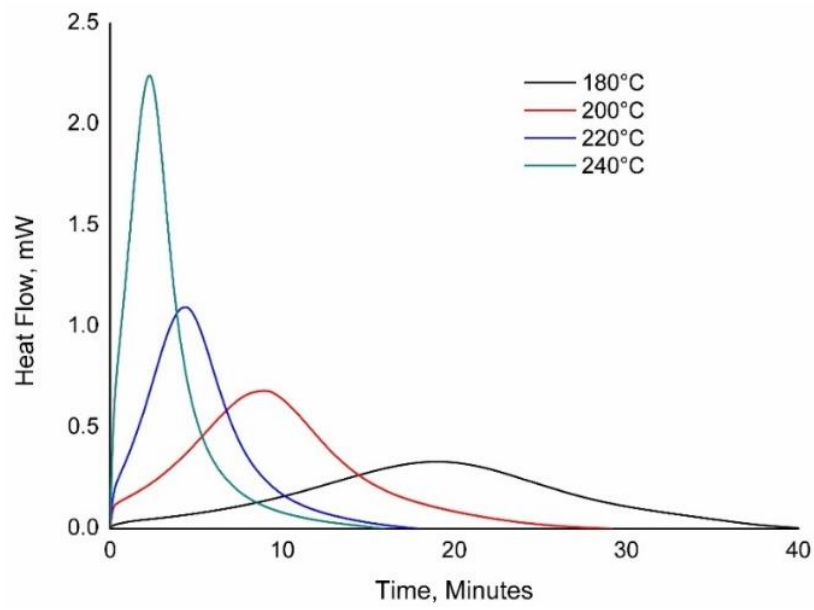
Figure 2. 9 Isothermal Heat Flow of Neat RTM6 Resin
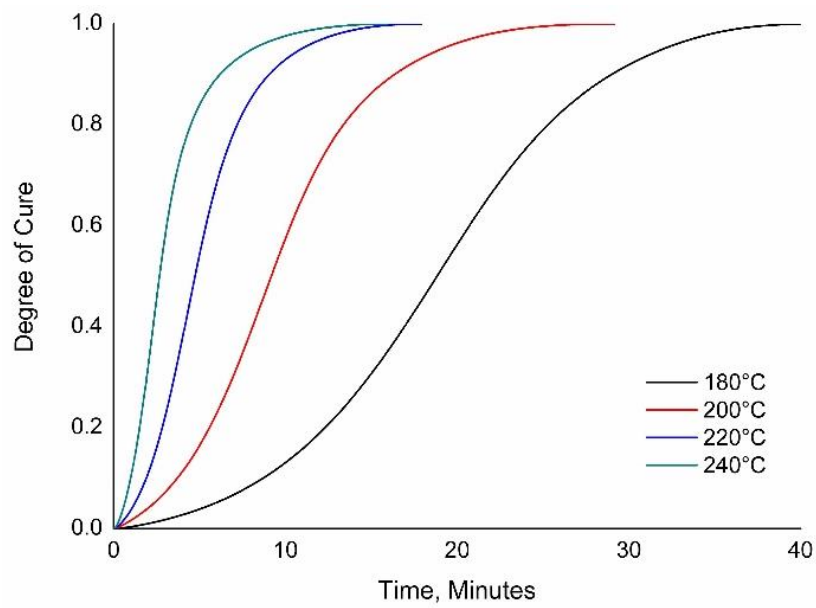
Figure 2. 10 Degree of Cure of RTM6 resin
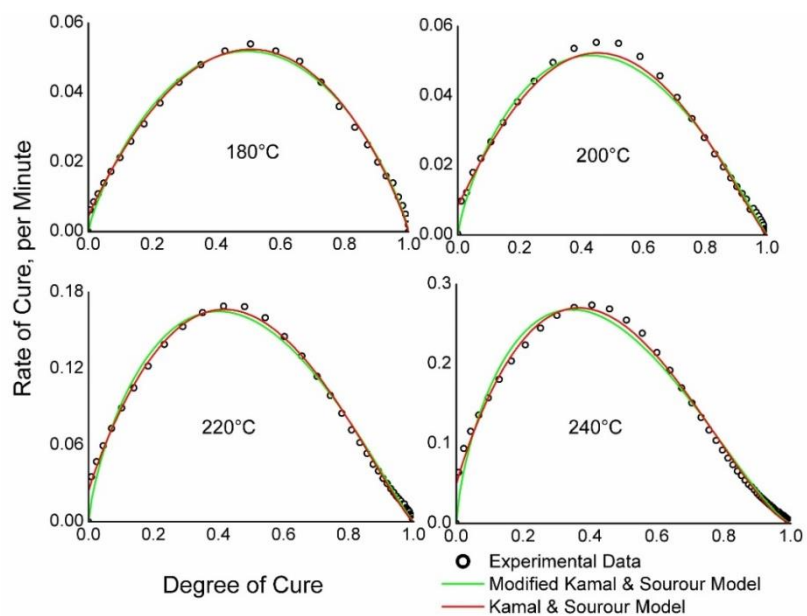
Figure 2. 11 RTM6 Resin Cure Kinetics Modelling
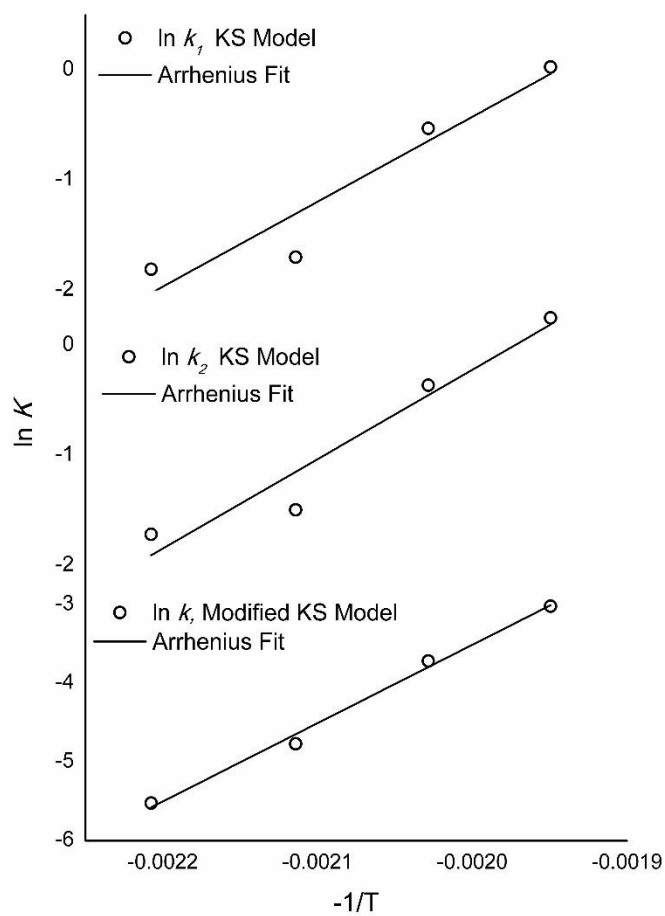
Figure 2. 12 Arrhenius Plot for RTM6 Resin Kinetics Modelling

Table 2. 4 Classical and Modified Kamal and Sourour Cure Kinetics Model Parameters

Classical Kamal and Sourour Cure Kinetics Model Parameters					
Temperature, °C	k_1, Minute^{-1}	k_2, Minute^{-1}	m	n	Correlation Coefficient
180	0.004	0.18	0.958	0.890	0.993
200	0.0085	0.2248	1.052	1.173	0.984
220	0.0244	0.6973	0.9616	1.24	0.997
240	0.049	1.284	0.962	1.51	0.996

$E_1 = 82.75$ kJ mol^{-1} $E_2 = 67.48$ kJ mol^{-1} $A_1 = 1.31$ x 10^7 min^{-1} $A_2 = 8.98$ x 10^6 min^{-1}

Modified Kamal and Sourour Cure Kinetics Model Parameters				
Temperature, °C	k, Minute^{-1}	m	n	Correlation Coefficient
180	0.164	0.824	0.835	0.989
200	0.183	0.797	1.051	0.976
220	0.589	0.755	1.137	0.992
240	1.029	0.720	1.366	0.991

$E = 64.07$ kJ mol^{-1} $A = 3.2$ x 10^6 min^{-1}

The cure data acquired through experimentation at temperatures of 180°C, 200°C, 220°C, and 240°C was employed to model the cure kinetics utilizing the Kamal and Sourour model. The parameters obtained from this modelling were then extrapolated to ascertain the RTM6 resin's curing behaviour across the entirety of the temperature spectrum. As a result, the comprehensive process window for the RTM6 heat application was formulated, depicted in **Figure 2.13**. The extrapolated model parameters for the remaining temperatures are tabulated in **Table 2.5**.
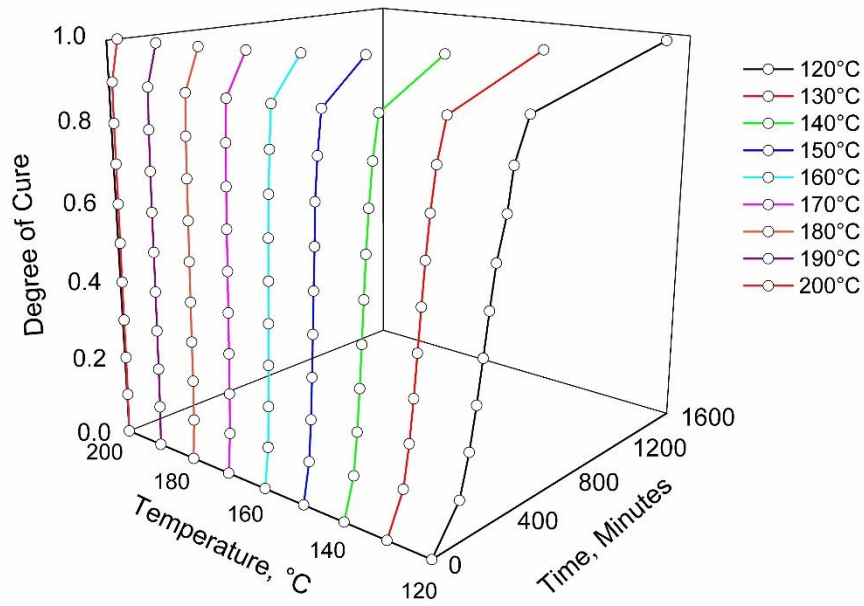
Figure 2. 13 Time-Temperature-Cure Process Window of RTM6 Resin

Table 2. 5 Kamal & Sourour Cure Kinetics Parameters for RTM6 Process Window

Temperature, °C	Temperature, K	K_1, min^{-1}	K_2, min^{-1}
100	373	4.97335E-05	0.005034048
110	383	9.63224E-05	0.008547045
120	393	0.000180383	0.014125861
130	403	0.000327448	0.022771159
140	413	0.000577496	0.0358685
150	423	0.000991529	0.055298244
160	433	0.001660422	0.083565297
170	443	0.00271658	0.123949594
180	453	0.004348977	0.18067785
190	463	0.00682219	0.259116566
200	473	0.010500082	0.365985849

$E_1 = 78.51$ kJ mol^{-1} $A_1 = 4917447$ s^{-1} $E_2 = 62.87$ kJ mol^{-1} $A_2 = 3213914$ s^{-1}

$m = 0.961$ $n = 1.213$

2.4 Summary

The primary objective of this chapter was to produce a time-temperature-cure process window for both neat vinyl ester and RTM6 resins. A methodology employing thermal characterization of the neat resin and cure kinetics modelling was introduced to attain the cure process window. Initially, the vinyl ester and RTM6 resins were thermally characterized using Differential Scanning Calorimetry (DSC) under isothermal and non-isothermal conditions. Subsequently, various cure kinetic models were examined to describe the cure kinetics of the vinyl ester and RTM6 resins.

For neat vinyl ester resin, the modified Kamal and Sourour three-parameter model emerged as the most adept in capturing both the degree of cure and the curing rate, exhibiting both qualitative and quantitative agreement. Conversely, in the case of neat RTM6 resin, both the Kamal & Sourour model and the modified Kamal & Sourour model 4 demonstrated robust alignment with our experimental data. Specifically, for vinyl ester resin composite part process simulations, the cure rate model $\frac{d\alpha}{dt} = (1.04 \times 10^9 \times e^{-7359.8/T} \times \alpha^{0.284}) \times (1 - \alpha)^{0.857}$ was effectively employed. On the other hand, during the simulation of RTM6 resin composite part processes, the cure rate model $\frac{d\alpha}{dt} = (3.2 \times 10^6 \times e^{-7706/T} \times \alpha^{0.774}) \times (1 - \alpha)^{1.097}$ exhibited commendable suitability.

This analysis was not limited to the experimental temperatures; rather, the model parameters were extrapolated to encompass broader operational temperature ranges, thereby yielding comprehensive cure evolution profiles. By extrapolating the cure kinetics model to resin processing temperatures, we derived Time-Temperature-Cure process windows for both vinyl ester and RTM6 resins. These process windows furnish invaluable insights by offering a means to predict the degree of cure and the corresponding cure time for any given temperature setting. Ultimately, this development proves instrumental in devising efficient strategies for designing the optimal cure cycles for composite parts.

Chapter 3

Reinforcement Mat Permeability Characterization using Mould-Filling Experiments

3.1 Introduction

The Resin Transfer Moulding (RTM) process simulation software packages are designed to replicate various aspects of the manufacturing process. These packages are capable of modelling essential factors such as the flow of resin, distribution of pressure and temperature, as well as the curing of resin. The most widely used software for simulating Liquid Composite Moulding (LCM) processes include LIMS [99], PAM-RTM [100], ANSYS Fluent [101] and COMSOL multi-physics [90]. However, the accuracy of these simulations heavily relies on the quality of input data. Hence, it is imperative to have precise processing parameters and material properties to achieve accurate simulations in order to mimic the real process.

These simulation packages primarily focus on reproducing the phase where the mould is filled with resin, accomplished by solving the flow of resin through a porous medium [102]. The flow pattern is established by linking variables like flow velocity, pressure gradient, fluid viscosity, permeability, and porosity of the porous medium [103]. The flow through porous media is represented by Darcy's law as given in **Equation (3.1)**

$$\vec{u} = \frac{-K}{\emptyset \mu} \nabla \text{P} \tag{3.1}$$

$\vec{u}$ denotes the fluid velocity vector, $\emptyset$ signifies porosity, μ represents resin viscosity and ∇p embodies pressure gradient. The tensor K symbolizes the permeability of the reinforcement mat as given in **Equation (3.2)**:

$$K = \begin{vmatrix} K_{xx} & K_{xy} & K_{xz} \\ K_{xy} & K_{yy} & K_{yz} \\ K_{xz} & K_{yz} & K_{zz} \end{vmatrix} \qquad (3.2)$$

For orthotropic mats, individual directional permeabilities are simplified to principle permeabilities in which **Equation (3.2)** deduces to **Equation (3.3)** as given below

$$K = \begin{vmatrix} K_{xx} & 0 & 0 \\ 0 & K_{yy} & 0 \\ 0 & 0 & K_{zz} \end{vmatrix} \qquad (3.3)$$

K_{xx}, K_{yy}, and K_{zz} denotes the principal permeabilities along the *x*, *y* and *z* directions, respectively.

The interaction between the fluid and the structure of the porous medium is simplified into a single variable, which is called permeability. Permeability refers to the degree of resistance offered by the reinforcement preform against the flow of the impregnating fluid. The accuracy of the reinforcement permeability is the primary requisite for the realistic RTM mould-filling process and thus, reinforcement permeability data becomes vital for any LCM process simulators. From the literature review, it was found that the reinforcement mat permeabilities were highly influenced by mould fill injection pressure, mat porosity, mat thickness and fluid viscosity [104], [105]. These parameters play a significant role in shaping the permeability and thus, the overall mould-fill pattern of the RTM process.

In this chapter, the permeability of reinforcement mats was evaluated by systematically varying both influential material (fluid viscosity, mat porosity, mat thickness) and process parameters (mould-filling injection pressure) through a series of mould-filling experiments. The main objective was to formulate a permeability model for reinforcement mats that considers the dependency on material and process parameters. This model was developed using machine learning techniques, with the aim of utilizing it to simulate the Resin Transfer Moulding (RTM) mould-filling process. The following subsections provide a comprehensive literature review exploring different methods employed to characterize the permeability of reinforcement mats and influential material and process parameters on mat permeability.

3.1.1 Bibliometric Analysis

A bibliometric analysis was conducted on August 20, 2023, utilizing the Web of Science core database. A collection of 150 articles was obtained through the primary search terms 'Permeability' within the topics section and 'resin flow' within the Author Keywords section. Bibliometric network visualization was carried out using the VOSviewer software[49], as

depicted in **Figure 3.1**. The analysis focused on bibliometric coupling occurrences of author keywords that appeared more than 3 times. Out of a pool of 334 keywords, 43 keywords met this threshold and were consequently selected for further examination.

From these 43 keywords, the cumulative strength of co-occurrence links with other keywords was computed. This computation guided the selection of keywords with the highest total link strength. Among these keywords, 'resin flow', 'permeability', 'process monitoring', and others emerged as prominent author keywords.
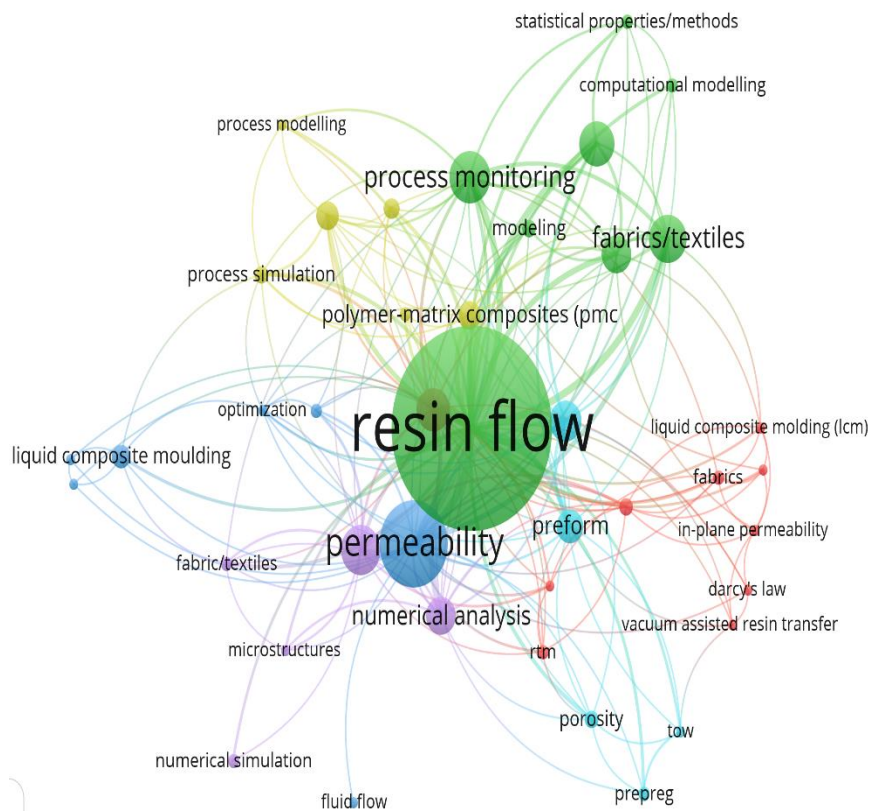
Figure 3. 1 Schematic Representation of the Bibliographic Networking Diagram Obtained from the Web of Science Core Database through the Search Conducted on August 20, 2023.

3.1.2 Literature Review

Resin Transfer Moulding (RTM) has emerged as a cost-effective and efficient technique for manufacturing composite parts. The process involved transferring resin from a reservoir into a reinforcing preform placed within a sealed mould [106]. Permeability properties were used to characterize resin flow within the preform and the resin-fibre wetting process. A comprehensive review of state-of-the-art literature, including both experimental and theoretical investigations for measuring permeability was presented [107]–[109].

Researchers developed unsaturated and saturated flow tests to measure the permeability of 1-D/isotropic reinforcement mats [110]–[112]. In unsaturated flow experiments, the fluid was introduced either at a constant pressure or a constant flow rate. In constant pressure injection experiments, the position of the flow front relative to filling time was tracked. On the other hand, in constant flow rate injection experiments, the position of the flow front increased linearly with time, and 1-D Darcy's law was used to measure the permeability. However, less accurate transient permeability data was obtained by constant flow rate injection experiments due to the complex interaction between flow and pressure drop [113]. As a result, many studies opted for mould-fill experiments based on constant pressure injection to measure mat permeability [114]–[117]. In saturated flow experiments, the transient variations of flow front position and flow rate/pressure were not taken into account and the permeability data was measured based on the complete resin-fibre saturation to the predefined mould dimension. It was also found that the saturated permeability for reinforcement is always greater than the unsaturated permeability.

Researchers have used radial flow experiments for the measurement of 2D permeability data [118]. In this experiment, the resin was introduced into the mould through a central injection port [119]. As the resin flows through the preform, the resulting flow front can be observed as circular or elliptical depending on the preform type. Circular flow fronts were observed in isotropic mats with equal permeability in all directions whereas elliptical flow fronts were observed in anisotropic mats with varying permeability in different directions [120].

Numerous efforts have been devoted to the study of fibre mat permeability using both one-dimensional and two-dimensional flow measurement techniques. Weitzenbock et al. [121] proposed an analytical approach for measuring 2-dimensional unsaturated permeability. The proposed analytical model equation was applicable to radial flow experiments. This proposed model helps to determine the permeability values from the experimentally obtained flow front positions as a function of elapsed mould-filling time. Fratta et al. [122] proposed a novel unidirectional permeability measurement approach to characterize permeability as a function of fibre volume content. In their experimental setup, they positioned one pressure transducer at the inlet gate and embedded the second one within the mould. They developed a rapid algorithm to extract data from these two sensors. This algorithm automatically generated the permeability distribution thereby eliminating the need for manual observation of the flow front.

Prosenjit Maji et al. [123] developed a methodology for determining the transverse permeability of prepregs using process modelling and simulations. The experimental and

process simulation approach was employed to predict the consolidated thickness and the corresponding times for various permeability values. The permeability value was considered the effective permeability of prepregs when the predicted and experimentally obtained consolidation times matched perfectly. Kuppusamy et al. [124] developed a methodology to determine the two-dimensional permeability of glass fibre mats. They compared simulated and experimental flow front positions over time. They utilized a sensitivity analysis approach to predict the effective mat permeability for matched temporal flow front positions.

Kim et al. [26] framed an analytical model to forecast the permeability of shear-deformed woven fabric and then, the modelled results were compared with the experimentally obtained permeability values. They characterized the in-plane permeability of woven composites by altering the fibre orientation of the deformed woven fabric. This was done to simulate the vacuum-assisted resin transfer moulding (VARTM) process accurately. Tan et al. [125] developed a constant flow rate injection experiment to study one-dimensional porous flow. Their study explored the influence of porosity on the inlet pressure profile. They utilized three different types of fibre mats unidirectional, bi-axial, and tri-axial to examine the relationship between 1-D permeability and the inlet pressure profile.

Many efforts have been devoted to measuring the permeability in natural and synthetic fibre mats [109], [126]–[129]. The influence of processing and material parameters on reinforcement mat permeabilities was also reported. This included investigating the effects of mat porosity, fluid injection pressure, variations in test fluids and their viscosities on the reinforcement mat permeabilities.

Effect of Porosity on the Reinforcement Mat Permeability: Many studies in the literature have investigated the effect of fibre mat porosity and architecture on their permeabilities [130], [131]. Yan Li et al. [132] assessed the permeability of hybrid natural fibre-reinforced composites. They noted increased permeability in hybrid composites due to the higher porosity of jute fibre when compared to ramie fibre. Franucci et al. [133] examined the correlation between permeability and the porosity of natural fibres. Their findings indicated that both saturated and unsaturated permeabilities increase with increased porosity. Moreover, saturated permeability was found to be higher than the unsaturated permeability. In comparison to glass fibre mats, the permeabilities of natural fibre mats decreased due to greater fluid absorption and swelling. Kim and Daniel [131] devised a setup to investigate the relationship between permeability and flow rate. They observed a continuous increase in both saturated and unsaturated permeability with an increase in the flow rate. The effect of stitching patterns and

seam distances on the mat porosity was also explored well in the literature. The findings indicated that an increase in porosity resulted in higher permeability [130], [134].

Effect of Fluid Injection Pressure on the Reinforcement Mat Permeability: From the literature review, it was found that the fluid injection pressure affects the transient permeability and the behaviour of the flow front. Additionally, it was observed that the transient permeability decreased with an increase in the injection pressure [135], [136]. Shojaei et al. [116] found enhanced permeabilities under both transient and steady-state conditions with increased flow rates. They conducted their research in a one-dimensional domain using woven glass fabrics with varying pressures. Amico and Lekakou [137] conducted unsaturated flow experiments using plain weave glass fabric. Their experiments involved the use of both silicone oil and epoxy resin. Their findings indicated that there was a decrease in transient permeability as the injection pressure was increased. Ma and Shishoo [114] investigated the relationship between permeability and the position of the flow front. They noted that the transient permeability increases with the flow advancement. These studies were conducted using various reinforcement materials.

Effect of Test Fluids on the Reinforcement Mat Permeability: The literature review revealed that the selection of test fluids can influence the measured permeability values. Research has shown that the steady-state and transient permeabilities increase with a slight magnitude with the decrease in the test fluid viscosities [114], [138]. From the existing studies, it was found that the influence of viscosity is minimal on the permeabilities when fluid viscosity is lesser with proper cavity filling. In contrast, there is an increased mould-filling complication with an increase in test fluid viscosities and hence, the permeability decreases with the increase in the test fluid viscosities [138], [139]. Luo et al. [140] examined the effect of test fluids on different types of reinforcement mats. They observed a minimal effect of test fluids on the mat permeability. This finding aligns with the observations made by Hammond and Loos [115]. They concluded that the measured permeability remained constant regardless of the liquid used. This observation demonstrated its independence from factors such as contact angle and capillary number.

To sum up, this chapter measures the permeability of natural and synthetic fibre reinforcements using mould-filling experiments. The investigation takes into account the influence of various parameters such as porosity, fluid injection pressure, preform thickness, and viscosity of the test fluid. Research findings have revealed the relationships between these parameters and permeability, providing valuable insights for the refinement of the RTM process. To the best of the investigator's knowledge, there are no published articles that have

addressed models encompassing the synergetic influence of processing parameters, fibre architecture, and resin properties on the permeabilities of reinforcement mats. To be specific, there are no research articles available that discuss the use of machine learning techniques, such as artificial neural networks (ANN) and adaptive neuro-fuzzy inference systems (ANFIS), to predict permeability as a function of multiple influencing parameters.

The main aim of this chapter is to measure the reinforcement mat permeabilities using mould-filling experiments, for its applicability in mould-filling simulations. To achieve this main objective, the following steps were followed: (i) Initially, a 2D radial constant-pressure injection setup coupled with a visualization technique was employed to measure the mat permeability. In this method, the permeability was obtained by matching the experimental and the simulated flow progressions iterated with guessed permeability values [124]. (ii) The fibre wetting analysis was performed using the contact angle measurement method for analysing the test fluid saturation at the reinforcement mats. (iii) Experimental permeability data were collected with the variations in the processing parameters, fibre architecture and resin properties. (iv) The ANN and ANFIS models were trained from the obtained experimental input data set for the prediction of reinforcement mat permeability as a function of four input key parameters. (v) Statistical analysis was performed and the results obtained through different machine learning techniques were compared.

3.2 Materials

In this work, five different reinforcement mats and five different test fluids were used to perform mould-filling experiments for the measurement of mat permeability. Woven roving and chopped strand glass fibre mats, woven roving carbon fibre mat, jute fibre and hemp fibre mats were used in this study. The porosity of the mats was computed using areal density data as given in **Equation (3.4)**.

$$\varphi = 1 - \left(\frac{N \times \rho_A}{h \times \rho_f} \right) \qquad (3.4)$$

where φ is the porosity, N is the number of mat layers, ρ_A is the areal density of the fibre mats in Kg/m^2, h is the thickness of fibre preform in m and ρ_f is the density of fibre in Kg/m^3. The measured areal density of the fibre mat and the calculated porosity for the single-layer mat are given in **Table 3.1**. The physical properties of test fluids used in this work are given in **Table 3.2**.

Table 3. 1 Fibre Mat Properties

Reinforcement Mat	Thickness of Fibre Mat, h (mm)	Fibre Density (Kg/m³), ρ_f	Mat Areal Density (g/m²), ρ_A	φ
Chopped Strand Glass Fibre Mat (CSM)	0.45	2450	450	0.59
90° Woven Roving Glass Fibre Mat (WRM)	0.49	2450	610	0.5
90° Woven Roving Carbon Fibre Mat	0.42	1770	400	0.46
Jute Fibre Mat	0.67	1450	266	0.726
Hemp Fibre Mat	0.77	1500	395	0.658

Table 3. 2 Test Fluid Properties.

Test Fluid	Density (Kg/m³)	Viscosity (Pa-s)
Edible Oil	922	0.0398
Glycerol	1260	1.412
Epoxy Araldite LY 556	1150	11.81
Epoxy Araldite LY 5052	1170	1.358
Epoxy Vinyl Ester	1050	0.35

3.3 Methodology

The permeability of the reinforcement mat was measured using the constant flow 2D radial injection experimental technique. This method involved tracking the experimental flow front through a flow visualization technique. Then, the mat permeability was computed by matching the experimental flow progression with simulated flow progressions obtained from iteratively guessed permeability values. Next, the contact angle of test fluids on different fibre

mats was measured to analyze fibre wet-out as a function of wetting time for different test fluids. Subsequently, ANFIS and ANN models were developed to predict the permeability of the reinforcement mat. These models utilized an experimental input dataset, which included four independent variables: viscosity of the test fluid, number of layers, porosity of the reinforcement mats, and injection pressure. The sole dependent variable in this dataset was the reinforcement mat permeability.

3.3.1 Permeability based on Flow Tracking using Visualization Technique

A constant flow 2D radial injection experimental setup as shown in **Figure 3.2** was used to determine the permeability of the fibre mat. The top and bottom halves of the mould were made of acrylic material, 60 cm long, 60 cm wide and 1 cm thick. A single injection port of diameter 0.3 cm was positioned at the centre of the top mould. The test fluid was injected at a constant injection pressure and a video camera was used to record the resin flow through the fibre mat. The flow front progression during mould filling was recorded using a NIKON D3500 DSLR video camera. A pressure controller was employed to maintain a constant fluid injection pressure throughout the experiment. The flow front position as a function of time was tracked using the temporal frames obtained from the video camera [124].

In sequence, the experimental mould-filling conditions were mimicked in the COMSOL Multi-Physics simulator. Darcy's law and the level set model physics were incorporated to execute the isothermal mould-filling simulations within the COMSOL platform. Comprehensive insights related to relevant models and their implementation in COMSOL Multi-Physics were detailed in **Chapter 4**. The permeability value was determined by comparing the experimental flow fronts with simulated flow fronts generated using guessed permeability values. The guessed permeability value was considered the effective permeability value when the simulated and experimentally obtained flow fronts matched perfectly at all the time frames.
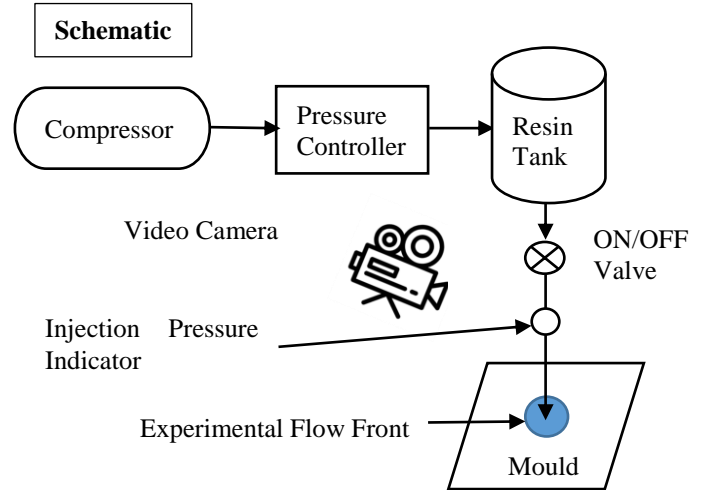
Figure 3. 2 Experimental Setup for Reinforcement Mat Permeability Measurement

3.3.2 Fibre Wetting Analysis

The fibre wetting analysis was performed using the contact angle measurement instrument HOLMARC (HO-IAD-CAM-01) by dropping 10μL of test fluid on the reinforcement fibre mat surface. The experiments were performed to analyse the test fluid saturation at the reinforcement mats using the change in droplet spread and its effect on reinforcement permeability[138].

3.3.3 ANFIS Modelling

ANFIS is a type of hybrid artificial intelligence (AI) model that combines the strengths of a fuzzy inference system (if-then rule) and ANN. This method effectively uses a fuzzy logic model with rules that are created during the model's training process using neural network theory. The membership function parameters of the fuzzy inference system (FIS) created by ANFIS were generated from the training samples [141]. In the present work, the ANFIS structure was constructed for four input parameters namely, the number of layers, porosity, test fluid viscosity and injection pressure and transient permeability as the output parameter. The rules for a Sugeno fuzzy model for a four-input system are as follows,

Rule 1: If x_1 is A_1, x_2 is A_2, x_3 is A_3 and x_4 is A_4, then $y_1 = c_1 + d_1x_1 + e_1x_2 + f_1x_3 + g_1x_4$

Rule 2: If x_1 is B_1, x_2 is B_2, x_3 is B_3 and x_4 is B_4, then $y_2 = c_2 + d_2x_1 + e_2x_2 + f_2x_3 + g_2x_4$

Rule 3: If x_1 is C_1, x_2 is C_2, x_3 is C_3 and x_4 is C_4, then $y_3 = c_3 + d_3x_1 + e_3x_2 + f_3x_3 + g_3x_4$

Rule 4: If x_1 is D_1, x_2 is D_2, x_3 is D_3 and x_4 is D_4, then $y_4 = c_4 + d_4x_1 + e_4x_2 + f_4x_3 + g_4x_4$

where A_1, A_2, A_3, and A_4 are the fuzzy sets that define the membership functions for the input variables x_1, x_2, x_3, and x_4, respectively. B_1, B_2, B_3 and B_4 are the negation of A_1, A_2, A_3, and A_4, respectively. C_1, C_2, C_3 and C_4 are the intersection of A_1 and A_2, A_2 and A_3, A_3 and A_4, and A_4 and A_1, respectively. D_1, D_2, D_3 and D_4 are the union of A_1 and A_2, A_2 and A_3, A_3 and A_4, and A_4 and A_1, respectively. The coefficients c, d, e, f, and g are constants that define the linear function of the input variables for each rule. These coefficients are determined using linear regression or other optimization techniques based on the input-output data.
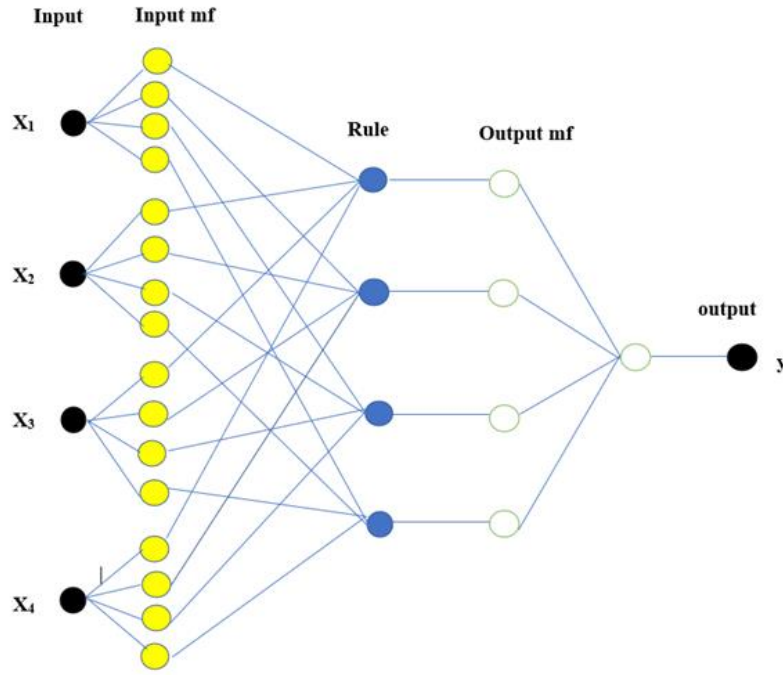
Figure 3. 3 ANFIS Topology for Modelling of Permeability

Figure 3.3 shows the five-layer architecture of the ANFIS model. The five layers structure of ANFIS can be explained as follows:

Layer 1 (Fuzzification Layer): The function of this layer is to transfer the incoming data to each fuzzy set's level of membership. Each input variable has a set of MFs attached to it, and a membership function equation is used to calculate how much of the input data belongs to each function. This layer produces a matrix showing the degree to which each input value is a member of each fuzzy set as given in **Equation (3.5)**.

$$O_i^1 = \mu_{A_i}(x), \text{ for } i = 1,2,3,4 \tag{3.5}$$

where O_i^j denotes the output of the ith node and j^{th} layer.

Layer 2 (Rule Layer): This layer's function is to decide how strongly each rule will apply depending on how much of the incoming data is a member of each fuzzy set. The membership

degree of the input data to each linked fuzzy set is multiplied to determine the firing strength (FS) of each rule. A vector representing the FS of each rule is the layer's output as given in **Equation (3.6)**.

$$O_i^2 = w_i = \mu_{A_i}(x_1) * \mu_{A'_i}(x_2), \text{ for } i = \textit{1,2,3,4} \tag{3.6}$$

Layer 3 (Normalization Layer): The role of this layer is to normalize the FS of the rules to ensure that they sum up to one. This is done by dividing the FS of each rule by the combined FS of all the rules. This layer's output is a vector representing the normalised FS of the rules as given in **Equation (3.7)**.

$$O_i^3 = \overline{w}_i = \frac{w_i}{\sum w_i}, \ i = \textit{1,2,3,4} \tag{3.7}$$

where $\overline{w}_i$ is the output of Layer 3.

Layer 4 (Consequent Parameters Layer): This layer's function is to compute the consequent parameters of each rule based on the input data and the normalized FS of the rule. This layer's output is a matrix of the consequent parameters of each rule as given in **Equation (3.8)**.

$$O_i^4 = \overline{w}_i * y_i \tag{3.8}$$

where, y_i is the output with parameter set {c, d, e, f, g}.

Layer 5 (Aggregation Layer): This layer's function is to combine the consequent parameters of all the rules to produce the output of the ANFIS model. This is done by summing the product of the consequent parameters of each rule and the normalized firing strength of the rule for combined rules. This layer's output is a single scalar value representing the output of the ANFIS model as given in **Equation (3.9)**.

$$O_i^5 = \sum_{i=1}^{n} \overline{w}_i * y_i \tag{3.9}$$

The experimental data were split into two portions for the ANFIS modelling. 75% of the data was used for training purposes. The remaining data (25%) was used to evaluate the model. In MATLAB R2016a, the fuzzy logic designer toolbox was used to produce FIS while taking the grid partition approach into account. The hybrid optimization approach was used to train the generated FIS, with 50 epochs and zero error tolerance. For the four input variables, five membership functions (MFs) were applied. In this work, it was attempted to optimise the outcomes using output MFs of the linear and constant types. The target data were the permeability values from experimental results. In the current work, the effective permeability prediction was determined using FIS created using the aforesaid technique. The created ANFIS model was evaluated using the following statistical criteria: R^2, RMSE and MAPE.

$$R^2 \text{ (correlation coefficient)} = 1 - \frac{\sum_{i=1}^{n}(y_i^e - y_i^p)^2}{\sum_{i=1}^{n}(y_i^e - \overline{y}_p)^2} \tag{3.10}$$

$$RMSE \text{ (root mean square error)} = \sqrt{\frac{1}{n}\sum_{i=1}^{n}\left(y_i^e - y_i^p\right)^2} \tag{3.11}$$

$$MAPE\,(\%)\,\text{(mean absolute percentage error)} = \left(\frac{100}{n}\right)\sum_{i=1}^{n}\left|\frac{y_i^e - y_i^p}{y_i^e}\right| \tag{3.12}$$

where y_i^e and y_i^p are the ith experimental and predicted data points of transient permeability values, respectively. Where n is the total data points and $\bar{y}_p$ is the mean of the predicted permeability values.

3.3.4 ANN Modelling

The function of the ANN is to train the neural network from past data and use this trained neural network for predicting future data. Generally, the multi-layered perceptron neural network consists of an input layer, a number of hidden layers and an output layer. These layers are interconnected via the weight and bias matrices [142]. The input layer sends the input data to the hidden layer, the hidden layer trains the data and the output layer predicts the data as shown in **Figure 3.4**. **Figure 3.4** shows the four input parameters, one hidden layer containing 10 neurons with log-sigmoid transfer function and an output layer with pure-linear transfer function. The input and output data were normalized between 0 and 1. The predicted output is calculated as a function of the input data provided and the weight and bias matrices using the following **Equation (3.13)**.

$$Y_i = f\left(\sum_{i=1}^{N} w_{ij}x_i + b_i\right) \tag{3.13}$$

where N is the total number of neurons, Y_i is the predicted output and x_i is the input connected to the ith neuron. w_{ij} and b_i are the weight and bias matrices, respectively. The ANN modelling was implemented in MATLAB software using the *nntool* function and the Levenberg–Marquard technique was used as a learning algorithm. The performance of the model was evaluated using the regression coefficient and the mean square error (MSE) between the predicted and targeted output. The MSE was computed using the following **Equation (3.14)**.

$$MSE = \frac{1}{n}\sum_{i=1}^{n}\left(Y_t - Y_p\right)^2 \tag{3.14}$$

Where n is the total number of data points, Y_t and Y_p are the experimental and predicted permeability data, respectively.
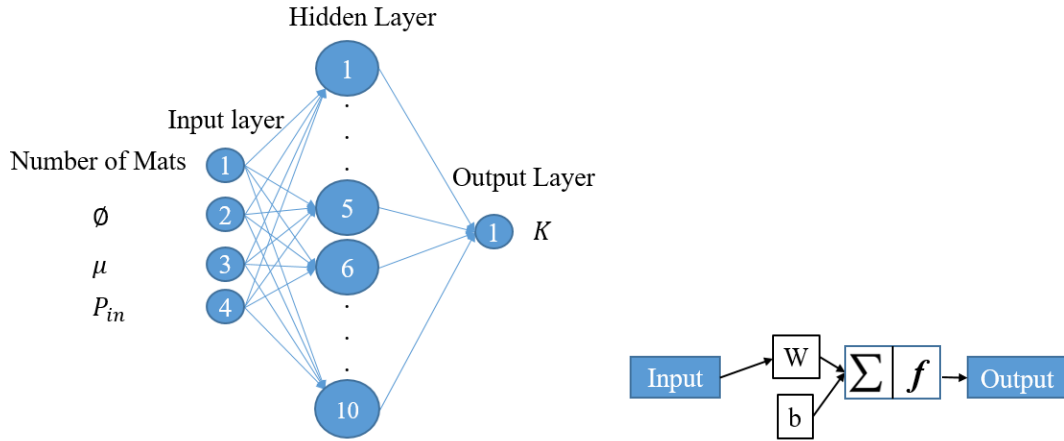
Figure 3. 4 ANN Topology for Modelling of Effective Permeability

3.4 Results and Discussions

3.4.1 Reinforcement Mats Permeabilities using Visualization Technique

The permeability of reinforcement mats was measured through temporal flow front-tracking using a visualization technique. A total of 67 experiments were performed with the variations in fibre architecture, resin injection pressure, resin viscosity and the number of mat layers. The permeability value was determined by comparing the experimental flow fronts with simulated flow fronts generated using guessed permeability values.

The experiments as shown in **Tables 3.3 and 3.4** were performed at 2 bar injection pressure for a CSM glass fibre mat having glycerol as test fluid. **Table 3.3** shows the comparison of the experimental flow front position with simulated flow fronts for different guessed permeability values at 100 seconds of fill time. From the experimental results, a circular flow front position was observed at all the time intervals and hence, an isotropic permeability value was considered. From the simulated flow fronts, there was not observed an appreciable movement in the flow fronts for guessed permeability values ranging from 1×10^{-10} m^2 to 6×10^{-10} m^2. The guessed permeability values in the range of 7×10^{-10} m^2 to 5×10^{-9} m^2 have shown a significant movement of flow fronts with time. Specifically, the simulated flow fronts were perfectly matched with experimental flow fronts for the guessed permeability value of 1×10^{-9} m^2 at 100 seconds of fill time.

Table 3.4 shows the matched experimental and simulated flow front positions obtained for the permeability value of 1×10^{-9} m^2 at every time interval of 20 s from 20 s to 100 s and it was found that the flow front positions were matching between experiments and simulations at every time frame studied. Therefore, a value of 1×10^{-9} m^2 was considered as the effective

permeability for the CSM reinforcement mat when the glycerol test fluid is injected at 2 bar pressure.

Table 3. 3 Sensitivity of Simulated Flow Front Positions for Different Permeability Values (Flow Front Position at 100 s, Injection Pressure: 2 bar, Fluid: Glycerol, Fibre Mat: Chopped Strand Mat)

Experimental Flow Front	$K=3\times10^{-10}\,m^2$	$K=4\times10^{-10}\,m^2$	$K=5\times10^{-10}\,m^2$	$K=6\times10^{-10}\,m^2$
$K=7\times10^{-10}\,m^2$	$K=8\times10^{-10}\,m^2$	$K=9\times10^{-10}\,m^2$	$K=1\times10^{-9}\,m^2$	$K=2\times10^{-9}\,m^2$

Table 3. 4 Experimental & Simulated Matched Flow Fronts at Different Intervals of Time for $K=1\times10^{-9}\,m^2$, Injection Pressure: 2 bar, Fluid: Glycerol, Fibre Mat: Chopped Strand Mat)

20s	40s	60s	80s	100s
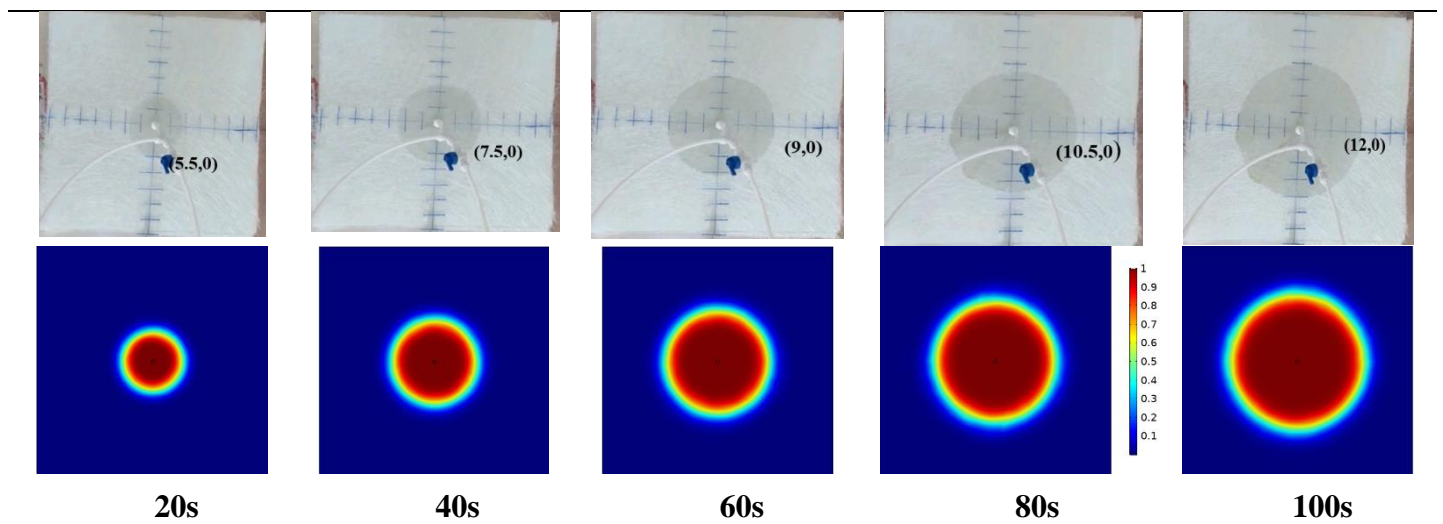
The experiments shown in **Tables 3.5 and 3.6** were performed at 1 bar injection pressure for a woven roving glass fibre mat having epoxy vinyl ester resin as test fluid. **Table**

3.5 shows the comparison of the experimental flow front position with simulated flow fronts for different guessed permeability values at 60 seconds of mould fill time. From the results, it was observed that the experimental and simulated flow front was perfectly matched for the permeability value of $2\times10^{-9}\,m^2$ at 60 seconds of mould fill time.

Table 3.6 shows the matched simulated & experimental flow fronts for $2\times10^{-9}\,m^2$ of permeability value at every time interval of 10 s from 10 s to 50 s. Therefore, a value of $2\times10^{-9}\,m^2$ was considered as the effective permeability for woven roving glass fibre mat when the epoxy vinyl ester resin is injected at 1 bar pressure.

Table 3. 5 Sensitivity of Simulated Flow Front Positions for Different Permeability Values (Flow Front Position at 60 s, Injection Pressure: 1 bar, Fluid: Vinyl Ester Resin, Fibre Mat: Woven Roving Glass Fibre Mat)

| Experimental Flow Front at 60 s Fill Time | $K=5\times10^{-10}\,m^2$ | $K=7\times10^{-10}\,m^2$ |
| $K=9\times10^{-10}\,m^2$ | $K=1\times10^{-9}\,m^2$ | $K=2\times10^{-9}\,m^2$ |
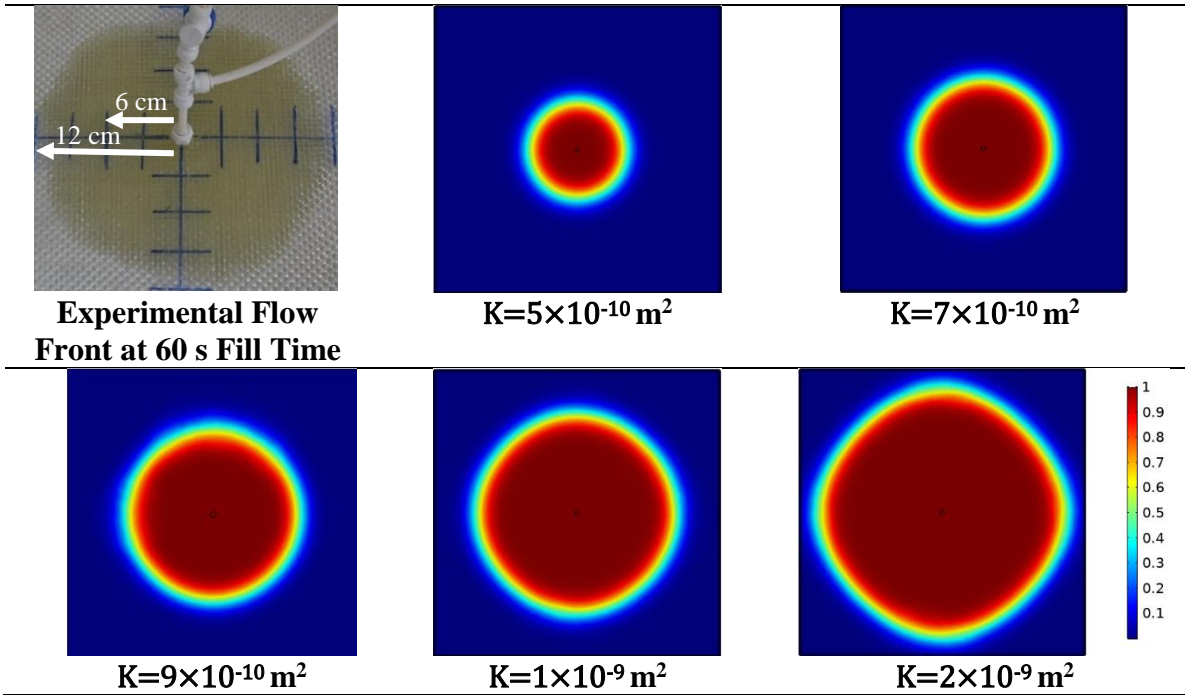
Table 3. 6 Experimental & Simulated Matched Flow Fronts at Different Intervals of Time for $K=2\times10^{-9}\,m^2$, Injection Pressure: 1 bar, Test Fluid: Vinyl Ester Resin, Fibre Mat: Woven Roving Glass Fibre Mat

| 10 s | 20 s | 30 s | 40 s | 50 s |
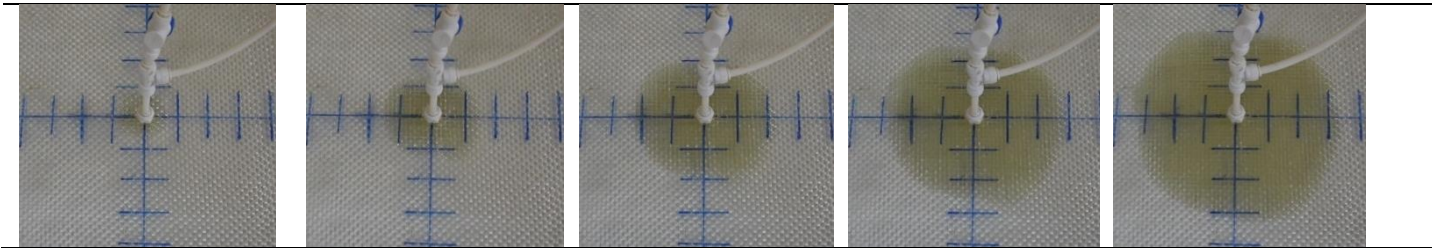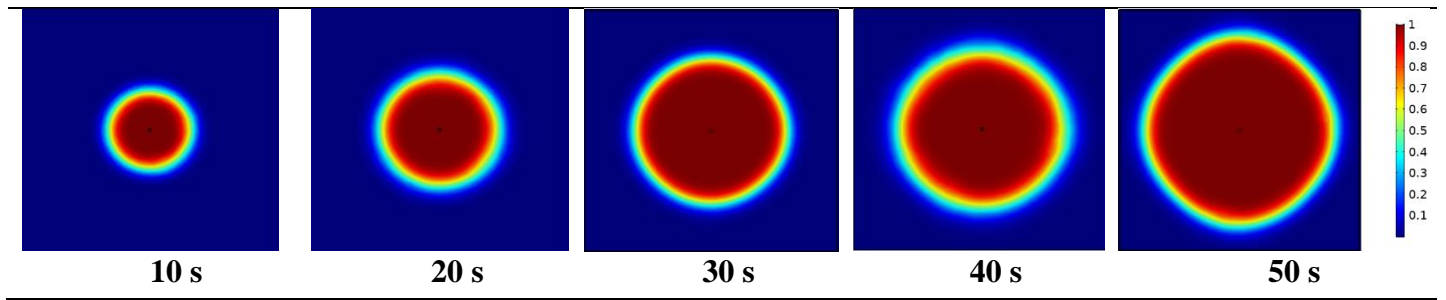
The experiments shown in **Tables 3.7 and 3.8** were performed at 1 bar injection pressure for a jute fibre mat having epoxy Araldite LY5052 resin as test fluid. **Table 3.7** shows the comparison of the experimental flow front position with simulated flow fronts for different guessed permeability values at 50 seconds of mould fill time. From the results, the guessed permeability values in the order of 10^{-9} m^2 have shown fast flow front progression with time compared to the order of 10^{-10} m^2 permeability value. It was also observed that the experimental and simulated flow front was perfectly matched for the permeability value of 5×10^{-9} m^2 at 50 seconds of mould fill time.

Table 3.8 shows the matched simulated & experimental flow fronts for 5×10^{-9} m^2 of permeability value at every time interval of 10 s from 10 s to 60 s. Therefore, a value of 5×10^{-9} m^2 was considered as the effective permeability for the jute fibre mat when the epoxy Araldite LY5052 resin was injected at 1 bar pressure. From the results, it was also observed that the permeability value obtained for the jute fibre mat was more than the CSM and WRM glass fibre mats (shown in **Tables 3.4 and 3.6**) due to their comparatively high porous nature.

Table 3. 7 Sensitivity of Simulated Flow Front Positions for Different Permeability Values (Flow Front Position at 50 s, Injection Pressure: 1 bar, Fluid: LY 5052 Resin, Fibre Mat: Jute Fibre Mat)

| Experimental Flow Front | K=8×10⁻¹⁰ m² | K=9×10⁻¹⁰ m² | K=1×10⁻⁹ m² |

<table>
<tr><td>K=2×10⁻⁹ m²</td><td>K=3×10⁻⁹ m²</td><td>K=4×10⁻⁹ m²</td><td>K=5×10⁻⁹ m²</td></tr>
</table>

| $K=2\times10^{-9}\,m^2$ | $K=3\times10^{-9}\,m^2$ | $K=4\times10^{-9}\,m^2$ | $K=5\times10^{-9}\,m^2$ |
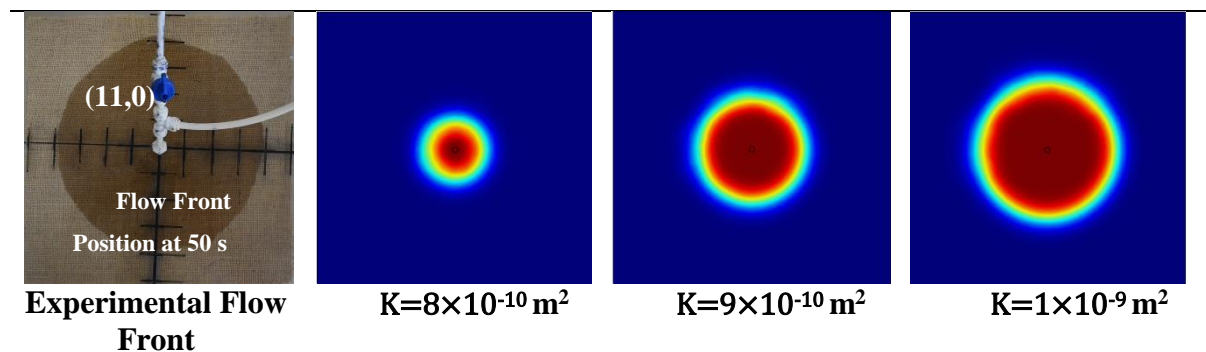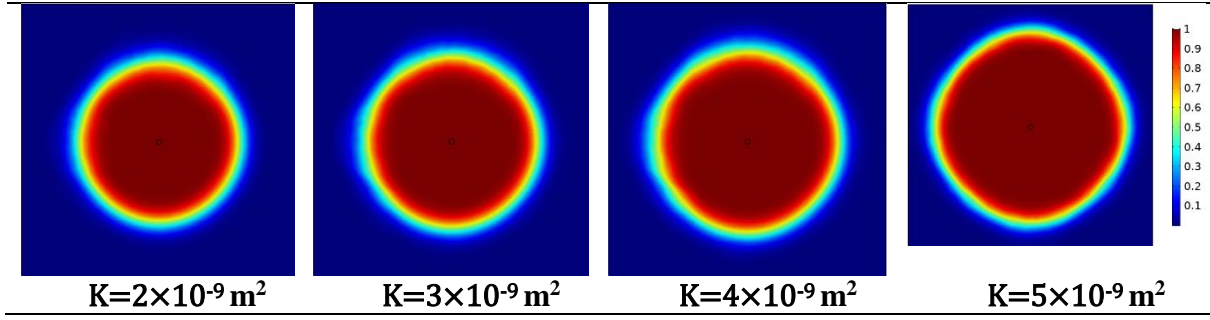
Table 3. 8 Experimental & Simulated Matched Flow Fronts at Different Intervals of Time for K=5×10⁻⁹ m², Experiment No-46, Injection Pressure: 1 bar, Fluid: Epoxy Araldite LY5052, Fibre Mat: Jute Fibre)

| 10 s | 20 s | 30 s | 40 s | 60 s |
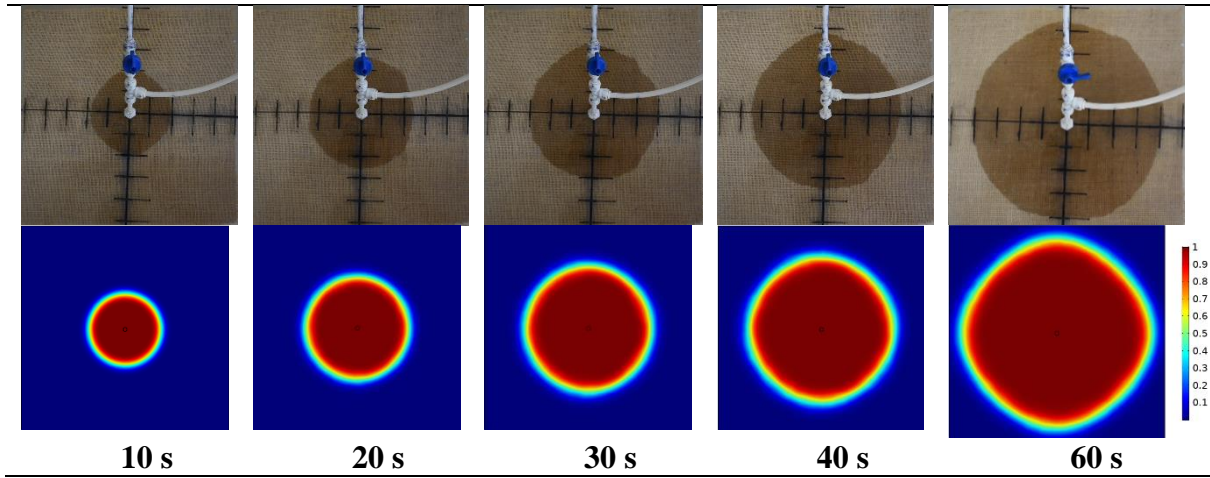
The experiment shown in **Table 3.9** was performed at 0.5 bar injection pressure for a carbon fibre mat having edible oil as test fluid. **Table 3.9** shows the mould top and bottom side experimental temporal flow fronts and matched simulated temporal flow fronts for a guessed permeability value of 1×10^{-9} m². From **Table 3.9** results, it can be seen that the fibre preform saturation time is similar on both sides of the preform. This signifies that there is no variation in permeability along the transverse direction. From **Table 3.9**, it is also observed that the simulated flow fronts for a guessed permeability value of 1×10^{-9} m² were perfectly matched with experimental flow fronts at each interval of filling time from 2 seconds to 14 seconds.

Table 3. 9 Experimental (top & bottom side) & Simulated Matched Flow Fronts at Different Intervals of Time for K=1.0×10⁻⁹ m², Injection Pressure: 0.5 bar, Fluid: Edible Oil, Fibre Mat: Carbon Fibre)

Top Side Flow Fronts				
Bottom Side Flow Fronts				
Simulated Flow Fronts				
Filling Time	2 seconds	4 seconds	8 seconds	14 seconds
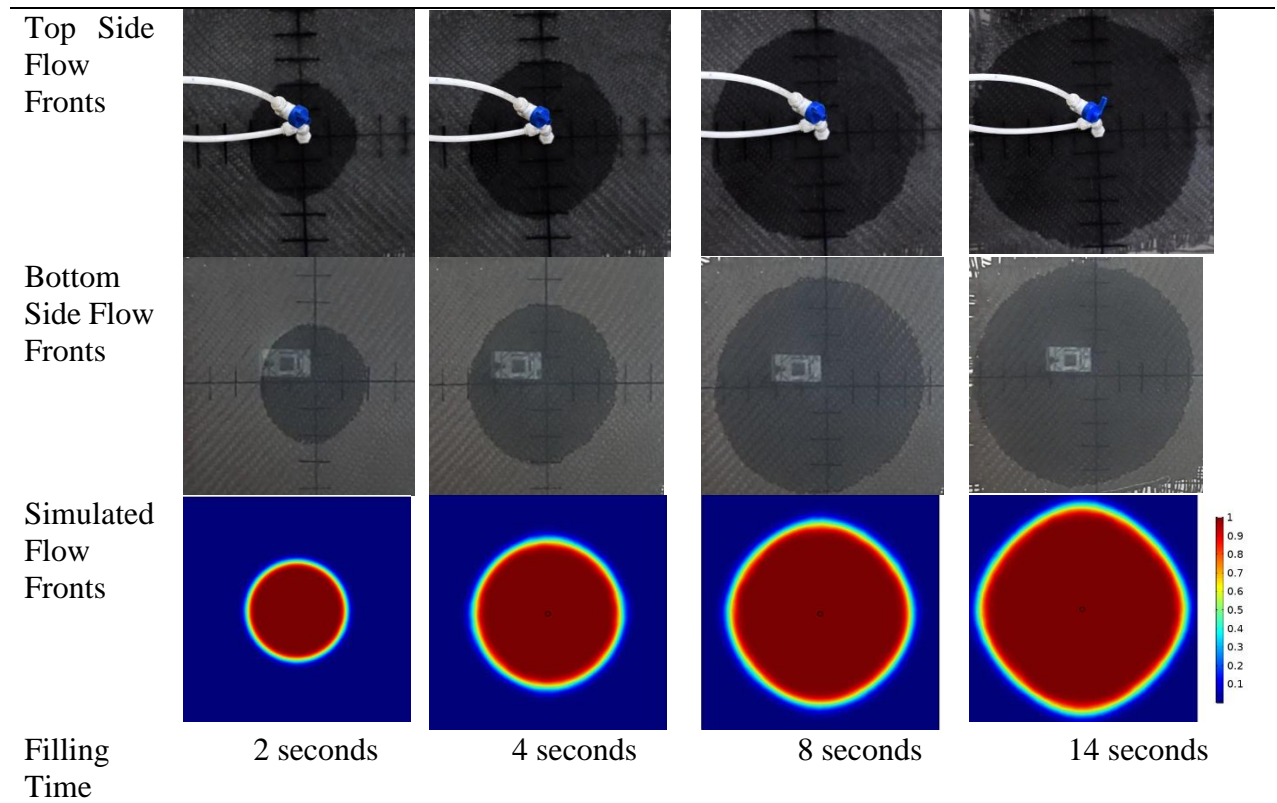
The experiment shown in **Table 3.10** was performed at 1 bar injection pressure for a carbon fibre mat having epoxy Araldite LY5052 resin as test fluid. **Table 3.10** shows the comparison of the experimental flow front position with simulated flow fronts for $2×10^{-9}$ m² of permeability value at every time interval of 30 s from 10 s to 120 s. From the results, the flow fronts obtained at guessed permeability values of $2×10^{-9}$ m² were perfectly matched with experimental flow fronts at each interval of mould fill time. Therefore, a value of $2×10^{-9}$ m² was considered as the effective permeability for carbon fibre mat when the epoxy Araldite LY5052 resin is injected at 1 bar pressure. From the results, it was also observed that the permeability value obtained for the carbon fibre mat was lesser than the jute fibre mat (shown in **Table 3.8**), due to its comparatively less porous nature.
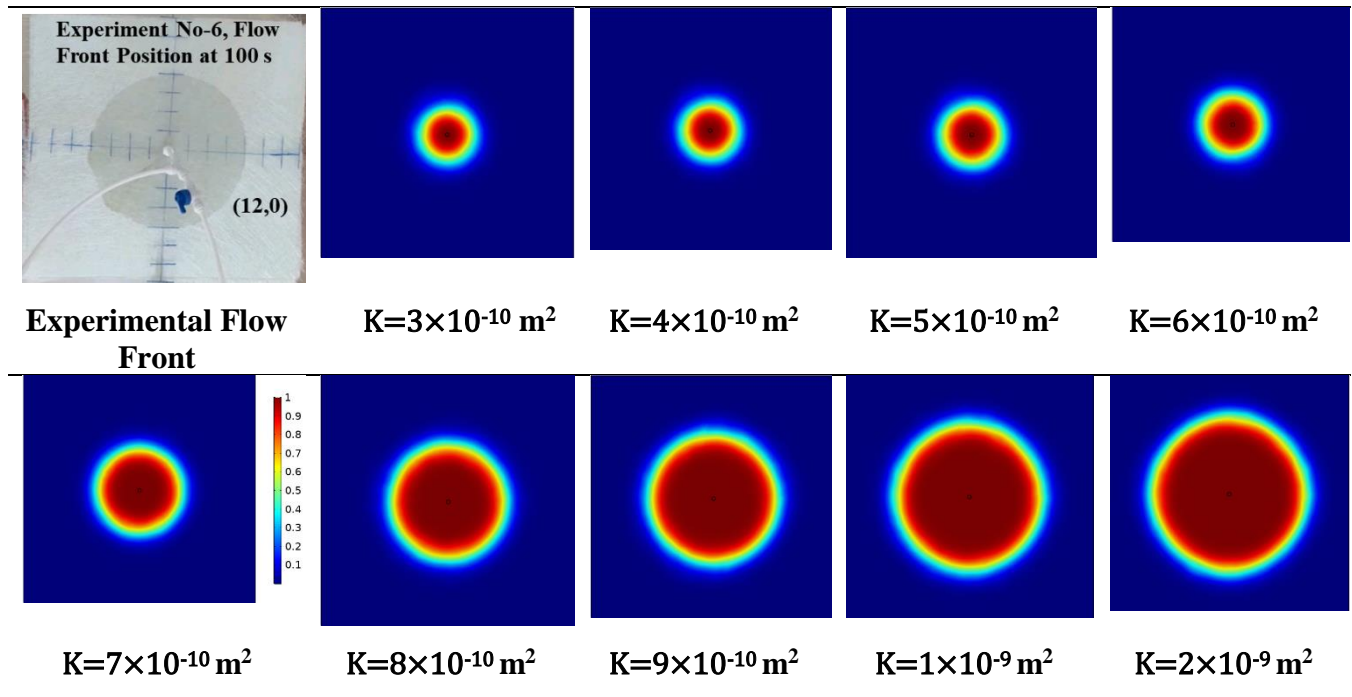
Table 3. 10 Experimental & Simulated Matched Flow Fronts at Different Intervals of Time for K=2×10⁻⁹ m², Injection Pressure: 1 bar, Test Fluid: Epoxy Araldite LY5052, Fibre Mat: Carbon Fibre)

| 10 s | 30 s | 60 s | 90 s | 120 s |
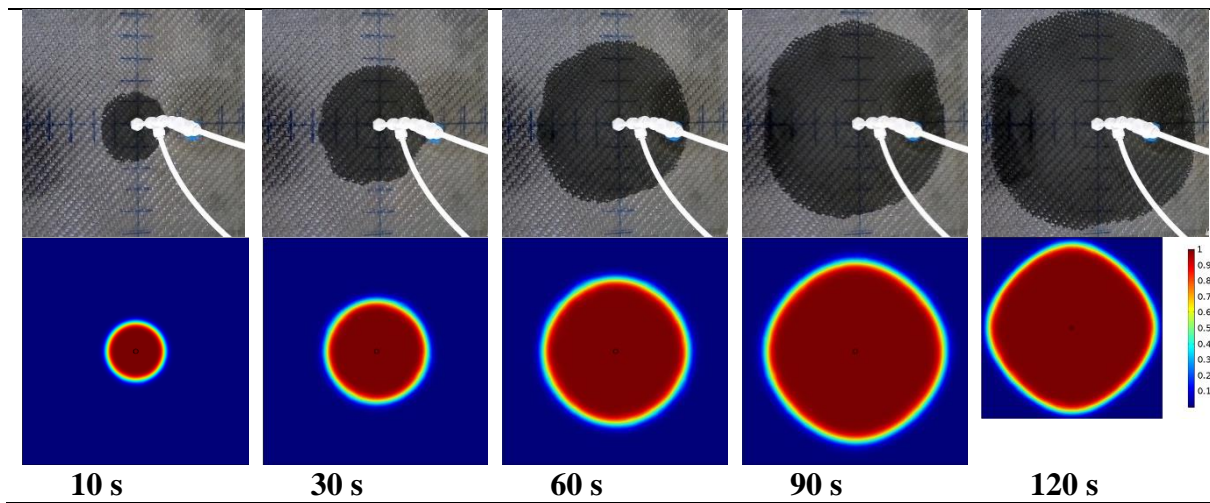
The permeability data obtained for 67 experiments with variations in the materials and process parameters is tabulated in **Table 3.11**. From the results, the order of permeability was obtained between 8×10^{-10} to 8×10^{-9} m² for chopped strand glass fibre mat, 8.8×10^{-10} to 8×10^{-9} m² for jute fibre mat, 8.9×10^{-10} to 8.5×10^{-9} m² for woven roving glass fibre mat, and 8.9×10^{-10} to 1×10^{-8} m² for hemp fibre mat.

Table 3. 11 Reinforcement Mat Permeability Data as a Function of Material and Process Parameters

Ex. No.	Reinforcement Fibre Mat	No. of mat Layers	Porosity	Test Fluid	Viscosity of Fluid (Pa-s)	Injection Pressure (bar)	Permeability m²
1	CSM Glass Fibre Mat	10	0.591837	Edible Oil	0.0398	1	3.91×10^{-10}
2	CSM Glass Fibre Mat	10	0.591837	Edible Oil	0.0398	1.5	3.5×10^{-10}
3	CSM Glass Fibre Mat	15	0.591837	Edible Oil	0.0398	1	3.32×10^{-10}
4	CSM Glass Fibre Mat	15	0.591837	Edible Oil	0.0398	1.5	3.1×10^{-10}
5	CSM Glass Fibre Mat	10	0.591837	Glycerol	1.412	1.5	1.61×10^{-9}

6	CSM Glass Fibre Mat	10	0.591837	Glycerol	1.412	2	1.16×10^{-9}
7	CSM Glass Fibre Mat	15	0.591837	Glycerol	1.412	1.5	5.19×10^{-10}
8	CSM Glass Fibre Mat	15	0.591837	Glycerol	1.412	2	9.5×10^{-10}
9	CSM Glass Fibre Mat	5	0.591837	Epoxy Araldite (LY556)	11.81	3	9.62×10^{-10}
10	CSM Glass Fibre Mat	3	0.591837	Epoxy Araldite (LY556)	11.81	3	1.23×10^{-9}
11	CSM Glass Fibre Mat	5	0.591837	Epoxy Araldite (LY556)	11.81	4	8.99×10^{-10}
12	CSM Glass Fibre Mat	3	0.591837	Epoxy Araldite (LY556)	11.81	4	1.58×10^{-9}
13	CSM Glass Fibre Mat	2	0.591837	Epoxy Araldite (LY556)	11.81	3	1.53×10^{-9}
14	CSM Glass Fibre Mat	4	0.591837	Epoxy Araldite (LY556)	11.81	3	1.15×10^{-9}
15	CSM Glass Fibre Mat	3	0.591837	Epoxy Araldite (LY5052)	1.358	1.5	2.1×10^{-9}
16	CSM Glass Fibre Mat	4	0.591837	Epoxy Araldite (LY5052)	1.358	1.5	1.31×10^{-9}
17	CSM Glass Fibre Mat	4	0.591837	Epoxy Araldite (LY556)	11.81	2	1.11×10^{-9}
18	CSM Glass Fibre Mat	3	0.591837	Epoxy Vinyl Ester	0.35	0.5	1×10^{-9}
19	CSM Glass Fibre Mat	4	0.591837	Epoxy Vinyl Ester	0.35	0.5	9×10^{-10}
20	CSM Glass Fibre Mat	5	0.591837	Epoxy Vinyl Ester	0.35	0.5	8.5×10^{-10}

21	CSM Glass Fibre Mat	3	0.591837	Epoxy Vinyl Ester	0.35	1	8.9×10^{-10}
22	CSM Glass Fibre Mat	4	0.591837	Epoxy Vinyl Ester	0.35	1	9×10^{-10}
23	CSM Glass Fibre Mat	20	0.591837	Edible Oil	0.0398	1	1.39×10^{-10}
24	WRM Glass Fibre Mat	3	0.45874	Epoxy Araldite (LY556)	11.81	4	3.02×10^{-9}
25	WRM Glass Fibre Mat	5	0.45874	Epoxy Araldite (LY556)	11.81	4	2.4×10^{-9}
26	WRM Glass Fibre Mat	3	0.45874	Epoxy Araldite (LY556)	11.81	3.5	3.31×10^{-9}
27	WRM Glass Fibre Mat	3	0.45874	Epoxy Araldite (LY556)	11.81	3	8.59×10^{-9}
28	WRM Glass Fibre Mat	4	0.45874	Epoxy Araldite (LY556)	11.81	3	7×10^{-9}
29	WRM Glass Fibre Mat	3	0.45874	Epoxy Araldite (LY5052)	1.358	1.5	1.8×10^{-9}
30	WRM Glass Fibre Mat	5	0.45874	Epoxy Vinyl Ester	0.35	0.5	1.55×10^{-9}
31	WRM Glass Fibre Mat	5	0.45874	Epoxy Vinyl Ester	0.35	1	1.2×10^{-9}
32	WRM Glass Fibre Mat	5	0.45874	Epoxy Araldite (LY5052)	1.358	1.5	8.9×10^{-10}
33	Carbon Fibre Mat	3	0.519173	Epoxy Araldite (LY5052)	1.358	1	2×10^{-9}
34	Hemp Fibre Mat	3	0.658009	Epoxy Vinyl Ester	0.35	0.5	3×10^{-9}

35	Hemp Fibre Mat	4	0.658009	Epoxy Vinyl Ester	0.35	0.5	2×10^{-9}
36	Hemp Fibre Mat	5	0.658009	Epoxy Vinyl Ester	0.35	0.5	1.5×10^{-9}
37	Hemp Fibre Mat	3	0.658009	Epoxy Vinyl Ester	0.35	1	1.7×10^{-9}
38	Hemp Fibre Mat	4	0.658009	Epoxy Vinyl Ester	0.35	1	9.8×10^{-10}
39	Hemp Fibre Mat	5	0.658009	Epoxy Vinyl Ester	0.35	1	8.9×10^{-10}
40	Hemp Fibre Mat	3	0.658009	Glycerol	1.412	0.5	1.02×10^{-8}
41	Hemp Fibre Mat	3	0.658009	Glycerol	1.412	1	6.51×10^{-9}
42	Hemp Fibre Mat	4	0.658009	Glycerol	1.412	0.5	9.31×10^{-9}
43	Hemp Fibre Mat	4	0.658009	Glycerol	1.412	1	5.86×10^{-9}
44	Hemp Fibre Mat	5	0.658009	Glycerol	1.412	0.5	7.47×10^{-9}
45	Hemp Fibre Mat	5	0.658009	Glycerol	1.412	1	4.15×10^{-9}
46	Jute Fibre Mat	3	0.726197	Epoxy Araldite (LY5052)	1.358	1	4.73×10^{-9}
47	Jute Fibre Mat	3	0.726197	Epoxy Araldite (LY5052)	1.358	0.5	5.39×10^{-9}
48	Jute Fibre Mat	3	0.726197	Epoxy Vinyl Ester	0.35	1	2.7×10^{-9}
49	Jute Fibre Mat	5	0.726197	Epoxy Vinyl Ester	0.35	1	1.5×10^{-9}

50	Jute Fibre Mat	3	0.726197	Epoxy Vinyl Ester	0.35	0.5	3.5×10^{-9}
51	Jute Fibre Mat	5	0.726197	Epoxy Vinyl Ester	0.35	0.5	2.5×10^{-9}
52	Jute Fibre Mat	4	0.726197	Epoxy Vinyl Ester	0.35	1	8.8×10^{-10}
53	Jute Fibre Mat	4	0.726197	Epoxy Vinyl Ester	0.35	0.5	2.8×10^{-9}
54	Jute Fibre Mat	3	0.726197	Glycerol	1.412	1	7.53×10^{-9}
55	Jute Fibre Mat	4	0.726197	Glycerol	1.412	1	6.04×10^{-9}
56	Jute Fibre Mat	5	0.726197	Glycerol	1.412	1	5.90×10^{-9}
59	Jute Fibre Mat	4	0.726197	Epoxy Araldite (LY5052)	1.358	0.5	5.19×10^{-9}
60	Jute Fibre Mat	4	0.726197	Epoxy Araldite (LY5052)	1.358	1	4.42×10^{-9}
61	Jute Fibre Mat	5	0.726197	Epoxy Araldite (LY5052)	1.358	0.5	4.48×10^{-9}
62	Jute Fibre Mat	5	0.726197	Epoxy Araldite (LY5052)	1.358	1	3.68×10^{-9}
63	Carbon Fibre Mat	3	0.519173	Edible Oil	0.0398	0.5	1.07×10^{-9}
64	WRM Glass Fibre Mat	3	0.45874	Edible Oil	0.0398	0.5	8.38×10^{-10}
65	Jute Fibre Mat	3	0.726197	Edible Oil	0.0398	0.5	1.28×10^{-9}
66	CSM Glass Fibre Mat	3	0.591837	Edible Oil	0.0398	0.5	1.22×10^{-9}

67	Hemp Fibre Mat	3	0.658009	Edible Oil	0.0398	0.5	1.24×10^{-9}

Figure 3.5 shows the effect of injection pressure, number of mat layers, test fluid viscosity and porosity on the reinforcement mat permeability. From **Figure 3.5a**, it was observed that for the same test fluid with the increase in porosity, the permeability increases. This may be attributed to the increase in the reinforcement mat pore volume with an increase in porosity. From **Figures 3.5b & 3.5c**, it can be seen that for the same fibre mat, the order of permeability decreases with the increase in the injection pressure and the number of fibre mat layers. From **Figure 3.5b**, the order of permeability decreased from 9×10^{-9} to 2×10^{-9} m^2 with an increase in injection pressure from 3 to 4 bar for woven roving glass fibre mat. Subsequently, the permeability decreased from 2×10^{-9} to 9×10^{-10} m^2 with an increase in the number of layers from 2 to 4 for the chopped strand fibre mat as shown in **Figure 3.5c**. This may be attributed to the increased through-thickness flow resistance with an increase in the number of layers.
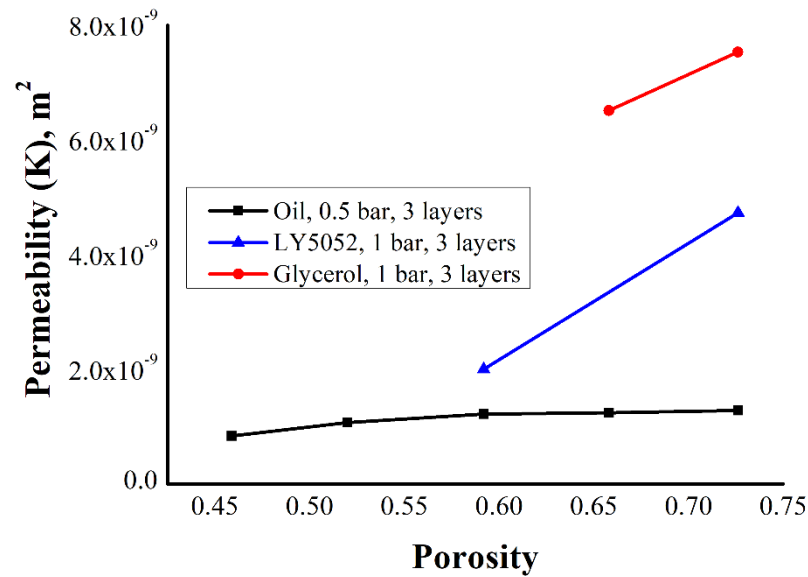
(a)
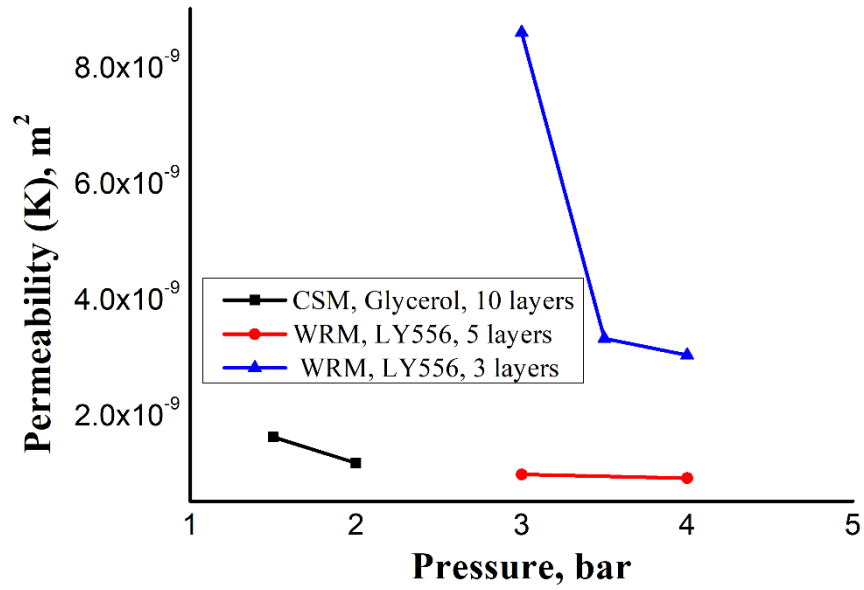
(b)
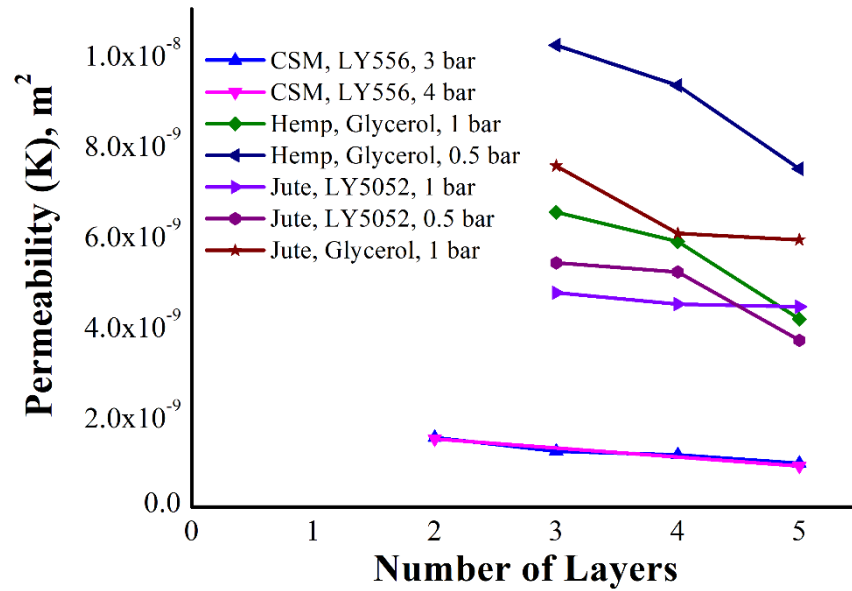
(c)

Figure 3. 5 Effect of Material and Process Parameters on Permeability shown in (a), (b) and (c)
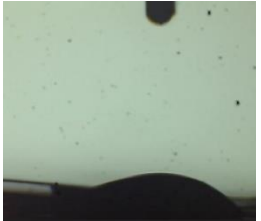
3.4.2 Fibre Wetting Analysis
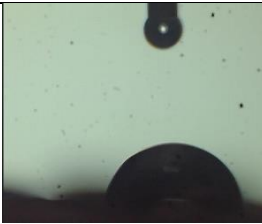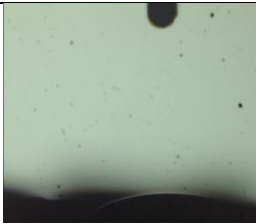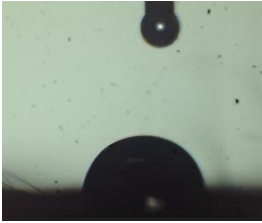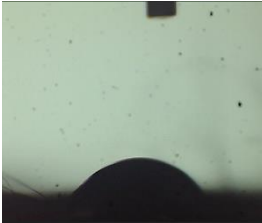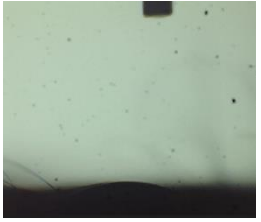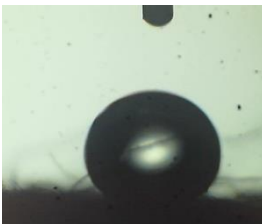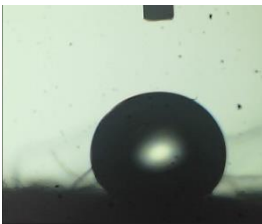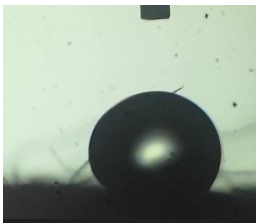
The fibre wetting analysis was performed for all the studied fibre mats using water and glycerol as test fluids. **Table 3.12** shows the snapshots of the test fluid-fibre wetting as a function of time for all the studied fibre mats. From **Table 3.12**, it was observed that the fibre wetting time required for glycerol was greater than that of water for all the fibre mats. This may be due to the hydrophilicity nature of the studied mat surface. In the case of CSM glass fibre mat, the complete fibre-wetting time required for water is less than 4 seconds and the

69

fibre-wetting time required for glycerol is more than 20 seconds. Similarly, for WRM glass fibre and carbon fibre mats, test fluid water wets instantaneously and it is required more than 20 seconds for glycerol as test fluid. It may also be mentioned that the test fluid spreading time was increased with the increase in fluid viscosity. It was also observed that the jute and hemp fibre mats required significantly higher wetting time compared to synthetic fibre for both test fluids. This may be due to the use of chemically untreated natural fibre mats.

From the fibre-wetting analysis, it was found that the fibre-wetting time and test fluid-fibre saturation have a strong influence on the fluid-mat permeation. From the results, it was observed that the fluid-mat permeation decreases when there is an increase in fibre wetting time and lesser mat surface saturation.

Table 3. 12 Fibre Wetting Analysis for Water and Glycerol for Different Fibre Mats

CSM Fibre Mat		
Water		
Wetting Time 0 seconds	2 seconds	4 seconds
Glycerol		
Wetting Time 0 seconds	10 seconds	20 seconds
WRM Fibre Mat		
Water		
Wetting Time 0 seconds		

Glycerol

| Wetting Time | 0 seconds | 10 seconds | 20 seconds |

Carbon Fibre Mat

Water

| Wetting Time | 0 seconds | | |

Glycerol

| Wetting Time | 0 seconds | 3 seconds | 6 seconds |

Jute Fibre Mat

Water

| Wetting Time | 0 seconds | 5seconds | 10 seconds |

Glycerol

| Wetting Time | 0 seconds | 5 seconds | 10 seconds |

Hemp Fibre Mat

Water

Wetting Time	0 seconds	10 seconds	15 seconds
Glycerol			
Wetting Time	0 seconds	30 seconds	60 seconds
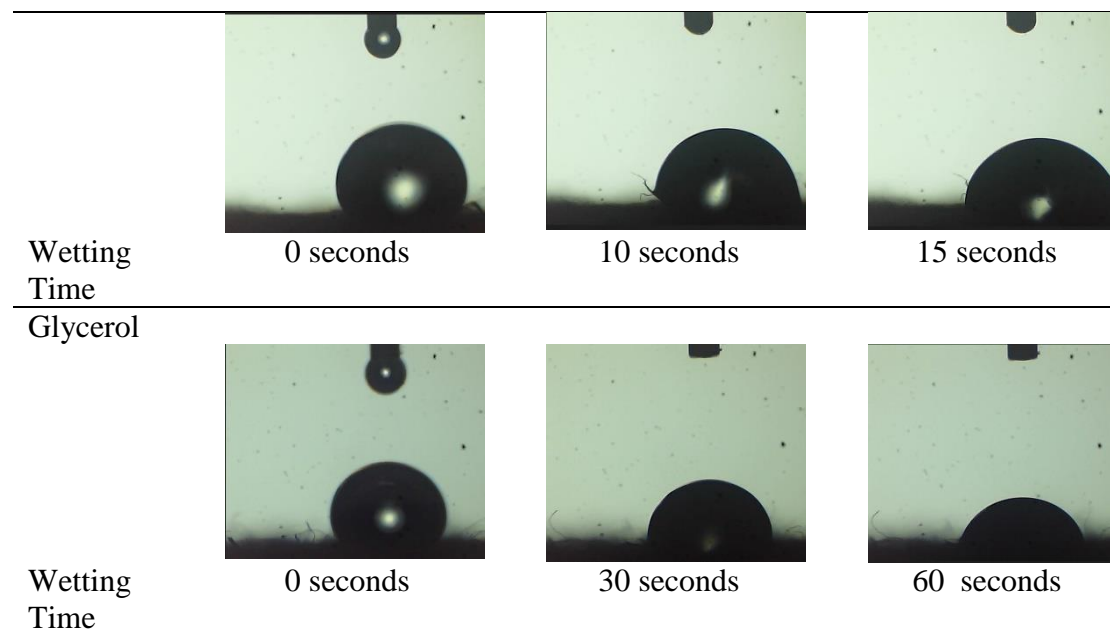
3.4.3 Results of ANFIS Modelling

ANFIS modelling was employed to forecast the effective permeability of reinforcement mats, factoring in both material and processing parameters. The dataset was characterized by four input parameters: porosity, mat layers, injection pressures, and test fluid viscosity. These inputs were represented using input membership functions encompassing Gaussian functions. The model's training was accomplished by integrating Gaussian membership functions for inputs and constant membership functions for outputs. In contrast, other membership functions like generalized bell, triangular, and trapezoidal functions were excluded from this study due to their association with elevated RMSE values. **Figure 3.6** provides an encompassing view of the ANFIS model's architecture, featuring four inputs, input membership functions (inputmf), an assemblage of rules ($3 \times 3 \times 3 \times 3 = 81$), an output membership function (outputmf), and a solitary output.

Figure 3.7 illustrates the rule viewer plot, showcasing the ANFIS model proficiency in forecasting output data based on given input information. For instance, by supplying input parameter values of 6 layers (input 1), 0.592 porosity (input 2), 0.881 Pa.s test fluid viscosity (input 3), and 1.24 bar injection pressure (input 4), the ANFIS model generated a permeability estimate of 2.02×10^{-10} m², as evidenced in **Figure 3.7**. Within the specified range of data, the model effectively predicted each output value corresponding to its respective input parameter. Moreover, the rule viewer allows users to choose inputs to generate desired outputs, showcasing the model's versatility. Notably, the model's predictive capabilities extend in both

directions – it can anticipate output permeability data from input values and vice versa. It's also worth mentioning that the model exhibits sensitivity, enabling it to forecast output permeability data even with slight adjustments in the input parameters.
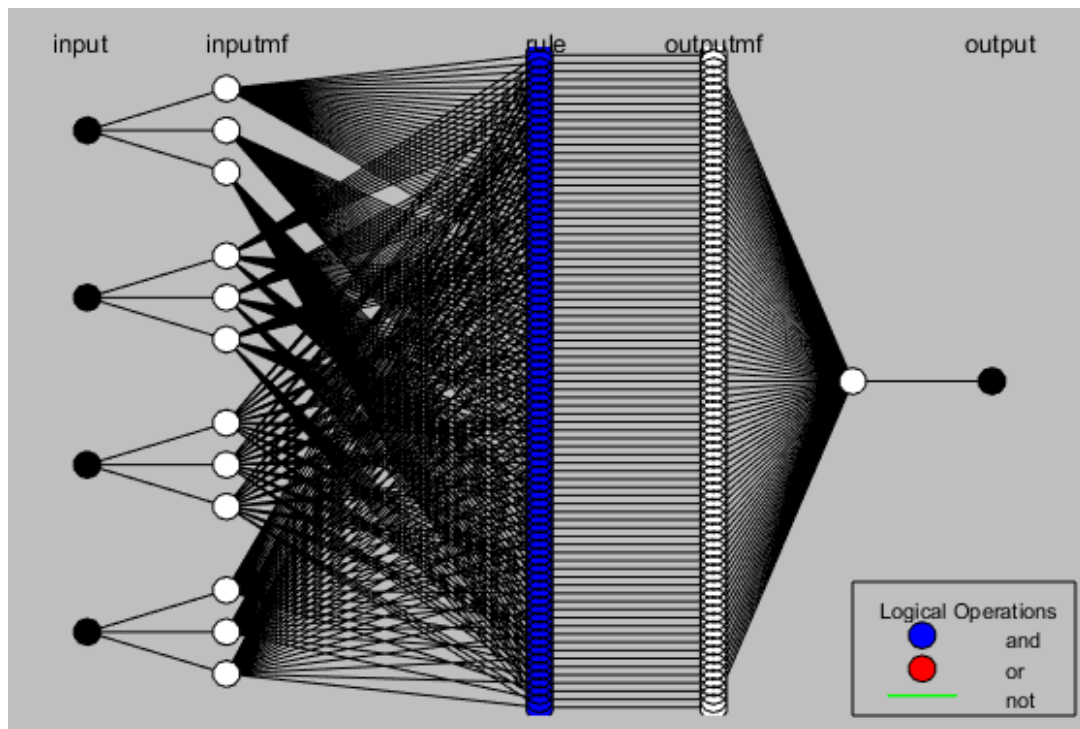
Figure 3. 6 ANFIS Modelling Structure from MATLAB for Four Input and One Output Parameters
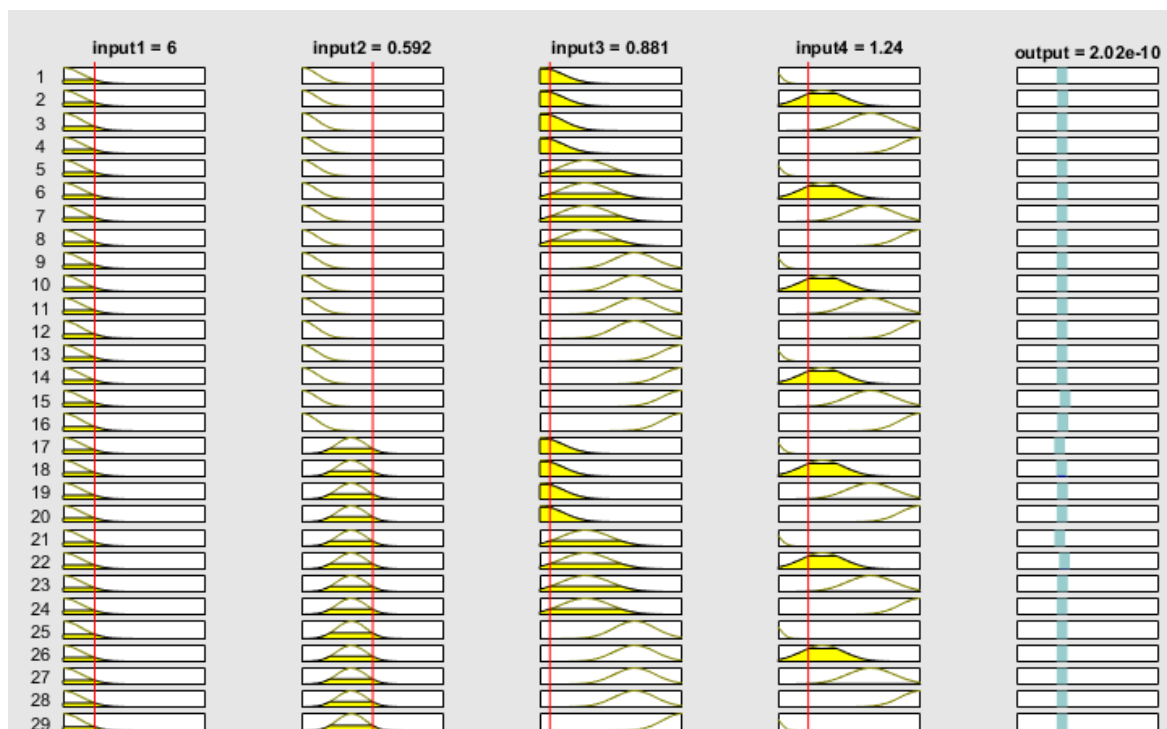
Figure 3. 7 ANFIS Rule Viewer Structure from MATLAB for Four Input and One Output Parameters

Figure 3.8 depicts the relationship between the experimental permeability and the permeability values predicted by the ANFIS model. The determination coefficient (R^2) for the combined dataset, encompassing both training and testing data, was calculated to be 0.975. This substantial R^2 value underscores the model's remarkable accuracy in forecasting effective permeability. The ANFIS model's predictive outcomes harmonize exceptionally well with the experimental results, signifying a strong alignment between the model's objectives and its achievements.

A comparison of the experimental and predicted outcomes of the ANFIS model across various test conditions is presented in **Figure 3.9**. Notably, the lines representing the experimental and predicted permeability closely coincide for all tested scenarios. This remarkable congruence underscores the ANFIS model's effectiveness in performance. As a result, it becomes evident that the fuzzy inference system provides a robust means to anticipate effective permeability based on the interplay of process and material parameters.
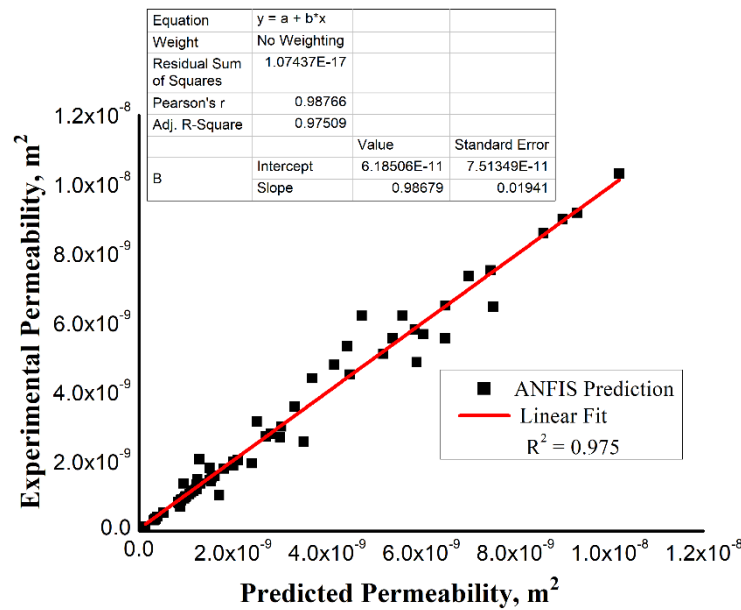
Figure 3. 8 Regression Model Analysis between Experimental and ANFIS Predicted Permeability

The mean absolute percentage error (MAPE) was calculated to assess the disparity between the experimental and predicted mat permeability datasets using **Equation (3.12).** The % MAPE value was determined to be 16.72% from the results. Furthermore, a sensitivity analysis was conducted utilizing the MAPE values in order to examine the impact of each input variable on the permeability of the reinforcement mat. By excluding individual input parameters from the combined training and testing dataset, the % MAPE values were compared. The results, presented in **Table 3.13**, illustrate the % MAPE values achieved

between the experimental and predicted mat permeability datasets for each input parameter that was excluded. The findings indicate that the reinforcement mat permeability is influenced by all of the input parameters. Notably, the fibre mat architecture holds the highest degree of influence, as evidenced by the % MAPE value of 49.82%. Following this is the viscosity of the test fluid at 38.52%, followed by the test fluid injection pressure at 32.4%. The input parameter with the least impact on the permeability is the number of layers, with a % MAPE value of 29.8%.
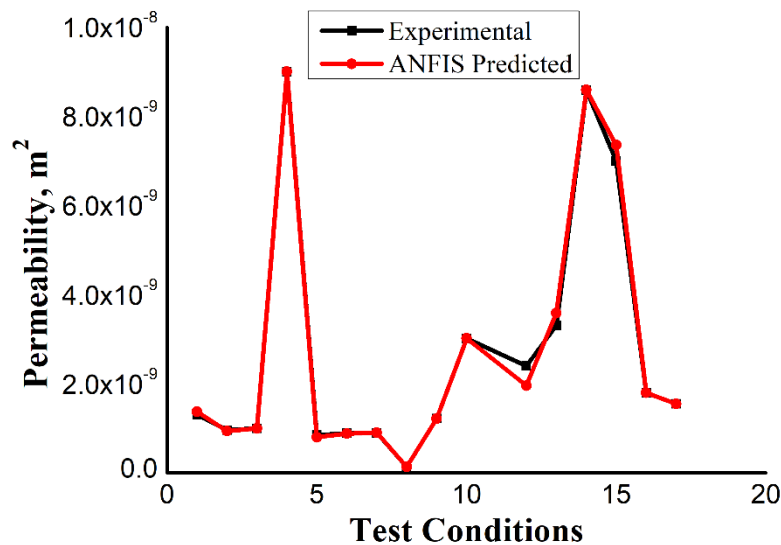
Figure 3. 9 Variation of Experimental and ANFIS Predicted Permeability Data for Different Test Conditions

Table 3. 13 MAPE Values Obtained between the Experimental and Predicted Mat Permeability Datasets for Excluded Input Parameter.

Excluded Parameter	Porosity	Test Fluid Viscosity	Test Fluid Injection Pressure	Number of Layers
% MAPE	49.82	38.52	32.4	29.8

The noise level within a dataset can be assessed through an error plot, providing insight into whether the error value diminishes with the inclusion of additional epochs. Examining **Figure 3.10**, it becomes evident that the error gradually decreased to a value of 3.4×10^{-10} by the 50th epoch.
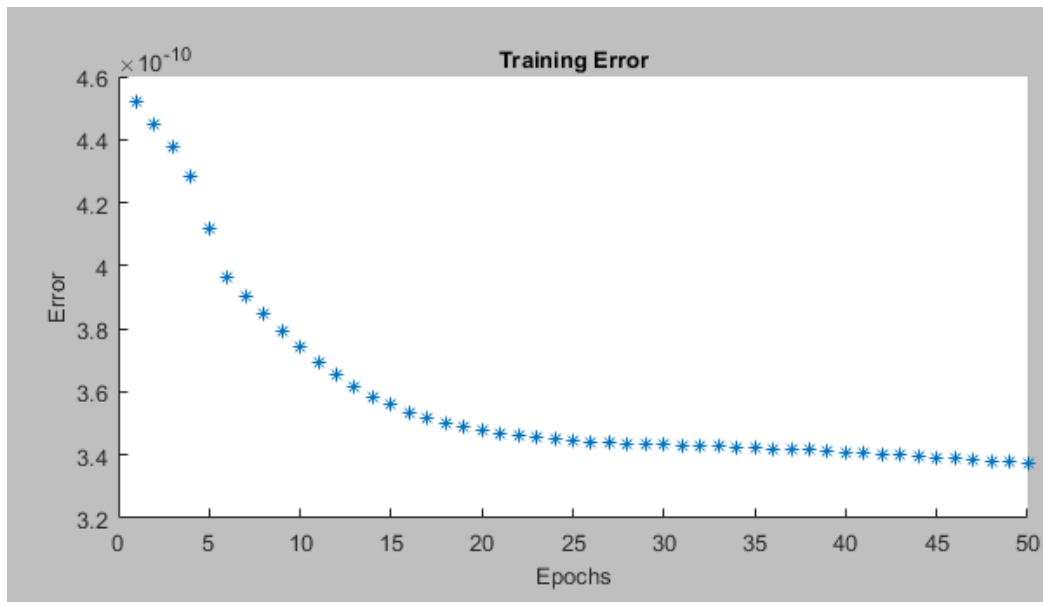
Figure 3. 10 Variation of Model Training Error with Epochs

3.4.4 ANN Modelling

Prior to the ANFIS modelling analysis, an Artificial Neural Network (ANN) approach was employed to forecast the effective permeability of reinforcement mats. Experimental outcomes were employed as the target for training and validation, utilizing input data. The neural network for modelling the experimental results consisted of a single hidden layer containing 10 neurons with a log-sigmoid transfer function, coupled with an output layer utilizing a pure linear transfer function. **Figure 3.11** visually portrays the comprehensive architecture of the ANN model, featuring four inputs, a hidden layer utilizing a log-sigmoid transfer function, an output layer employing a pure linear transfer function, and a single output.
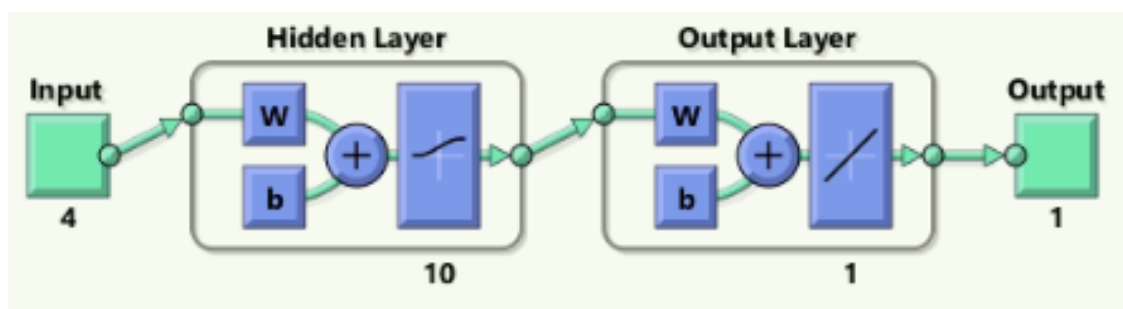
Figure 3. 11 ANN Modelling Structure from MATLAB

The dataset was partitioned into training (50%), validation (25%), and testing (25%) subsets. The neural network underwent training on the combined training and validation data

over 12 epochs, achieving a minimum mean squared error value of 0.018908 at epoch 6, depicted in **Figure 3.12**.
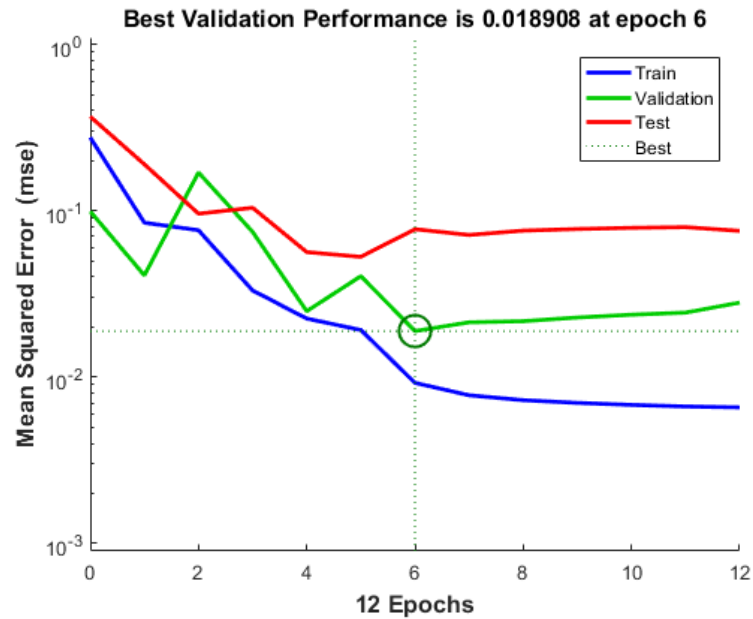
Figure 3. 12 Performance Analysis of Data for Different Conditions
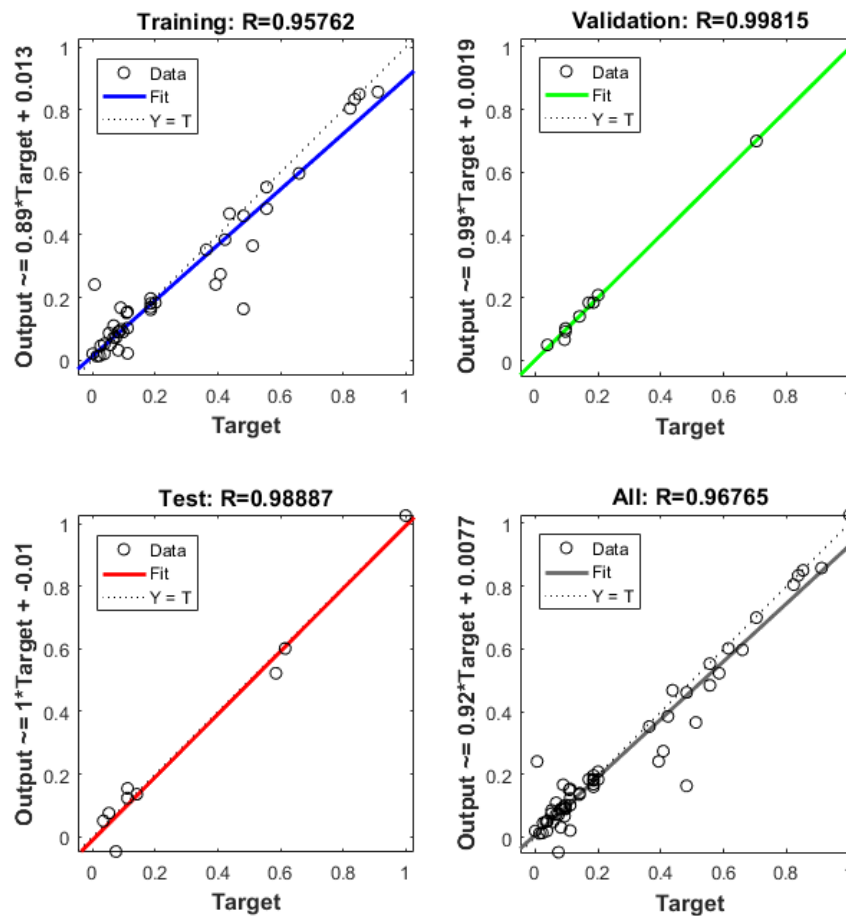
Figure 3. 13 ANN Model Regression Analysis for Predicting the Mat Permeability

The regression coefficients for the training, validation, and testing datasets were determined as 0.95762, 0.99815, and 0.98887 respectively. Collectively, the overarching regression coefficient yielded by the ANN modelling reached 0.96765. **Figure 3.13** features a linear relationship demonstrated by the straight line, showcasing the connection between the predicted data (output) and the experimental data (target).

3.4.5 Comparative Assessment between Machine Learning Techniques

The obtained ANN results were compared with the ANFIS model results. ANFIS modelling showed better prediction than ANN modelling. On the other hand, the tree-based machine learning regression models were used to predict the permeability by directly importing these models from the scikit-learn library in google colab notebook. **Figure 3.14** shows the comparison between all the ML models used in this study. It was observed that all the models had a correlation coefficient greater than 80%. In comparison with the other regression models like DecisionTreeRegressor, BaggingRegressor, RandomForestRegressor, ExtraTreesRegressor and GradientBoostingRegressor, The XGBoost regression model showed superior performance with a greater correlation coefficient of about 0.963 and lowest error indices despite a training process based on a relatively sparse input dataset. However, the highest R^2 value was found to be 0.975 for the ANFIS model. This shows the effective performance of the ANFIS model.
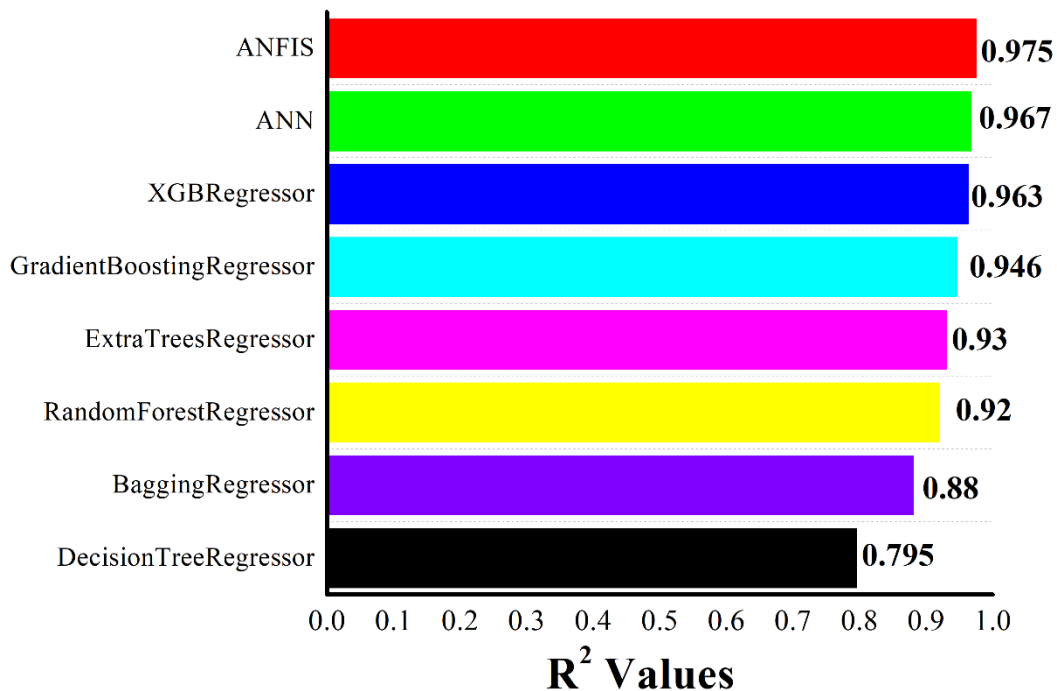
Figure 3. 14 Regression Analysis for Different ML Models

3.5 Summary

The main objective of this chapter was to measure the reinforcement mat permeabilities using mould-filling experiments, for its applicability in mould-filling simulations. Additionally, the effect of processing and material parameters on the reinforcement mat permeability was evaluated using mould-filling experiments. Subsequently, the permeability of the reinforcement mat as a function of material and process parameters was predicted using machine learning techniques. At first, the mould-filling experiment coupled with the visualization technique was implemented for in-plane permeability measurement. In this method, the effective permeability value was obtained by matching the experimental flow front progression with the isothermal mould-filling simulated flow front progressions with iterative guessed permeability values.

A total of 67 isothermal mould-filling experiments were performed to relate mat permeability as a function of fibre mat porosity, mat layers, test fluid viscosity and injection pressure. From the results, a circular flow front position was observed for all the studied experiments and hence, an isotropic permeability value was obtained. It was observed that the fibre preform permeability was increased with an increase in porosity, and decreased with an increase in the number of mat layers, fluid viscosity and test fluid injection pressure. From the results, the order of permeability was obtained between 7×10^{-9} to 7×10^{-8} m^2 for chopped strand glass fibre mat, 7.5×10^{-9} to 4×10^{-8} m^2 for jute fibre mat, 8×10^{-9} to 1.5×10^{-8} m^2 for woven roving glass fibre mat, and 6×10^{-9} to 6.4×10^{-8} m^2 for hemp fibre mat. From the fibre-wetting analysis, it was found that the fibre-wetting time and test fluid-fibre saturation have a strong influence on the fluid-mat permeation. From the fibre-wetting results, it was also observed that the fluid-mat permeation decreases when there is an increase in fibre-wetting time and lesser mat surface saturation.

ANFIS and ANN machine learning models were developed in MATLAB using the Sugeno and nntool toolboxes, respectively. These models were trained for four input key parameters (number of layers, porosity, test fluid viscosity and injection pressure) and one output parameter (effective permeability) using the obtained experimental data. From the results, both models have shown excellent correlation and a minimum mean square error. The R^2 values obtained for the ANN and ANFIS techniques were 0.967 and 0.975, respectively. Different tree-based regression machine-learning models were trained from the scikit-learn library for statistical analysis with the ANFIS and ANN models. From the comparative analysis, ANFIS has shown an excellent correlation with the experimental permeability as a

function of input key parameters than the other machine learning approaches. Thus, the fuzzy inference system offers an efficient way to predict effective permeability as a function of process and material parameters.

Chapter 4

Development of an Optimized RTM Mould-Filling Process using Multi-Objective Optimization Algorithms

4.1 Introduction

The resin transfer moulding (RTM) technique stands as a pivotal liquid composite moulding (LCM) process for the manufacturing of complex and large composite components [143]. Among the essential stages influencing the ultimate quality of the composite parts, the mould-filling phase serves as a critical cornerstone for the development of an efficient manufacturing process [17]. During the mould-filling phase, the pressurized resin is injected into the mould via designated injection ports ultimately leading to the complete saturation of the fibre preform [14]. Given the intricate nature of composite parts characterized by their complexity and scale, the utilization of multiple injection ports and strategically positioned vents emerges as a crucial strategy. This multifaceted approach ensures the uniform saturation of the entire mould, effectively mitigating the formation of undesirable dry spots prior to the initiation of resin gelation [20].

Notably, effective mitigation of the dry spots becomes a significant challenge, especially at the cut edges of composite parts where the race-tracking phenomenon becomes influential [144]. The phenomenon of race-tracking highlights the tendency for the formation of dry spots along cut-edges underscoring the need for careful attention during the mould-filling process. In addition, dry spots are also formed with the collisions of flow fronts rising

from different injection gates [118]. As a result, the optimum design of the mould fill phase requires adequate numbers and appropriate positions of mould gates and vents along with the implementation of an appropriate race-tracking effect [20], [145].

In this context, the current chapter develops multi-objective optimization algorithms to thoroughly explore the mould-filling phase of the resin transfer moulding technique. These developed algorithms are integrated with a finite element simulator to investigate the complex interaction between resin flow dynamics, injection port arrangements, vent placements, and the management of race-tracking effects. This research aims to contribute to the refining of the RTM process for manufacturing industrially viable components such as automotive bonnet and aircraft wing flap composite parts. This investigation not only seeks to advance the scientific understanding of RTM but also holds the promise of finding novel insights that could potentially revolutionize the manufacturing landscape for large and complex composite structures. Through a comprehensive analysis of these critical elements, this chapter aims to enhance precision, efficiency and reliability in RTM-based composite part production.

4.1.1 Bibliometric Analysis

A bibliometric analysis was conducted on August 21, 2023, utilizing the Web of Science core database. A collection of 119 articles was obtained through the primary search terms 'Resin Transfer Moulding' within the topics section and 'resin flow' within the Author Keywords section. Bibliometric network visualization was carried out using the VOSviewer software [49], as depicted in **Figure 4.1**. The analysis focused on bibliometric coupling occurrences of author keywords that appeared more than 2 times. Out of a pool of 268 keywords, 68 keywords met this threshold and were consequently selected for further examination. From these 68 keywords, the cumulative strength of co-occurrence links with other keywords was computed. This computation guided the selection of keywords with the highest total link strength. Among these keywords, 'resin flow', 'process monitoring', 'resin transfer moulding', and others emerged as prominent author keywords.
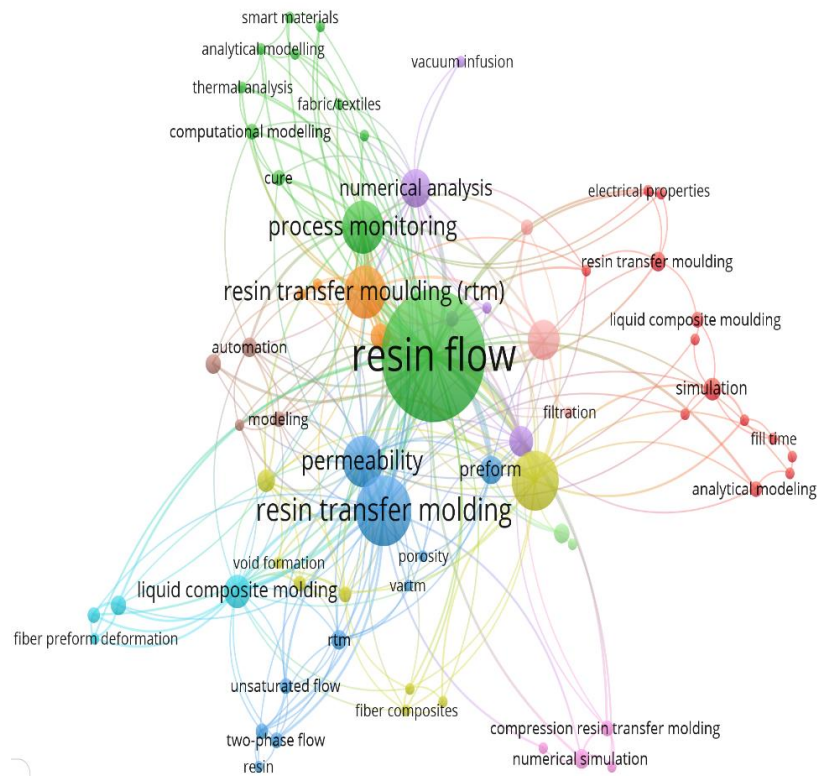
Figure 4. 1 Schematic Representation of the Bibliographic Networking Diagram Obtained from the Web of Science Core Database through the Search Conducted on August 21, 2023.

4.1.2 Literature Review

The growing demand for lightweight structural components particularly in sectors like aerospace and automotive has emphasized the need for efficient high-volume composite manufacturing capabilities [5], [7]–[10], [25], [146]. Over the span of several decades, the RTM process has consistently evolved and shown significant promise in offering cost-effective solutions for producing composites in large quantities [147], [148]. The RTM process involves four stages: preforming, mould filling, curing and demoulding of parts. Among these stages, the mould-filling phase holds importance as it significantly impacts production efficiency and final product quality [149], [150]. During this phase, the resin is introduced through injection gates to saturate the dry fibrous reinforcement while simultaneously removing air, volatile elements and excess resin through air vents. The primary objective of the mould-filling stage is to achieve complete saturation of the fibre preform with resin while minimizing the formation of undesired dry spots.

Several experimental works have been reported in the literature in averting the formation of dry spots during the mould-filling process using flow visualization [124], [151] and sensor [152] techniques. However, the development of an optimized RTM production

83

process using experimental trials with intricately embedded sensors was proven to be sub-optimized, laborious, costly and time-consuming. Alternatively, using RTM process simulations and optimizations was proven to be an inexpensive and effective approach that results in optimal solutions with iterations [20]. From the literature, the commonly used finite element, finite volume and control volume finite element method-based simulators were COMSOL Multi-physics, PAM-RTM, RTM-Worx, LIMS, and ANSYS Fluent for performing the mould filling process simulations [27], [29], [101].

Spiridon Koutsonas [153] modelled the race-tracking variability for curved composite parts for the resin transfer moulding process. They developed the finite element/control volume modelling approach to predict the 2D and 3D race-tracking permeability for any composite structure. Shevtsov et al. [90] performed a trial and error numerical simulation using a COMSOL multi-physics simulator for mould gate-vent location optimization of large and complex shape composite structures. They considered three trials and analyzed the flow front progression and dry spot formation for each trial studied. Kuppusamy et al. [100] performed trial-and-error numerical simulations to obtain an optimal injection strategy for the cab front composite part. They performed the isothermal mould-filling simulations and analyzed the fill time and dry spot formation using the PAM-RTM simulator for each trial studied. Solanki et al. [101] have published isothermal mould-filling simulations for natural fibre-reinforced composites using the ANSYS Fluent simulator. They analyzed the effect of swelling on the isothermal mould-filling phase in natural fibre porous media.

Yang et al. [55] have studied non-isothermal mould filling and curing phases using ANSYS fluent simulator. Yang et al. utilized the composite structure and material parameters from the research work published by Fei Shi and Xianghuai Dong [154]. The author analysed the sensitivity of mould fill time and degree of cure with the change in process temperature with the help of subroutines. However, the use of subroutines increases computational complexity and convergence issues. In summary, the evolution of RTM optimization strategies is marked by a shift from predominantly experimental endeavours towards simulation-driven approaches. Through these studies, the potential of simulation-based techniques to enhance RTM processes and optimize critical parameters becomes increasingly evident.

In the domain of optimization algorithms, the literature review revealed that the widely employed techniques for optimizing mould-filling gate-vent locations include the genetic algorithm (GA), ant swarm strategy and the non-dominated sorting genetic algorithm-II (NSGA-II) [155]–[159]. These techniques were used to optimize various objective functions

such as process time, void content, weld lines, setup costs and others within the framework of RTM process optimization [160], [161].

Ye, Xugang et al.[149] developed a graph-based heuristic algorithm for optimizing the single gate and multiple vent locations. They considered six different 2D geometries. Initially, the gate location was fixed and then the locations of the vents were optimized by minimizing the maximum distance between the gate and the vents. However, a single injection port may not be sufficient for large and complex structures to achieve complete saturation of the fibre preform within the minimum mould filling time. Liu et al.[162] proposed a hybrid simulated annealing genetic algorithm (SAGA) for multiple mould gate location optimizations to improve the convergence rate. They varied the gate configurations from two to five and compared the results obtained from SAGA with those of GA. They found an improvement in convergence rate for SAGA than GA with an increase in the number of mould gates. J. Wang et al.[163] implemented the iterative Lloyd's algorithm for multiple-gate injection optimization based on the Centroidal Voronoi Diagram (CVD) approach. They found that the CVD method required fewer simulation runs to achieve minimum fill time compared to the exhaustive search technique and GA.

Okabe et al.[164] and Oya et al.[118] used a multi-objective optimization algorithm with fixed vent positions and searched for the optimal positions of multi-point injection ports. Also, they varied the distance between gates and vents to obtain the trade-off between the weld line, fill time, resin wasted and dry spot content. Seyednourani et al.[99] designed a two-stage optimization methodology for optimizing the gate-vent locations using GA. They used the concept of distribution media (DM) layout and incorporated the race-tracking effect to develop a robust LCM process. However, the work was more focused on implementing a DM layout with a pre-fixed number of gates and vents to optimize their locations.

The injection strategy containing the least numbers and appropriate positions of mould gates-vents is vital for attaining the optimized mould fill phase. From the literature review, it was found that the optimization of mould gate and vent locations was independently addressed using different heuristic and deterministic optimization techniques. Also, it was found only one research article that implemented the effect of race-tracking along with the multi-objective optimization algorithms [99]. According to the knowledge of the investigator, there were no straight reports found in the literature that directly deal with simultaneous optimization of the numbers and positions of mould gates-vents together. Also, there were no straight reports found on the development of robust optimization techniques for multiple-complex industrial composite structures with varied resin-fibre properties.

In the realm of optimization algorithms, researchers have handled the optimizations of the mould fill phase using variants of GA. However, from the comparative studies, the differential evolution (DE) algorithm performed significantly better than GA for multi-objective optimization problems [50]. This finding underscores the potential of exploring alternative optimization techniques to elevate the efficiency and effectiveness of the optimization process. Digging deeper, the non-dominated sorting differential evolution (NSDE) algorithm stands out as a promising avenue for further research. By combining differential evolution with non-dominated sorting principles, this algorithm has the potential to simultaneously minimize mould fill time and dry spot content offering a novel approach to addressing multiple optimization objectives.

Furthermore, no reports were found regarding the development of a multi-objective stochastic optimization (MOSO) algorithm that predicts both the optimal gate-vent numbers and positions while simultaneously minimizing dry spot content, mould filling time and the total number of ports. This multifaceted approach holds the promise of providing a comprehensive optimization solution that effectively addresses the intricate challenges posed by the mould-fill phase. In a domain-specific context, the application of robust MOO techniques integrated with multi-physics process simulation for manufacturing aircraft wing flaps and automotive bonnet composite parts using the RTM process remains largely unexplored. This gap represents a unique research opportunity where integrating developed optimization methodologies with the COMSOL multi-physics simulator for these composite components could lead to transformative advancements in the manufacturing landscape.

This chapter examines a comprehensive comparative analysis between trial and error process simulations and developed multi-objective optimization algorithms to refine the RTM mould-filling process. The focus of this study centres on two specific composite components: vinyl ester-glass fibre-reinforced automotive bonnet and RTM6-carbon fibre-reinforced aircraft wing flap. Initially, the mould-filling simulation trials were performed by changing the number and position of gates and vents for both the selected composite parts. Then mould-filling phase optimization was performed using the in-house coded evolutionary optimization algorithms. A novel in-house coded non-dominated sorting differential evaluation (NSDE) and multi-objective stochastic optimization (MOSO) algorithms were developed. The NSDE algorithm was developed for the simultaneous minimization of dry spot content and mould-fill time by changing the locations of mould gates and vents with a constraint of pre-fixed port numbers. The MOSO algorithm was developed for the simultaneous minimization of dry spot content, mould-fill time and total number of ports by changing both the numbers and locations

of gates and vents. Finally, comparisons were made between the optimized mould fill phase results obtained from the trial and error process and the developed optimization algorithms for the studied composite structures.

4.2 Process Models

The process models that simulate multi-phase fluid flow in porous media and resin cure kinetics of the RTM process using Darcy's law, the level set model and the thermo-chemical model were implemented as given below.

4.2.1 Multi-Phase Fluid Flow in Porous Media

The fluid flow through the porous media is modelled using Darcy's law as given in **Equation (4.1)** and the associated flow mass balance is modelled using the continuity equation as given in **Equation (4.2)**. The level set model as given in **Equation (4.3)** is used to track the flow front progression through the fibre preform.

$$\vec{u} = -\frac{K}{\mu}\nabla P \tag{4.1}$$

$$\frac{\partial(\emptyset\rho_r)}{\partial t} + \nabla.(\rho_r\vec{u}) = 0 \tag{4.2}$$

$$\frac{d\theta}{dt} + \vec{u}.\nabla\theta = \gamma\nabla.(\varepsilon\nabla\theta - \theta\frac{\nabla\theta}{|\nabla\theta|}) \tag{4.3}$$

where $\vec{u}$ is the velocity vector, $\emptyset$ is the porosity of the fibre mat, ρ_r is the density of resin, K is the fibre mat permeability tensor, ∇P is the pressure gradient and μ is the viscosity of the resin. Also θ, ε, and γ represent the fluid volume function, the thickness of the interface and the initialization factor, respectively from the interface tracking level set model.

$$\text{Where } \theta \text{ is defined as,} \quad \theta = \begin{cases} 0 & \text{resin unfilled domain} \\ (0,1) & \text{resin flow front} \\ 1 & \text{resin} - \text{saturated domain} \end{cases}$$

The boundary conditions associated with **Equations (4.1-4.3)** are given as,

$$\text{Mould-gate:} \quad P = P_0$$

$$\text{Air-vent and resin flow interface:} \quad P = 1 \text{ atmosphere}$$

$$\text{Mould boundary:} \quad -n.\rho_r\vec{u} = 0 \; ; \; n.\left(\varepsilon\nabla\theta - \theta\frac{\nabla\theta}{|\nabla\theta|}\right) = 0$$

where P_0 is the injection pressure of resin at the gate.

4.2.2 Thermo-Chemical Process Model

In industrial practices, both the resin injection and mould are kept at elevated temperatures to enhance the porous media fluid flow and to reduce mould filling time. The

transient energy balance for the cure analysis during mould filling that includes conduction, convection and resin cure is given in **Equation (4.4)**,

$$(\emptyset\rho_r C_{Pr} + (1 - \emptyset)\rho_f C_{Pf})\frac{\partial T}{\partial t} + \rho_r C_{Pr}(\vec{u}.\nabla T) + \nabla.(-k_c\nabla T) = -\rho_r\emptyset\Delta H\frac{\partial \alpha}{\partial t} \qquad (4.4)$$

The thermal conductivity of the composite part is computed using the rule of mixture as given in **Equation (4.5)**,

$$k_c = \frac{k_r k_f}{k_r\emptyset + k_f(1-\emptyset)} \qquad (4.5)$$

where ΔH denotes the reaction heat and subscript '*r*' and '*f*' denotes the resin and fibre physical properties, respectively.

The resin cure kinetic model is demonstrated as follows,

$$\frac{d\alpha}{dt} = Ae^{\frac{-E}{RT}}\alpha^m(1 - \alpha)^n \qquad (4.6)$$

The boundary conditions allied to address the **Equations (4.4 - 4.6)** are given as,

$$\text{Initial time } t = 0: T = T_0 ; \alpha = 0 \text{ and } \frac{d\alpha}{dt} = 0$$

$$\text{mould boundary:} \quad T = T_{mould};$$

T_0 denotes the initial temperature and T_{mould} denotes the mould temperature.

E denotes activation energy, *A* denotes frequency factor, *T* denotes temperature, *R* denotes an ideal gas constant, and *m* and *n* denote the order of the reaction.

4.3 Raw Materials and Methodology

4.3.1 Raw Materials

A vinyl ester Derakane 8084 and Mono-component RTM6 epoxy resins supplied by Ashland and Hexcel, respectively were used as the resin matrices in this study. A twill-weave carbon fibre mat having 400 g/m^2 areal density and 46% porosity and a twill-weave glass fibre mat having 610 g/m^2 areal density and 51% porosity were used as the reinforcement mats for this study. The reinforcement mats used in this study were supplied by Sree Industrial Composite Products, Hyderabad, India.

4.3.2 Raw Material Parameters

The cure kinetics parameters for vinyl ester and RTM6 resins were sourced from **Chapter 2**, while the permeability values obtained for the glass and carbon fibre mats were extracted from **Chapter 3**. From the thermal conductivity experiments, an average thermal conductivity of 0.164 W/m-K at 50 ^{0}C was obtained for the neat vinyl ester resin. The physical

properties of vinyl ester and RTM6 resins were supplied from their respective technical data sheet. The physical properties of glass and carbon fibre mats were collected from the literature. The respective material properties were tabulated in **Table 4.1**.

Table 4. 1 Resin and Fibre Properties

Parameters	Values	Parameters	Values
RTM6 resin properties [91], [95], [165]			
Density of resin ρ_r	1117 kg m^{-3}	Thermal conductivity of the resin k_r	$\frac{1+0.35\,\alpha}{-33.6+0.05T}$ W m^{-1}K^{-1}
ΔH	5.04×10^8 J/m^{-3}		
Viscosity of resin μ_r	0.06 Pa.s at 120 ⁰C	Specific heat of the resin C_{pr}	$1208.15 + 15.1969\,T - 0.0499T^2$ Jkg^{-1}K^{-1}
Vinyl ester resin properties [166]			
Density of resin ρ_r	1040 kg m^{-3}	Thermal conductivity of the resin k_r	0.16 W m^{-1}K^{-1}
ΔH	1.54×10^8 J/m^{-3}		
Viscosity of resin μ_r	0.36 Pa.s at 25 ⁰C	Specific heat of the resin C_{pr}	1208.15 Jkg^{-1}K^{-1}
Carbon fibre properties [165]			
Thermal conductivity of fibre (k_f)	2.7 W m^{-1}K^{-1}	Specific heat of fibre C_{pf}	$577.4 + 6.85165T - 0.01807T^2$ Jkg^{-1}K^{-1}
Density of fibre ρ_f	1770 kg m^{-3}	Porosity	0.46
Glass fibre properties [55]			
Thermal conductivity of fibre (k_f)	0.0335 W m^{-1}K^{-1}	Specific heat of fibre C_{pf}	670 Jkg^{-1}K^{-1}
Density of fibre ρ_f	2540 kg m^{-3}	Porosity	0.51

4.3.3 RTM Process Composite Parts

The RTM process was developed for the vinyl ester-glass fibre-reinforced automotive bonnet and the RTM6-carbon fibre-reinforced aircraft wing flap composite parts. **Figures 4.2 and 4.3** show the dimensions of the automotive bonnet and aircraft wing flap structures, respectively. The composite parts of the automotive bonnet and aircraft wing flap were used with thicknesses of 12 mm and 5 mm, respectively.

A grid independence test was conducted on the automotive bonnet, wherein the number of domain elements varied from 16155 to 176685, as depicted in **Figure 4.4**. It was observed that a coarser mesh with 16155 domain elements led to a slower progression of the resin flow front,

resulting in an extended mould filling time. Conversely, there was no significant change in mould-filling time for domain elements ranging from 26000 to 180000. For the bonnet structure, process simulations were conducted using a tetrahedron mesh with a maximum element size of 50 mm and 45178 domain elements.

Similarly, a grid independence test was performed on the aircraft wing flap by altering the domain elements from 1800 to 33000. The outcomes indicated no noticeable alterations in mould-filling time within the examined range. For the wing flap structure, process simulations utilized a tetrahedron mesh with a maximum element size of 50 mm and 8854 domain elements. However, there were minor variations in the total number of domain elements due to changes in the count of injection ports and vents for both composite parts.

Resin injection temperatures of 120°C and 25°C were used during the mould-fill phase simulations for the wing flap and bonnet composite parts, respectively. A 10 mm diameter mould gates and vents and the resin injection pressure of 4×10^5 Pa was used during the mould-filling simulations. The process models and respective initial and boundary conditions given in **Equations (4.1 - 4.6)** were addressed during the mould-filling simulations. The re-initialization parameter γ and interface thickness ε from the level set module were tuned to obtain the numerical stability in the simulation results. From the literature[90], [167] the interface thickness ε value was suggested as half of the maximum element mesh size. The sensitivity of γ on the numerical stability of mould filling simulations was analyzed and a value of 0.001 m/s was observed as the tuned value.

The concept of race-tracking was applied to the boundary edges of the composite parts, as there is less observed flow resistance across the cut edges compared to the fibre preform. Hence, by considering race-tracking channels a highly permeable media, the race-tracking permeability was used 100 times higher than the fibre mat permeability.
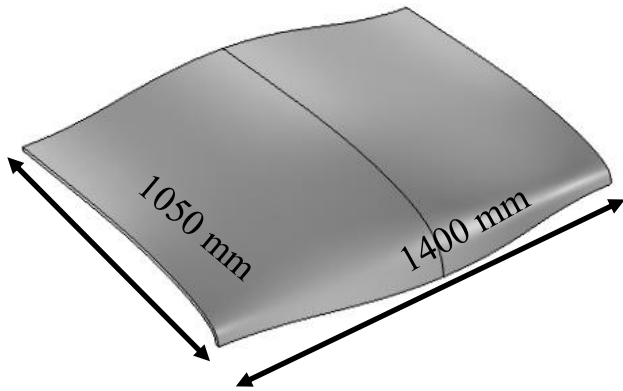
Figure 4. 2 Automotive Bonnet Structure   **Figure 4. 3 Aircraft Wing Flap Structure**
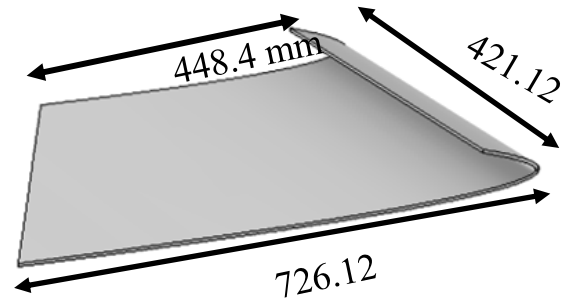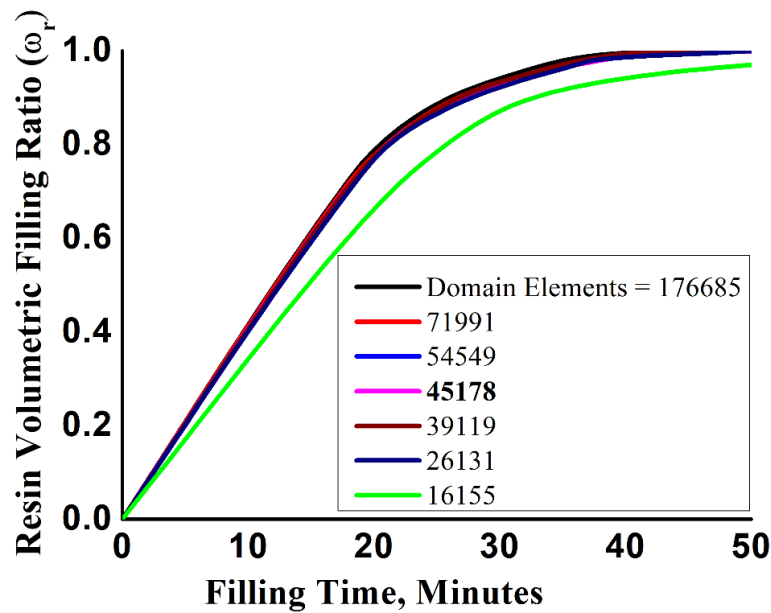
Figure 4. 4 A Grid Independence Study for Automotive Bonnet Composite Part

4.3.4 Trial and Error Process Simulation

The non-isothermal mould filling simulations were performed to obtain the effective injection strategy based on a trial and error process for the selected composite structures. Several simulation trials were performed by changing the number and position of injection ports and air vents. Salient simulation trials are tabulated in **Tables 4.2** and **4.3** for the automotive bonnet and aircraft wing flap structures, respectively.

Table 4. 2 Trial Injection Strategies for Automotive Bonnet Structure
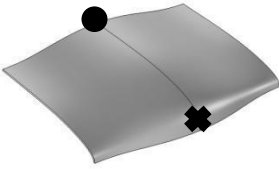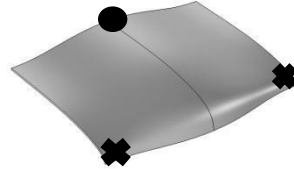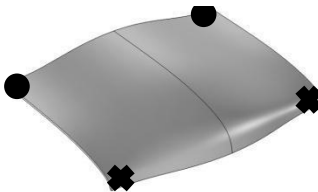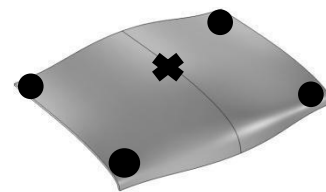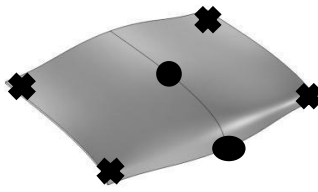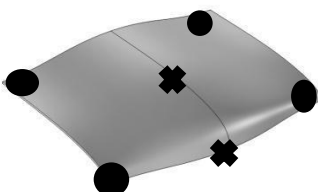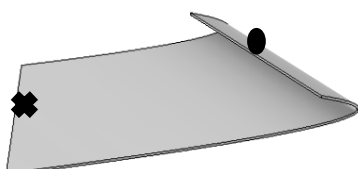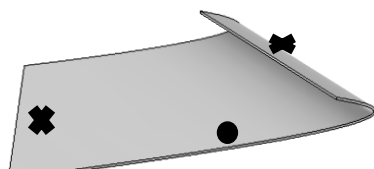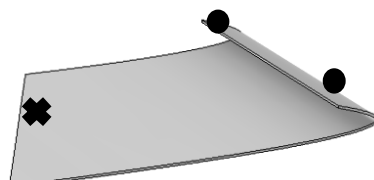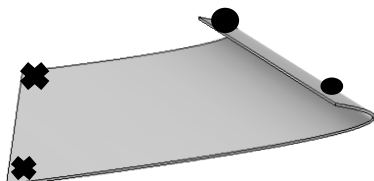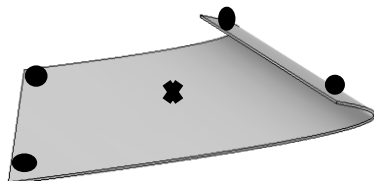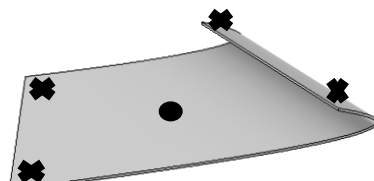
Trial 1. One gate and one vent	Trial 2. Two gates and one vent	Trial 3. One gate and two vents

Trial 5. Two Gates and Two Vents	Trial 5. One gate and four vents	Trial 6. Four gates and one vent

Trial 8. Two gates and four vents	Trial 8. Four gates and two vents	Gate position ●
		Vent position ✖

Table 4. 3 Trial Injection Strategies for Aircraft Wing Flap Structure

● Gate position	✖ Vent position

Trial 1: One gate and one vent	Trial 2: One gate and two vents	Trial 3: Two gates and one vent

Trial 4: Two gates and two vents	Trial 5: Four gates and one vent	Trial 6: One gate and four vents

92

4.3.5 Non-Dominated Sorting Differential Evolution (NSDE) Algorithm

The non-dominated sorting differential evolution (NSDE) algorithm was developed to optimize the positions of gates and air vents for a fixed number of ports (gates + vents). The NSDE algorithm is a class of multi-objective optimization (MOO) techniques which is simply an extension of the differential evolution (DE) algorithm to address the MOO problems. Many researchers used GA for optimizing the mould fill phase [99], [162]–[164], however from the comparative studies, the DE algorithm has performed significantly better than GA for MOO problems [50]. In this work, the DE algorithm was developed for the multi-objective optimization of the RTM-mould fill phase. The optimization objectives considered were the minimization of dry spot content and mould-filling time. Dry spot content is the unsaturated area of resin in the composite part when the resin reaches the vents and it is calculated based on the total number of unfilled nodes using **Equation (4.7).** Filling time is calculated as the amount of time required for the resin to reach the vents. These two objectives were simultaneously optimized by finding the optimum locations of gates and vents within the geometry search space R^D. In addition, the minimum distance between any two ports was constrained to be 200 mm for the bonnet and 100 mm for the wing flap parts in consideration of their dimensions. The mathematical formulation of the optimization problem described above is given in **Equation (4.8).**

$$\% \text{ dry spot content} = \sum_{i=1}^{total\ number\ of\ nodes} \left(\frac{1 - resin\ fill\ fraction\ of\ node\ i}{total\ number\ of\ nodes} \right) \times 100 \quad (4.7)$$

$$\text{Minimization} \quad dry\ spot\ content, filling\ time \quad (4.8)$$

$$subject\ to$$

$$Location\ of\ gates\ and\ vents \in \pmb{R^D}$$

The NSDE algorithm was coupled with finite element simulation to find the optimal positions of gates and vents for a fixed number of ports. The number of ports was pre-defined as two gates and four vents for the bonnet part and one gate and four vents for the wing flap part in consideration of their dimensions and geometric complexity. The generation of input parameters (positions of gates and vents) and elitism of dominated solutions based on the NSDE optimization algorithm was programmed in MATLAB. These generated input parameters were utilized to perform the mould-filling process model simulations in COMSOL software. The integration of the optimization algorithm and mould-filling simulation was programmed in MATLAB using COMSOL Live-Link for MATLAB. This Live-Link interface enables the COMSOL simulation to be loaded into the MATLAB directory using the 'mphload' command. The implementation guidelines for the Live-Link interface were referenced from

the user guidelines for Live-Link for MATLAB[168]. The following steps were incorporated for the implementation of the NSDE algorithm for simultaneous minimization of dry spot content and mould-filling time.

Step 1: In this step, the process was initiated by defining parameters namely crossover probability (C_p), mutation factor (F), population size (N_p), and the maximum number of generations (max_gen).

Initially, six and five different mesh node elements were randomly predicted in the plain geometry (without adding inlet-outlet ports) for the bonnet and wing flap, respectively. These randomly generated nodal elements were imported to COMSOL using the 'model.param.set' command. The inlet (gate) and outlet (vent) cylinders were constructed based on the predicted nodal elements from the composite part. The dimensions of the gate and vents were pre-defined as 5 mm in radius and 10 mm in height. After building the geometry with new positions of gate and vent, the generation of meshing is programmed with a tetrahedron type of mesh. Then, the mould-filling simulation was programmed using the 'model.sol('sol1').runAll' command function. The mould-filling process model simulations were performed using the new positions of the gate and vent. Upon completion of the mould-filling simulation, the results of the resin filling fraction reached to the nodal elements of the geometry at filling time 't' were extracted programmatically in MATLAB using the 'model. result' command function. The resin filling fraction at each vent node is computed at filling time 't' and then, the objective functions were computed for the obtained resin content value of 0.9 and above at each vent node. For resin filling fraction lesser than 0.9 at the vent node, the mould-filling simulations were performed for the extended time loops until a value of 0.9 and above. From the composite part dimension and viscosity of the resin, the initial mould-filling time was defined as 10 minutes for the bonnet and 80 seconds for the wing flap. A time step of 5 minutes and 5 seconds was used for each subsequent time loop for the bonnet and wing flap parts, respectively. The generation of input parameters and subsequent computation of % dry spot content and filling time from the mould-filling process simulation was performed for a population size of N_p. The complete dataset generated for a population size of N_p was designated as the parent population (P_g).

Step 2: This step involved mutation and crossover processes.

Three random vectors were selected from the parent population (P_g) to generate a mutated population (M_g). The mutated vectors were obtained by applying mutation to the locations of the gate and vent as given in **Equation (4.9)**. Similar to Step 1, % dry spot content and fill time values were computed for the mutated population.

$$M_{g,i} = P_{g,r1} + F(P_{g,r2} - P_{g,r3}) \tag{4.9}$$

Here $r1, r2$, and $r3$ indicate three distinct random numbers. Subsequently, the binomial crossover was performed utilizing the mutated and parent populations to create a child population (Q_g) as given in **Equation (4.10)**. The mutation factor (F) and crossover probability (C_p) were set to 0.8 and 0.25, respectively. The mathematical implementation of the Differential Evolution (DE) algorithm was referenced from the research work published by Karaboga and Okdem[169].

$$Q_g = \begin{cases} P_g, & if\ rand > \text{Cp} \\ M_g, & if\ rand \leq Cp \end{cases} \tag{4.10}$$

Step 3: In this step, a selection process takes place to determine the best solutions from the current generation to undergo further next-generation evolutionary steps.

A dominance check was conducted between the parent population (P_g) and the child population (Q_g). If a vector in the child population dominates a vector in the parent population, the child vector is included in the new population (P_{g+1}) for the next generation. Conversely, if a parent vector dominates a child vector, the parent vector is retained in the new population (P_{g+1}). After calculating the dominance of each solution in the population, the rankings are assigned to the new population (P_{g+1}) based on the dominance check. Typically, solutions that are not dominated by any other solution (Pareto front solutions) are given the highest rank (rank 1). Solutions that are dominated by rank 1 solutions but dominate other solutions are assigned the next rank (rank 2), and so forth. Additionally, the crowding distance measure is also computed to differentiate between solutions with the same rank. The crowding distance measures how close a solution is to its neighbours in the objective space. Solutions with higher crowding distances are preferred because they provide better coverage of the Pareto front. The dominance check of the NSDE algorithm was performed using the non-dominated sorting approach based on the NSGA-II algorithm[170].

Steps 2 and 3 were repeated for the defined maximum number of generations to iteratively improve the solution. The outcome was a Pareto front depicting the trade-offs between % dry spot content and filling time. The vector in rank 1 represents the Pareto optimal solution. **Figure 4.5** illustrates the flow diagram for the implementation of an in-house coded NSDE algorithm to find the optimal positions of a gate and vent for the pre-defined port numbers. The population size was set at 10 and the maximum number of generations was set to 30.
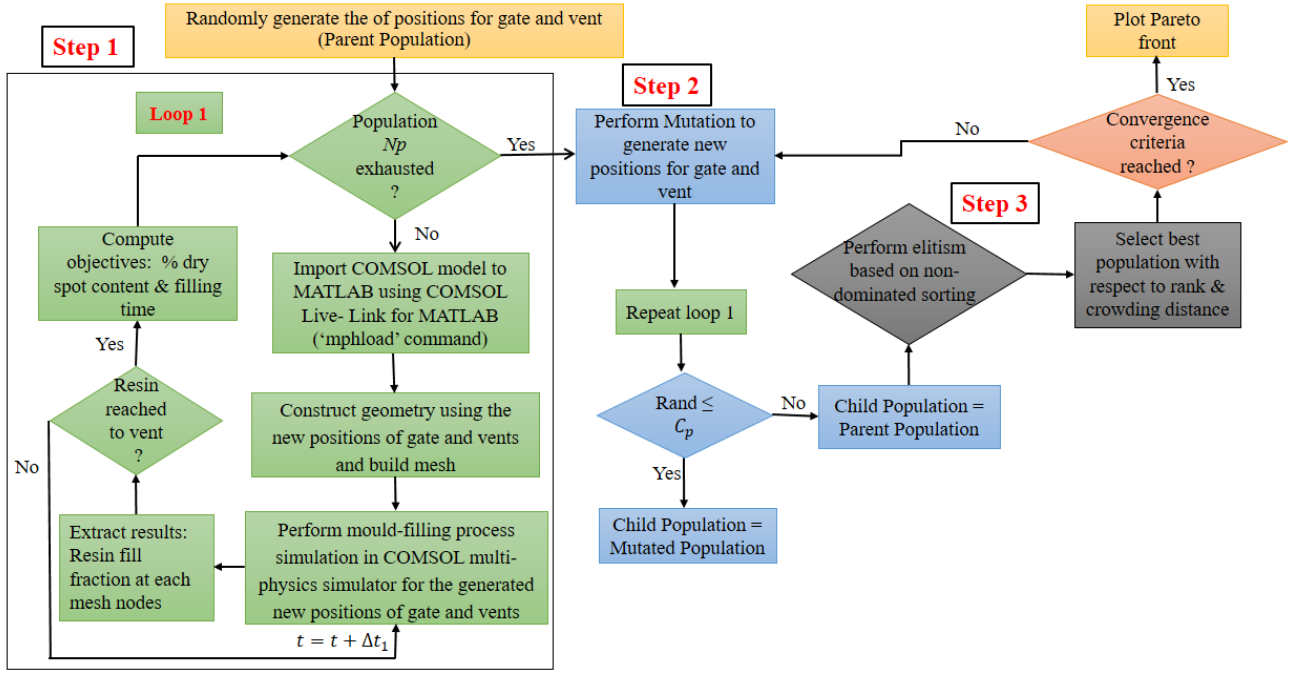
Figure 4. 5 Flow Diagram for In-House Coded NSDE Algorithm for Location Optimization of the Pre-fixed Numbers of Gates and Vents

4.3.6 Multi-Objective Stochastic Optimization (MOSO) Algorithm

The meta-heuristics optimization algorithms such as the cuckoo search algorithm, particle swarm optimization, GA and DE compute the new generation population with an improved search direction using a step size. These algorithms efficiently deliver global or nearer-to-global optimal solutions. However, these algorithms require significant computational time based on the complexity of the problem. In the context of the RTM mould-filling process, utilizing a lesser number of ports would lead to extended computational time in order to saturate the entire mould with resin. Conversely, utilizing a larger number of ports might result in reduced mould-filling time but it would elevate the intricacy of the actual mould design. Therefore, there is a necessity to develop an algorithm that can effectively explore the entire search space of composite panels to define gate-vent numbers and positions within a shorter computational time.

Therefore, the multi-objective stochastic optimization (MOSO) algorithm was developed for the simultaneous optimization of numbers and locations of gates and vents. The optimization objectives considered under this algorithm were the minimization of dry spot content, the total number of ports, and the mould-filling time. The total number of ports was calculated using the total number of gates and the total number of vents used for each simulation. The in-house coded MOSO algorithm adapts the random exploration of geometry search space using uniform distribution probability and then, it adapts an elitism selection using

96

NSGA-II. In this work, the number of gates and vents was limited to four to avoid the complexity of the actual mould design. In addition, the minimum distance between any two ports was constrained to be 200 mm for the automotive bonnet and 100 mm for the aircraft wing flap parts in consideration of their dimensions. The mathematical formulation of the optimization problem described above is given in **Equation (4.11).**

$$Minimization \quad dry\ spot\ content,\ total\ number\ of\ ports, filling\ time \quad (4.11)$$

$$subject\ to$$

$$1 \leq number\ of\ gates \leq 4$$

$$1 \leq number\ of\ vents \leq 4$$

$$Location\ of\ gates\ and\ vents \in \boldsymbol{R^D}$$

This optimization problem was implemented in MATLAB by combining the finite element (FE) simulation package using the COMSOL live link for MATLAB. The total configurations were computed based on the number of combinations of gates and vents**.** A total number of 4 gates and 4 vents were used. Therefore, a total of 16 combinations were obtained for gates and vents as shown in **Figure 4.6**. Also, the total number of ports was obtained from the summation of the number of gates and number of vents used for each configuration.
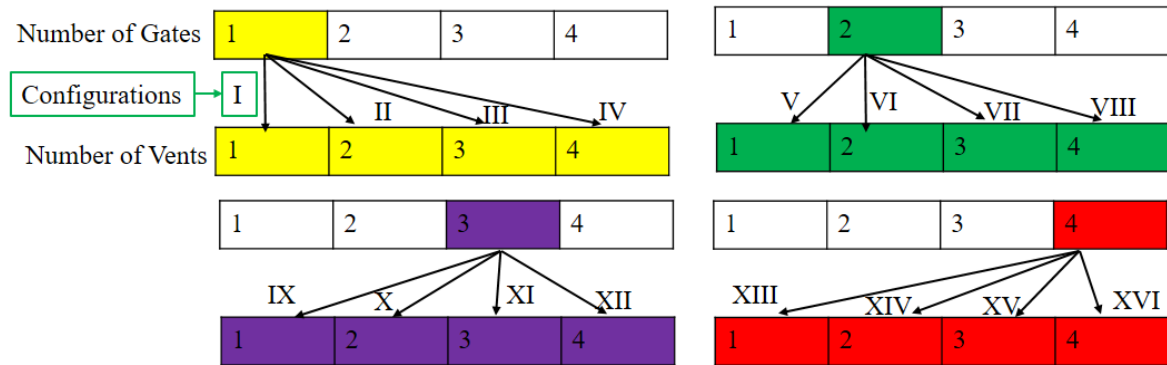
Figure 4. 6 Number of Gates and Vents Pattern for a Defined Configuration

The following steps were incorporated for the implementation of the MOSO algorithm to identify the optimum number and positions of gates and vents

Step 1 Population Generation: In this step, the process was initiated by defining parameters such as geometry search space R^D, bounds on the number of gates and vents, total number of configurations and maximum number of generations (*max_gen*).

Initially, the locations of gates and vents were randomly predicted for each configuration of the ports (gates + vents). The prediction and generation of gate and vent locations followed a similar procedure described in the NSDE algorithm in Section 3.4.1. The mould-filling simulations were performed for each configuration of the gate and vent. Upon

completion of the mould-filling simulation, the results of the resin-filling fraction at each vent node were extracted programmatically in MATLAB using the 'model. result' command function. The filling time, the total number of ports, and the percentage of dry spot content were computed for each configuration.

Step 2 Selection: During elitism, the solutions obtained from the previous generation were compared with the current generation for a similar number of ports. For example, the solutions obtained from 1st configuration of the previous generation were compared with the 1st configuration of the current generation. However, the ranking and non-dominated sorting were implemented based on NSGA-II on all the configurations. Then, the fronts of different ranks were obtained between dry spot content, the total number of ports and the mould-filling time. **Figure 4.7** shows the flow diagram for the implementation of an in-house coded MOSO algorithm for the simultaneous optimization of numbers and positions of gates and vents.
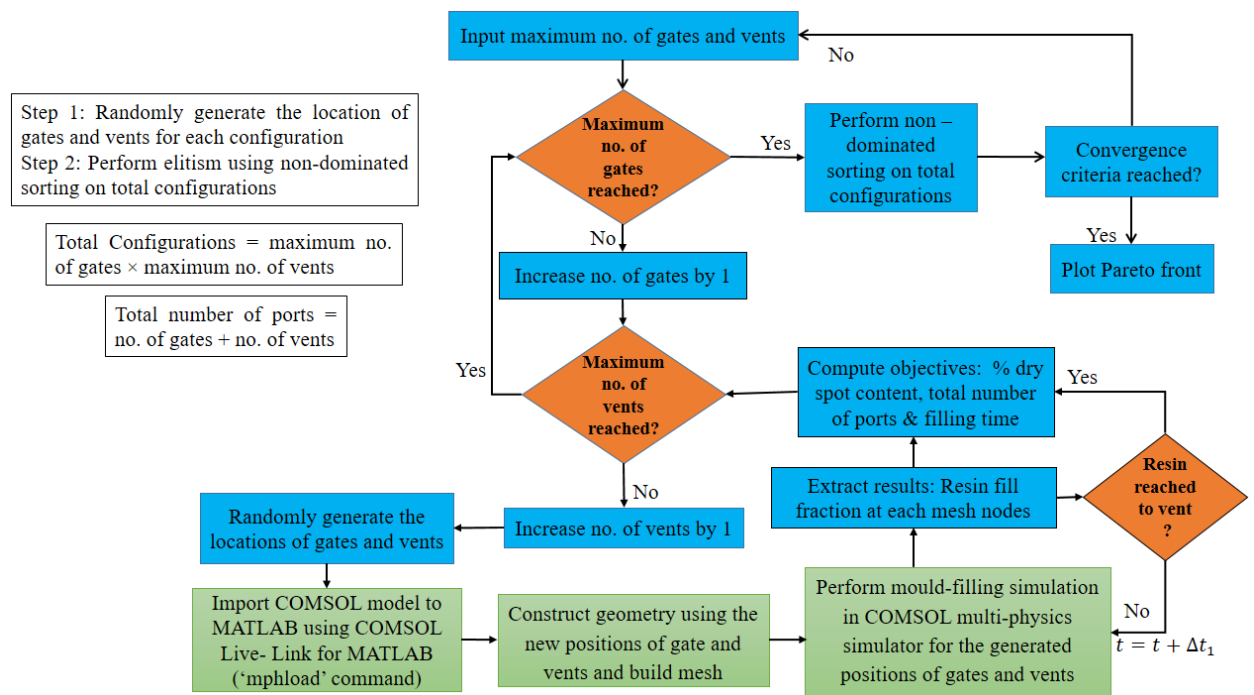
Figure 4. 7 Flow Diagram for In-House Coded MOSO Algorithm for the Simultaneous Optimization of Numbers and Positions of Gates and Vents

4.4 Results and Discussion

The main objective of mould fill phase optimization is to search for an optimized injection strategy that contains the least number of gates and vents which are placed at optimal positions. Importantly, the optimized injection strategy should deliver uniform mould filling and minimum filling time without the formation of dry spots. A non-uniform mould filling

occurs when the flow fronts rising from the two different mould gates collide with each other. Dry spots are formed once the resin flow front reaches mould vents before saturating the entire mould. The mould fill phase optimization was performed for the automotive bonnet and aircraft wing flap composite parts using the trial and error process model simulation, non-dominated sorting differential evolution (NSDE) algorithm and multi-objective stochastic optimization (MOSO) algorithm. The effect of race-tracking was implemented in the NSDE and MOSO algorithms by incorporating race-tracking permeability at the boundary cut edges. A value of 2.0×10^{-7} m^2 and 1.0×10^{-7} m^2 were used as the race-tracking permeabilities for the automotive bonnet and aircraft wing flap composite parts, respectively. The comparisons of mould-filling results obtained for both geometries through trial and error process simulations, NSDE and MOSO algorithms are discussed in the following sections.

4.4.1 Trial and Error Mould Filling Simulation Results
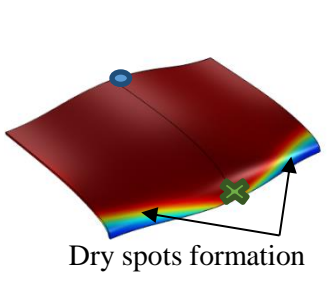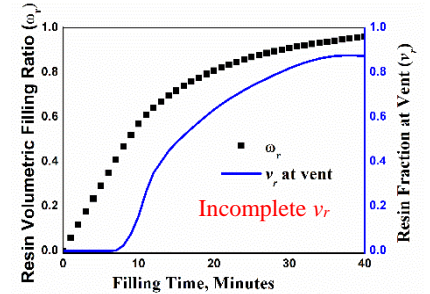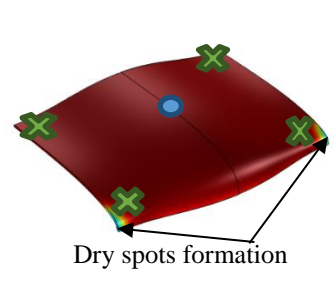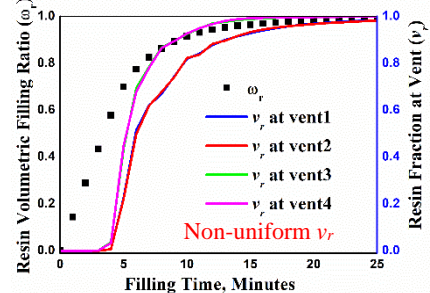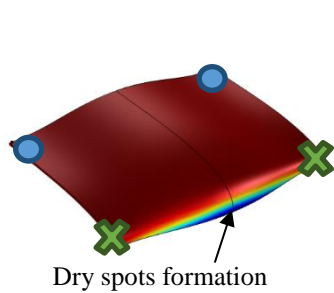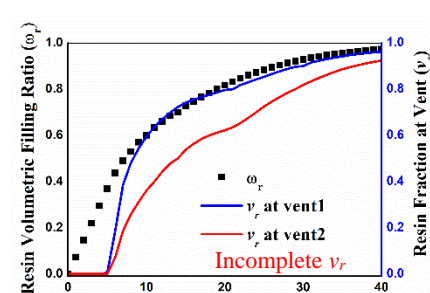
The trial and error mould-filling simulations were performed by manually changing the numbers and positions of gates and vents. The simulated results of resin-filled surface plots, resin fraction at the vent and resin volumetric filling ratio at the composite part for the studied trials are demonstrated in **Tables 4.4 and 4.5** for the automotive bonnet and aircraft wing flap composite parts, respectively. The resin volumetric filling ratio (ω_r) is measured as the ratio of resin volume filled in the composite panel at any time 't' to the total resin volume at the complete mould fill. The resin fraction at vent (v_r) is measured as the ratio of resin volume reached to the vent at any time 't' to the total volume of resin and air at the vent. At the surface plots, the resin-filled area is demonstrated in the dark red colour and the unfilled area is demonstrated in the blue colour. The formation of dry spots with a change in the numbers and locations of gates and vents is also exhibited in **Tables 4.4 and 4.5**.

From **Table 4.4**, the dry spot contents and non-uniform resin filling pattern were observed for trial cases 1-3. This may be attributed to the insufficient number of gates and vents. Irrespective of no dry spot content, a non-uniform resin fill pattern at the vents was observed for trials 4 and 5. This may be due to the improper positioning of gates and vents. With all trial cases compared, injection strategies adopted in trials 7 and 8 produced lesser filling time and uniform resin fill pattern without dry spots content. However, in trial 8, it was observed that the resin flow fronts rising from four different gates moved at different speeds towards the vents and thus, large differential filling times were observed between the two vents. Simulation trial 7 having the injection strategy of two gates positioned at the centre and front middle edge and four vents positioned at the four corners of the composite part was obtained

as an optimum injection strategy for the automotive bonnet composite part. This optimum injection strategy requires a minimum filling time of 15 minutes with a smooth resin filling and with no dry spot formation.

From **Table 4.5**, the dry spot contents were observed for the injection strategies adopted in trials 1-5. Also, an incomplete resin volumetric filling ratio and resin filling fraction at the vents for trials 1-3 were observed due to the insufficient number of gates and vents. Additionally, a non-uniform resin filling pattern was observed in injection strategies given in trials 4 and 5 due to the improper positioning of gates and vents. The injection strategy as shown in trial 6 requires a minimum fill time of 120 seconds with no dry spot contents formed. Thus, the injection strategy of one gate at the centre and four vents at the corners as adopted in simulation trial 6 was obtained as an optimum injection strategy for the aircraft wing flap composite part.

Table 4. 4 Mould Filling Simulation Trials for Automotive Bonnet Composite Part

Injection Strategy	Resin Flow Front	Resin Filling Fraction
	Gate Position	
	Vent Position	
Trial 1 One gate and one vent *Gate position:* Rear middle edge *Vent position:* Front middle edge • Filling time 40 minutes • Dry spots formation	Dry spots formation	
Trial 2 One gate and four vents *Gate position:* Rear middle edge *Vent position:* Four corners • Filling time 25 minutes • Dry spots formation	Dry spots formation	
Trial 3 Two gates and two vents *Gate position:* Two corners at the rear *Vent position:* Two corners in front • Filling time 40 minutes • Dry spots formation	Dry spots formation	
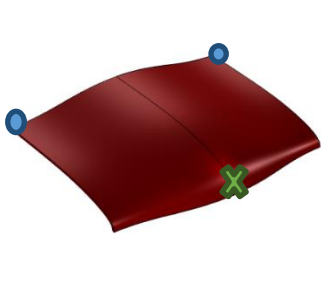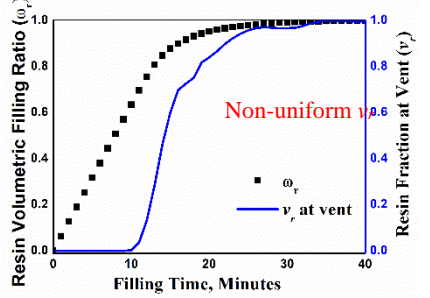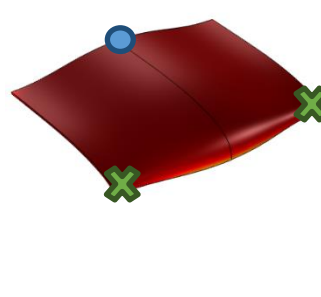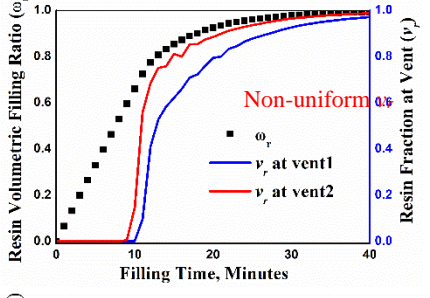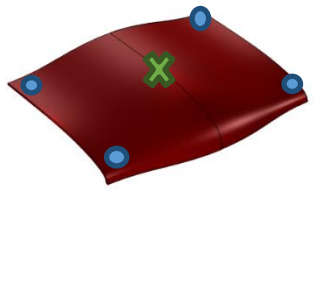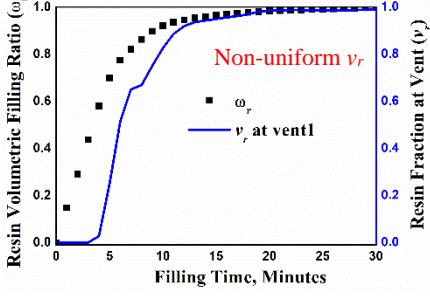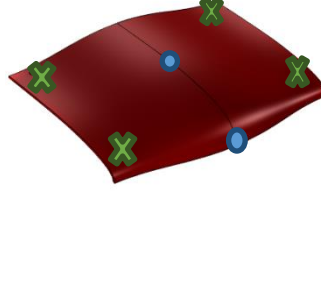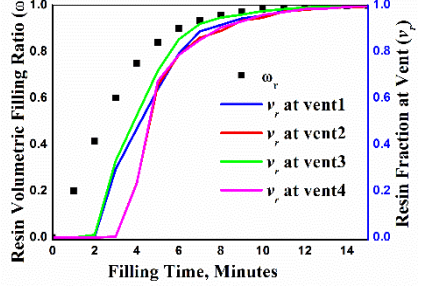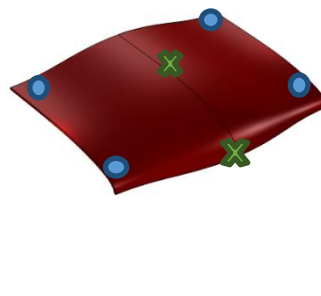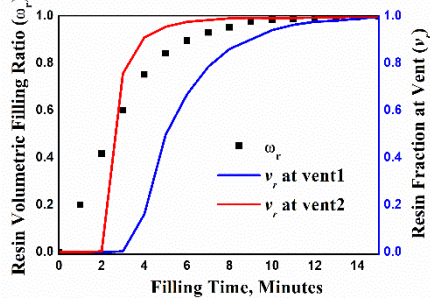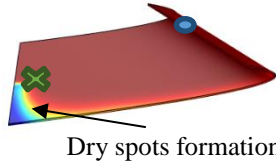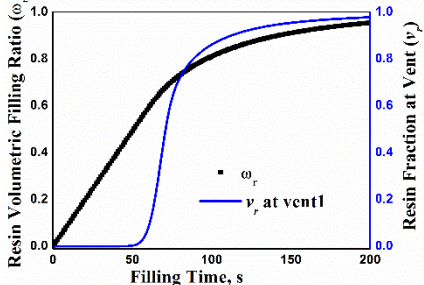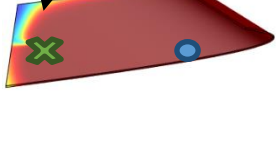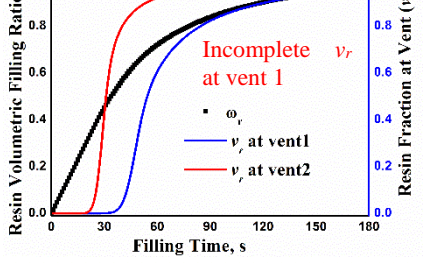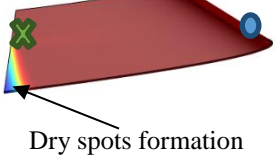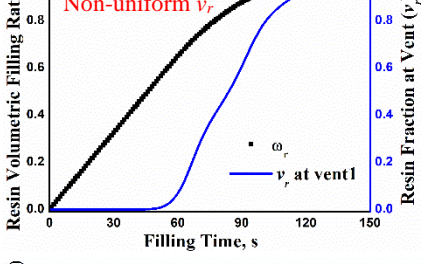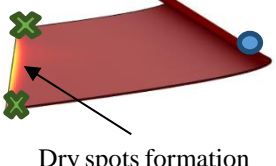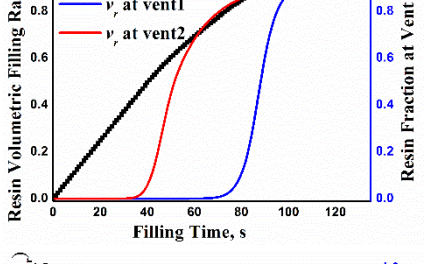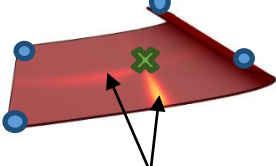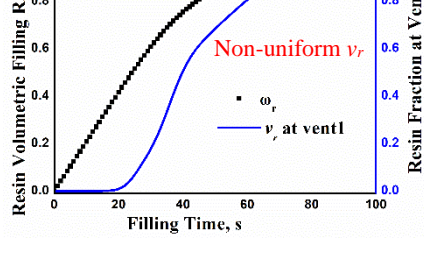
Trial 4

Two gates and one vent

Gate position: Two corners at the rear

Vent position: Front middle edge

- Filling time 40 minutes
- No dry spot formation

Trial 5

One gate and two air vents

Gate position: Rear middle edge

Vent position: Two corners at the front

- Filling time 40 minutes
- No dry spot formation

Trial 6

Four gates and one vent

Gate position: Four corners

Vent position: Centre of middle edge

- Filling time 30 minutes
- No dry spot formation

Trial 7

Two gates and four vents

Gate position: Centre and front of the middle edge

Vent position: Four corners

- Filling time 15 minutes
- No dry spot formation

Trial 8

Four gates and two vents

Gate position: Four corners

Vent position: Centre and front of the middle edge

- Filling time 15 minutes
- No dry spot formation

Table 4. 5 Mould Filling Simulation Trials for Aircraft Wing Flap Composite Part

Injection Strategy	Resin Flow Front 🔵 Gate Position ❌ Vent Position	Resin Filling Fraction
Trial 1 One gate and one vent *Gate position:* Rear middle edge *Vent position:* Front middle edge • Filling time 200 s • Dry spots formation	Dry spots formation	
Trial 2 One gate and two vents *Gate position:* Rear middle edge *Vent position:* Four corners • Filling time 180 s • Dry spots formation	Dry spots formation	Incomplete v_r at vent 1
Trial 3 Two gates and one vent *Gate position:* Two corners at the rear *Vent position:* Front middle edge • Filling time 150 s • Dry spots formation	Dry spots formation	Non-uniform v_r
Trial 4 Two gates and two vents *Gate position:* Two corners at the rear *Vent position:* Two corners in front • Filling time 135 s • Dry spots formation	Dry spots formation	
Trial 5 Four gates and one vent *Gate position:* Four corners *Vent position:* Centre of middle edge • Filling time 100 s • Dry spots formation	Dry spots formation	Non-uniform v_r

Trial 6		
Two gates and four vents *Gate position:* Centre and front of the middle edge *Vent position:* Four corners • Filling time 120 s • No dry spot formation		
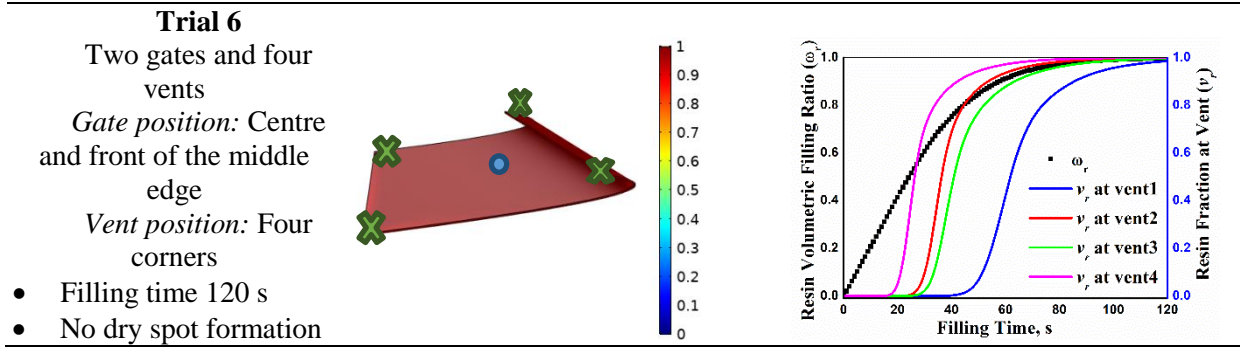
4.4.2 Gate and Vent Location Optimization using NSDE Algorithm

At first, the positions of gates and vents were optimized using the NSDE algorithm for a pre-fixed number of gates and vents. The two gates and four vents for the automotive bonnet and one gate and four vents for the aircraft wing flap were used as the prefixed numbers of gates and vents and their locations were optimized using the NSDE algorithm. A population size of 10 and 30 generations was used to perform the iterative simulation runs. The non-dominated solutions of rank 1 were extracted for different generations and the effect of generations on the Pareto front solutions was also studied.

Figure 4.8 shows the Pareto optimal solutions obtained between the dry spot content and the mould fill time for the automotive part. **Figure 4.8a** shows the rank 1 fronts for generations 1 to 30 with a difference of 5 generations. From **Figure 4.8a**, it was observed an improvement in the Pareto optimal solutions with the increase in generation number. Thus, it may be mentioned that the adopted NSDE algorithm effectively explores the search space for obtaining the optimal positions of gates and vents with the increase in generation number. It was also found that there are no significant differences in the Pareto optimal solutions obtained after the 30th generation. This signifies the efficacy of the NSDE algorithm for obtaining the converged optimal solutions for the framed objectives. **Figure 4.8b** shows the rank 1 and 2 fronts obtained at the 30th generation. The solutions in rank 1 were considered as Pareto optimal solutions. From **Figure 4.8b**, the obtained Pareto optimal solutions are in conflict in nature with the corresponding objective function. For a minimum mould filling time, dry spot content is more and vice versa. The Pareto optimal point corresponding to a minimum dry spot content of 0.93 % and a corresponding filling time of 35 minutes was used for the comparative assessment.

Figure 4.9 shows the Pareto optimal solutions obtained between the dry spot content and mould fill time for the aircraft part. There was an improvement in Pareto optimal solutions with the increase in generation number as shown in **Figure 4.9a**. It was also observed that there

are no significant differences in the Pareto optimal solutions after the 20th generation. **Figure 4.9b** shows the rank 1-5 fronts obtained at the 20th generation. The Pareto optimal point corresponding to dry spot content of 0.617 % and a corresponding filling time of 100 s was used for the comparative assessment.

(a)   (b)
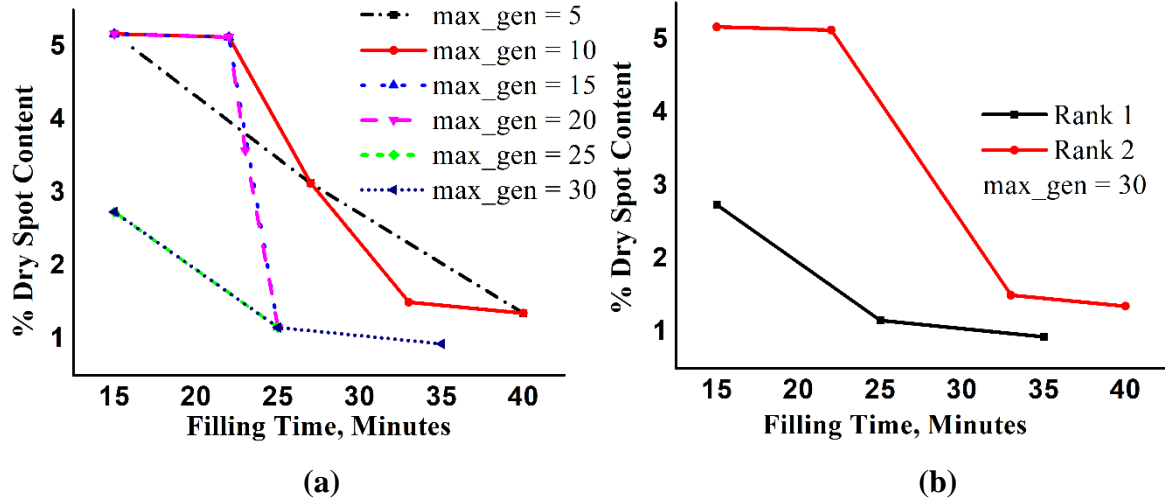
Figure 4. 8 Results of Bonnet Part for Two Gates and Four Vents Injection Strategy: (a) Pareto Fronts of Dry Spot Content vs. Fill Time for Different Generations, (b) Dry Spot Content vs. Fill Time Fronts at Maximum Generation 30.

(a)   (b)
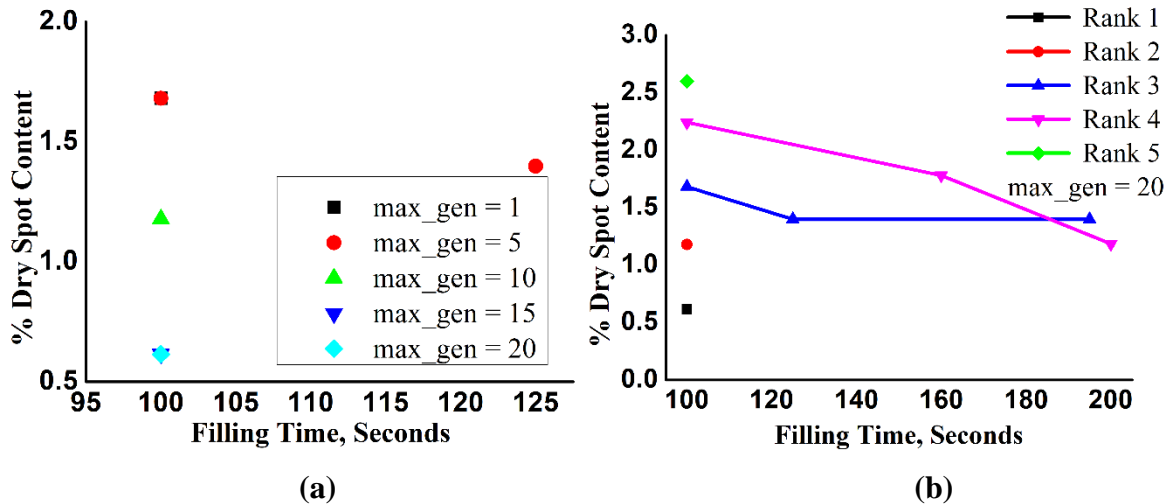
Figure 4. 9 Results of Wing Flap Part for One Gate and Four Vents Injection Strategy: (a) Pareto Fronts of Dry Spot Content vs. Fill Time for Different Generations, (b) Dry Spot Content vs. Fill Time Fronts at Maximum Generation 20.

4.4.3 Simultaneous Number and Position Optimization for Gates and Vents using MOSO Algorithm

The numbers and locations of gates and vents were simultaneously optimized using the MOSO algorithm. A population size of 16 and 5 generations was used to perform the iterative simulation runs. The Pareto fronts were obtained between the dry spot content, mould-filling

time and the total number of ports (gates + vents) for the automotive bonnet and aircraft wing flap composite parts.

Figure 4.10 shows the Pareto fronts obtained between % dry spot content, mould-filling time and total number of ports for the bonnet part. From Figure 4.10, the obtained Pareto optimal solutions are conflicting in nature with the corresponding objective functions as expected. Figure 4.10 shows that more dry spot content was observed for fewer ports and shorter filling times, and vice versa. Figure 4.10a shows the rank 1 fronts for generations 1 to 5. In Figure 4.10a, an improvement in the Pareto optimal solutions was observed with the increase in generation number. From the results, it was also observed that there were no significant differences in the Pareto optimal solutions after the 5th generation. This shows the fast exploration and efficient convergence of the MOSO algorithm for obtaining the optimal solutions within the five generations. Figure 4.10b depicts the rank 1 and rank 2 fronts between the dry spot content, filling time and the total number of ports at the 5th generation. From the results in Figure 4.10b, a distinction in solutions was observed between each rank and neighbourhood solution. This shows the efficacy of elitism selection using non-dominated sorting and crowding distance.

Table 4.6 shows the number and positions of gates and vents for substantial Pareto optimal points obtained at the 5th generation. From Table 4.6, it can be seen that the positions of gates and vents are quite apart from each other for all the Pareto points. This signifies the efficacy of the MOSO algorithm to search for an optimal number and position of gates and vents. From Table 4.6, it was also observed that the dry spot content was not observed at the edges due to the addition of a race-tracking effect at the boundary edges. The dry spot content obtained using the MOSO algorithm was within the acceptable range of 1%. Also, the dry spot content observed near the vent port is due to the immediate termination of the simulation when reaches the vent port. Furthermore, the dry spot content and filling time were computed when the resin reached the vents. It may be mentioned the final dry spot content obtained around the vents may become insignificant when the simulation time elapses. The Pareto optimal point corresponding to the total number of ports 5, filling time of 25 minutes and the corresponding % dry spot content of 0.259 % was used for the comparative assessment.

(a)   **(b)**
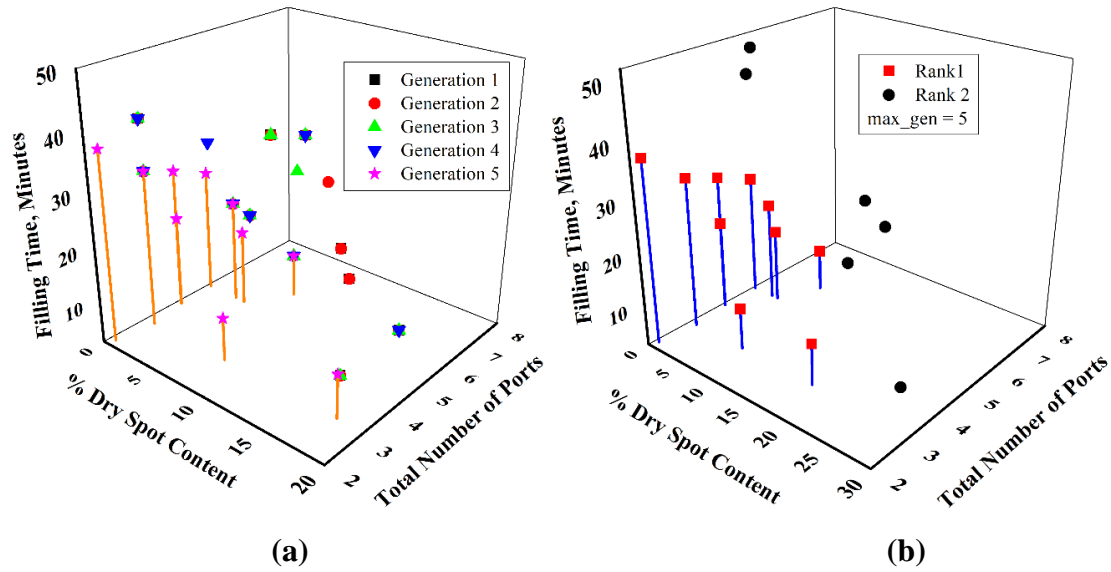
Figure 4. 10 Results of Automotive Bonnet Composite Part using MOSO Algorithm (a) Pareto Front of Dry Spot Content vs. Total Number of Ports vs. Mould-Filling Time for Different Generations, (b) Different Rank Fronts for Dry Spot Content vs. Total Number of Ports vs. Mould-Filling Time at Generation 5

Table 4. 6 Pareto Optimal Numbers and Positions of Gates and Vents at the Automotive Bonnet Composite Part (max_gen = 5)
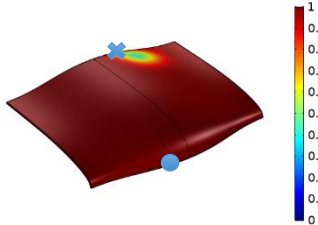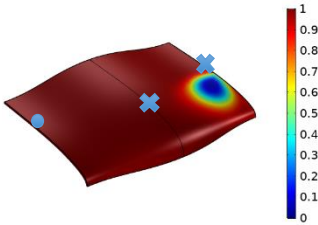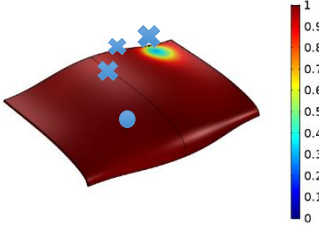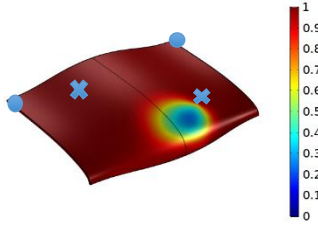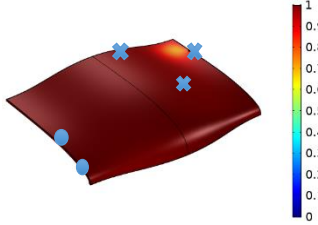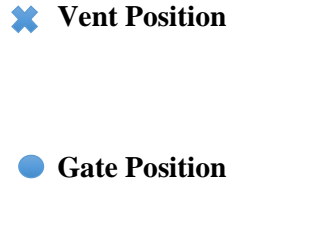
One Gate – One Vent	One Gate – Two Vents	One Gate – Three Vents
% Dry Spot Content = 0.526; Fill Time = 37 Minutes	% Dry Spot Content = 1.0015; Fill Time = 31 Minutes	% Dry Spot Content = 0.367; Fill Time = 28 Minutes

Two Gates – Two Vents	Two Gates – Three Vents	
		✖ **Vent Position** ● **Gate Position**
% Dry Spot Content = 0.421; Fill Time = 30 Minutes	% Dry Spot Content = 0.295; Fill Time = 25 Minutes	

Figure 4.11 shows the Pareto fronts obtained between % dry spot content, filling time and the total number of ports for the aircraft wing flap composite part. **Figure 4.11a** shows the rank 1 fronts for generations 1 - 5 and **Figure 4.11b** shows the rank 1, rank 2 and rank 3 fronts

at the 5th generation. From the results, it was found that the Pareto optimal front was obtained within the 5th generation and with the increase in generations, the rank 1 fronts were converging to the optimal set of solutions. Also, after the 5th generation, it was found no significant differences in the optimal solutions. This signifies the efficacy of obtaining the converged solutions using the MOSO algorithm.

Table 4.7 shows the numbers and positions of gates and vents for the Pareto front at the 5th generation. From **Table 4.7**, it can be seen that the positions of gates and vents have effectively occupied the geometry space using the MOSO algorithm and there is a significant distance between gates and vents for each Pareto optimal point. From **Table 4.7**, it was also observed that the dry spot content was not observed at the edges due to the addition of the race-tracking effect. Similar to the automotive part, a dry spot content was observed around the vents due to immediate simulation termination before complete resin venting. It may be mentioned the final dry spot content obtained around the vents may become insignificant when the simulation time elapses. The Pareto optimal point corresponding to the 2 gates and 2 vents injection strategy with 0.45% of dry spot content at 100 s of filling time was used for comparative assessment.
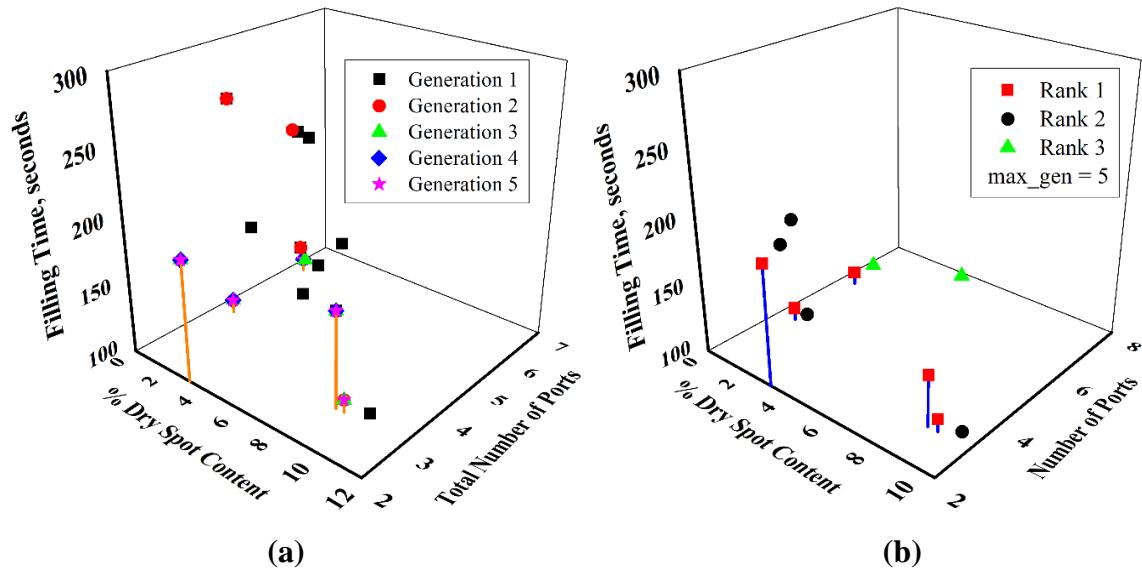
Figure 4. 11 Results of Aircraft Wing Flap Composite Part using MOSO Algorithm (a) Pareto Front of Dry Spot Content vs. Total Number of Ports vs. Mould-Filling Time for Different Generations, (b) Different Rank Fronts for Dry Spot Content vs. Total Number of Ports vs. Mould-Filling Time at Generation 5.

Table 4. 7 Pareto Optimal Numbers and Positions of Gates and Vents at the Aircraft Wing Flap Composite Part (max_gen = 5)

One Gate-One Vent

% Dry Spot Content = 3.29
Mould-Filling Time = 185 s

One Gate-Three Vents

% Dry Spot Content = 1.55
Mould Filling Time = 100 s

Three Gates-One Vent

% Dry Spot Content = 0.92
Mould Filling Time = 150 s

Two Gates-Two Vents

% Dry Spot Content = 0.45
Mould Filling Time = 100 s

Three Gates- Three Vents

% Dry spot content = 0.269
Mould-Filling Time = 100 s

✖   **Vent Position**

●   **Gate Position**
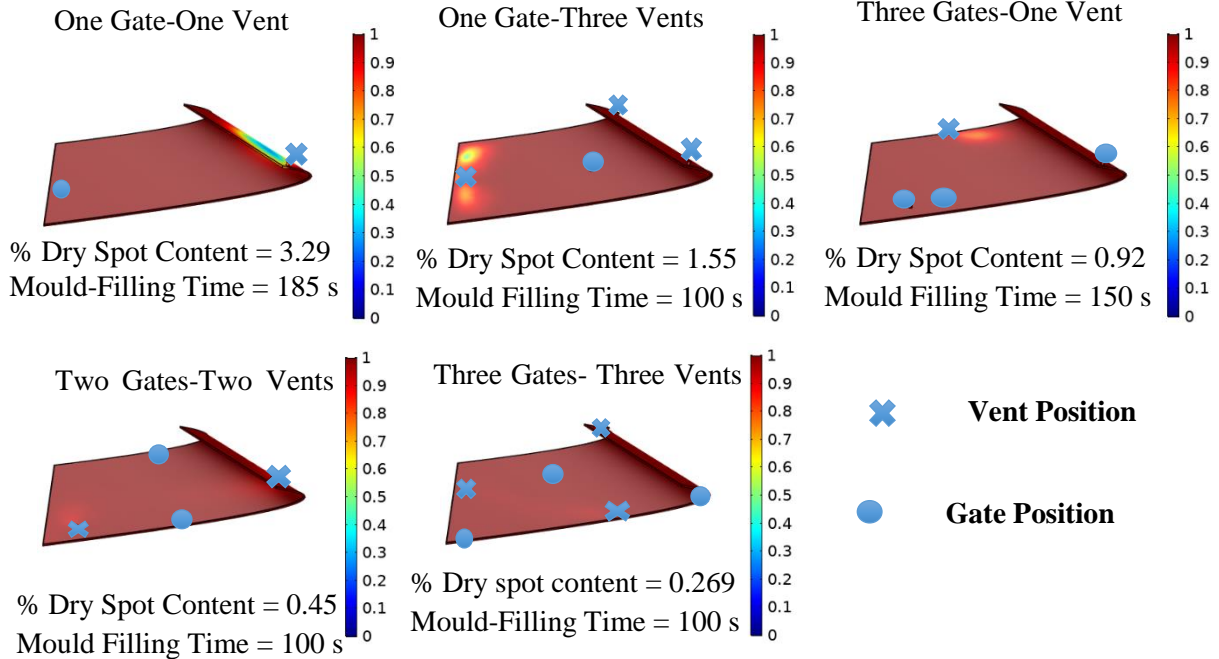
4.4.4 Comparative Assessment between Trial and Error Process, NSDE and MOSO Algorithms for Mould Fill Phase Optimization

The comparative assessments were done based on the optimal solutions obtained from the trial and error process simulation, NSDE and MOSO algorithms. The results were compared in terms of dry spot content, the total number of ports, resin fraction at vent (v_r), fill time, resin volumetric filling ratio (w_r), number of function evaluations (NFEs), and the total computational time.

Table 4.8 shows a comparison of the optimal solutions obtained for the automotive bonnet composite part. From the results, it was observed that the trial and error process predicted a lesser mould fill time of 15 minutes without dry spots when compared with the adopted two in-house optimization algorithms. However, the dry spot content obtained using the NSDE and MOSO algorithms was within the acceptable range of 1%. From the w_r and v_r versus time plots, there observed a uniform resin fill pattern for all three techniques. However, the resin flow fronts rising from two different gates moved at different speeds towards the vents in the case of NSDE and MOSO algorithms. This results in large differential filling times between the vents, which was evident from the w_r and v_r versus time plots. The trial and error process performed effectively for automotive bonnet composite parts in terms of dry spot content, mould fill time and uniform speed of resin flow front progression towards all vents

108

when compared to the optimization algorithms. The MOSO algorithm predicted a better optimal solution in terms of lesser dry spot content, lesser mould fill time and lesser total number of ports than the NSDE algorithm. Notably, the MOSO algorithm was capable of optimizing three objectives simultaneously whereas the NSDE algorithm was limited to optimizing two objectives simultaneously.

Table 4.9 shows a comparison of the optimal solutions for the aircraft wing flap composite part. From the results, it was observed that the NSDE algorithm predicted a dry spot content of 0.617% with a mould fill time of 100 seconds for one gate and four vents injection strategy. The MOSO algorithm predicted a dry spot content of 0.45% and mould filling time of 100 seconds for two gates and two vents injection strategy. From the w_r and v_r versus time plots, the resin flow front rising from the mould gate moved at different speeds towards the different vents in the case of NSDE and trial and error process compared to the MOSO algorithm. For the aircraft wing flap composite part, the MOSO algorithm outperformed the NSDE algorithm and trial and error process in terms of uniform speed of resin flow front progression towards the vents, lesser mould-filling time and lesser number of ports. This may be attributed due to the uniform flow front arising from two different gates instead of one gate and thus proved, the efficacy of the MOSO algorithm in the automatic selection of numbers as well as the positions of mould gates and vents.

From the results, it was found that the trial and error process performed effectively in terms of dry spot content, mould fill time and uniform resin flow front progression towards the vents when compared to the optimization algorithms for the automotive bonnet composite part. However, the trial and error process needed intuitions, experiences and manual efforts to obtain a single optimal solution. Also, the process required more iterations with trials in numbering and positioning ports, and there was no clue of obtaining the optimality. Thus, the trial and error process was always found to be a sub-optimized method. As mentioned, several trials and iterations were performed for both composite structures and the best solutions were reported as optimized injection strategies. Conversely, the MOO algorithms are automated and need less manual effort and problem-specific experience to obtain the number of Pareto optimal solutions. Furthermore, the MOO algorithms give several choices for the user in selecting the application-specific best design. Specifically, the MOSO algorithm was programmed to choose the number and locations of gates and vents automatically from the defined geometry space without manual interference.

Table 4.10 shows a comparison of the dry spot content, fill time, total number of ports, number of function evaluations (NFEs) and the total computational time between the trial and

error process, NSDE and MOSO algorithms. From **Table 4.10**, it can be seen that the NFEs and total computational time required for the MOSO algorithm were significantly lesser than the NSDE algorithm. This may be attributed to the fast exploration quality of the MOSO algorithm. The NFEs and computational time for the trial and error process were not considered. Because each simulation trial was performed separately and therefore, the computation of NFEs and computational time were not programmed. The MOSO algorithm outperformed both the composite structures in terms of dry spot content, the total number of ports, mould fill time and computational time when compared to the NSDE optimization algorithm. The automotive bonnet and aircraft wing flap composite parts mould filling optimizations were performed with an Intel i7-9700 CPU, 32 GB RAM computer and an Intel E3-1240 CPU, 32 GB RAM computer, respectively.

Table 4. 8 Comparative Assessment between Trial and Error Process Model Simulations, NSDE and MOSO Algorithms for Automotive Bonnet Composite Part
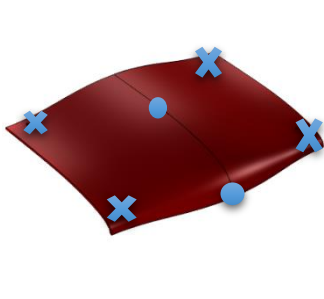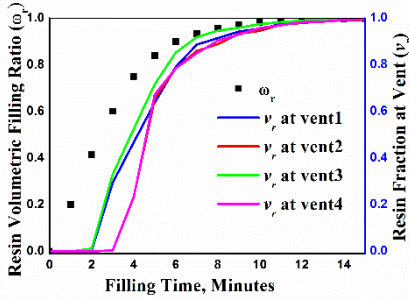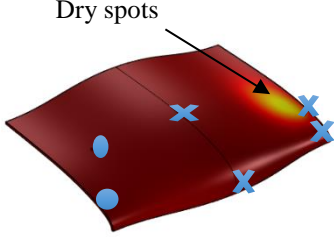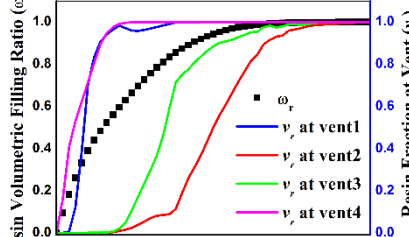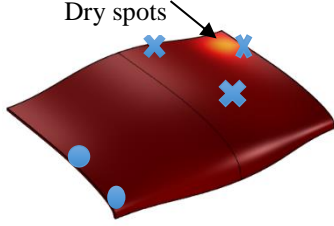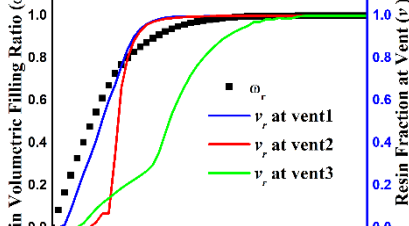
Trial and Error Process

Injection Strategy: Two gates and four vents

- Filling time 15 minutes

- No dry spot formation

NSDE Algorithm

Injection Strategy: two gates and four vents

- Filling time 35 minutes

- Dry spot content 0.93%

MOSO Algorithm

Injection Strategy: two gates and three vents

- Filling time 25 minutes

- Dry spot content 0.295%

Table 4. 9 Comparative Assessment between Trial and Error Process Model Simulations, NSDE and MOSO Algorithms for Aircraft Wing Flap Composite Part
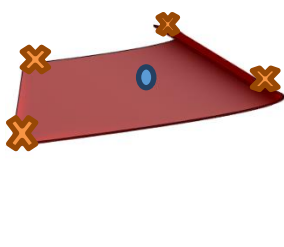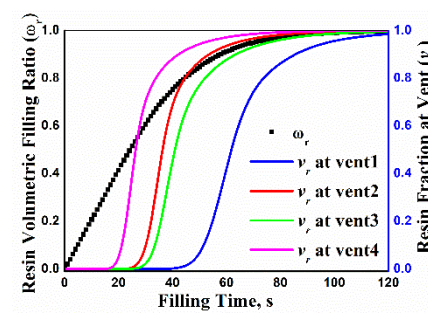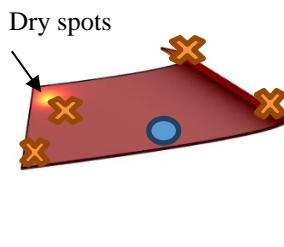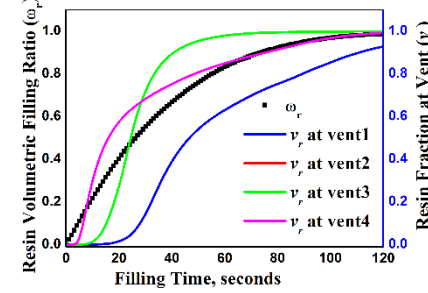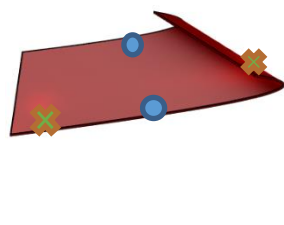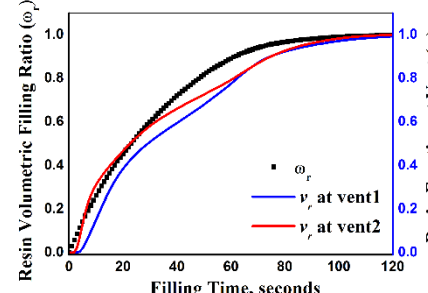
Trial and Error Process

Injection Strategy: One gate and four vents

- Filling time 120 s
- No dry spot formation

NSDE Algorithm

Injection Strategy: One gate and four vents

- Filling time 100 s
- Dry spot content 0.617%

MOSO Algorithm

Injection Strategy: Two gates and three vents

- Filling time 100 s
- Dry spot content 0.45%

Table 4. 10 Comparative Assessment between Trial and Error Process Model Simulations, NSDE and MOSO Algorithms

Technique	Filling time	% Dry spot content	Total number of ports	No. of function evaluations (NFEs)	Approximate computational time, hours
Automotive Bonnet Composite Part					
Trial and Error Process	15 minutes	-	6	-	-
NSDE Algorithm	35 minutes	0.93	6	300	50
MOSO Algorithm	25 minutes	0.295	5	96	9
Aircraft Wing Flap Composite Part					
Trial and Error Process	120 seconds	-	5	-	-
NSDE Algorithm	100 seconds	0.639	5	200	34
MOSO Algorithm	100 seconds	0.45	4	160	27

4.5 Summary

The objective of this work was to develop an in-house coded multi-objective optimization algorithm for the development of an optimized mould fill phase of the resin transfer moulded composite parts. A vinyl ester-glass fibre-reinforced automotive bonnet and an RTM6-carbon fibre-reinforced aircraft wing flap composite parts were used as the case studies. At first, the trial and error process simulations were performed to identify an optimized injection strategy at the mould-filling phase. Then, a novel in-house coded NSDE algorithm was implemented for simultaneous optimization of two objectives namely, dry spot content and mould-fill time by changing the locations of gates and vents at the fixed input numbers of gates and vents. Consecutively, a newly proposed MOSO algorithm was implemented for simultaneous optimization of three objectives namely, dry spot content, mould-fill time and total number of ports by changing both the numbers as well as locations of gates and vents.

From the automotive bonnet composite part results, the trial and error process predicted a lesser mould fill time of 15 minutes without dry spots when compared with the adopted two in-house optimization algorithms for the two gates and four vents injection strategy. However, the dry spot content obtained using the NSDE and MOSO algorithms was within the acceptable range of 1%. NSDE algorithm predicted a lesser dry spot content of 0.35% with a mould-filling time of 35 minutes for pre-fixed 2 gates and 4 vents injection strategy. In contrast, the MOSO algorithm predicted a dry spot content of 0.295% and a mould-filling time of 25 minutes for two gates and three vents injection strategy. From the aircraft wing flap composite part results, the NSDE algorithm predicted a lesser dry spot content of 0.617% with a mould fill time of 100 seconds for one gate and four vents injection strategy. On the other hand, the MOSO algorithm predicted a dry spot content of 0.45% and mould filling time of 100 seconds for two gates and two vents injection strategy. Notably, the inclusion of a race-tracking effect at the boundary edges led to the absence of dry spot content at the edges of both composite parts. Additionally, it is worth noting that the final dry spot content observed around the vents in both composite parts may become insignificant as the simulation progresses and the allotted time elapses.

From the comparative assessment, the trial and error process was observed to be effective to other algorithms in terms of dry spot content, mould fill time, and uniform resin flow front progression towards the vents when compared to the optimization algorithms for the automotive bonnet composite part. However, the trial and error process required more iterations with trials in numbering and positioning ports and manual efforts for obtaining a

single optimal solution. Conversely, the MOO algorithms were automated and needed less manual effort and problem-specific experience to obtain the number of Pareto optimal solutions. Significantly, the MOO algorithms deliver multiple optimality for the user in selecting the application-specific best design. Specifically, the MOSO algorithm was programmed to choose the number and locations of gates and vents automatically from the defined geometry space without manual interference. In comparison to the NSDE algorithm, the MOSO algorithm exhibited several advantages, including lower dry spot content, a reduced number of required ports, a more consistent speed of resin flow front progression towards the vents, significantly fewer evaluations (NFEs), and shorter computational time as given in Table 4.10. It is worth noting that the MOSO algorithm had the capability to simultaneously optimize three objectives while the NSDE algorithm was limited to concurrently optimizing only two objectives.

Chapter 5

Development of an Optimized RTM Curing Process using Multi-Objective Optimization Algorithms

5.1 Introduction

In various industries such as aerospace, navigation and automotive, the growing demand for enhanced performance and reduced weight has encouraged the widespread utilization of fibre-reinforced polymer composites. This preference is attributed to their high specific stiffness and strength characteristics. Notably, intricate composite components especially those used in automotive and aircraft structures are predominantly fabricated through Resin Transfer Moulding (RTM) processes [143]. Among the pivotal stages that influence the ultimate quality of these composite parts, the curing process holds paramount significance.

During the composite curing process, a predefined cure cycle from the neat resin cure profile is imposed onto the resin-saturated preforms [15]. Manufacturers typically recommend a neat resin cure temperature profile to provide guidance for successful composite part curing. This prescribed profile may not universally suit all component types specifically for thick-sectioned composite parts. In the case of thick-sectioned composite parts, effectively transferring heat from the surface to the mid-thickness of the parts presents a challenge due to the low thermal conductivity and substantial thickness of the preforms. Utilizing the manufacturer-recommended profile under these conditions might cause significant thermal gradients within thick composite parts leading to problems like resin degradation, uneven curing and residual stresses [16].

In industrial practice, the complexities arising from temperature gradients in thick composite parts often lead to the adoption of conservative cure cycles or trial-and-error approaches. Unfortunately, this cautious approach inevitably extends processing times and increases manufacturing costs. Hence, there is a need to establish an optimal curing temperature profile capable of minimizing thermal gradients and addressing other defects that may arise during the curing process. The successful optimization of such a thermal-cure profile requires a comprehensive understanding of the physio-chemical transformations occurring within composite parts during the curing process [52].

This chapter aims to address these challenges by introducing a multi-objective optimization algorithm specifically designed to improve the RTM cure temperature profile for composite parts. This algorithm is seamlessly integrated with a finite element simulation platform, enabling in-depth exploration of the intricate interplay between resin cure kinetics and heat transfer phenomena. The main objective of this chapter is to refine the RTM cure process for the production of industrially viable components such as automotive bonnet and aircraft wing flap composite parts. This chapter provides insights into enhancing the composite curing process and its optimization.

5.1.1 Bibliometric Analysis

A bibliometric analysis was conducted on August 24, 2023, utilizing the Web of Science core database. A collection of 966 articles was obtained through the primary search term 'Composite Curing Optimization' within the topics section. Bibliometric network visualization was carried out using the VOSviewer software[49], as depicted in **Figure 5.1**. The analysis focused on bibliometric coupling occurrences of author keywords that appeared more than 5 times. Out of a pool of 2692 keywords, 120 keywords met this threshold and were consequently selected for further examination. From these 120 keywords, the cumulative strength of co-occurrence links with other keywords was computed. This computation guided the selection of keywords with the highest total link strength. Among these keywords, 'optimization', 'mechanical properties', 'curing', and others emerged as prominent author keywords.

Figure 5. 1 Schematic Representation of the Bibliographic Networking Diagram Obtained from the Web of Science Core Database through the Search Conducted on August 24, 2023.

5.1.2 Literature Review

The composite processing techniques are extensively developed to manufacture large and complex thick-sectioned composite parts [143]. Curing is the crucial stage for the production of composite parts, despite the use of any manufacturing techniques. Extensive investigations on the curing phase are needed to develop the optimized manufacturing process for industrial composite components[17], [171]. During curing, the resin undergoes the formation of the 3D networked structure with exothermal heat with a state change from liquid to gel, then to rigid solid [15]. The exothermal heat generated during resin curing can lead to temperature overshoots and thus, affect the quality of the manufactured composite part [16]. Hence, the optimal design of the curing phase requires a well-defined mould heating temperature profile to reduce thermal overshoots and gradients [52].

Several experimental works were reported monitoring the resin curing process using temperature and viscosity sensors [172], [173]. However, the development of an optimized composite production process using experimental trials with intricately embedded sensors was proven to be sub-optimized, laborious, costly, and time-consuming. Alternatively, cure process simulations and optimizations were proven to be an inexpensive and effective approach that results in optimal solutions with iterations [20]. From the literature, the commonly used finite

116

element and control volume finite element method-based simulators were COMSOL Multi-physics, ABAQUS and ANSYS for performing cure process simulations [27], [29], [101]. Through the use of these platforms, researchers have skillfully analyzed intricate curing processes. This analysis has provided valuable insights into how changing temperatures influence the fundamental dynamics of curing.

Within the realm of cure process optimization, it was found that the optimizations of the thermal-cure profile were addressed using different single and multi-objective optimization techniques. The extensively used optimization techniques were the simplex method, genetic algorithm (GA), ant swarm strategy, non-dominated sorting genetic algorithm-II (NSGA-II), and multi-objective optimization genetic algorithm (MOOGA) toolbox[155]–[159]. Objective functions based on cure process time, temperature overshoot, residual stresses, setup cost, temperature gradient, and so on were considered for the cure process optimization [160], [161].

Shevtsov et al. [174] developed a curing model for a helicopter rotor blade in the COMSOL multi-physics simulator and optimized the thermal profile for both the solidification and liquefaction stages using a built-in optimization toolbox. However, the built-in optimization toolbox is limited to a few traditional optimization techniques and the obtained results were dependent on the initial guesses which reduced the efficacy of obtained results. Also, the toolbox was limited to the use of advanced hybrid multi-objective optimization techniques. Jahromi et al. [58] designed the artificial neural network (ANN) toolbox to minimize the temperature differences between two selected points. The sequential quadratic programming (SQP) deterministic optimization technique was used to achieve the uniform temperature and degree of cure along the thickness of the fibre-reinforced composite part.

Struzziero and Skordos [35] developed the multi-objective optimization strategy by combining the finite element simulation package with the MOOGA for cure process optimization for both thick and ultra-thick composites. They considered three different structures for two different thicknesses and analyzed the results obtained from the standard two-dwell and multi-dwell thermal profiles. From the results, they found with an increase in the thickness of composites the multi-dwell thermal profile performed better than the standard two-dwell thermal profile. Tifkitsis et al. [36] developed a stochastic multi-objective optimization algorithm by integrating GA with the coupled surrogate model and Monte Carlo simulator for optimizing the thermal-cure profile of thick composite parts. They compared the results obtained from the one-dwell and two-dwell mould heating profiles between deterministic and stochastic multi-objective optimization algorithms. Gao et al. [175] developed a multi-objective optimization strategy by combining the Latin hypercube sampling

method with the neural network model and NSGA-II for optimizing the thermal-cure profile of ultra-thick composite parts. The cure time, maximum cure gradient, and maximum thermal gradient were simultaneously optimized and the results were compared with the manufacturer-recommended cure cycle (MRCC). Yuan et al. [176] developed a multi-objective strategy by combining the multi-physics finite element process model with the radial basis function (RBF) surrogate model and NSGA-II for cure process optimization of thick composites. They reported the efficacy of the developed optimization strategy over the MRCC by comparing the obtained thermal-cure profiles.

From the in-depth literature review, it was found that researchers have handled cure phase optimization mainly using the variants of GA. However, from the comparative studies, the differential evolution (DE) algorithm performed significantly better than GA for multi-objective optimization problems [177]. According to the knowledge of the authors, there were no straight reports found in the literature that directly deal with the development of the non-dominated sorting differential evolution (NSDE) algorithm for the simultaneous optimization of the thermal gradient and cure time of the composite processing technique. With problem specific, there are no published reports on the development of robust multi-objective optimization techniques with varied composite part thickness and resin-fibre properties for the automotive bonnet and aircraft wing flap composite parts. Precisely, there were no published works found in the literature that address the comparative analysis between trial and error process simulations and multi-objective optimization algorithms for the development of vinyl ester-glass fibre reinforced automotive bonnet and RTM6-carbon fibre reinforced aircraft wing flap composite parts.

This work proposes the in-house coded multi-objective optimization algorithm for the development of the optimized cure process for vinyl ester-glass fibre-reinforced automotive bonnet and RTM6-carbon fibre-reinforced aircraft wing flap composite parts. Initially, the two-dwell and one-dwell thermal profile was designed for the 12 mm thick automotive bonnet and 5 mm thick aircraft wing flap composite parts, respectively. Then, the newly proposed NSDE algorithm was developed to optimize the thermal-cure process through the minimization of part thickness thermal gradients and cure time for the studied composite structures. Subsequently, to evaluate the efficacy of the developed NSDE algorithm, the NSGA-II algorithm was in-house coded for the simultaneous minimization of thermal gradient and cure time for the studied composite structures. Then, the trial and error process model simulations were performed by manually changing the mould heating rates and dwell times for both the selected composite parts. Finally, comparisons between the optimized thermal-cure cycles obtained

from the NSDE and NSGA-II optimization algorithms and the trial and error process were reported to ascertain the efficacy of the developed NSDE algorithm.

5.2 Thermo-Chemical Process Model

In industrial practices, moulds are kept at elevated temperatures to enhance the cure reaction and to reduce the cure process time. In general, various temperature ramps and dwells are practised to obtain the final isothermal temperatures. Hence, the resin curing analysis is analyzed with the multi-dwell mould heating profile. The transient energy balance for the cure analysis that includes conduction and resin cure is given in **Equation (5.1)** in the Cartesian coordinate system,

$$\rho_c C_{Pc} \frac{\partial T}{\partial t} = \frac{\partial}{\partial x}\left(k_x \frac{\partial T}{\partial x}\right) + \frac{\partial}{\partial y}\left(k_y \frac{\partial T}{\partial y}\right) + \frac{\partial}{\partial z}\left(k_z \frac{\partial T}{\partial z}\right) - \frac{\partial Q}{\partial t} \qquad (5.1)$$

ρ, C_P and k represents the density, heat capacity and thermal conductivity of respective materials. The thermal conductivity of the material is represented by k_i (where $i = x, y, z$) in their respective orthogonal directions.

The thermal conductivity, specific heat and density of the composite part are computed using the rule of mixture as given in **Equations (5.2), (5.3)** and **(5.4)**, respectively [178].

$$k_c = \frac{k_r k_f}{k_r \emptyset + k_f (1-\emptyset)} \qquad (5.2)$$

$$C_{Pc} = C_{Pr}\emptyset + C_{Pf}(1-\emptyset) \qquad (5.3)$$

$$\rho_c = \rho_r \emptyset + \rho_f (1-\emptyset) \qquad (5.4)$$

Subscript 'r', 'f', and 'c' denote the resin, fibre and composite material physical properties, respectively. Here, $\emptyset$ denotes the porosity of the fibre mat. An experimentally measured thermal conductivity of 2.7 W m^{-1}K^{-1} was used for the woven roving carbon fibre mat as published by Villiere et al.[165]

The internal heat consumption sink term $\left(\frac{\partial Q}{\partial t}\right)$ corresponds to the endothermic nature of the resin-curing reaction. When the resin flow within the composite part is not taken into account, the sink term $\left(\frac{\partial Q}{\partial t}\right)$ can be directly linked to the cure rate $\left(\frac{\partial \alpha}{\partial t}\right)$ through the following **Equation (5.5)** [67].

$$\frac{\partial Q}{\partial t} = \rho_r \emptyset \Delta H \frac{\partial \alpha}{\partial t} \qquad (5.5)$$

Where, H_r denotes the heat of reaction. The resin cure rate model $\frac{\partial \alpha}{\partial t}$ is defined as a function of temperature T and degree of cure α as follows,

$$\frac{d\alpha}{dt} = Ae^{\frac{-E}{RT}}\alpha^m(1 - \alpha)^n \qquad\qquad (5.6)$$

The boundary conditions allied to address the **Equations (5.1-5.6)** are as follows,

Initial condition at time $t = 0$: $\quad T = T_0$; $\alpha = 0$ and $\frac{d\alpha}{dt} = 0$

At the mould wall: $\quad T = T_{mould}$

T_0 represents the initial temperature and T_{mould} represents the mould temperature.

A is the frequency factor, E is the activation energy, R is the ideal gas constant, T is the temperature and m and n represent the order of the reaction.

5.3 Materials and Methods

5.3.1 Materials

Mono-component RTM6 epoxy resin supplied by Hexcel company and vinyl ester Derakane 8084 epoxy resin supplied by Ashland company were used as the resin matrices in this study. These resins have been specifically designed for advanced composite parts and for use in advanced liquid composite moulding processes. The vinyl ester resin was cured by applying methyl ethyl ketone peroxide as the catalyst along with cobalt octoate as the accelerator both of which were provided by Hexcel company. A twill-weave carbon fibre mat having 400 g/m^2 areal density and 46% porosity, and a twill-weave glass fibre mat having 610 g/m^2 areal density and 51% porosity, were used as the reinforcement mats for this study. The reinforcement mats used in this study were supplied by Sree Industrial Composite Products, Hyderabad, India. The cure kinetics for vinyl ester and RTM 6 resins is reported in **Chapter 2**. The material parameters used for curing optimizations are listed in **Table 4.3** of **Chapter 4**.

5.3.2 RTM Process Composite Parts

In this work, the RTM process was developed for the vinyl ester-glass fibre-reinforced automotive bonnet and the RTM6-carbon fibre-reinforced aircraft wing flap composite parts as shown in **Figures 4.2 and 4.3**, respectively. The process models that are given in **Equations (5.1 to 5.6)** with their associated initial and boundary conditions were used to perform the curing simulations. The initial temperature (T_0) of mould heating was selected based on the resin injection temperature during mould-filling experiments. The vinyl ester and RTM6 resin were injected at 298 K and 393 K, respectively during mould-filling experiments. The choice of resin injection temperature was selected using recommended process parameters from the RTM6 [91] and vinyl ester [166] resins supplier technical datasheet.

The COMSOL multi-physics simulator was employed to simulate the composite parts curing process. The non-isothermal energy balance during the curing stage was computed using the COMSOL heat transfer module and the cure kinetics of the composite panel was studied by manually defining the cure rate model in the domain ordinary differential equations (ODEs) and differential algebraic equations (DAEs) module. The heat transfer in solids and domain ODEs and DAEs physics were coupled to address the cure reaction dependency on temperature. The relevant initial and boundary conditions corresponding to energy balance and cure kinetics were solved to analyse the thermal-cure profile of composites. The process flow for performing the curing simulation of the composite panel in the COMSOL multi-physics simulator is depicted in **Figure 5.2**.

Define cure kinetic parameters of resin (m, n, A, E), initial temperature (T_0), heat of reaction (H_r) and mould-heating parameters

Import or create the geometry of composite structure

Add materials (resin & fibre), add respective material properties (Table 4.3)

Add Physics
1. **Heat Transfer in Solids**: Non-isothermal energy balance during curing stage
2. **Domain ODEs and DAEs**: Cure rate model
3. Incorporate the relevant initial and boundary conditions in the selected physics

Create mesh and Define time dependent study

Post processing of results: Degree of cure profile, T_{max} and T_{min}

Figure 5. 2 COMSOL Model Implementation for Composite Panel Cure Process Simulation

5.3.3 Trial and Error Isothermal Cure Process Simulations

Once the mould filling is completed, the mould is heated to elevated cure temperatures using electrical cartridge heaters with higher ramp rates of more than 20°C/min. The differential cure occurring between mould filling temperature and cure temperatures was assumed to be negligible due to the use of higher ramp rates (smaller dynamic heating time compared to isothermal cure time) and the temperature rises from lower to higher values. Hence, dynamic heating time is not considered in the total cure cycle time. Due to the zero flow velocity and assumption of no air voids, neat resin cure data can be compared with

composite panel cure data for the applied mould temperatures. In this work, temperatures ranging from 393 K to 513 K were selected as mould temperatures to perform isothermal curing simulations for the aircraft wing flap composite part. From the curing simulations, the time-temperature-degree of cure window for the composite panel was obtained. Then, cure differences between neat resin and composite panel were obtained as a function of time and temperature.

5.3.4 Trial and Error Non-Isothermal Cure Process Simulations

The objective of the trial-and-error cure process simulation is to search for optimum values of mould heating parameters to attain the minimum thermal gradient, cure differences and cure time with negligible temperature overshoot. Usually, the components having a thickness greater than 10 mm and 50 mm were considered thick and ultra-thick components, respectively. From past studies, it was found that the multi-dwell heating profile is desirable for thick and ultra-thick components to reduce the temperature overshoot and thermal gradient within the composite part. However, with an increase in the number of dwells, the associated independent variables are increased and the thermal profile becomes more dependent on the mould heating parameters. In this work, an automotive bonnet part with 12 mm thickness was selected and a two-dwell temperature profile was used to cure this thick sectioned composite part. In contrast, a thin-sectioned aircraft wing flap composite structure with 5 mm thickness was also selected and a one-dwell temperature profile was used to cure the composite part. **Figures 5.3** and **5.4** show the two-dwell and one-dwell mould heating temperature profiles used for the cure process simulations of the automotive bonnet and aircraft wing flap composite parts, respectively.

The trial and error non-isothermal cure process simulations were performed by manually changing the values of mould heating parameters, 1st ramp rate a, 2nd ramp rate b, 1st dwell time t_1, 1st hold time t_2 and 2nd dwell time t_3. Numerous simulation trials were executed by varying the values of mould heating parameters. Salient simulation trials are tabulated in **Tables 5.1** and **5.2** for the automotive bonnet and aircraft wing flap composite parts, respectively.
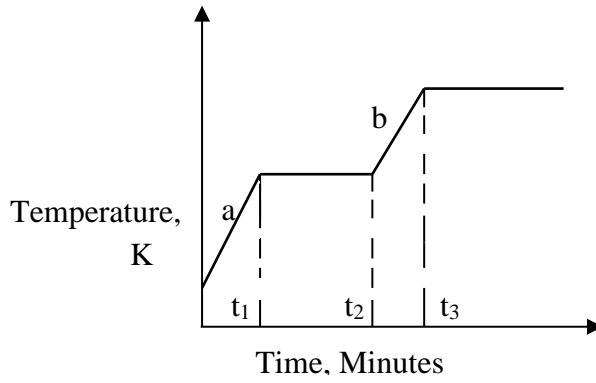
Figure 5. 3 Two-Dwell Mould Heating Profile for Automotive Bonnet Composite Part
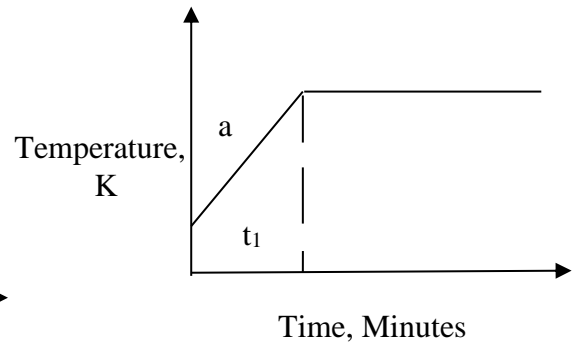
Figure 5. 4 One-Dwell Mould Heating Profile for Aircraft Wing Flap Composite Part

Table 5. 1 Cure Process Simulation Trials for Automotive Bonnet Composite Part

Trial Number	1st Ramp Rate a, K/min	1st Dwell Time t_1, Minutes	1st Hold Time t_2, Minutes	2nd Ramp Rate b, K/min	2nd Dwell Time t_3, Minutes
1	3	10	40	1	50
2	4	10	40	1	50
3	2	10	30	1	35
4	3	10	30	1	35
5	2	20	50	1	60
6	2	20	40	1	50

Table 5. 2 Cure Process Simulation Trials for Aircraft Wing Flap Composite Part

Trial Number	Ramp Rate a, K/min	Dwell Time t_1, Minutes
1	1	10
2	1	20
3	5	10
4	5	20

5.3.5 Curing Optimization using NSDE Algorithm

The main objective of this optimization was to minimize the thermal gradient and cure time (t_{cure}) during the composite curing process. The thermal gradient was computed as the

difference between the mould surface temperature (T_{max}) and the composite panel mid-thickness temperature (T_{min}). The curing optimization was performed to obtain the optimum mould heating profile with negligible temperature overshoot during the curing phase of the studied composite parts. The two-dwell mould heating profile was considered for the curing phase optimization of the bonnet composite part. However, the two-dwell mould heating profile converges to one dwell when there are no appreciable temperature differences between the adjacent dwells. The framed objectives were optimized simultaneously by optimizing the four parameters: (i) ramp rate a, (ii) 1st dwell time t_1, (iii) 1st hold time t_2 and (iv) 2nd dwell time t_3. Also, the average degree of cure (α_{avg}) at the end of the curing process was constrained to 0.9 to ensure the composite part cure completion. The mathematical formulation for the curing phase optimization of the automotive bonnet composite part is given in **Equation (5.7)**.

$$\text{Minimization} \qquad f_1 = T_{max} - T_{min} \ at \ t_{cure}, f_2 = t_{cure} \qquad (5.7)$$

$$subject \ to,$$

$$\alpha_{avg} \geq 0.90$$

$$1 \leq a \leq 4$$

$$5 \leq t_1 \leq 10$$

$$t_1 \leq t_2 \leq 40$$

$$t_2 \leq t_3 \leq 60$$

$$b = 1$$

Minimization of the thermal gradient and cure time were the objective functions considered for the curing of the wing flap composite part using a one-dwell temperature profile. The mathematical formulation of the problem is given in **Equation (5.8)**.

$$\text{Minimization} \qquad f_1 = T_{max} - T_{min} \ at \ t_{cure}, f_2 = t_{cure} \qquad (5.8)$$

$$subject \ to,$$

$$\alpha_{avg} \geq 0.90$$

$$1 \leq a \leq 5$$

$$5 \leq t_1 \leq 20$$

A non-dominated sorting differential evolution (NSDE) algorithm coupled with finite element simulation was adopted to solve the curing multi-objective optimization problem. The generation of input parameters and elitism of dominated solutions based on the NSDE optimization algorithm was programmed in MATLAB. These generated input parameters were utilized to perform the cure process model simulations in COMSOL software. The integration of the optimization algorithm and cure process simulation was programmed in MATLAB using

COMSOL Live-Link for MATLAB. This Live-Link interface enables the COMSOL simulation to be loaded into the MATLAB directory using the 'mphload' command. The implementation guidelines for the Live-Link interface were referenced from the user guidelines for Live-Link for MATLAB[168]. The following steps were incorporated for the implementation of the NSDE algorithm for simultaneous optimization of thermal gradient and cure time.

Step 1: In this step, the process was initiated by defining parameters such as crossover probability (C_p), mutation factor (F), population size (N_p), and the maximum number of generations (max_gen). Initially, dwell times and ramp rates were randomly generated within the specified limits. These randomly generated input parameter values were imported to COMSOL using the 'model.param.set' command and the cure process simulation was programmed using the 'model.sol ('sol1').runAll' command function. The cure process model simulations were performed using the new input parameter values for ramp rates and dwell times at the cure time of *t*. Upon completion of the cure process simulation, the results of T_{max}, T_{min} and α_{avg} at cure time '*t*' were extracted programmatically in MATLAB using the 'model. result' command function. The α_{avg} value was computed at cure time '*t*' and then, the objective functions were computed for the obtained α_{avg} value of 0.9 and above. For α_{avg} value lesser than 0.9, the cure process simulations were performed for the extended time loops until a value of 0.9 and above. From the resin cure cycles, the initial cure time was defined as 30 minutes and a time step of 5 minutes was used for each subsequent time loop. The generation of input parameters and subsequent computation of thermal gradient and cure time from the cure process simulation was performed for a population size of N_p. The complete dataset generated for a population size of N_p was designated as the parent population (P_g).

Step 2: This step involved mutation and crossover processes. Three random vectors were selected from the parent population (P_g) to generate a mutated population (M_g). The mutated vectors were obtained by applying mutation to the dwell time and ramp rate values as given in **Equation (5.9)**. Similar to Step 1, thermal gradient and cure time values were computed for the mutated population.

$$M_{g,i} = P_{g,r1} + F(P_{g,r2} - P_{g,r3}) \qquad (5.9)$$

Here $r1, r2$, and $r3$ indicate three distinct random numbers. Subsequently, the binomial crossover was performed utilizing the mutated and parent populations to create a child population (Q_g) as given in **Equation (5.10)**. The mutation factor (F) and crossover probability (C_p) were set to 0.8 and 0.25, respectively. The mathematical implementation of the

Differential Evolution (DE) algorithm was referenced from the research work published by Karaboga and Okdem[169].

$$Q_g = \begin{cases} P_g, & if\ rand > \text{Cp} \\ M_g, & if\ rand \leq Cp \end{cases} \tag{5.10}$$

Step 3: In this step, a selection process takes place to determine which solutions from the current generation will be part of the next generation or undergo further evolutionary steps. A dominance check was conducted between the parent population (P_g) and the child population (Q_g). If a vector in the child population dominates a vector in the parent population, the child vector is included in the new population (P_{g+1}) for the next generation. Conversely, if a parent vector dominates a child vector, the parent vector is retained in the new population (P_{g+1}). After calculating the dominance of each solution in the population, the rankings are assigned to the new population (P_{g+1}) based on the dominance check. Typically, solutions that are not dominated by any other solution (Pareto front solutions) are given the highest rank (rank 1). Solutions that are dominated by rank 1 solutions but dominate other solutions are assigned the next rank (rank 2), and so forth. Additionally, the crowding distance measure is also computed to differentiate between solutions with the same rank. The crowding distance measures how close a solution is to its neighbours in the objective space. Solutions with higher crowding distances are preferred because they provide better coverage of the Pareto front. The dominance check of the NSDE algorithm was performed using the non-dominated sorting approach based on the NSGA-II algorithm[170].

Steps 2 and 3 were repeated for the defined maximum number of generations to iteratively improve the solution. The outcome was a Pareto front depicting the trade-offs between thermal gradient and cure time. The vector in rank 1 represents the Pareto optimal solution. **Figure 5.5** illustrates the flow diagram for the implementation of an in-house coded NSDE algorithm to find the optimal thermal-cure profiles. The population size was set at 10 and the maximum number of generations was set to 20.
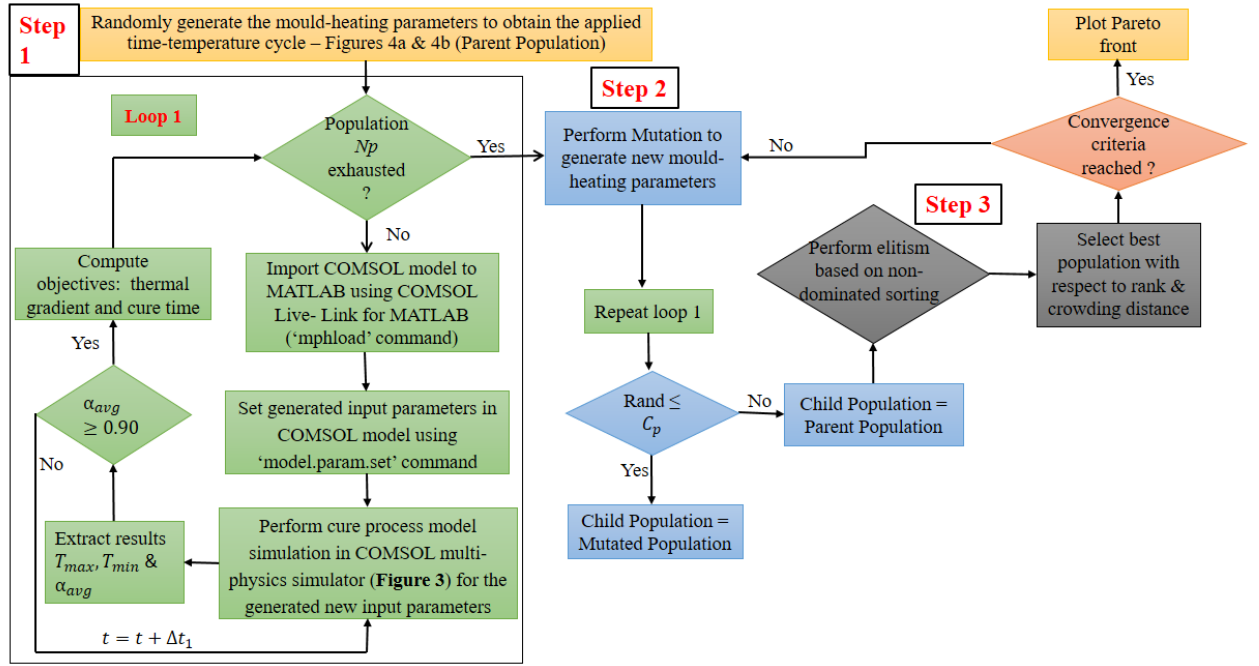
Figure 5. 5 In-House Coded NSDE Algorithm to Optimize the Composite Parts Thermal-Cure Profile

5.3.4 Curing Optimization using NSGA-II Algorithm

The NSGA-II algorithm was also employed to assess the effectiveness of the proposed NSDE algorithm. The problem formulation presented in **Equations (5.7 & 5.8)** was addressed to simultaneously minimize the thermal gradient and cure time for the selected composite parts. The integration of the NSGA-II algorithm with the COMSOL Multi-physics simulator followed a similar procedure to that of the NSDE algorithm. The implementation process was also similar to the NSDE algorithm except for the generation of mutated and crossover populations. Mutation and crossover were performed using a real-coded genetic algorithm with a two-point crossover and a mutation rate of 0.01[170].

5.4 Results and Discussion

5.4.1 Isothermal Curing Simulations

The extent of the cure reaction within the composite panel was simulated using the experimental RTM6 resin time-temperature cure cycles. To analyse the through-thickness cure variations, the degrees of cure at the panel surface and degrees of cure at the mid-thickness of the panel were computed and compared. The averaged degree of cure of the composite part was also computed and compared with the surface and mid-thickness degrees of cure. From the simulated results, it was found there were negligible cure variations within the part through-

thickness due to the smaller thickness of the composite part. The simulated surface, mid-thickness and averaged composite panel degrees of cure obtained for 180°C, 200°C, 220°C, and 240°C temperatures are shown in **Figure 5.6**. From **Figure 5.6**, it can be seen that the cure variations compared were found to be negligible and thus, surface, mid-thickness and averaged composite panel degrees of cure overlaps in the cure-temporal plots at all studied temperatures. Therefore for further analysis of simulated time-temperature cure cycles, average degrees of cure within the composite panel are considered.
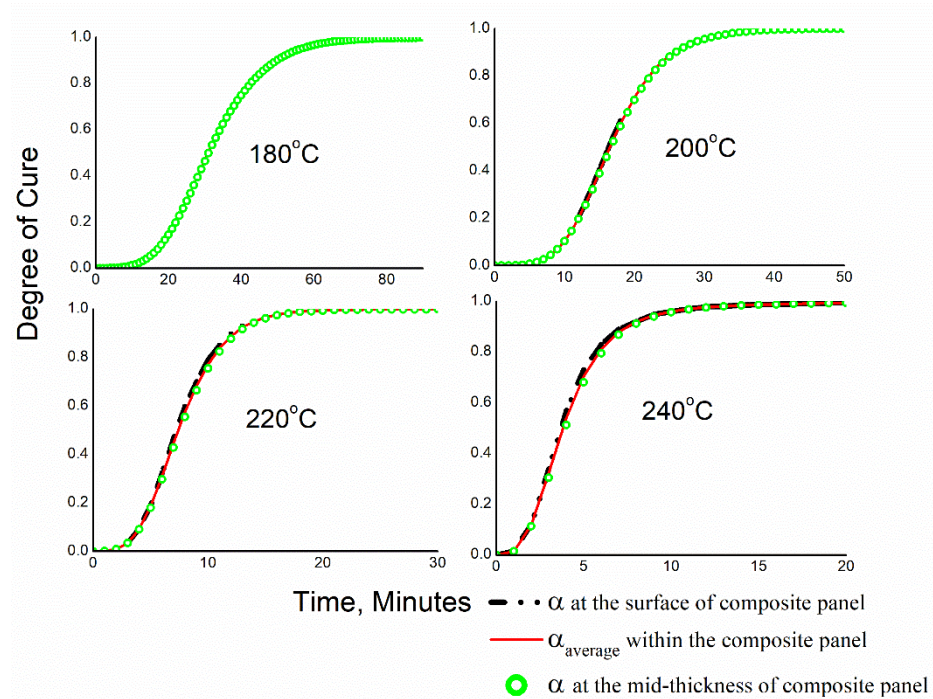
Figure 5. 6 Effect of Part Thickness on the Curing of Composite Wing Flap

5.4.2.1 Cure Process Window

Figure 5.7 illustrates the cure process window developed for composite panel cure. The composite panel cure was simulated for different isothermal temperatures using the neat resin cure kinetics. The simulated composite panel degree of cure and rate of cure was used to develop a composite panel cure process window using the same procedure as described in **Figure 2.2**. With a similar approach, the composite panel rate of cure was modelled as a function of the degree of cure and temperature using classical cure rate models. From the results, the rate of cure versus degree of cure curves of the composite panel fits well with the modified Kamal and Sourours kinetics model for all the temperatures studied. The composite panel cure kinetic parameters with their correlation coefficients are tabulated in **Table 5.3**. The activation energy and frequency factor for composite panel cure were obtained from the Arrhenius plot. From the kinetics modelling, the activation energies obtained for neat resin cure

and composite panel cure are almost similar to 64.07 kJ-mol^{-1} and 64.007 kJ-mol^{-1}, respectively.

The cure process window shows the evolution of the cure for the composite panel as a function of temperature and time. In **Figure 5.7**, it was observed a similar trend in the progression of cure between neat RTM6 resin (shown in **Figure 2.13**) and composite panel for the applied cure cycles. It was also observed that the time for cure completion decreases with an increase in process temperatures for the composite panel. It may also be observed that the neat resin cure conversion is higher than the composite panel cure conversion at any instance of time-temperature cure cycles. This may be attributed to the fibre thermal resistance for the heat flow within the composite panel. From the cure process windows, a slow cure rate was observed at the initial cure stages. Then, the rate of cure increases steeply with time until an approximate 90% cure conversion. This cure progression may be due to autocatalytic phenomena induced by exothermal heat flow. Finally, the rate of cure decreases to a very low value due to vitrification phenomena at the latter stages of curing.
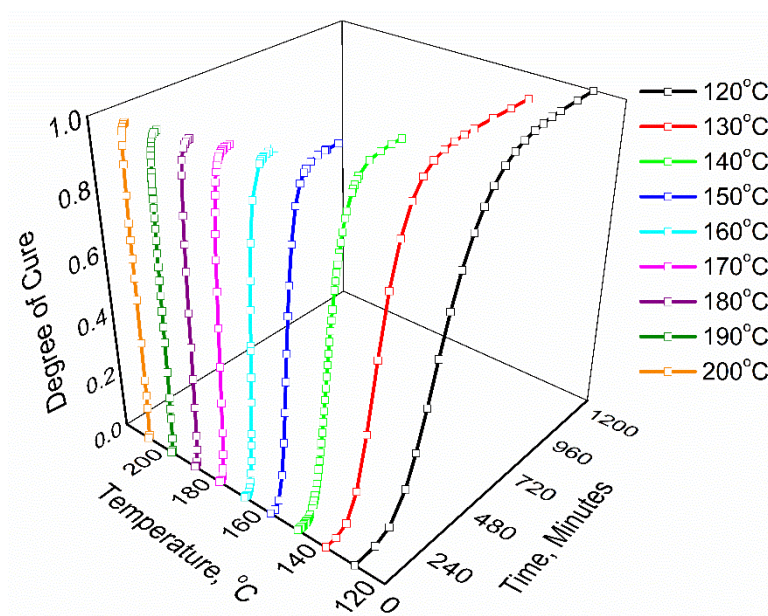
Figure 5. 7 Simulated Wing Flap Composite Panel Cure Process Window

Table 5. 3 Modified Kamal and Sourour Cure Kinetics Model Parameters for Wing Flap Composite Panel

Temperature, °C	*k*, per Minute	*m*	*n*	Correlation Coefficient
180	0.118	0.733	1.054	0.999
200	0.243	0.740	1.099	0.996

220	0.464	0.710	1.101	0.997
240	0.867	0.681	1.301	0.998

$$E = 64.007 \text{ kJ mol}^{-1} \qquad A = 2.84 \times 10^6 \text{ min}^{-1}$$

5.4.2.2 Cure Difference Window

A detailed cure comparison between neat resin and composite panel at different applied temperatures is shown in **Figure 5.8**. From **Figure 5.8**, it is observed that for lower temperatures cure differences between neat resin and composite panel are larger due to the lesser thermal conductivity of fibre mat. However, the differences in cure curves tend to decrease with an increase in applied process temperatures. The final cure process time required for the composite panel and neat resin is similar when the temperatures are greater than 220°C. It may also be observed that the cure differences between the composite panel and neat resin are negligible at 240°C and hence, merged cure curves are obtained after 80% cure conversion. This may be attributed to the increase in exothermal heat flow during composite panel curing at higher mould temperatures.

A cure difference window was computed as a function of time and temperature for the detailed analysis of cure differences between neat resin and the composite panel. The trend, magnitude and peak values of cure differences between neat resin and the composite panel with varying cure cycles are depicted in **Figure 5.9**. As can be seen in **Figure 5.9**, for a given temperature the cure differences between neat resin and composite panel increases with time until they reach the peak value and then gradually decreases. It is also observed that for a given time, the cure differences between neat resin and the composite panel decrease with an increase in temperature and become negligible at 240°C. It may be mentioned that the magnitude of the cure difference curve and the peak values decreases with an increase in the temperature.
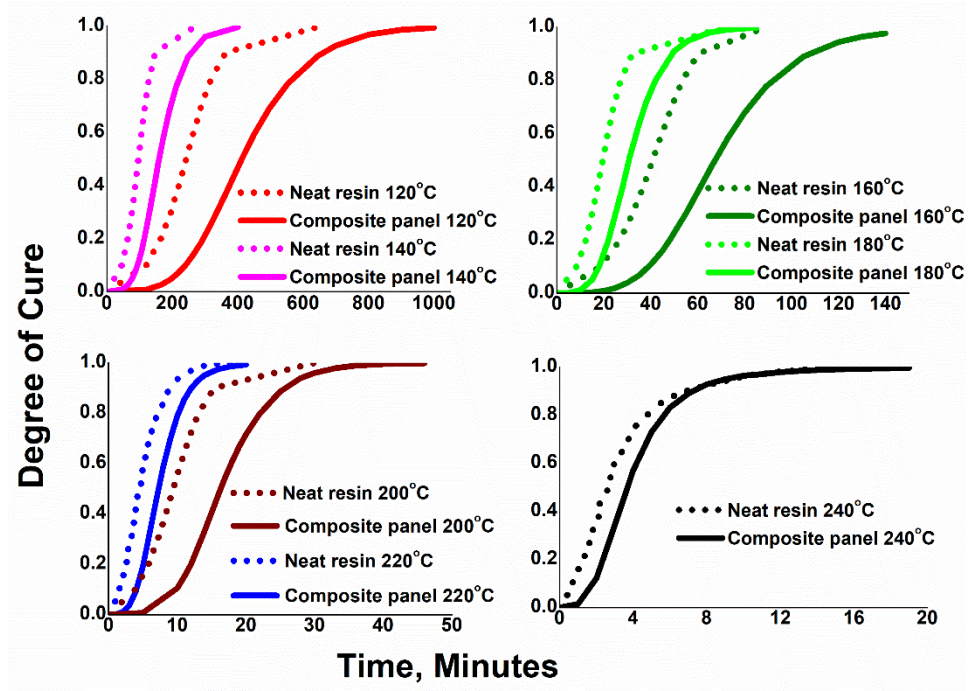
Figure 5. 8 Cure Comparison between Neat RTM6 Resin and Composite Panel
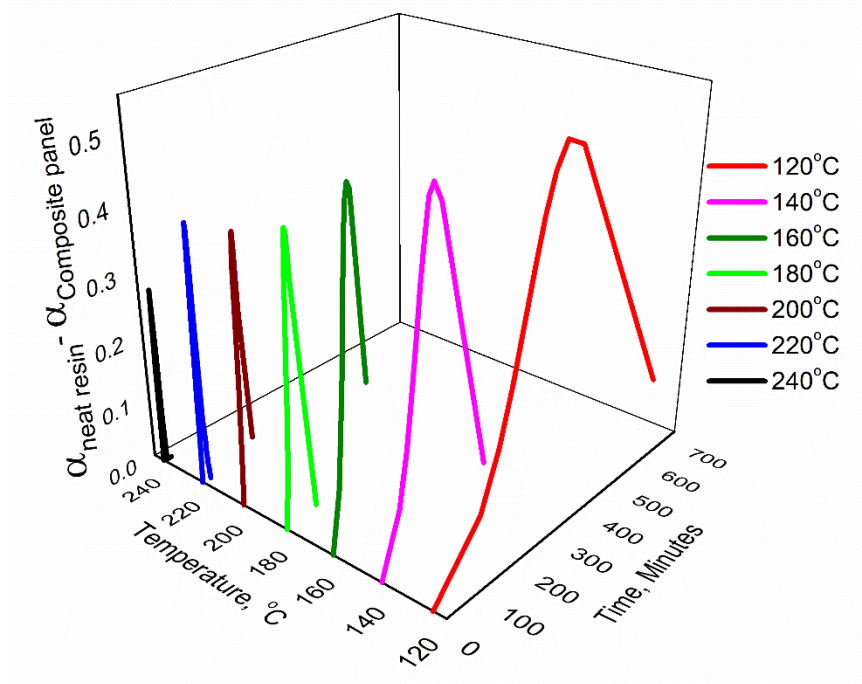
Figure 5. 9 Cure Difference Window of Neat RTM6 Resin and Composite Panel

5.4.2.3 Peak Cure Differences

The peak values of cure differences $\left(\text{i.e } \Delta\alpha_{peak}\right)$ between neat resin and composite panel were plotted as a function of time and temperature in **Figure 5.10**. The comparisons between the neat resin and composite panel cure conversions at $\Delta\alpha_{peak}$ were also shown in **Figure 5.10**. From **Figure 5.10**, it can be seen that the $\Delta\alpha_{peak}$ value as well as cure time at

$\Delta\alpha_{peak}$ (i. e $t_{\Delta\alpha_{peak}}$) decreases with an increase in applied temperatures. The composite panel cure conversion at $\Delta\alpha_{peak}$ increases with an increase in temperature and conversely, the neat resin cure conversion at $\Delta\alpha_{peak}$ decreases with an increase in temperature.

Using non-linear regression analysis, several mathematical models were tried to develop $\Delta\alpha_{peak}$ and $t_{\Delta\alpha_{peak}}$ as a function of temperature. From the results, it was found that the cubic and logistic functions were fitting well to relate $\Delta\alpha_{peak}$ = f(temperature) and $t_{\Delta\alpha_{peak}}$ = f(temperature), respectively. **Figure 5.11** shows the comparisons between $t_{\Delta\alpha_{peak}}$ and $\Delta\alpha_{peak}$ data and the modelled results. The developed models and their associated parameters are given in **Equations (5.11 & 5.12)**.

$$t_{\Delta\alpha_{peak}} = 1/(a_1{}^T \times a_2) \; : R^2 = 0.999$$

$$a_1 = 1.04552, a_2 = 1.50773 \times 10^{-5} \quad R^2 = 0.999$$

$$(5.11)$$

$$\Delta\alpha_{peak} = b_1 T^3 + b_2 T^2 + b_3 \; : R^2 = 0.967$$

$$b_1 = -4.04 \times 10^{-8}, b_2 = 5.24 \times 10^{-6}, b_3 = 0.53 \qquad (5.12)$$
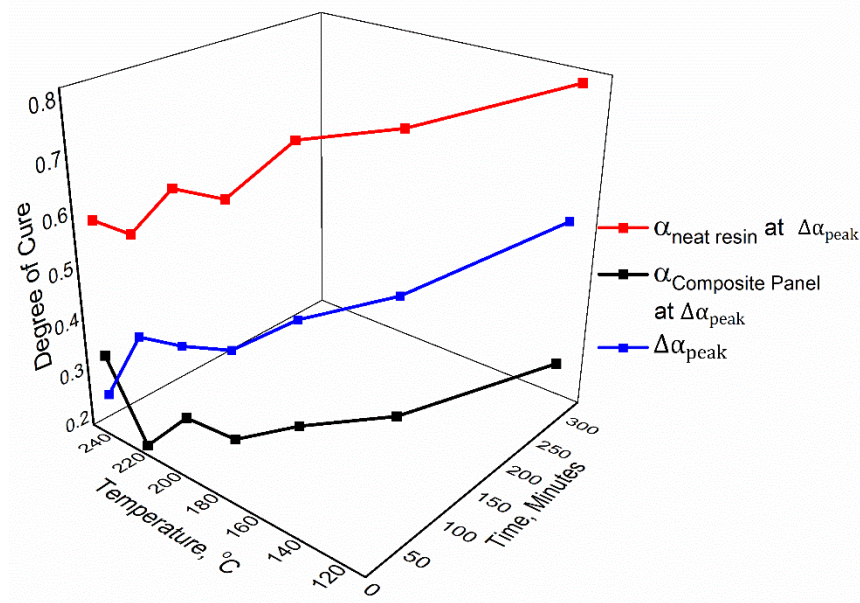
Figure 5. 10 Neat Resin and Composite Panel Cure Conversions at $\Delta\alpha_{peak}$
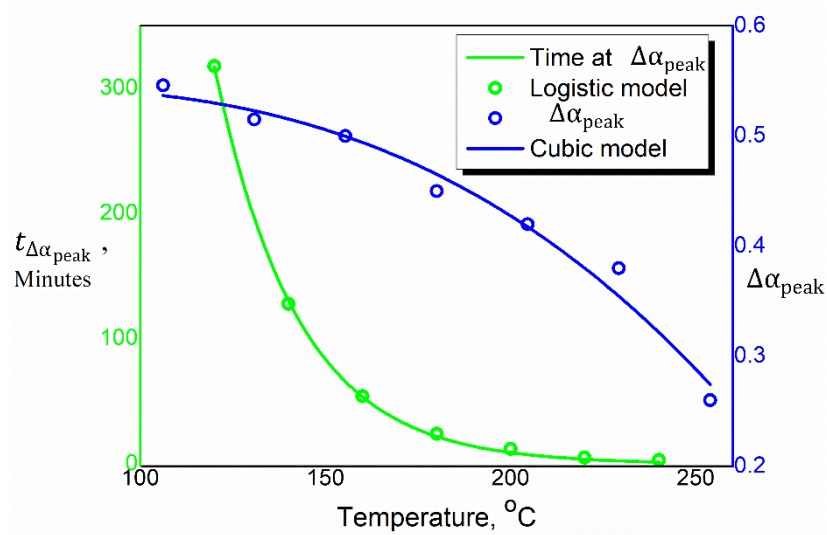
Figure 5. 11 $\Delta\alpha_{\mathrm{peak}}$ **and** $t_{\Delta\alpha_{\mathrm{peak}}}$ **as a Function of Temperature.**

5.4.2.4 Cure Rate at $\Delta\alpha_{peak}$

Figure 5.12 shows the rate of cure versus time for both the neat resin and composite panel at different isothermal temperatures. As can be seen from **Figure 5.12**, the peak of the cure rate increases with increasing temperature and the peak cure time decreases with an increase in temperature for both the neat resin and composite panel. It is also observed that for a given temperature, the peak value of the cure rate for the neat resin is higher than that of the peak value of the cure rate for the composite panel. However, the difference in peak values of cure rate between neat resin and composite panel decreases with an increase in temperature. The rate of cure at $\Delta\alpha_{\mathrm{peak}}$ and the corresponding cure rate time at $\Delta\alpha_{\mathrm{peak}}$ ($t_{\Delta\alpha_{\mathrm{peak}}}$) is shown by a dotted line in **Figure 5.12**. From **Figure 5.12**, it is observed that for a given temperature, the cure rate at $\Delta\alpha_{\mathrm{peak}}$ falls at the termination phase after peaking of neat resin cure whereas the cure rate at $\Delta\alpha_{\mathrm{peak}}$ falls at the cure progression zone before peaking for the composite panel.
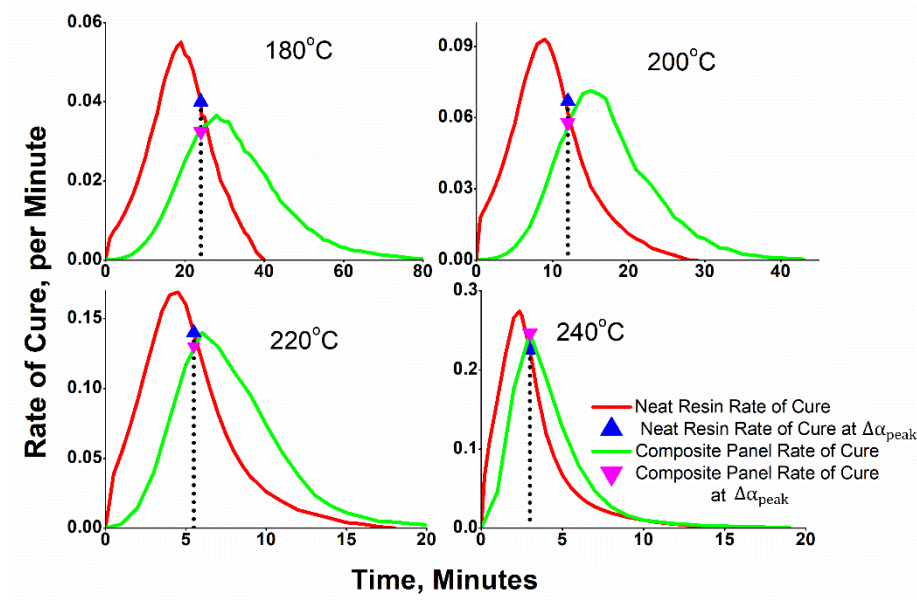
Figure 5. 12 Cure Rate of Neat RTM6 Resin and Composite Panel

5.4.2.5 Kinetics of Cure Difference Progression

The kinetics of cure difference progression between neat resin and composite panel was modelled as a function of neat resin cure conversion for the applied process temperatures. **Figure 5.13** shows the degree of cure difference ($\Delta\alpha$) between neat resin and composite panel as a function of neat resin cure conversion for different temperatures. From **Figure 5.13**, the peak value of $\Delta\alpha$ $\left(\text{i. e } \Delta\alpha_{\text{peak}}\right)$ decreases with an increase in temperature and the $\Delta\alpha_{\text{peak}}$ value reaches earlier neat resin conversions with an increase in applied temperature. At a given temperature, $\Delta\alpha$ increases with the neat resin conversion and attains a maximum at $0.4 < \alpha_{neat\ resin} < 0.7$, then gradually decreases to zero. At a given neat resin conversion, the higher the temperature, the lesser the value of $\Delta\alpha$ and the lesser the time to complete the cure reaction.

Several models were tried to fit the relationship between $\Delta\alpha$ and neat resin degree of cure. From the results, it was found that the modified Kamal and Sourour autocatalytic kinetic model was fitted well to the $\Delta\alpha$ versus neat resin cure conversion data at all studied temperatures. **Figure 5.13** shows the modelled results of $\Delta\alpha$ versus neat resin cure conversions for 180°C, 200°C, 220°C and 240°C temperatures. The Modified Kamal and Sourour's model for relating $\Delta\alpha$ as a function of neat resin conversion and temperature is given in **Equation (5.13)**. The modelled kinetic parameters are tabulated in **Table 5.4**.

Figure 5.14 shows the temperature dependency of the kinetic rate constants and their functional relationship was obtained by fitting to the modified Arrhenius form as given in

Equation (5.14). The associated activation energy and frequency factor obtained from the Arrhenius plot are tabulated in **Table 5.4**.

From the kinetics of cure difference progression, it is possible to predict the cure differences between neat resin and composite panel from the experimental neat resin cure conversion data with the applied time-temperature cycles. Thus, composite panel cure conversion can also be predicted from the cure difference data. This will help to adjudge the operable cure cycle for the composite part from the experimental neat resin cure conversion data. From the results, it was found that the mould temperature of 240°C has the minimum cure differences at any resin cure conversion.

$$\Delta\alpha(t) = k\alpha_{neat\ resin}{}^{m}(1 - \alpha_{neat\ resin})^{n} \qquad (5.13)$$

$$k = Ae^{-E/RT} + b \qquad (5.14)$$
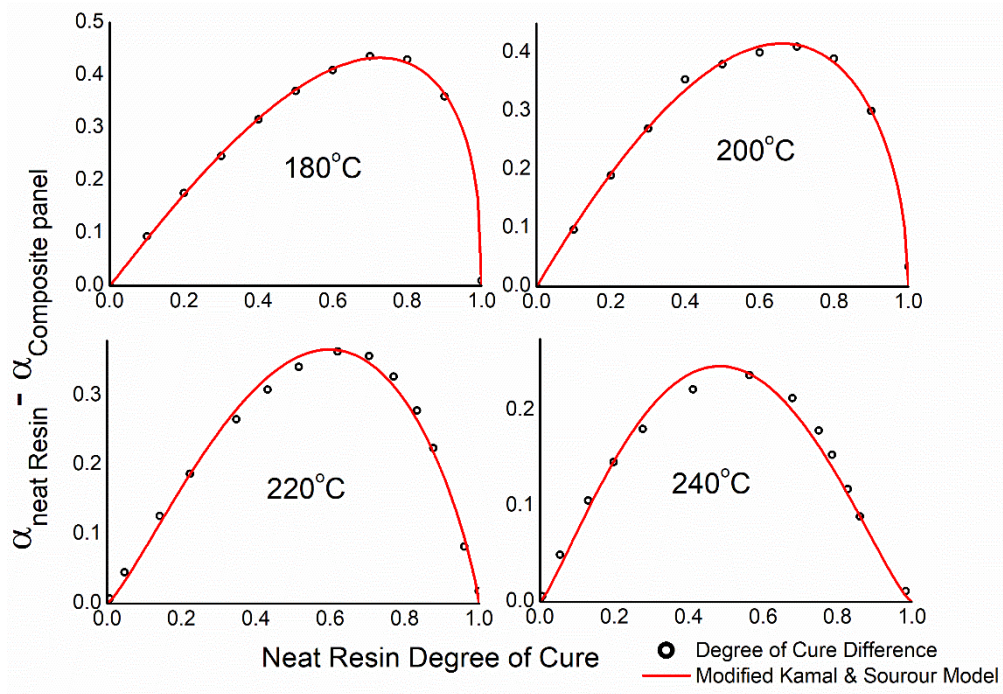
Figure 5. 13 Kinetics of Cure Difference Progression
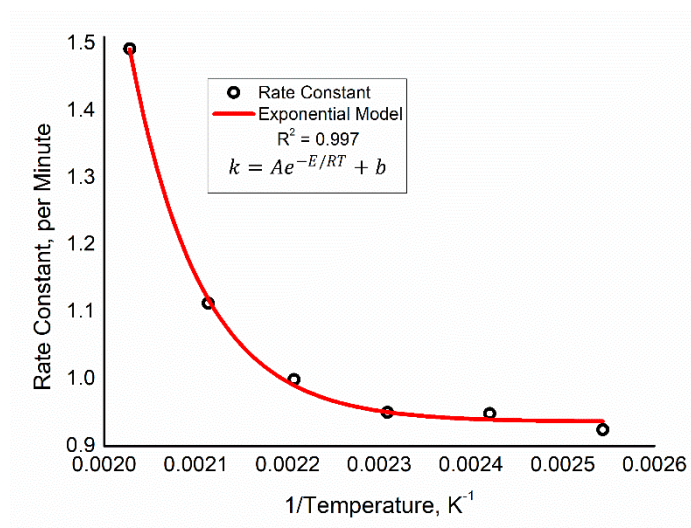
Figure 5. 14 Arrhenius Form

Table 5. 4 Modified Kamal and Sourour Cure Kinetics Model Parameters for Cure Difference Progression

Temperature, °C	K	m	n	Correlation Coefficient
120	0.9245	1.0183	0.1919	0.965
140	0.9485	1.028	0.240	0.98
160	0.9504	1.009	0.241	0.978
180	0.9994	1.033	0.389	0.998
200	1.113	1.01	0.52	0.991
220	1.4925	1.244	0.838	0.992
240	1.502	1.248	1.339	0.981

$k = Ae^{-E/RT} + b$ $\quad$ A = 1.49×10^{11} min^{-1} $\quad$ E = 107.885 kJ mol^{-1}

b = 0.936 min^{-1}

5.4.3 Trial and Error Non-Isothermal Cure Process Simulations

The trial-and-error non-isothermal cure process simulations were performed by manually changing the values of mould heating parameters as described in Section 5.3.4. From the selected mould heating parameters, the mould surface temperature was obtained as a

function of time. Then, for the given mould surface temperature profile, part mid-thickness temperature and averaged cure conversion within the composite panel were computed as a function of time. Several cure trials were performed using different mould heating parameters and the case studies were tabulated in **Tables 5.5** and **5.6** for the bonnet and wing flap parts, respectively. The cure case studies were analyzed to obtain the optimum thermal cure profile with the proper choice of mould heating parameters that deliver minimum temperature overshoot, thermal gradient and cure time as shown in **Figures 5.15** and **5.16**.

Table 5.5 and Figure 5.15 show the two-dwell cure process simulation trials for the bonnet part. From the results, the mid-thickness temperature overshoot of 7 - 9 K was observed for trials 1, 3, and 5. This may be attributed to the increased exothermal heat at the ramp applied. Additionally, it was found either a faster onset cure rate or non-uniform cure progression at the cure curves due to the improper choice of mould heating parameters at these trials. In contrast, a negligible mid-thickness temperature overshoot along with uniform cure progression was found at trials 2, 4, and 5. This may be attributed to the temporal effect of exotherm and cure progression with applied mould temperatures obtained from the proper choice of mould heating parameters. With all the trials studied, trial 6 containing mould heating parameters of a = 2 K/min, t_1 = 20 min, t_2 = 40 min, and t_3 = 50 min delivered a negligible temperature overshoot, a minimum thermal gradient of 0.48 K, and a minimum cure time of 60 minutes.

Table 5.6 and Figure 5.16 show the one-dwell trial and error cure process simulations for the wing flap part. In all trials studied, it was found an increase in thermal gradient and a decrease in cure time with the increase in ramp rate and dwell time. Trial 1 predicted the lowest thermal gradient of 0.0317 K and the highest cure time of 400 minutes to attain the target value of 90 % cure extent. Also, trial 4 predicted the highest thermal gradient of 2.1946 K and the lowest cure time of 30 minutes to attain the target value of 90 % cure extent. With all the trials studied, trial 3 containing mould heating parameters of a = 5 K/min and t_1 = 10 minutes delivered a good balance between the thermal gradient and cure time which is 0.248 K and 80 minutes, respectively. From the results, the trial and error process was found significantly challenging to optimize the multiple parameters simultaneously for both the composite parts.

Table 5. 5 Cure Process Simulation Trials for Bonnet Part

Trials	Input Parameters				Output Parameters		
	a, K/min	t_1, minutes	t_2, minutes	t_3, minutes	Mould Temperature , K	Thermal Gradient, K	Overshoot , K
1	3	10	40	50	338	0.07	9.23
2	4	10	40	50	348	0.505	0
3	2	10	30	35	323	0.177	7.36
4	3	10	30	35	333	0.513	0
5	2	20	50	60	348	0.28	9.58
6	2	20	40	50	348	0.48	0

Trial 1

Trial 2
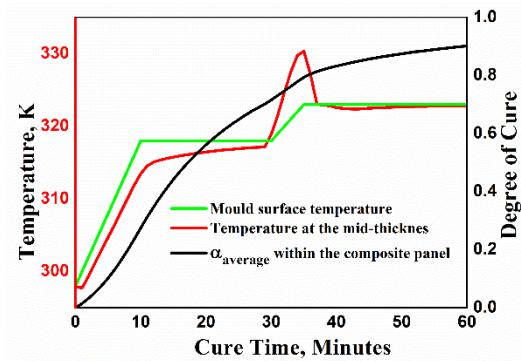
Trial 3
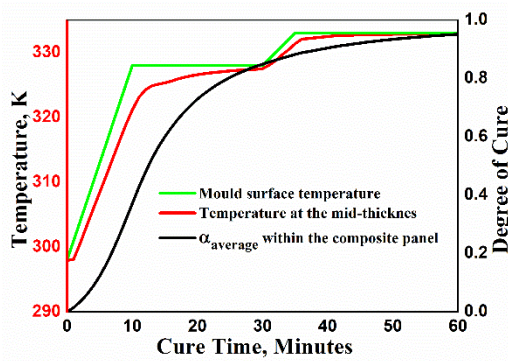
Trial 4
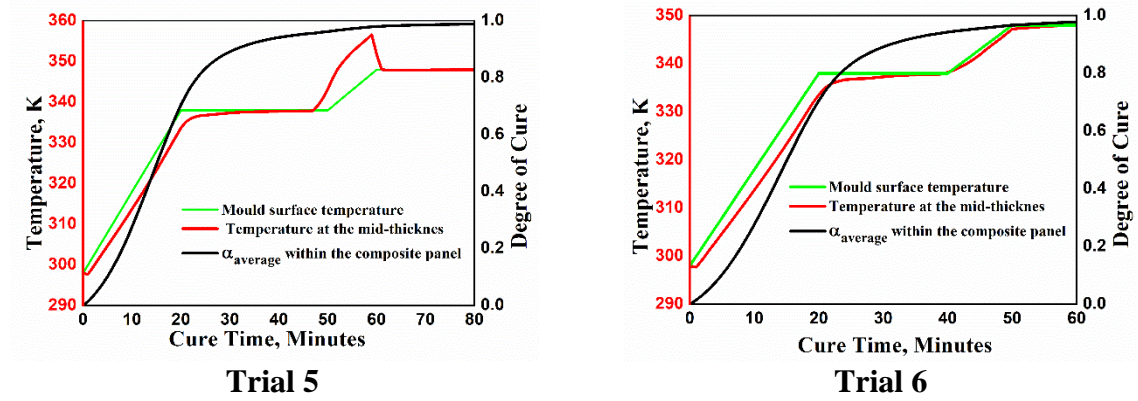
Trial 5

Trial 6

Figure 5. 15 (Trials 1-6) Cure profiles for Bonnet Part

Table 5. 6 Cure Process Simulation Trials for Wing Flap Part

Trials	Input Parameters		Output Parameters	
	a, K/min	t_3, minutes	Mould Temperature, K	Thermal Gradient, K
1	1	10	403	0.0317
2	1	20	413	0.0665
3	5	10	423	0.177
4	5	20	493	0.513

Trial 1

Trial 2

<div align="center">

Trial 3   **Trial 4**
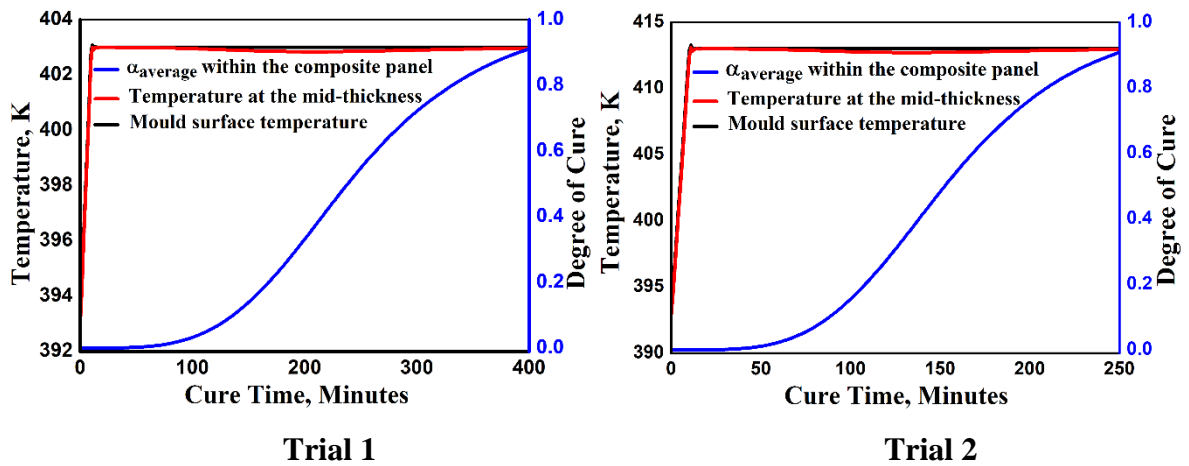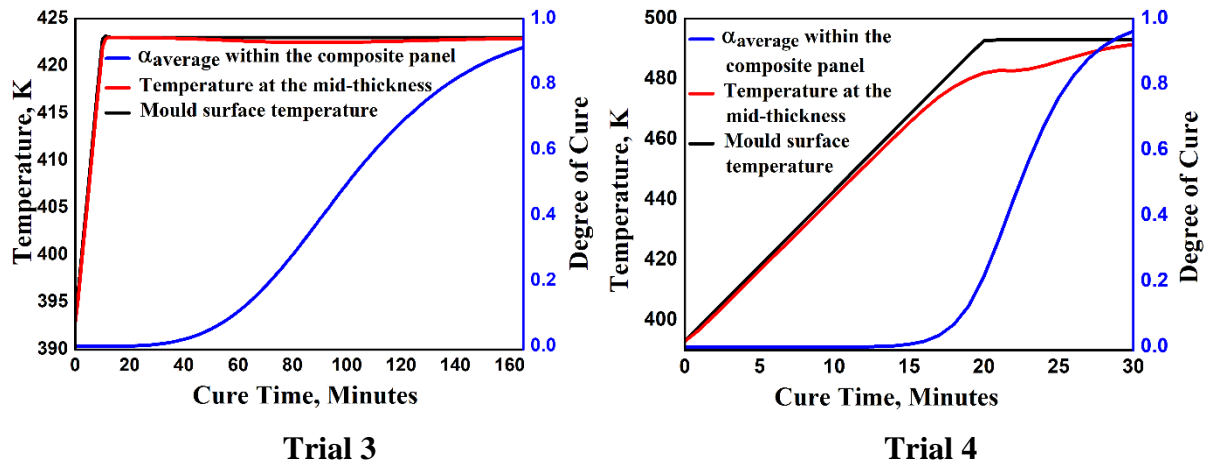
Figure 5. 16 (Trials 1 - 4) Cure profiles for Wing Flap Part

</div>

5.4.4 Curing Optimization using NSDE Algorithm

The thermal-cure profiles were optimized using the in-house coded NSDE algorithm for both composite parts. The Pareto fronts were obtained between the thermal gradient and cure time. The effect of population size and the total number of generations were studied on the obtained rank 1 fronts as shown in **Figures 5.17 and 5.20**. The Pareto optimal fronts in **Figures 5.17 and 5.20** are in the form of an L-shape curve. This encompasses three regions: (i) the vertical region corresponds to the significant change in thermal gradient values with a small change in cure time; (ii) the horizontal region corresponds to the significant change in cure time with small changes in thermal gradient values; and (iii) the curved region which delivers the good balance between the thermal gradient and curing time.

Figure 5.17 shows the Pareto front between the thermal gradient and cure time for the automotive bonnet composite part. From **Figures 5.17a** and **5.17b**, it was observed that an increase in population size increases the range of the optimal solutions. From **Figure 5.17a**, at a population size of 5 and generation 10, the maximum thermal gradient and cure time were found to be 0.09 K, and 75 minutes respectively. From **Figure 5.17b**, at a population size of 10 and generation 5, the maximum thermal gradient and cure time was observed to be 0.6 K, and 120 minutes respectively. This may be attributed to the widening of search space with an increase in population size. However, the extreme broadening of search space can delay the convergence rate and thus, result in more generations. Therefore, a population size of 10 was used and the total number of generations varied from 5-15 and the results were analyzed for generations 5, 10 and 15.

Figure 5.18 shows the effect of mould temperature on the Pareto front between thermal gradient and cure time at generation 5 and population size of 10 for automotive bonnet

composite part. From **Figure 5.18**, it was observed that for a given mould temperature, the higher the thermal gradient the lesser the cure time and vice versa, as expected. **Figure 5.19** shows the effect of ramp rate on the Pareto front between thermal gradient and cure time. From **Figure 5.19**, it was found an increase in thermal gradient and a decrease in cure time with the increase in ramp rates. This may be attributed to the increased exothermal heat with the increase in ramp rates and mould temperatures.

(a) (b)
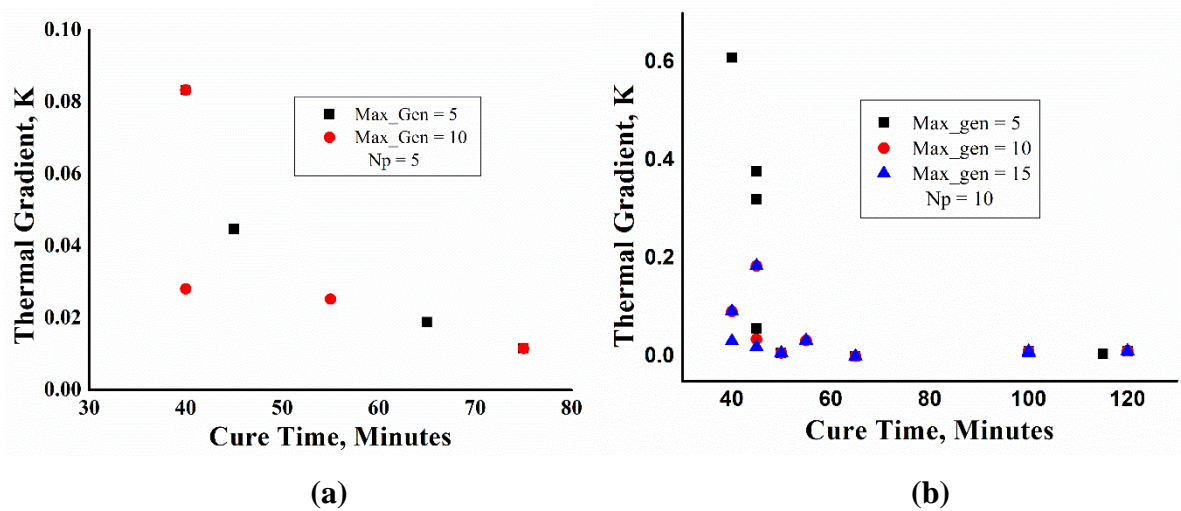
Figure 5. 17 Pareto Front of Thermal Gradient vs. Cure Time for Bonnet Composite Part: (a) **Np = 5 and max_gen = 5 and 10,** (b) **Np = 10 and max_gen = 5, 10 and 15**
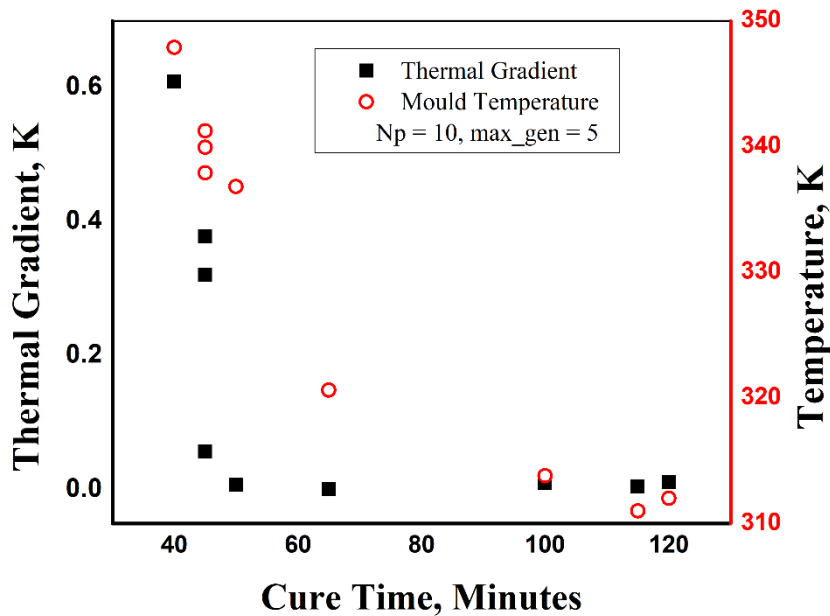
Figure 5. 18 Effect of Mould Temperature on Thermal Gradient and Cure Time for Np = 10 and max_gen = 5 for Bonnet Part
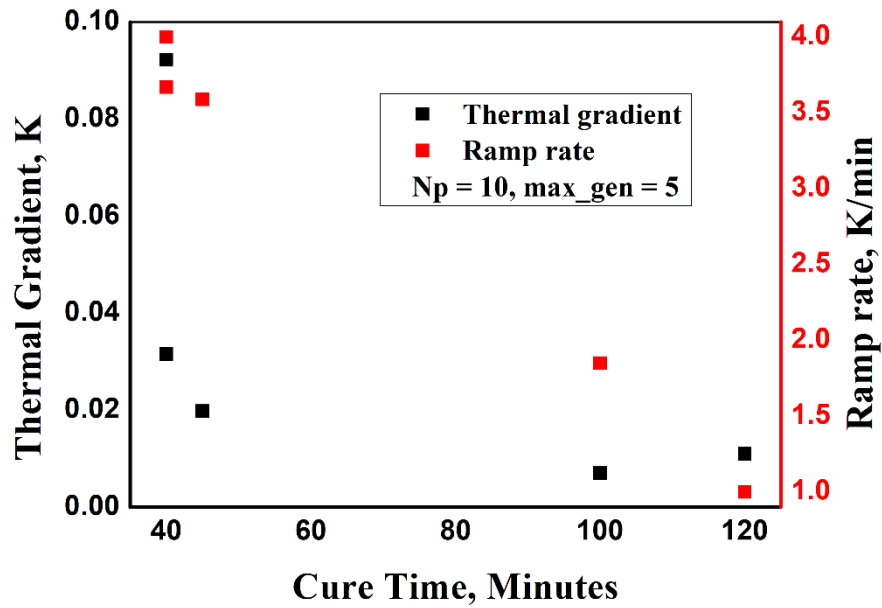
Figure 5. 19 Effect of Ramp Rate on Thermal Gradient and Cure Time for Np = 10 and max_gen = 5 for Bonnet Part

Figure 5.20 shows the Pareto front between the thermal gradient and cure time for the aircraft wing flap composite part. **Figures 5.20a, 5.20b and 5.20c** show the Pareto fronts for the population size of 5, 10 and 20, respectively for different generations. From the results, it can be seen that with the decrease in thermal gradient, there perceived an increase in cure time and vice versa. The extreme minimum and maximum thermal gradients values range from 0.004 K to 1.49 K and the cure time value ranges from 30 minutes to 300 minutes, respectively.

Figure 5.21 shows the effect of mould temperature variations on the Pareto front between thermal gradient and cure time for the aircraft wing flap composite part. From the results, it can be seen that with the increase in mould temperature, the thermal gradient values are increased and cure time values are reduced. From the results, it was also found that the thermal gradients are significantly reduced after 50 minutes of cure time and more crowded solutions can be seen in the horizontal region for both the composite parts. This shows the efficacy of the NSDE algorithm for optimizing the thermal cure profile for the studied composite parts.

142
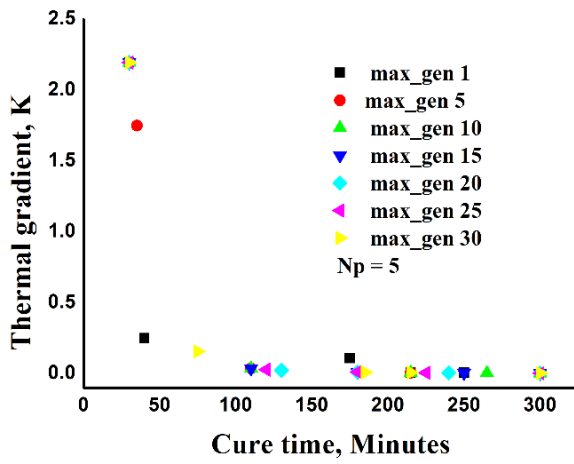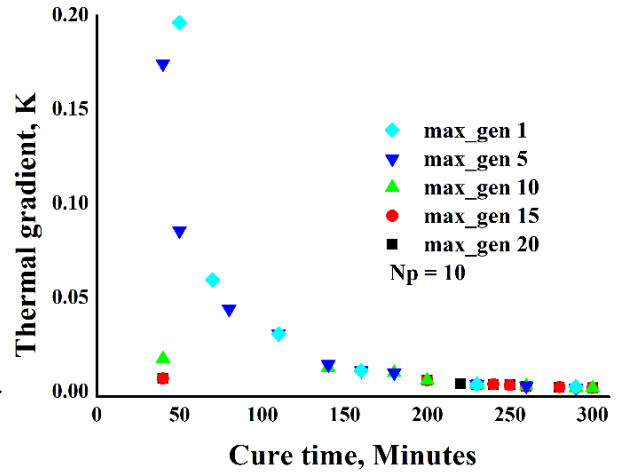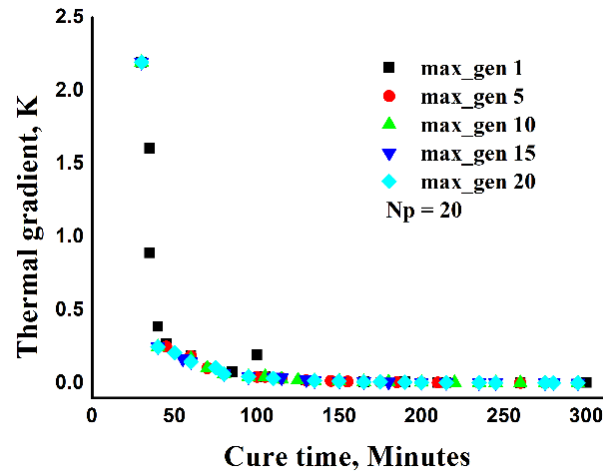
Figure 5. 20 Pareto Front of Thermal Gradient vs. Cure Time for Aircraft Wing Flap Composite Part: (a) **Np = 5 and max_gen = 1 to 30 with a Difference of 5 Generations,** (b) **Np = 10 and max_gen = 1 to 20 with a Difference of 5 Generations,** (c) **Np = 20 and max_gen = 1 to 20 with a Difference of 5 Generations**
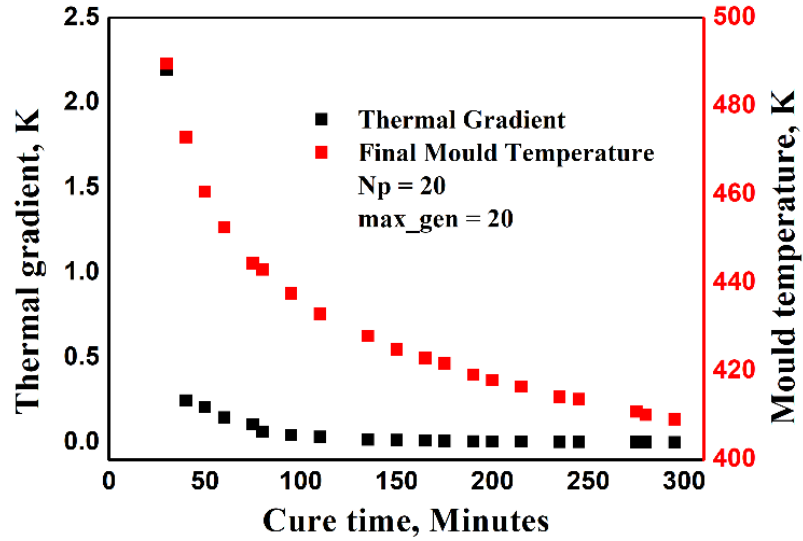
Figure 5. 21 Effect of Mould Temperature on Thermal Gradient and Cure Time for Np = 20 and max_gen = 20 for Aircraft Wing Flap Part

5.4.5 Curing Optimization using NSGA-II Algorithm

Pareto fronts between thermal gradient and cure time were obtained using the NSGA-II algorithm. The population size and maximum number of generations were set to 10. The Pareto fronts obtained from the NSGA-II algorithm were compared with those obtained from the NSDE algorithm by using similar population size and number of generations as shown in **Figures 5.22a and 5.22b. Figures 5.22a and 5.22b** show the Pareto fronts obtained for the bonnet and wing flap parts, respectively.

From the results, it can be seen that the Pareto fronts obtained from the NSGA-II algorithm also exhibit an L-shaped curve. From the results, it can be seen that with the increase in cure time thermal gradient values are decreased and vice versa. The extreme minimum and maximum thermal gradient values range from 0.0068 K to 0.828 K for the bonnet part and 0.007 K to 0.39 K for the wing flap part, respectively. Similarly, the extreme minimum and maximum cure time values range from 40 minutes to 120 minutes for the bonnet part and 40 minutes to 490 minutes for the wing flap part, respectively. From the results, it was also observed that with an increase in the number of generations, the NSGA-II algorithm explored the search space more extensively, resulting in slower convergence rates. This indicates that the NSGA-II algorithm excels in exploration but lags in exploitation leading to a higher number of function evaluations and increased computational time.

In comparison, most solutions obtained from the NSDE algorithm are concentrated in the curved region of the Pareto front. This indicates that the NSDE-obtained solutions achieve a good balance between thermal gradient and cure time. Additionally, the NSDE solutions

converged relatively faster than those obtained from the NSGA-II algorithm. For the NSDE algorithm, the extreme minimum and maximum thermal gradient values range from 0.0008 K to 0.609 K for the bonnet part and 0.0022 K to 0.17 K for the wing flap part, respectively. Similarly, the extreme minimum and maximum cure time values range from 40 minutes to 120 minutes for the bonnet part and 35 minutes to 300 minutes for the wing flap part, respectively. This indicates that the NSDE algorithm is more effective in achieving faster convergence with less cure process and computational time when compared to the NSGA-II algorithm.

(a)   (b)
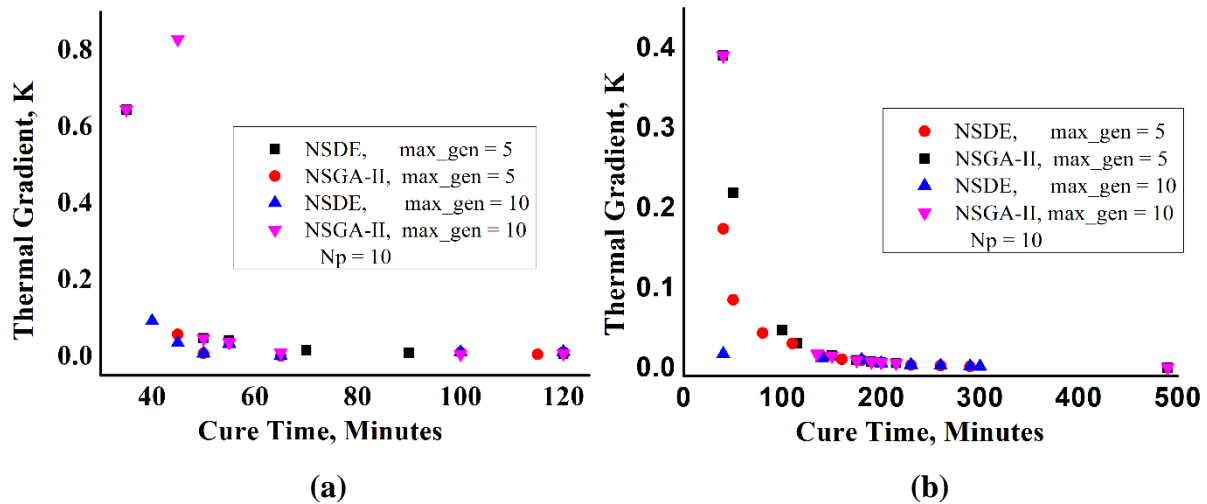
Figure 5. 22 Pareto Front of Thermal Gradient vs. Cure Time: (a) Automotive Bonnet Composite Part, (b) Aircraft Wing Flap Composite Part

5.4.6 Comparative Assessment between Trial and Error Process Simulations, NSDE and NSGA-II Optimization Algorithms

The efficacy of the NSDE algorithm was evaluated by comparing the Pareto optimal solutions obtained from the NSDE algorithm with solutions obtained from the trial and error process simulations and the NSGA-II algorithm for both selected composite parts. The comparisons were made from the solutions obtained from either similar ramp rates or identical final mould temperatures at the cure cycle. The comparisons were analyzed in terms of a thermal gradient, cure time and uniform cure progression at the applied temperature cycles.

Case 1 in **Figure 5.23** compares the thermal-cure cycles obtained for the bonnet part using closely identical final mould temperatures. From the Case 1 results, it can be seen that the composite panel mid-thickness temperatures predicted from the NSDE and NSGA-II algorithms were found to be uniformly progressive with the applied mould surface temperatures when compared to the trial and error predictions. Thus, the thermal gradient predicted using the NSDE and NSGA-II algorithms at the final cure time was significantly lesser than the trial and error process as can be seen in **Table 5.7**. However, the thermal gradient

predicted using the NSDE algorithm was comparatively lesser than the NSGA-II algorithm. Case 2 in **Figure 5.23** compares the thermal-cure cycles obtained for the bonnet part using identical ramp rates. From the Case 2 results, it can be seen that the NSDE algorithm predicted the targeted degree of cure at 90% within the 1st dwell and hence, there were no further computations found at the 2nd dwell. Whereas, trial and error simulations predicted degrees of cure at both dwells due to its manual approach. Moreover, the NSGA-II algorithm predicted a lower value for dwell times, necessitating a two-dwell thermal profile and requiring more cure time as can be seen in **Table 5.7**.

Table 5.8 and **Figure 5.24** show a comparison of cure process results between the studied simulation trials and the Pareto optimal solutions generated by the NSDE and NSGA-II algorithms at the 10th generation with a population size of 10 for the wing flap composite part. From the results of Case 1, it is evident that the NSGA-II algorithm predicted a maximum cure time of 490 minutes, while trial and error simulations resulted in a maximum cure time of 400 minutes and the NSDE algorithm predicted a maximum cure time of of only 300 minutes. Furthermore, in the Case 2 results, trial and error simulations predicted a higher thermal gradient of 2.1946 K, whereas the NSDE and NSGA-II algorithms predicted thermal gradients of 0.07 K and 0.06 K, respectively. Hence, the efficacy of the NSDE algorithm is confirmed in predicting converged solutions with reduced cure time and thermal gradient compared to both trial and error simulations and the NSGA-II algorithm. In addition, one of the thermal-cure profiles predicted by the NSDE algorithm matched the optimal thermal-cure profile obtained from trial and error simulation in Case 3. However, the NSGA-II algorithm was unable to predict this similar cure profile. This reinforces the effectiveness of the NSDE algorithm in providing a greater number of optimal choices for thermal cure cycles.

From the results, it was found that the NSDE algorithm predictions were effective in terms of a thermal gradient, cure time and automatic selection of the mould heating parameters when compared to the trial and error simulations and NSGA-II algorithm for both the studied composite parts. This may be attributed to the effective tuning of mould heating parameters through supervised learning iterations of the NSDE algorithm.

Table 5. 7 Comparative Assessment for Bonnet Part

Case	Input Parameters				Output Parameters		
	a, K/min	t_1, min	t_2, min	t_3, min	Mould Temperature, K	Thermal Gradient, K	Cure Time, Minutes

Case 1	Trial and Error Simulation	3	10	30	35	333	0.513	60
	NSGA-II Algorithm	3.43	7	27	35	330	0.0469	50
	NSDE Algorithm	3.59	7	25	35	333.13	0.0198	45
Case 2	Trial and Error Simulation	4	10	40	50	348	0.505	60
	NSGA-II Algorithm	4	5	26	27	319	0.0099	65
	NSDE Algorithm	4	9	-	-	334	0.01	40

Case 1   **Case 2**
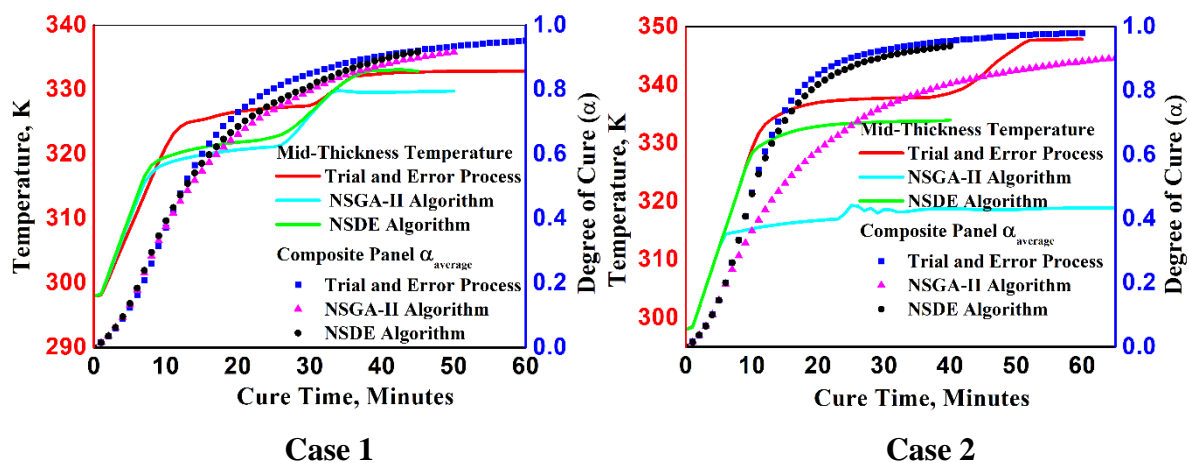
Figure 5. 23 (Case 1 & 2) Thermal-Cure Profiles Comparative Assessment for Bonnet Part

Table 5. 8 Comparative Assessment for Wing Flap Part

Case		Input Parameters		Output Parameters		
		a, K/min	t_1, minutes	Mould Temperature, K	Thermal Gradient, K	Cure Time, Minutes
Case 1	Trial and Error Simulation	1	10	403	0.0317	400
	NSGA-II Algorithm	1	5	398	0.0007	490
	NSDE Algorithm	2	8	409	0.0022	300
Case 2	Trial and Error Simulation	5	20	493	2.1946	30

147

	NSGA-II Algorithm	4.71	17	473	0.39	40
	NSDE Algorithm	4.6	20	485	0.0177	35
Case 3	Trial and Error Simulation	5	10	443	0.0646	80
	NSGA-II Algorithm	3.49	14	441	0.0717	85
	NSDE Algorithm	5	10	443	0.0646	80

Case 1   Case 2
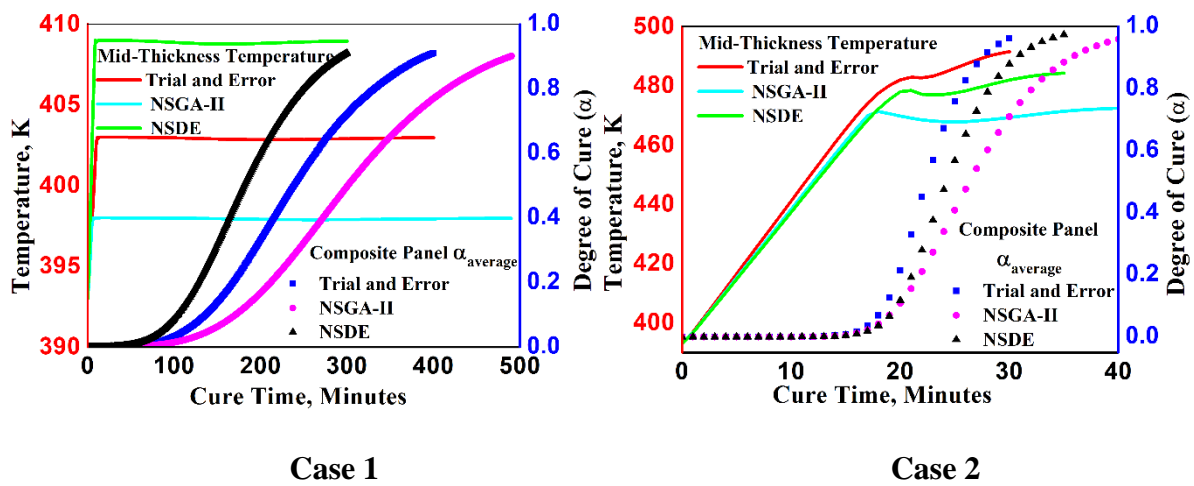
Figure 5. 24 (Case 1&2) Thermal-Cure Profiles Comparative Assessment for Wing Flap Part

5.5 Summary

The main objective of this chapter was to develop a simpler and cost-effective multi-objective optimization algorithm for the cure cycle optimization of industrial composite parts. A vinyl ester-glass fibre-reinforced automotive bonnet and an RTM6-carbon fibre-reinforced aircraft wing flap composite parts were used as the optimization case studies. At first, isothermal trial and error cure process simulations were performed to obtain the time-temperature-degree of cure window for the aircraft wing flap composite panel using the identical temperature cycles used in RTM6 DSC experiments as reported in Chapter 2. Then, non-isothermal trial and error cure process simulations were performed by manually changing the mould heating parameters to optimize the composite part cure profile of both composite parts. The thermal-cure process optimizations were performed using two-dwell and one-dwell mould heating parameters for the 12 mm thick automotive bonnet and the 5 mm thick aircraft wing flap composite parts, respectively. Subsequently, a novel in-house coded NSDE

algorithm was developed and implemented for the simultaneous minimization of composite part thermal gradients and cure process time for both the studied composite parts. To evaluate the efficacy of the developed NSDE algorithm, the NSGA-II algorithm was also in-house coded for the simultaneous optimization of framed objectives. The efficacy of the proposed algorithm was examined with the trial and error process model simulations and NSGA-II optimization algorithm in terms of a thermal gradient, cure time and uniform cure progression at the applied temperature cycles.

From the isothermal trial and error cure process simulation results, the rate of cure for the composite panel was found to be slower than that of the neat resin cure rate due to fibre thermal resistance. From the cure difference analysis, the magnitude and the peak values of cure differences decreased with an increase in applied mould temperatures. Finally, the kinetics of cure difference progression was modelled as a function of neat resin cure conversion using the modified Kamal and Sourour autocatalytic model. From the kinetics of cure difference progression, it is possible to predict the cure differences between neat resin and composite panel from the experimental neat resin cure conversion data with the applied time-temperature cycles. Thus, composite panel cure conversion can also be predicted from the cure difference data. This will help to adjudge the operable cure cycle for the composite part from the experimental neat resin cure conversion data.

From the non-isothermal trial and error cure process simulation results, the composite part thermal profiles were obtained with a mid-thickness temperature overshoot of 7 to 9 K due to the improper choice of mould heating parameters for the bonnet part. In all trials studied for the wing flap part, it was found an increase in thermal gradient and a decrease in cure time with the increase in ramp rate and dwell time. Importantly, the trial and error process was found significantly challenging to optimize the multiple parameters simultaneously for both the composite parts. From the optimization results, the NSGA-II algorithm predicted a thermal gradient of 0.0068 K and a cure time of 40 minutes for the bonnet part and a thermal gradient of 0.007 K and a cure time of 40 minutes for the wing flap part. The NSDE algorithm predicted a lesser thermal gradient of 0.0008 K and cure time of 40 minutes than trial and error cure simulation and NSGA-II algorithm for the bonnet part and a lesser thermal gradient of 0.0022 K and cure time of 35 minutes for the wing flap part.

From the comparative assessment, the NSGA-II algorithm was found to be good at exploration but lags in exploitation leading to increased function evaluations and computational time. The NSDE algorithm was found to be effective in achieving faster convergence with less cure process and computational time when compared to the NSGA-II algorithm. The NSDE

algorithm was observed to be effective in terms of a thermal gradient and cure time with the automated selection of the mould heating parameters when compared to the trial and error simulations. This may be attributed to the effective tuning of mould heating parameters through supervised learning iterations of the NSDE algorithm. Whereas, the trial and error simulation-based optimizations were found to be significantly challenging and time-consuming with the iterative manual selection of thermal-cure process parameters.

Chapter 6

Overall Conclusions and Scope for Future Work

6.1 Conclusions

The main objective of this work was to develop the in-house coded MOO algorithm for the manufacturing of resin transfer moulded composite parts. A vinyl ester-glass fibre-reinforced automotive bonnet and an RTM6-carbon fibre-reinforced aircraft wing flap composite parts were selected as the composite parts. An in-house coded MOSO and NSDE algorithms were developed to optimize mould-fill and curing phases for the selected composite parts. At first, vinyl ester and RTM6 resins were thermally characterized to develop the cure process windows through which the appropriate time-temperature cure cycles were identified for the curing of composite parts. Subsequently, the permeabilities of reinforcement fibre mats were measured using mould-filling experiments for their applicability in the mould-filling simulations. Then, a novel in-house coded NSDE algorithm was implemented for simultaneous optimization of two objectives namely, dry spot content and mould-fill time by changing the locations of gates and vents at the fixed input numbers of gates and vents. Consecutively, a newly proposed MOSO algorithm was implemented for the simultaneous optimization of three objectives namely dry spot content, mould-fill time and total number of ports by changing both the numbers as well as locations of gates and vents, simultaneously. Then, the efficacy of the proposed algorithms was examined with the trial and error process model simulations.

The thermal-cure process optimizations were performed using two-dwell and one-dwell mould heating parameters for the 12 mm thick automotive bonnet and the 5 mm thick aircraft wing flap composite parts, respectively. Subsequently, a novel in-house coded NSDE algorithm was developed and implemented for the simultaneous minimization of composite part thermal gradients and cure process time for both the studied composite parts. To evaluate the efficacy of the developed NSDE algorithm, the NSGA-II algorithm was also in-house coded for the simultaneous minimization of composite part thermal gradients and cure process time. The efficacy of the proposed algorithm was examined with the trial and error process model simulations and NSGA-II optimization algorithm in terms of a thermal gradient, cure time and uniform cure progression at the applied temperature cycles.

From the thermal characterization of neat resins, the modified Kamal and Sourour three-parameter model was effectively fitted to the experimental degree of cure vs. cure rate data for both vinyl ester and RTM6 resins. The obtained cure kinetic models, $\frac{d\alpha}{dt} = (1.04 \times 10^9 \times e^{-7359.8/T} \times \alpha^{0.284}) \times (1 - \alpha)^{0.857}$ and $\frac{d\alpha}{dt} = (3.2 \times 10^6 \times e^{-7706/T} \times \alpha^{0.774}) \times (1 - \alpha)^{1.097}$ were effectively employed during the simulation of vinyl ester resin and RTM6 resin composite parts processes, respectively.

From the mould-filling experiments, the effect of processing and material parameters on the reinforcement mat permeability was evaluated using mould-filling experiments. From the results, the reinforcement mat permeability was increased with an increase in porosity and decreased with an increase in injection pressure, number of mat layers and fluid viscosity. Subsequently, the permeability of the reinforcement mat as a function of material and process parameters was predicted using machine learning techniques. From the modelling analysis, the ANN and ANFIS techniques predicted permeability values qualitatively and quantitatively with R^2 values of 0.967 and 0.975, respectively. The effective permeability of $2.0 \times 10^{-9}\,\mathrm{m}^2$ and $1.0 \times 10^{-9}\,\mathrm{m}^2$ were used for the mould-filling simulations of the vinyl ester - glass fibre reinforced automotive bonnet and RTM6- carbon fibre reinforced aircraft wing flap composite parts, respectively.

From the mould-filling phase optimization results, the trial and error process predicted a lesser mould fill time of 15 minutes without dry spots when compared with the developed optimization algorithms for the bonnet part. However, the dry spot content obtained using the NSDE and MOSO algorithms was within the acceptable range of 1%. NSDE algorithm predicted a lesser dry spot content of 0.35% with a mould-filling time of 35 minutes for pre-fixed 2 gates and 4 vents injection strategy. In contrast, the MOSO algorithm predicted a dry

spot content of 0.295% and a mould-filling time of 25 minutes for two gates and three vents injection strategy. For wing flap composite part, the MOSO algorithm outperformed the NSDE algorithm and trial and error predictions in terms of lower dry spot content of 0.45%, utilizing only two gates and two vents of injection strategy, uniform speed of resin flow front progression towards the vents, lesser NFEs and a shorter computational time. Notably, the inclusion of a race-tracking effect at the boundary edges led to the absence of dry spot content at the edges of both composite parts. Additionally, it is worth noting that the final dry spot content observed around the vents in both composite parts may become insignificant as the simulation progresses and the allotted time elapses.

From the comparative assessment, the trial and error process was observed to be effective to other algorithms in terms of dry spot content, mould fill time, and uniform resin flow front progression towards the vents when compared to the optimization algorithms for the automotive bonnet composite part. However, the trial and error process required more iterations with trials in numbering and positioning ports and manual efforts for obtaining a single optimal solution. Conversely, the MOO algorithms were automated and needed less manual effort and problem-specific experience to obtain the number of Pareto optimal solutions. Significantly, the MOO algorithms deliver multiple optimality for the user in selecting the application-specific best design. Specifically, the MOSO algorithm was programmed to choose the number and locations of gates and vents automatically from the defined geometry space without manual interference. In comparison to the NSDE algorithm, the MOSO algorithm exhibited several advantages, including lower dry spot content, a reduced number of required ports, a more consistent speed of resin flow front progression towards the vents, significantly fewer evaluations (NFEs) and shorter computational time. It is worth noting that the MOSO algorithm had the capability to simultaneously optimize three objectives while the NSDE algorithm was limited to concurrently optimizing only two objectives.

In cure phase optimization, initially, isothermal trial and error cure process simulations were performed to obtain the time-temperature-degree of cure window for the aircraft wing flap composite panel using the identical temperature cycles used in RTM6 DSC experiments. From the isothermal trial and error cure process simulation results, the rate of cure for the composite panel was found to be slower than that of the neat resin cure rate due to fibre thermal resistance. From the cure difference analysis, the magnitude and the peak values of cure differences decreased with an increase in applied mould temperatures. Finally, the kinetics of cure difference progression was modelled as a function of neat resin cure conversion using the modified Kamal and Sourour autocatalytic model. From the kinetics of cure difference

progression, it is possible to predict the cure differences between neat resin and composite panel from the experimental neat resin cure conversion data with the applied time-temperature cycles. Thus, composite panel cure conversion can also be predicted from the cure difference data. This will help to adjudge the operable cure cycle for the composite part from the experimental neat resin cure conversion data. From the results, it was found that the mould temperature of 240ºC has the minimum cure differences at any resin cure conversion.

Then, non-isothermal trial and error cure process simulations were performed by manually changing the mould heating parameters to optimize the composite part cure profile of both composite parts. From the non-isothermal trial and error cure process simulation results, the composite part thermal profiles were obtained with a mid-thickness temperature overshoot of 7 to 9 K due to the improper choice of mould heating parameters for the bonnet part. In all trials studied for the wing flap part, it was found an increase in thermal gradient and a decrease in cure time with the increase in ramp rate and dwell time. Importantly, the trial and error process was found significantly challenging to optimize the multiple parameters simultaneously for both the composite parts. From the optimization results, the NSGA-II algorithm predicted a thermal gradient of 0.0068 K and a cure time of 40 minutes for the bonnet part and a thermal gradient of 0.007 K and a cure time of 40 minutes for the wing flap part. The NSDE algorithm predicted a lesser thermal gradient of 0.0008 K and cure time of 40 minutes than trial and error cure simulation and NSGA-II algorithm for the bonnet part and a lesser thermal gradient of 0.0022 K and cure time of 35 minutes for the wing flap part.

From the comparative assessment, the NSGA-II algorithm was found to be good at exploration but lags in exploitation leading to increased function evaluations and computational time. The NSDE algorithm was found to be effective in achieving faster convergence with less cure process and computational time when compared to the NSGA-II algorithm. The NSDE algorithm was observed to be effective in terms of a thermal gradient and cure time with the automated selection of the mould heating parameters when compared to the trial and error simulations. This may be attributed to the effective tuning of mould heating parameters through supervised learning iterations of the NSDE algorithm. Whereas, the trial and error simulation-based optimizations were found to be significantly challenging and time-consuming with the iterative manual selection of thermal-cure process parameters.

6.2 Future Scope

The research has successfully developed and implemented in-house coded MOSO and NSDE algorithms for optimizing the mould-fill and curing phases of the resin transfer moulding process. Future work can focus on refining these algorithms further.

1. Exploring the MOSO Algorithm for Micro-Scale and Meso-Scale Voids Investigation:

The developed MOSO (Multi-Objective Stochastic Optimization) algorithm has shown promise in optimizing complex systems. Extending the application of this algorithm to investigate micro-scale and meso-scale voids can be a substantial area of research. Simultaneously optimizing the total void content (combining macro, meso, and micro voids), mould-fill time and the number of ports is a challenging task. Future research can delve into refining the existing optimization model and algorithm to handle these multi-objective functions efficiently. This could involve refining the algorithm to handle intricate geometries and material properties and conducting comprehensive simulations and experiments to validate its effectiveness in void detection and analysis.

2. Addressing Cure Phase Optimization for Simultaneously Minimizing Temperature Overshoot, Cure Time and Thermal Gradients Using NSDE Algorithm:

The cure phase optimization of composite processing is crucial for determining the final properties of the product. Optimizing parameters such as temperature overshoot, cure time and thermal gradients is essential to achieve high-quality composite parts. The developed NSDE (Non-dominated Sorting Differential Evolution) algorithm provides an opportunity to tackle this optimization problem. Future research can focus on enhancing the capability of the algorithm by incorporating temperature overshoot as a new objective function for handling varying material properties and geometries. Furthermore, conducting detailed simulations and experimental studies to validate the optimized parameter's impact on the final product's structural integrity and performance would be valuable.

3. Implementation of Real-Time Process Control:

Developing a real-time process control system based on the optimized parameters could be an area of future research. Implementing sensors and actuators in the manufacturing setup that can adjust parameters dynamically based on real-time feedback can enhance the efficiency and quality of the manufacturing process. NSDE algorithm could be employed for predictive analytics, enabling the system to anticipate issues and adjust parameters proactively.

4. Development of User-Friendly Software Tool:

Translating complex algorithms and methodologies into a user-friendly software tool could significantly impact industrial adoption. Developing an intuitive interface that allows engineers and manufacturers to input their parameters, visualize the optimization process and interpret results could bridge the gap between academic research and practical industrial applications.

5. Real-World Implementation and Industrial Applications:

One of the crucial steps in any research is the practical implementation of developed algorithms and methodologies in real-world industrial settings. Future work can focus on collaborating with industries to implement optimized processes on their production lines. Case studies and feedback from industrial partners can provide valuable insights into the applicability, efficiency and economic viability of the developed algorithms. This practical validation can lead to the development of best practices and guidelines for implementing similar optimization techniques in various manufacturing sectors.

In summary, the future work in this PhD thesis can encompass a broad spectrum of research activities ranging from algorithmic enhancements and integration to practical implementations in industrial contexts. These efforts would not only contribute significantly to the academic community but also have a substantial impact on the efficiency and quality of manufacturing processes in diverse industries.

Thesis Contributions

The research work performed in this PhD thesis has made significant contributions to the research community in the process and product development of resin transfer moulded composite parts. The main objective of this work was to develop in-house coded multi-objective optimization (MOO) algorithms for the manufacturing of composite parts and the algorithm's efficacy was exhibited with the case studies of vinyl ester-glass fibre-reinforced automotive bonnet and RTM6-carbon fibre-reinforced aircraft wing flap composite parts.

1. Development of Novel In-House Coded MOO Algorithms: One of the primary contributions of this research is the development of two novel in-house coded MOO algorithms, namely the Multi-Objective Stochastic Optimization (MOSO) and the Non-dominated Sorting Differential Evolution (NSDE) algorithms. These algorithms were designed to optimize the mould-filling and curing phases of the composite parts by addressing critical aspects of the RTM manufacturing process.

2. Development of Simulation-based Optimization Framework: A robust and cost-effective methodology was developed to simulate and optimize the RTM mould-filling and curing processes through a framework based on simulation-driven optimization. This was accomplished by integrating a multi-objective optimization algorithm with process simulation through coupled multi-phase porous flow, transient heat transfer and resin cure kinetics models. The developed framework was implemented using COMSOL Livelink for MATLAB.

3. Development of Cure Process Window: The research provided a valuable contribution by developing the Time-Temperature-Cure Process Window of neat vinyl ester and RTM6 resins using thermal characterization. The obtained cure process window can help the composite practitioners to predict the cure completion time and degree of curing for the applied time- temperature cycles.

4. Reinforcement Fibre Mats Permeability Analysis: The study involved measuring reinforcement mat permeability as a function of various processing and material parameters through mould-filling experiments. The experimental data was utilized for predicting permeability values using Artificial Neural Network (ANN) and Adaptive Neuro-Fuzzy Inference System (ANFIS) machine learning models. These techniques provide valuable tools for researchers and engineers involved in the resin transfer moulding process.

4. Multi-Objective Optimization for Mould Filling: The development and application of the NSDE and MOSO algorithms for the simultaneous optimization of multiple objectives related to mould filling such as dry spot content, mould-fill time and the number and location of ports represent a significant advancement in the field. These algorithms design an effective injection strategy by simultaneously optimizing gate-vent numbers and locations. These algorithms offer efficient ways to achieve optimal mould-filling process by reducing manufacturing defects and improving efficiency.

5. Cure Phase Optimization: The research addressed the critical phase of curing in composite manufacturing. It developed a novel in-house coded NSDE algorithm for the simultaneous minimization of composite part thermal gradients and cure process time. The algorithm was compared to the widely used NSGA-II algorithm by providing insights into the strengths and weaknesses of different optimization approaches.

6. Cure Difference Modelling: The study introduced a novel approach to model cure differences between neat resins and composite panels by enabling the prediction of cure conversion for composite parts based on neat resin data. This approach has the potential to streamline the determination of operable cure cycles for composite manufacturing.

In summary, this PhD thesis has contributed significantly to the research community by developing innovative optimization algorithms and providing valuable data on resin thermal characterization and permeability. Additionally, it has advanced the understanding and optimization of critical phases in the manufacturing of composite parts. These contributions can benefit both academic researchers and industry professionals working in the field of composite materials and manufacturing.

References

[1]   T. W. Clyne and D. Hull, *An introduction to composite materials*. Cambridge university press, 2019.

[2]   R.-M. Wang, S.-R. Zheng, and Y. G. Zheng, *Polymer matrix composites and technology*. Elsevier, 2011.

[3]   S. G. Advani and E. M. Sozer, *Process modeling in composites manufacturing*. CRC press, 2002.

[4]   S. J. Joo, M. H. Yu, W. Seock Kim, J. W. Lee, and H. S. Kim, "Design and manufacture of automotive composite front bumper assemble component considering interfacial bond characteristics between over-molded chopped glass fiber polypropylene and continuous glass fiber polypropylene composite," *Compos. Struct.*, vol. 236, no. November 2019, p. 111849, 2020, doi: 10.1016/j.compstruct.2019.111849.

[5]   K. Friedrich and A. A. Almajid, "Manufacturing aspects of advanced polymer composites for automotive applications," *Appl. Compos. Mater.*, vol. 20, no. 2, pp. 107–128, 2013, doi: 10.1007/s10443-012-9258-7.

[6]   L. W. Cheah, "Cars on a diet: the material and energy impacts of passenger vehicle weight reduction in the US," Massachusetts Institute of Technology, 2010.

[7]   H. Mohammadi *et al.*, "Lightweight Glass Fiber-Reinforced Polymer Composite for Automotive Bumper Applications: A Review," *Polymers (Basel).*, vol. 15, no. 1, pp. 1–30, 2023, doi: 10.3390/polym15010193.

[8]   W. Zhang and J. Xu, "Advanced lightweight materials for Automobiles: A review," *Mater. Des.*, vol. 221, p. 110994, 2022, doi: 10.1016/j.matdes.2022.110994.

[9]   R. Slayton and G. Spinardi, "Radical innovation in scaling up: Boeing's Dreamliner and the challenge of socio-technical transitions," *Technovation*, vol. 47, no. September, pp. 47–58, 2016, doi: 10.1016/j.technovation.2015.08.004.

[10]   Y. Li, Y. Xiao, L. Yu, K. Ji, and D. Li, "A review on the tooling technologies for composites manufacturing of aerospace structures: materials, structures and processes," *Compos. Part A Appl. Sci. Manuf.*, vol. 154, no. June 2021, p. 106762, 2022, doi: 10.1016/j.compositesa.2021.106762.

[11]   S. G. Advani and K.-T. Hsiao, *Manufacturing techniques for polymer matrix composites (PMCs)*. Elsevier, 2012.

[12]   M. Torres, "Parameters' monitoring and in-situ instrumentation for resin transfer

moulding: A review," *Compos. Part A Appl. Sci. Manuf.*, vol. 124, p. 105500, 2019.

[13] E. M. Sozer, P. Simacek, and S. G. Advani, "Resin transfer molding (RTM) in polymer matrix composites," in *Manufacturing techniques for polymer matrix composites (PMCs)*, Woodhead Publishing Limited, 2012, pp. 245–309.

[14] C. H. Park, A. Lebel, A. Saouab, J. Bréard, and W. Il Lee, "Modeling and simulation of voids and saturation in liquid composite molding processes," *Compos. Part A*, vol. 42, pp. 658–668, 2011, doi: 10.1016/j.compositesa.2011.02.005.

[15] X. Hui, Y. Xu, W. Zhang, and W. Zhang, "Cure process evaluation of CFRP composites via neural network: From cure kinetics to thermochemical coupling," *Compos. Struct.*, vol. 288, p. 115341, 2022, doi: 10.1016/j.compstruct.2022.115341.

[16] D. Dolkun, H. Wang, H. Wang, and Y. Ke, "An efficient thermal cure profile design method for autoclave curing of large size mold," *Int. J. Adv. Manuf. Technol.*, vol. 114, no. 7–8, pp. 2499–2514, 2021, doi: 10.1007/s00170-021-07015-4.

[17] Y. K. Hamidi and M. C. Altan, "Process Induced Defects in Liquid Molding Processes of Composites," *Int. Polym. Process.*, vol. 32, no. 5, pp. 527–544, 2017.

[18] P. Mitschang, A. Ogale, J. Schlimbach, F. Weyrauch, and C. Weimer, "Preform technology: a necessary requirement for quality controlled LCM-processes," *Polym. Polym. Compos.*, vol. 11, no. 8, pp. 605–622, 2003.

[19] K. Raghu Raja Pandiyan, G. Kundu, S. Neogi, and J. Patel, "Development of manufacturing technology for cab front using resin transfer molding process," *J. Compos. Mater.*, vol. 44, no. 18, pp. 2217–2231, 2010, doi: 10.1177/0021998310364168.

[20] B. X. Chai *et al.*, "Simulation-based optimisation for injection configuration design of liquid composite moulding processes: A review," *Compos. Part A Appl. Sci. Manuf.*, vol. 149, no. June, p. 106540, 2021, doi: 10.1016/j.compositesa.2021.106540.

[21] G. Struzziero and A. A. Skordos, "Multi-objective optimisation of the cure of thick components," *Compos. Part A Appl. Sci. Manuf.*, vol. 93, pp. 126–136, 2017.

[22] R. R. PANDIYAN KUPPUSAMY and S. Neogi, "Influence of curing agents on gelation and exotherm behaviour of an unsaturated polyester resin," *Bull. Mater. Sci.*, vol. 36, pp. 1217–1224, 2013.

[23] R. R. P. Kuppusamy, V. M. Shinde, and S. Neogi, "Measurement of effective permeability of reinforcement mats using sensitivity analysis," *Polym. Compos.*, vol. 33, no. 8, pp. 1445–1454, 2012.

[24] B. Yenilmez and E. M. Sozer, "A grid of dielectric sensors to monitor mold filling and

resin cure in resin transfer molding," *Compos. part a Appl. Sci. Manuf.*, vol. 40, no. 4, pp. 476–489, 2009.

[25] S. Mouton, D. Teissandier, P. Sebastian, and J.-P. Nadeau, "Manufacturing requirements in design: The RTM process in aeronautics," *Compos. Part A Appl. Sci. Manuf.*, vol. 41, no. 1, pp. 125–130, 2010.

[26] H. Grössing, N. Stadlmajer, E. Fauster, M. Fleischmann, and R. Schledjewski, "Flow front advancement during composite processing: predictions from numerical filling simulation tools in comparison with real-world experiments," *Polym. Compos.*, vol. 37, no. 9, pp. 2782–2793, 2016.

[27] K. Raghu Raja Pandiyan and S. Neogi, "Simulation of air entrapment and resin curing during manufacturing of composite cab front by resin transfer moulding process," *Arch. Metall. Mater.*, vol. 62, 2017.

[28] S. Pavel, "Desirable Features in Mold Filling Simulations for Liquid Composite Molding Processes," *Polym. Compos.*, vol. 25, no. 4, pp. 355–367, 2004, doi: 10.1002/pc.20029.

[29] Y. Geng, J. Jiang, and N. Chen, "Local impregnation behavior and simulation of non-crimp fabric on curved plates in vacuum assisted resin transfer molding," *Compos. Struct.*, vol. 208, pp. 517–524, 2019, doi: 10.1016/j.compstruct.2018.10.054.

[30] R. Masoodi, K. M. Pillai, N. Grahl, and H. Tan, "Numerical simulation of LCM mold-filling during the manufacture of natural fiber composites," *J. Reinf. Plast. Compos.*, vol. 31, no. 6, pp. 363–378, 2012, doi: 10.1177/0731684412438629.

[31] A. N. Sina, A. Forghani, R. Vaziri, and A. Poursartip, "A three-phase integrated fl ow-stress model for processing of composites," *Mech. Mater.*, vol. 117, no. March 2017, pp. 152–164, 2018, doi: 10.1016/j.mechmat.2017.10.012.

[32] S. G. Advani, *2 . 2 Role of Process Models in Composites Manufacturing*, vol. 2. Elsevier Ltd., 2018.

[33] S. C. Amico, J. Á. Souza, A. Gilson, and B. De Lima, "Resin transfer molding process : a numerical and experimental investigation," *Int. J. Multiphys.*, vol. 7, no. 2, pp. 125–136, 2013.

[34] J. Luo, Z. Liang, C. Zhang, and B. Wang, "Optimum tooling design for resin transfer molding with virtual manufacturing and artificial intelligence," *Compos. Part A Appl. Sci. Manuf.*, vol. 32, no. 6, pp. 877–888, 2001.

[35] G. Struzziero and A. A. Skordos, "Multi-objective optimisation of the cure of thick components," *Compos. Part A Appl. Sci. Manuf.*, vol. 93, no. November, pp. 126–136,

2017, doi: 10.1016/j.compositesa.2016.11.014.

[36] K. I. Tifkitsis, T. S. Mesogitis, G. Struzziero, and A. A. Skordos, "Stochastic multi-objective optimisation of the cure process of thick laminates," *Compos. Part A Appl. Sci. Manuf.*, vol. 112, no. June, pp. 383–394, 2018, doi: 10.1016/j.compositesa.2018.06.015.

[37] S. P. Adam, S.-A. N. Alexandropoulos, P. M. Pardalos, and M. N. Vrahatis, "No free lunch theorem: A review," *Approx. Optim. Algorithms, Complex. Appl.*, pp. 57–82, 2019.

[38] J. Nocedal and S. J. Wright, *Numerical optimization*. Springer, 1999.

[39] K. Deb, *Optimization for engineering design: Algorithms and examples*. PHI Learning Pvt. Ltd., 2012.

[40] K. DEB, *Optimization for engineering design*, 2nd ed. Prentice Hall, 2004.

[41] R. S. Parpinelli, H. S. Lopes, and A. A. Freitas, "Data mining with an ant colony optimization algorithm," *IEEE Trans. Evol. Comput.*, vol. 6, no. 4, pp. 321–332, 2002.

[42] X.-S. Yang and S. Deb, "Cuckoo search: recent advances and applications," *Neural Comput. Appl.*, vol. 24, no. 1, pp. 169–174, 2014.

[43] P. Civicioglu and E. Besdok, "A conceptual comparison of the Cuckoo-search, particle swarm optimization, differential evolution and artificial bee colony algorithms," *Artif. Intell. Rev.*, vol. 39, no. 4, pp. 315–346, 2013.

[44] J. J. D. Nesamalar, P. Venkatesh, and S. C. Raja, "Managing multi-line power congestion by using Hybrid Nelder–Mead – Fuzzy Adaptive Particle Swarm Optimization (HNM-FAPSO)," *Appl. Soft Comput.*, vol. 43, pp. 222–234, 2016, doi: https://doi.org/10.1016/j.asoc.2016.02.013.

[45] A. F. Ali and M. A. Tawhid, "A hybrid particle swarm optimization and genetic algorithm with population partitioning for large scale optimization problems," *Ain Shams Eng. J.*, vol. 8, no. 2, pp. 191–206, 2017, doi: https://doi.org/10.1016/j.asej.2016.07.008.

[46] A. Zade, N. Patel, and N. Padhiyar, "Effective Constrained Handling by Hybridized Cuckoo Search Algorithm with Box Complex Method," in *IFAC-PapersOnLine*, 2017, vol. 50, no. 2, doi: 10.1016/j.ifacol.2017.12.038.

[47] M. Lin, M. Murphy, and H. Hahn, "Resin Transfer Molding Process Optimization," *Compos. Part A*, no. April 2000, 2000, doi: 10.1016/S1359-835X(99)00054-8.

[48] G. Struzziero, J. J. E. Teuwen, and A. A. Skordos, "Numerical optimisation of thermoset composites manufacturing processes: A review," *Compos. Part A Appl. Sci. Manuf.*, vol.

124, p. 105499, 2019, doi: https://doi.org/10.1016/j.compositesa.2019.105499.

[49] N. Van Eck and L. Waltman, "Software survey: VOSviewer, a computer program for bibliometric mapping," *Scientometrics*, vol. 84, no. 2, pp. 523–538, 2010.

[50] T. Tušar and B. Filipič, "Differential evolution versus genetic algorithms in multiobjective optimization," in *International Conference on Evolutionary Multi-Criterion Optimization*, 2007, pp. 257–271.

[51] K. Raghu Raja Pandiyan and S. Neogi, "Viscosity modeling of a medium reactive unsaturated polyester resin used for liquid composite molding process," *J. Appl. Polym. Sci.*, vol. 125, no. 2, pp. 1400–1408, 2012.

[52] R. Matsuzaki, R. Yokoyama, T. Kobara, and T. Tachikawa, "Multi-Objective Curing Optimization of Carbon Fiber Composite Materials Using Data Assimilation and Localized Heating," *Compos. Part A*, vol. 119, pp. 61–72, 2019, doi: 10.1016/j.compositesa.2019.01.021.

[53] E. Ruiz and F. Trochu, "Multi-criteria thermal optimization in liquid composite molding to reduce processing stresses and cycle time," *Compos. Part A*, vol. 37, pp. 913–924, 2006, doi: 10.1016/j.compositesa.2005.06.010.

[54] R. Raja Pandiyan K, S. Chakraborty, G. Kundu, and S. Neogi, "Curing kinetics of medium reactive unsaturated polyester resin used for liquid composite molding process," *J. Appl. Polym. Sci.*, vol. 114, no. 4, pp. 2415–2420, 2009.

[55] W. Yang, S. Lu, L. Xiang, and W. Liu, "Simulation of non-isothermal resin transfer molding process cycle and optimization of temperature system," *J. Reinf. Plast. Compos.*, vol. 38, no. 1, pp. 3–14, 2019, doi: 10.1177/0731684418800599.

[56] K. I. Tifkitsis, T. S. Mesogitis, G. Struzziero, and A. A. Skordos, "Stochastic multi-objective optimisation of the cure process of thick laminates," *Compos. Part A*, vol. 112, pp. 383–394, 2018.

[57] B. Lucio and J. L. De La Fuente, "Kinetic and thermodynamic analysis of the polymerization of polyurethanes by a rheological method," *Thermochim. Acta*, vol. 625, pp. 28–35, 2016, doi: 10.1016/j.tca.2015.12.012.

[58] P. E. Jahromi, A. Shojaei, and S. M. R. Pishvaie, "Prediction and optimization of cure cycle of thick fiber-reinforced composite parts using dynamic artificial neural networks," *J. Reinf. Plast. Compos.*, vol. 31, no. 18, pp. 1201–1215, 2012, doi: 10.1177/0731684412451937.

[59] S. Du, Z.-S. Guo, B. Zhang, and Z. Wu, "Cure kinetics of epoxy resin used for advanced composites," *Polym. Int.*, vol. 53, no. 9, pp. 1343–1347, 2004.

[60] B. Janković, "The kinetic analysis of isothermal curing reaction of an unsaturated polyester resin: Estimation of the density distribution function of the apparent activation energy," *Chem. Eng. J.*, vol. 162, no. 1, pp. 331–340, 2010.

[61] B. L. Grunden and C. S. P. Sung, "Cure characterization of unsaturated polyester resin by near-IR and mid-IR spectroscopy," *Macromolecules*, vol. 36, no. 9, pp. 3166–3173, 2003.

[62] M. Henne, C. Breyer, M. Niedermeier, and P. Ermanni, "A new kinetic and viscosity model for liquid composite molding simulations in an industrial environment," *Polym. Compos.*, vol. 25, no. 3, pp. 255–269, 2004.

[63] Y. Liu, J. Gao, and R. Zhang, "Thermal properties and stability of boron-containing phenol-formaldehyde resin formed from paraformaldehyde," *Polym. Degrad. Stab.*, vol. 77, no. 3, pp. 495–501, 2002.

[64] I. B. Recalde, D. Recalde, R. Garc\'\ia-Lopera, and C. M. Gómez, "FTIR isothermal cure kinetics and morphology of dicyanate ester resin/polysulfone blends," *Eur. Polym. J.*, vol. 41, no. 11, pp. 2635–2643, 2005.

[65] J. L. Martin, "Kinetic analysis of two DSC peaks in the curing of an unsaturated polyester resin catalyzed with methylethylketone peroxide and cobalt octoate," *Polym. Eng. \& Sci.*, vol. 47, no. 1, pp. 62–70, 2007.

[66] A. Arrillaga, A. M. Zaldua, R. M. Atxurra, and A. S. Farid, "Techniques used for determining cure kinetics of rubber compounds," *Eur. Polym. J.*, vol. 43, no. 11, pp. 4783–4799, 2007.

[67] T. Behzad and M. Sain, "Finite element modeling of polymer curing in natural fiber reinforced composites," *Compos. Sci. Technol.*, vol. 67, pp. 1666–1673, 2007, doi: 10.1016/j.compscitech.2006.06.021.

[68] M. R. Kamal and S. Sourour, "Kinetics and thermal characterization of thermoset cure," *Polym. Eng. \& Sci.*, vol. 13, no. 1, pp. 59–64, 1973.

[69] J. M. Kenny, "Determination of autocatalytic kinetic model parameters describing thermoset cure," *J. Appl. Polym. Sci.*, vol. 51, pp. 761–764, 1994.

[70] L. Zhao and X. Hu, "A variable reaction order model for prediction of curing kinetics of thermosetting polymers," *Polymer (Guildf).*, vol. 48, no. 20, pp. 6125–6133, 2007.

[71] Z. Zhang and C. P. Wong, "Modeling of the curing kinetics of no-flow underfill in flip-chip applications," *Ieee Trans. Components Packag. Technol.*, vol. 27, no. 2, pp. 383–390, 2004.

[72] V. M. Gonzalez-Romero and N. Casillas, "Isothermal and temperature programmed

kinetic studies of thermosets," *Polym. Eng. \& Sci.*, vol. 29, no. 5, pp. 295–301, 1989.

[73] A. Yousefi, P. G. Lafleur, and R. Gauvin, "Kinetic studies of thermoset cure reactions: a review," *Polym. Compos.*, vol. 18, no. 2, pp. 157–168, 1997.

[74] A. O. Siddiqui, P. Sudher, and B. V. S. R. Murthy, "Cure kinetics modeling of cyanate-ester resin system," *Thermochim. Acta*, vol. 554, pp. 8–14, 2013, doi: 10.1016/j.tca.2012.12.009.

[75] M. Javdanitehran, D. C. Berg, E. Duemichen, and G. Ziegmann, "An iterative approach for isothermal curing kinetics modelling of an epoxy resin system," *Thermochim. Acta*, vol. 623, pp. 72–79, 2016, doi: 10.1016/j.tca.2015.11.014.

[76] M. A. Vargas, H. Vázquez, and G. Guthausen, "Non-isothermal curing kinetics and physical properties of MMT-reinforced unsaturated polyester (UP) resins," *Thermochim. Acta*, vol. 611, pp. 10–19, 2015, doi: 10.1016/j.tca.2014.12.024.

[77] J. Lv *et al.*, "Study of the curing kinetics of melamine/phthalonitrile resin system," *Thermochim. Acta*, vol. 683, no. November 2019, p. 178442, 2020, doi: 10.1016/j.tca.2019.178442.

[78] V. García-Martínez, M. R. Gude, and A. Ureña, "Understanding the curing kinetics and rheological behaviour of a new benzoxazine resin for carbon fibre composites," *React. Funct. Polym.*, vol. 129, pp. 103–110, 2018, doi: 10.1016/j.reactfunctpolym.2017.02.005.

[79] S. S. Hwang, S. Y. Park, G. C. Kwon, and W. J. Choi, "Cure kinetics and viscosity modeling for the optimization of cure cycles in a vacuum-bag-only prepreg process," *Int. J. Adv. Manuf. Technol.*, vol. 99, no. 9–12, pp. 2743–2753, 2018, doi: 10.1007/s00170-018-2467-y.

[80] S. Jaswal and B. Gaur, "New trends in vinyl ester resins," *Rev. Chem. Eng.*, vol. 30, no. 6, pp. 567–581, 2014, doi: 10.1515/revce-2014-0012.

[81] T. F. Scott, W. D. Cook, and J. S. Forsythe, "Photo-DSC cure kinetics of vinyl ester resins. I. Influence of temperature," *Polymer (Guildf).*, vol. 43, no. 22, pp. 5839–5845, 2002, doi: 10.1016/S0032-3861(02)00490-1.

[82] S. Crawford and C. T. Lungu, "Influence of temperature on styrene emission from a vinyl ester resin thermoset composite material," *Sci. Total Environ.*, vol. 409, no. 18, pp. 3403–3408, 2011, doi: 10.1016/j.scitotenv.2011.05.042.

[83] M. S. Hong and I. J. Chung, "The cure behavior of vinyl ester resin with low profile additive I. Cure kinetics and TTT cure diagram," *Polym. J.*, vol. 23, no. 6, pp. 747–755, 1991, doi: 10.1295/polymj.23.747.

[84] M. Sultania, J. S. P. Rai, and D. Srivastava, "Modeling and simulation of curing kinetics for the cardanol-based vinyl ester resin by means of non-isothermal DSC measurements," *Mater. Chem. Phys.*, vol. 132, no. 1, pp. 180–186, 2012, doi: 10.1016/j.matchemphys.2011.11.022.

[85] J. S. Martin, J. M. Laza, M. L. Morraás, M. Rodriíguez, and L. M. Leoón, "Study of the curing process of a vinyl ester resin by means of TSR and DMTA," *Polymer (Guildf).*, vol. 41, no. 11, pp. 4203–4211, 2000, doi: 10.1016/S0032-3861(99)00631-X.

[86] W. D. Cook, G. P. Simon, P. J. Burchill, M. Lau, and T. J. Fitch, "Curing kinetics and thermal properties of vinyl ester resins," *J. Appl. Polym. Sci.*, vol. 64, no. 4, pp. 769–781, 1997, doi: 10.1002/(SICI)1097-4628(19970425)64:4<769::AID-APP16>3.0.CO;2-P.

[87] B. N. V. S. Ganesh Gupta K, M. M. Hiremath, B. C. Ray, and R. K. Prusty, "Improved mechanical responses of GFRP composites with epoxy-vinyl ester interpenetrating polymer network," *Polym. Test.*, vol. 93, no. December 2020, p. 107008, 2021, doi: 10.1016/j.polymertesting.2020.107008.

[88] A. Osei Bonsu, W. Liang, C. Mensah, and B. Yang, "Assessing the mechanical behavior of glass and basalt reinforced vinyl ester composite under artificial seawater environment," *Structures*, vol. 38, no. May 2021, pp. 961–978, 2022, doi: 10.1016/j.istruc.2022.02.053.

[89] J. Thomason and G. Xypolias, "Hydrothermal Ageing of Glass Fibre Reinforced Vinyl Ester Composites: A Review," *Polymers (Basel).*, vol. 15, no. 4, 2023, doi: 10.3390/polym15040835.

[90] S. Shevtsov, I. Zhilyaev, S. H. Chang, J. K. Wu, N. Snezhina, and J. P. Huang, "Two-stage numerical approach for reliable recognition of dry spots at the VAP infusion of large composite parts of complex shape," *Compos. Struct.*, vol. 259, no. December 2020, p. 113437, 2021, doi: 10.1016/j.compstruct.2020.113437.

[91] HEXCEL, "HexFlow RTM6," *HexFlow RTM6 180°C mono-component epoxy system for Resin Transfer Moulding and Infusion technologies Product Data*, 2016.

[92] N. Causse *et al.*, "Polymerization study and rheological behavior of a RTM6 epoxy resin system during preprocessing step," *J. Therm. Anal. Calorim.*, vol. 119, no. 1, pp. 329–336, 2015, doi: 10.1007/s10973-014-4147-y.

[93] P. Navabpour, A. Nesbitt, B. Degamber, G. Fernando, T. Mann, and R. Day, "Comparison of the curing kinetics of the RTM6 epoxy resin system using differential scanning calorimetry and a microwave-heated calorimeter," *J. Appl. Polym. Sci.*, vol.

99, no. 6, pp. 3658–3668, 2006, doi: 10.1002/app.22869.

[94] A. A. Skordos and I. K. Pazitridge, "Cure Kinetics Modeling of Epoxy Resins Using a Non-Pa rametric Nu me rica l Procedure," *Polym. Eng. Sci.*, vol. 41, no. 5, pp. 793–805, 2001.

[95] G. Struzziero, B. Remy, and A. A. Skordos, "Measurement of thermal conductivity of epoxy resins during cure," *J. Appl. Polym. Sci.*, vol. 136, no. 5, pp. 1–10, 2019, doi: 10.1002/app.47015.

[96] X. A. Aduriz *et al.*, "Quantitative control of RTM6 epoxy resin polymerisation by optical index determination," *Compos. Sci. Technol.*, vol. 67, no. 15–16, pp. 3196–3201, 2007, doi: 10.1016/j.compscitech.2007.04.008.

[97] T. S. Gross, H. Jafari, I. Tsukrov, H. Bayraktar, and J. Goering, "Curing cycle modification for RTM6 to reduce hydrostatic residual tensile stress in 3D woven composites," *J. Appl. Polym. Sci.*, vol. 133, no. 17, pp. 1–7, 2016, doi: 10.1002/app.43373.

[98] Y. Nawab, C. Sonnenfeld, A. Saouab, R. Agogué, and P. Beauchêne, "Characterisation and modelling of thermal expansion coefficient of woven carbon/epoxy composite and its application to the determination of spring-in," *J. Compos. Mater.*, vol. 51, no. 11, pp. 1527–1538, 2017, doi: 10.1177/0021998316661404.

[99] M. Seyednourani, M. Yildiz, and H. S. Sas, "A two-stage optimization methodology for gate and vent locations and distribution media layout for liquid composite molding process," *Compos. Part A Appl. Sci. Manuf.*, vol. 149, no. June, p. 106522, 2021, doi: 10.1016/j.compositesa.2021.106522.

[100] K. R. R. Pandiyan, G. Kundu, S. Neogi, and J. Patel, "Development of Manufacturing Technology for Cab Front Using Resin Transfer Molding Process," *J. Compos. Mater.*, vol. 44, no. 18, pp. 2217–2231, 2010, doi: 10.1177/0021998310364168.

[101] S. Salokhe, M. Rahmati, and R. Masoodi, "Numerical modelling of the flow in a swelling preform during LCM mould filling," *J. Reinf. Plast. Compos.*, vol. 40, no. 13–14, pp. 490–504, 2021, doi: 10.1177/0731684420975197.

[102] D. Pantaloni, A. Bourmaud, C. Baley, M. J. Clifford, M. H. Ramage, and D. U. Shah, "A review of permeability and flow simulation for liquid composite moulding of plant fibre composites," *Materials (Basel).*, vol. 13, no. 21, pp. 1–23, 2020, doi: 10.3390/ma13214811.

[103] I. D. Patiño and C. Nieto-Londoño, *Boundary element techniques for multiscale filling simulations in dual-scale fibrous reinforcements using two lumped approaches*, vol. 68,

no. 6. Springer Berlin Heidelberg, 2021.

[104] N. K. Naik, M. Sirisha, and A. Inani, "Permeability characterization of polymer matrix composites by RTM/VARTM," *Prog. Aerosp. Sci.*, vol. 65, pp. 22–40, 2014, doi: 10.1016/j.paerosci.2013.09.002.

[105] M. A. Kabachi, L. Stettler, S. Arreguin, and P. Ermanni, "Concurrent characterization of through-thickness permeability and compaction of fiber reinforcements," *Compos. Part A Appl. Sci. Manuf.*, vol. 141, p. 106203, 2021, doi: 10.1016/j.compositesa.2020.106203.

[106] B. Räckers, "Introduction to resin transfer moulding," in *Resin Transfer Moulding for Aerospace Structures*, T. M. Kruckenberg and R. Paton, Eds. Dordrecht: Springer Netherlands, 1998, pp. 1–24.

[107] F. Lionetto, F. Montagna, and A. Maffezzoli, "Out-Of-Plane permeability evaluation of carbon fiber preforms by ultrasonic wave propagation," *Materials (Basel).*, vol. 13, no. 12, pp. 1–18, 2020, doi: 10.3390/ma13122684.

[108] A. A. X. da Silva, J. A. Souza, A. Manes, and S. C. Amico, "In-plane Permeability and Mechanical Properties of R-Glass/Aramid Hybrid Composites," *J. Mater. Eng. Perform.*, vol. 29, no. 7, pp. 4484–4492, 2020, doi: 10.1007/s11665-020-04944-1.

[109] E. Rodríguez, F. Giacomelli, and A. Vazquez, "Permeability-porosity relationship in RTM for different fiberglass and natural reinforcements," *J. Compos. Mater.*, vol. 38, no. 3, pp. 259–268, 2004, doi: 10.1177/0021998304039269.

[110] M. L. Diallo, R. Gauvin, and F. Trochu, "Key factors affecting the permeability measurement in continuous fiber reinforcements," in *Proceedings of ICCM*, 1997, vol. 11, p. 441.

[111] H. Tan and K. M. Pillai, "Effect of fiber-mat anisotropy on 1D mold filling in LCM: a numerical investigation," *Polym. Compos.*, vol. 29, no. 8, pp. 869–882, 2008.

[112] T. S. Lundström, B. R. Gebart, and E. Sandlund, "In-plane permeability measurements on fiber reinforcements by the multi-cavity parallel flow technique," *Polym. Compos.*, vol. 20, no. 1, pp. 146–154, 1999.

[113] R. S. Parnas, "Preform permeability," in *Resin Transfer Moulding for Aerospace Structures*, T. M. Kruckenberg and R. Paton, Eds. Dordrecht: Springer Netherlands, 1998, pp. 177–224.

[114] Y. Ma and R. Shishoo, "Permeability Characterization of Different Architectural Fabrics," *J. Compos. Mater.*, vol. 33, no. 8, pp. 729–750, 1999, doi: 10.1177/002199839903300805.

[115] V. H. Hammond and A. C. Loos, "The Effects of Fluid Type and Viscosity on the Steady-State and Advancing Front Permeability Behavior of Textile Preforms," *J. Reinf. Plast. Compos.*, vol. 16, no. 1, pp. 50–72, Jan. 1997, doi: 10.1177/073168449701600105.

[116] A. Shojaei, F. Trochu, S. R. Ghaffarian, S. M. H. Karimian, and L. Lessard, "An experimental study of saturated and unsaturated permeabilities in resin transfer molding based on unidirectional flow measurements," *J. Reinf. Plast. Compos.*, vol. 23, no. 14, pp. 1515–1536, 2004.

[117] S. Amico and C. Lekakou, "An experimental study of the permeability and capillary pressure in resin-transfer moulding," *Compos. Sci. Technol.*, vol. 61, no. 13, pp. 1945–1959, 2001, doi: https://doi.org/10.1016/S0266-3538(01)00104-X.

[118] Y. Oya, T. Matsumiya, A. Ito, R. Matsuzaki, and T. Okabe, "Gate optimization for resin transfer molding in dual-scale porous media: Numerical simulation and experiment measurement," *J. Compos. Mater.*, vol. 54, no. 16, pp. 2131–2145, 2020, doi: 10.1177/0021998319890122.

[119] K. Hoes *et al.*, "New set-up for measurement of permeability properties of fibrous reinforcements for RTM," *Compos. Part A Appl. Sci. Manuf.*, vol. 33, no. 7, pp. 959–969, 2002, doi: https://doi.org/10.1016/S1359-835X(02)00035-0.

[120] M. Bodaghi, S. V Lomov, P. Simacek, N. C. Correia, and S. G. Advani, "On the variability of permeability induced by reinforcement distortions and dual scale flow in liquid composite moulding: A review," *Composites Part A: Applied Science and Manufacturing*, vol. 120. Elsevier Ltd, pp. 188–210, 2019, doi: 10.1016/j.compositesa.2019.03.004.

[121] J. R. Weitzenböck, R. A. Shenoi, and P. A. Wilson, "Radial flow permeability measurement. Part A: theory," *Compos. Part A Appl. Sci. Manuf.*, vol. 30, no. 6, pp. 781–796, 1999, doi: 10.1016/S1359-835X(98)00183-3.

[122] C. Di Fratta, F. Klunker, F. Trochu, and P. Ermanni, "Characterization of textile permeability as a function of fiber volume content with a single unidirectional injection experiment," *Compos. Part A Appl. Sci. Manuf.*, vol. 77, pp. 238–247, 2015, doi: https://doi.org/10.1016/j.compositesa.2015.05.021.

[123] P. Maji, A. Jain, N. Dutta, A. O. Siddiqui, D. Niyogi, and S. Neogi, "Characterization of effective permeability of prepreg fibers under autoclave molding process conditions using process model simulations," *J. Text. Inst.*, vol. 112, no. 1, pp. 1–7, 2021, doi: 10.1080/00405000.2020.1748803.

[124] R. R. P. Kuppusamy, V. M. Shinde, and S. Neogi, "Measurement of Effective Permeability of Reinforcement Mats using Sensitivity Analysis," *Polym. Compos.*, 2012, doi: 10.1002/pc.22272.

[125] H. Tan, T. Roy, and K. M. Pillai, "Variations in unsaturated flow with flow direction in resin transfer molding: An experimental investigation," *Compos. Part A Appl. Sci. Manuf.*, vol. 38, no. 8, pp. 1872–1892, 2007, doi: 10.1016/j.compositesa.2007.04.002.

[126] E. Heardman, C. Lekakou, and M. G. Bader, "In-plane permeability of sheared fabrics," *Compos. Part A Appl. Sci. Manuf.*, vol. 32, no. 7, pp. 933–940, 2001.

[127] D. S. Cairns, D. R. Humbert, and J. F. Mandell, "Modeling of resin transfer molding of composite materials with oriented unidirectional plies," *Compos. Part A Appl. Sci. Manuf.*, vol. 30, no. 3, pp. 375–383, 1999.

[128] M. Ehresmann, A. Amiri, and C. Ulven, "The effect of different variables on in-plane radial permeability of natural fiber mats," *J. Reinf. Plast. Compos.*, vol. 37, no. 19, pp. 1191–1201, Apr. 2016, doi: 10.1177/0731684416646458.

[129] R. Umer, S. Bickerton, and A. Fernyhough, "Characterising wood fibre mats as reinforcements for liquid composite moulding processes," *Compos. Part A Appl. Sci. Manuf.*, vol. 38, no. 2, pp. 434–448, 2007, doi: https://doi.org/10.1016/j.compositesa.2006.03.003.

[130] G. Rieber and P. Mitschang, "2D Permeability changes due to stitching seams," *Compos. Part A Appl. Sci. Manuf.*, vol. 41, no. 1, pp. 2–7, 2010, doi: https://doi.org/10.1016/j.compositesa.2009.09.006.

[131] S. K. Kim and I. M. Daniel, "Observation of permeability dependence on flow rate and implications for liquid composite molding," *J. Compos. Mater.*, vol. 41, no. 7, pp. 837–849, 2007, doi: 10.1177/0021998306067061.

[132] Y. Li, L. Xie, and H. Ma, "Permeability and mechanical properties of plant fiber reinforced hybrid composites," *Mater. Des.*, vol. 86, pp. 313–320, 2015, doi: 10.1016/j.matdes.2015.06.164.

[133] G. Francucci, E. S. Rodríguez, and A. Vázquez, "Study of saturated and unsaturated permeability in natural fiber fabrics," *Compos. Part A Appl. Sci. Manuf.*, vol. 41, no. 1, pp. 16–21, 2010, doi: 10.1016/j.compositesa.2009.07.012.

[134] R. Umer, S. Bickerton, and A. Fernyhough, "The effect of yarn length and diameter on permeability and compaction response of flax fibre mats," *Compos. Part A Appl. Sci. Manuf.*, vol. 42, no. 7, pp. 723–732, 2011, doi: https://doi.org/10.1016/j.compositesa.2011.02.010.

[135] E. M. Languri and K. Pillai, "Effect of aspect ratio on measured permeability and flow-front progress in 1D flow experiment," *Int. J. Fluid Mech. Res.*, vol. 38, no. 6, 2011.

[136] J. S. U. Schell, M. Siegrist, and P. Ermanni, "Experimental Determination of the Transversal and Longitudinal Fibre Bundle Permeability," *Appl. Compos. Mater.*, vol. 14, no. 2, pp. 117–128, 2007, doi: 10.1007/s10443-007-9035-1.

[137] "Amico and Lekakau." .

[138] D. A. Steenkamer, S. H. McKnight, D. J. Wilkins, and V. M. Karbhari, "Experimental characterization of permeability and fibre wetting for liquid moulding," *J. Mater. Sci.*, vol. 30, pp. 3207–3215, 1995.

[139] D. A. Steenkamer, D. J. Wilkins, and V. M. Karbhari, "Influence of test fluid on fabric permeability measurements and implications for processing of liquid moulded composites," *J. Mater. Sci. Lett.*, vol. 12, pp. 971–973, 1993.

[140] Y. Luo, I. Verpoest, K. Hoes, M. Vanheule, H. Sol, and A. Cardon, "Permeability measurement of textile reinforcements with several test fluids," *Compos. Part A Appl. Sci. Manuf.*, vol. 32, no. 10, pp. 1497–1504, 2001, doi: https://doi.org/10.1016/S1359-835X(01)00049-5.

[141] K. M. Yashawantha and A. V. Vinod, "ANFIS modelling of effective thermal conductivity of ethylene glycol and water nanofluids for low temperature heat transfer application," *Therm. Sci. Eng. Prog.*, vol. 24, no. April, p. 100936, 2021, doi: 10.1016/j.tsep.2021.100936.

[142] K. M. Yashawantha and A. V. Vinod, "ANN modelling and experimental investigation on effective thermal conductivity of ethylene glycol:water nanofluids," *J. Therm. Anal. Calorim.*, vol. 145, no. 2, pp. 609–630, 2021, doi: 10.1007/s10973-020-09756-y.

[143] S. G. Advani and M. E. Sozer, *Process Modeling in Composites Manufacturing*. 2003.

[144] J. M. Lawrence, J. Barr, R. Karmakar, and S. G. Advani, "Characterization of preform permeability in the presence of race tracking," *Compos. Part A Appl. Sci. Manuf.*, vol. 35, no. 12, pp. 1393–1405, 2004, doi: 10.1016/j.compositesa.2004.05.002.

[145] G. Struzziero, "Optimisation of the VARTM process," 2015.

[146] A. Lefeuvre, S. Garnier, L. Jacquemin, B. Pillain, and G. Sonnemann, "Anticipating in-use stocks of carbon fiber reinforced polymers and related waste flows generated by the commercial aeronautical sector until 2050," *Resour. Conserv. Recycl.*, vol. 125, pp. 264–272, 2017, doi: 10.1016/j.resconrec.2017.06.023.

[147] S. Jiang, C. Zhang, and B. Wang, "A process performance index and its application to optimization of the RTM process," *Polym. Compos.*, vol. 22, no. 5, pp. 690–701, 2001.

[148] G. Struzziero and A. A. Skordos, "Multi-objective optimization of Resin Infusion," *Adv. Manuf. Polym. \& Compos. Sci.*, vol. 5, no. 1, pp. 17–28, 2019.

[149] X. Ye, C. Zhang, Z. Liang, and B. Wang, "Heuristic Algorithm for Determining Optimal Gate and Vent Locations for RTM Process Design," *J. Manuf. Syst.*, vol. 23, no. 4, 2004.

[150] J. Gou, C. Zhang, Z. Liang, B. Wang, and J. Simpson, "Resin transfer molding process optimization using numerical simulation and design of experiments approach," *Polym. Compos.*, vol. 24, no. 1, pp. 1–12, 2003.

[151] H. Yokoi, N. Masuda, and H. Mitsuhata, "Visualization analysis of flow front behavior during filling process of injection mold cavity by two-axis tracking system," *J. Mater. Process. Technol.*, vol. 130–131, pp. 328–333, 2002, doi: 10.1016/S0924-0136(02)00742-2.

[152] P. Carlone and G. S. Palazzo, "Unsaturated and Saturated Flow Front Tracking in Liquid Composite Molding Processes using Dielectric Sensors," *Appl. Compos. Mater.*, vol. 22, no. 5, pp. 543–557, 2015, doi: 10.1007/s10443-014-9422-3.

[153] S. Koutsonas, "Modelling race-tracking variability of resin rich zones on 90° composite 2.2 twill fibre curved plate," *Compos. Sci. Technol.*, vol. 168, no. April, pp. 448–459, 2018, doi: 10.1016/j.compscitech.2018.08.001.

[154] F. Shi and X. Dong, "3D numerical simulation of filling and curing processes in non-isothermal RTM process cycle," *Finite Elem. Anal. Des.*, vol. 47, no. 7, pp. 764–770, 2011, doi: 10.1016/j.finel.2011.02.007.

[155] E. Ruiz and F. Trochu, "Comprehensive Thermal Optimization of Liquid Composite Molding to Reduce Cycle Time and Processing Stresses," *Polym. Compos.*, 2005, doi: 10.1002/pc.20077.

[156] P. Carlone and G. S. Palazzo, "A Simulation Based Metaheuristic Optimization of the Thermal Cure Cycle of Carbon-Epoxy Composite Laminates," in *AIP Conf. Proc*, 2014, no. April, doi: 10.1063/1.3589483.

[157] V. Achim, F. Ratle, and F. Trochu, "Evolutionary operators for optimal gate location in liquid composite moulding," *Appl. Soft Comput.*, vol. 9, pp. 817–823, 2009, doi: 10.1016/j.asoc.2008.05.008.

[158] I. V Tarasov, S. N. Shevtsov, V. Evlanov, E. E. Orozaliev, V. Tarasov, and V. Evlanov, "Model-Based Optimal Control of Polymeric Composite Cure in Autoclave System," in *IFAC-PapersOnLine*, 2015, vol. 48, no. 11, pp. 204–210, doi: 10.1016/j.ifacol.2015.09.184.

[159] G. Struzziero and A. A. Skordos, "Multi-objective optimisation of the cure of thick

components," *Compos. Part A*, vol. 93, no. November, 2016, doi: 10.1016/j.compositesa.2016.11.014.

[160] J. Wang, P. Simacek, and S. G. Advani, "Use of medial axis to find optimal channel designs to reduce mold filling time in resin transfer molding," *Compos. Part A Appl. Sci. Manuf.*, vol. 95, pp. 161–172, 2017, doi: 10.1016/j.compositesa.2017.01.003.

[161] G. Struzziero, *Optimisation of the VARTM process*. 2015.

[162] J. Liu, J. Xie, and L. Chen, "A hybrid optimization algorithm for gate locations in the liquid composite molding process," *Text. Res. J.*, pp. 1–9, 2022, doi: 10.1177/00405175221109625.

[163] J. Wang, P. Simacek, and S. G. Advani, "Composites : Part A Use of Centroidal Voronoi Diagram to find optimal gate locations to minimize mold filling time in resin transfer molding," *Compos. Part A*, vol. 87, pp. 243–255, 2016, doi: 10.1016/j.compositesa.2016.04.026.

[164] T. Okabe *et al.*, "Multi-objective optimization for resin transfer molding process," *Compos. Part A Appl. Sci. Manuf.*, vol. 92, pp. 1–9, 2017, doi: 10.1016/j.compositesa.2016.09.023.

[165] M. Villière, D. Lecointe, V. Sobotka, N. Boyard, and D. Delaunay, "Experimental determination and modeling of thermal conductivity tensor of carbon/epoxy composite," *Compos. Part A Appl. Sci. Manuf.*, vol. 46, no. 1, pp. 60–68, 2013, doi: 10.1016/j.compositesa.2012.10.012.

[166] I. Ashland, *DERAKANE 8084 Epoxy Vinyl Ester Resin designed to offer increased adhesive strength , superior resistance to DERAKANE ® Epoxy Vinyl Ester Resins*. 2006, pp. 1–3.

[167] M. Yeager and S. G. Advani, "Numerical model of fiber wetting with finite resin volume," *Integr. Mater. Manuf. Innov.*, vol. 4, no. 1, pp. 21–36, 2015, doi: 10.1186/s40192-015-0032-1.

[168] COMSOL, *LiveLink for MATLAB User's Guide*. 2009, p. 329.

[169] D. Karabo\uga and S. Ökdem, "A simple and global optimization algorithm for engineering problems: differential evolution algorithm," *Turkish J. Electr. Eng. Comput. Sci.*, vol. 12, no. 1, pp. 53–60, 2004.

[170] K. Deb, A. Pratap, S. Agarwal, and T. Meyarivan, "A fast and elitist multiobjective genetic algorithm: NSGA-II," *IEEE Trans. Evol. Comput.*, vol. 6, no. 2, pp. 182–197, 2002.

[171] A. Zade and R. R. P. Kuppusamy, "A review on numerical optimization in liquid

composite moulding processes," *Mater. Today Proc.*, vol. 19, pp. 329–332, 2019, doi: 10.1016/j.matpr.2019.07.605.

[172] B. Yenilmez and E. Murat Sozer, "A grid of dielectric sensors to monitor mold filling and resin cure in resin transfer molding," *Compos. Part A Appl. Sci. Manuf.*, vol. 40, no. 4, pp. 476–489, 2009, doi: 10.1016/j.compositesa.2009.01.014.

[173] S. Kobayashi, R. Matsuzaki, and A. Todoroki, "Multipoint cure monitoring of CFRP laminates using a flexible matrix sensor," *Compos. Sci. Technol.*, vol. 69, no. 3–4, pp. 378–384, 2009, doi: 10.1016/j.compscitech.2008.10.029.

[174] S. N. Shevtsov, I. Zhilyaev, and I. A. Parinov, "Optimization of the Composite Cure Process Based on the Thermo-Kinetic Model," *Adv. Mater. Res.*, vol. 569, no. September, pp. 185–192, 2012, doi: 10.4028/www.scientific.net/AMR.569.185.

[175] Y. Gao *et al.*, "Optimization strategy for curing ultra-thick composite laminates based on multi-objective genetic algorithm," *Compos. Commun.*, vol. 31, no. December 2021, p. 101115, 2022, doi: 10.1016/j.coco.2022.101115.

[176] Z. Yuan *et al.*, "Multi-objective approach to optimize cure process for thick composite based on multi-field coupled model with RBF surrogate model," *Compos. Commun.*, vol. 24, no. February, p. 100671, 2021, doi: 10.1016/j.coco.2021.100671.

[177] M. Köppen and K. Yoshida, "Evolutionary Multi-Criterion Optimization," *Evol. Multi-Criterion Optim.*, vol. 4403, no. May 2014, pp. 727–741, 2007, doi: 10.1007/978-3-540-70928-2.

[178] B. Mutnuri and W. Virginia, "Thermal Conductivity Characterization of Composite Materials," 2006.

List of Publications

International Journals

1. **Zade A**, Neogi S, Kuppusamy RRP. Design of Effective Injection Strategy and Operable Cure Window for an Aircraft Wing Flap Composite Part using Neat Resin Characterization and Multi-Physics Process Simulation, *Polymer Composites*, 2022;43(6):3426-3455. https://doi.org/10.1002/pc.26626 **(Q1 SCI Journal Impact Factor: 5.2)**

2. **Zade A,** Neogi S, Kuppusamy RRP. Development of non-dominated sorting differential evolution algorithm for cure cycle optimization of industrial composite parts. *Journal of Reinforced Plastics and Composites*. 2023; 0(0). doi:10.1177/07316844231212527 **(Q1 SCI Journal Impact Factor: 3.1)**

3. **Zade A**, Kumar S, Neogi S, Kuppusamy RRP, Simultaneous Port Number and Location Optimization of Mould Gates-Vents using In-House Coded Stochastic Multi-Objective Optimization Algorithms, **Under Review (Polymer Composites - Q1 SCI Journal Impact Factor: 5.2)**

4. **Zade A**, Neogi S, Kuppusamy RRP, Effect of Process and Material Parameters on the Permeabilities of Reinforcement Mats: Experimentations and Machine Learning Techniques, **Under Review (Fibers and Polymers - SCI Journal Impact Factor: 2.5)**

5. **Zade A**, Pakala, S, Kuppusamy, RRP. Finite element modelling of non-isothermal curing kinetics for resin transfer moulding process, Materials Today: Proceedings, 2021; 47: 5281-5288. (SCOPUS)

6. Kuppusamy RRP, **Zade A**, Kumar K. Time-temperature-cure process window of epoxy-vinyl ester resin for applications in liquid composite moulding processes, Materials Today: Proceedings, 2021; 39:1407-1411. https://doi.org/10.1016/j.matpr.2020.05.048 (SCOPUS)

7. **Zade A**, Kuppusamy RRP. A comprehensive review on process optimization of composite moulding processes. Journal of Manufacturing Technology & Research. 2020; 13:1-17. (SCOPUS)

8. **Zade A**, Kuppusamy RRP. Mould fill time sensitivity analysis using isothermal mould filling simulations for applications in liquid composite moulding processes. Materials Today: Proceedings. 2020; 27:167-71. https://doi.org/10.1016/j.matpr.2019.09.212 (SCOPUS)

9. **Zade A**, Kuppusamy RRP. A review on numerical optimization in liquid composite moulding processes. Materials Today: Proceedings. 2019; 19:329-32. https://doi.org/10.1016/j.matpr.2019.07.605 (SCOPUS)

International Conferences

1. **Zade A**, Pakala, S, Kuppusamy, RRP "Finite Element Modelling of Non-isothermal Curing Kinetics for Resin Transfer Moulding (RTM) Process" i-SMaRT 2021, 22 - 23 April 2021, FISAT Angamaly, Ernakulum Dt., Kerala, India.

2. **Zade A**, Neogi S, Kuppusamy RRP "Optimization of Thermal Profile for Automotive Composite Part using Non-isothermal RTM Cure Simulation" at 2nd International Conference on Theoretical, Analytical and Computational Methods for Composite Materials and Composite Structures (online) 5-7 March 2021.

3. **Zade A**, Kuppusamy RRP "A Comprehensive review on Single and Multi-Objective Optimization of Liquid Composite Moulding Process" ICEM 2020, 10 – 12 December 2020, MNIT Jaipur, Rajasthan, India.

4. Kuppusamy RRP, **Zade A**, Kumar K. "Time-Temperature cure process window for Epoxy-vinyl ester resin for applications of Liquid Composite Moulding processes" IMME 19, 27 – 28 December 2019, NIT Trichy, Tamil Nadu, India. **Received the best poster award.**

5. **Zade A**, Kuppusamy RRP "Mould fill time sensitivity analysis using isothermal mould filling simulations for applications in liquid composite moulding processes" ICRAMM 2019, 12 – 14 September 2019, KLE Dr. M S Sheshgiri College of Engineering & Technology, Belgavi, Karnataka, India.

6. **Zade A**, Kuppusamy RRP "A Review on Numerical Optimization in Liquid Composite Moulding (LCM) Processes" ICMMSE 2019, 16 – 17 August 2019, CMR Institute of Technology, Hyderabad, Telangana, India.

Book Chapter

1. **Zade A**, Kuppusamy RR. A Comprehensive Review on Single- and Multi-Objective Optimization of Liquid Composite Moulding Process, In: Recent Advances in Smart Manufacturing and Materials, Springer Nature Singapore Pte Ltd. Chapter 6, 2020. (SCOPUS).

Curriculum Vitae

Name   Zade Anita Dnyanba

Gender   Female

Nationality   Indian

Date of Birth   03/04/1992

Email   anitazade1@gmail.com

Address   S.S. Gade, Naik Nagar, Opposite to New Collector Office, Nanded Road, Hingoli – 431513, India.

Education

Degree	Stream	College	Year of Study
PhD	Chemical Engineering	National Institute of Technology (NIT) Warangal, India	2018 – Present
M. Tech	Chemical Engineering	Indian Institute of Technology (IIT) Gandhinagar, India	2014 -2016
B. Tech	Chemical Engineering	Shri Guru Gobind Singh ji Institute of Engineering and Technology (SGGSIE&T), Nanded	2010 - 2014

Experience

Research Project Staff at IIT Gandhinagar, India   2016 - 2018

Achievements

- Held the position of Girls Senator during 2017-2018 at IIT Gandhinagar.

- Received best poster presentation award at an international conference, IMME 2019, held on 27 – 28 December 2019, NIT Trichy, Tamil Nadu, India.